
**Measurement of the $t\bar{t}H$ Production Cross-Section in
the Non-Resonant Four Lepton Final State in pp
Collisions at $\sqrt{s} = 13$ TeV with the ATLAS Detector**

Dissertation

zur Erlangung des mathematisch-naturwissenschaftlichen Doktorgrades
„Doctor rerum naturalium“
der Georg-August-Universität Göttingen

im Promotionsstudiengang Physik
der Georg-August University School of Science (GAUSS)

vorgelegt von

Stephen Eggebrecht

aus Kassel

Göttingen, 2024

Betreuungsausschuss

Prof. Dr. Arnulf Quadt

II. Physikalisches Institut, Georg-August-Universität Göttingen

Prof. Dr. Stanley Lai

II. Physikalisches Institut, Georg-August-Universität Göttingen

Prof. Dr. Steffen Schumann

Institut für Theoretische Physik, Georg-August-Universität Göttingen

Mitglieder der Prüfungskommission:

Referent: Prof. Dr. Arnulf Quadt

II. Physikalisches Institut, Georg-August-Universität Göttingen

Koreferent: Dr. Frédéric Déliot

CEA, Université Paris-Saclay

Weitere Mitglieder der Prüfungskommission:

PD Dr. Andrea Helen Knue

Fakultät für Physik, Technische Universität Dortmund

Prof. Dr. Karl-Henning Rehren

Institut für Theoretische Physik, Georg-August-Universität Göttingen

Prof. Dr. Ansgar Reiners

Institut für Astrophysik, Georg-August-Universität Göttingen

Prof. Dr. Steffen Schumann

Institut für Theoretische Physik, Georg-August-Universität Göttingen

Tag der mündlichen Prüfung: 3. Februar 2025

Measurement of the $t\bar{t}H$ Production Cross-Section in the Non-Resonant Four Lepton Final State in pp Collisions at $\sqrt{s} = 13$ TeV with the ATLAS Detector

Abstract

This thesis presents the measurements of the associated production of a top quark pair with a Standard Model Higgs boson in multi-lepton final states, focusing on the measurement of the inclusive cross-section in the 4ℓ channel. The analysis uses the full Run 2 data set, corresponding to an integrated luminosity of 140 fb^{-1} , collected in proton-proton collisions at a centre-of-mass energy of $\sqrt{s} = 13$ TeV. The analysis covers six final states, defined by the number and flavour of charged-lepton candidates. Machine learning techniques are used for all channels to improve signal sensitivity. Leading prompt background contributions from $t\bar{t}Z$, $t\bar{t}W$, and diboson production are constrained by additional regions populated with those backgrounds. Moreover, contributions from fake and non-prompt leptons are estimated using data-driven methods such as the fake factor or template method. The observed signal strength, the ratio of the measured signal yield over the Standard Model prediction, is extracted using a profile likelihood fit. For the 4ℓ channel, the observed signal strength is

$$\mu_{t\bar{t}H} = 0.53^{+0.67}_{-0.53} = 0.53^{+0.66}_{-0.51} (\text{stat.})^{+0.13}_{-0.13} (\text{sys.}),$$

corresponding to an observed (expected) significance of 0.95σ (1.80σ). The measured signal strength for the combination of all six channels is

$$\mu_{t\bar{t}H} = 0.63^{+0.20}_{-0.19} = 0.63^{+0.17}_{-0.16} (\text{stat.})^{+0.11}_{-0.10} (\text{sys.}).$$

It corresponds to an observed (expected) significance of 3.3σ (5.3σ). The measured inclusive cross-section is found to be $321^{+102}_{-99}\text{ fb}$. The compatibility is 7.2 % with the Standard Model prediction of $507^{+35}_{-50}\text{ fb}$. The signal strength is also measured in bins of the Higgs boson transverse momentum and demonstrates a compatibility of 28 % with the Standard Model prediction.

Messung des $t\bar{t}H$ Wirkungsquerschnitts im Nicht-Resonanten Endzustand mit vier Leptonen in pp-Kollisionen bei $\sqrt{s} = 13$ TeV mit dem ATLAS Detektor

Zusammenfassung

Diese Arbeit beschreibt die Messung der assoziierten Produktion von einem Top-Quarkpaar mit einem Standardmodell Higgs Boson in Multi-Leptonen Endzuständen, mit einem Fokus auf die Messung des inklusiven Wirkungsquerschnitts im 4ℓ Kanal. Die Analyse verwendet den Run 2 Datensatz, welcher einer integrierten Luminosität von 140 fb^{-1} entspricht und in Proton-Proton-Kollisionen bei einer Schwerpunktsenergie von $\sqrt{s} = 13 \text{ TeV}$ aufgenommen worden ist. Die Analyse deckt sechs Endzustände ab, die durch die Anzahl und Flavour der geladenen Leptonen Kandidaten definiert sind. Techniken des maschinellen Lernens werden in allen Kanälen angewendet, um die Signalsensitivität zu erhöhen. Die wichtigsten Untergründe entstehen durch die $t\bar{t}Z$, $t\bar{t}W$, und Diboson Produktion, welche durch zusätzliche Analyseregionen abgeschätzt werden. Weiterhin werden Beiträge von *Fake* und *Non-Prompt* Leptonen mit auf Daten basierten Methoden, wie etwa der *Fake Factor* oder *Template* Methode, abgeschätzt. Die beobachtete Signalstärke, das Verhältnis des gemessenen Beitrages von Signal im Verhältnis zur Vorhersage des Standardmodells, wird von einem Profile-Likelihood-Fit bestimmt. Für den 4ℓ Kanal beträgt die beobachtete Signalstärke:

$$\mu_{t\bar{t}H} = 0.53^{+0.67}_{-0.53} = 0.53^{+0.66}_{-0.51} (\text{stat.})^{+0.13}_{-0.13} (\text{sys.}),$$

was einer beobachteten (erwarteten) Signifikanz von 0.95σ (1.80σ) entspricht. Die gemessene Signalstärke für die Kombination aller Kanäle beträgt:

$$\mu_{t\bar{t}H} = 0.63^{+0.20}_{-0.19} = 0.63^{+0.17}_{-0.16} (\text{stat.})^{+0.11}_{-0.10} (\text{sys.}).$$

Dies entspricht einer beobachteten (erwarteten) Signifikanz von 3.3σ (5.3σ). Der inklusive Wirkungsquerschnitt beträgt $321^{+102}_{-99} \text{ fb}$. Die Kompatibilität mit der Standardmodell-Vorhersage von $507^{+35}_{-50} \text{ fb}$ beträgt 7.2 %. Die Signalstärke wird zusätzlich in Werten des transversalen Impulses des Higgs Bosons gemessen und zeigt eine Kompatibilität von 28 % mit der Standardmodell-Vorhersage.

Contributions by the Author

The ATLAS collaboration has approximately 6 000 members and 3 000 scientific authors who work on multiple aspects of the ATLAS experiment. The maintenance and operation of the ATLAS experiments involve several groups, highly specialised for specific tasks. However, detector operation and quality checks of the collected data are not the only tasks. Other groups work on optimising reconstruction methods for physics objects, such as electrons, muons, and jets, providing recommendations for analyses. Other work on tool and framework development for statistical analysis. The latter requires predictions, which are realised with Monte Carlo simulations of high-energy collisions. The production of Monte Carlo samples is done centrally.

Each analysis uses data and simulated samples by applying specific cuts or additional event information or variables. All of the previously mentioned fields are so extensive that it would be impossible for a single person to manage them. This is also true for the analysis, which is performed by a roughly fifty-member team. Therefore, the contributions of the author are summarised briefly.

The author is part of the $t\bar{t}H$ multi-lepton analysis and is the leading analyst of the non-resonant $t\bar{t}H \rightarrow 4\ell$ channel. This work involves the production of smaller channel-specific Monte Carlo samples, often called N-tuples. They include additional variables for the training of a dense neural network for signal and background event separation. Optimisation steps to choose the lepton definition in the 4ℓ channel are made by the author, together with the training and evaluation of a dense neural network. The latter is used to design signal and control regions for statistical analysis.

The author designed additional control regions to estimate fake lepton backgrounds and include them in the statistical analysis. Extensive studies of the fit model were conducted. The work is documented in an internal ATLAS note, providing more detail¹. The author participated in the main N-tuple production of the $t\bar{t}H$ multi-lepton analysis, improving parts of the production procedure. Furthermore, the author included and evaluated PDF-related uncertainties for the analysis.

The analysis strategy and fake background estimation of channels other than the

¹The internal note can be found on the CERN document server: <https://cds.cern.ch/record/2874777>. It is not publicly accessible.

4ℓ channel are described briefly in Section 6.3 to Section 6.6 and in Section 7.2 to Section 7.4. The 3ℓ channel was analysed by David Munoz Perez and Lorenzo Variale, and the $2\ell\text{SS}+0\tau_{\text{had}}$ by Chen Jia and Jialin Li. The $2\ell\text{SS}+1\tau_{\text{had}}$ channel was analysed by Nello Bruscano and Luca Martinelli. Wei-Ming Yao and Babar Ali mainly contributed to the $2\tau_{\text{had}}$ channels. Alberto Carnelli studied the CP interpretation, while Vera Maiboroda performed the Higgs transverse momentum reconstruction for the STXS setup. Gianna Loeschcke Centeno combined all analysis channels.

Besides the work on the $t\bar{t}H$ multi-lepton analysis, the author contributed to the inner detector radiation damage group by studying the impact of radiation damage to the PIXEL end-caps. Other contributions were part of developing the *Prompt Lepton Isolation Tagger* (PLIT) for Run 3. The author worked on software building for modelling and validation studies for the PLIT application to electrons.

Acknowledgements

The path towards a PhD is long, but fortunately, a PhD student is not alone on his journey. I was lucky to be accompanied by many great people. First, I want to thank Arnulf Quadt, my PhD supervisor. You gave me the opportunity to do a PhD in particle physics and be part of your working group. Furthermore, you allowed me to join multiple schools and conferences and be at CERN. I also appreciated the numerous non-physics discussions we had. Moreover, I want to thank Steffen Schumann and Stanley Lai for being members of my thesis advisory committee.

I want to thank Elizaveta Shabalina for supervising and discussing each and every aspect of my analysis. This thesis would not have been possible without your help, guidance, and patience. I want to say thanks to the $t\bar{t}H$ multi-lepton analysis team. Thank you, Baptiste Ravina, for your help, especially at the beginning of the analysis and for proofreading. I also thank Marcello Bindi, Jörn Große-Knetter, Karsten Köneke, Maximilian Horzela, Tim, Matthias, Felix, Thomas, Anne, Marike, and Benjamin for proofreading many sections and interesting discussions.

Thanks to all of my friends from the second institute. I am grateful for the lunch and coffee breaks, the many discussions, and the funny situations we had. Thank you for the memes created over the last few years. Thank you for the Aperol evenings and other *Post work social* activities!

Ich möchte mich vor allem bei meiner Familie bedanken. Ich danke meiner Mutter und meinem Vater, die mich in jeder Situation unterstützen. Dieser Dank geht ebenso an meine Oma, meine Schwester Sarah, meinen Bruder Andreas und meinen Schwager Michael. Danke, dass ihr für mich da seid. Ein neues Mitglied der Familie möchte ich noch erwähnen, nämlich meinen Neffen Elias.

Zum Schluss möchte ich noch dem wichtigsten Menschen in meinem Leben danken. Ich danke dir, David, für deine ständige Unterstützung!

Contents

1	Introduction	1
2	The Standard Model of Particle Physics	5
2.1	Introduction to the SM	7
2.2	Quantum Chromodynamics	8
2.3	Electroweak Unification and Higgs Mechanism	10
2.4	The Higgs Boson	14
2.5	The Top Quark	17
2.6	The $t\bar{t}H$ Process	20
3	Particle Physics and Simulation	25
3.1	Matrix Element Generation	26
3.2	Parton Shower	28
3.3	Hadronisation Models	30
3.4	Monte Carlo Samples	31
4	Experimental Setup	37
4.1	The Large Hadron Collider	37
4.2	The ATLAS Experiment	41
4.3	Radiation Damage Effects on the Pixel Detector	48
5	Definition and Reconstruction of Physics Objects	53
5.1	Event Quality and Trigger Strategy	54
5.2	Object Reconstruction and Definition	55
5.3	Overlap Removal	67
6	Analysis Strategy for the $t\bar{t}H$ Multi-Lepton Process	69
6.1	Machine Learning Introduction and Application	73
6.2	The 4ℓ Channel	77
6.3	The $3\ell+0\gamma_{\text{had}}$ Channel	94

6.4	The $2\ell\text{SS}+0\tau_{\text{had}}$ Channel	94
6.5	The $2\ell\text{SS}+1\tau_{\text{had}}$ Channel	95
6.6	The $2\ell\text{OS}+2\tau_{\text{had}}$ and $1\ell+2\tau_{\text{had}}$ Channels	96
6.7	Higgs Boson Transverse Momentum Reconstruction	96
7	Fake Background Estimation for the $t\bar{t}H$ Multi-Lepton Analysis	99
7.1	Fake Background Estimation in the 4ℓ Channel	102
7.2	Fake Background Estimation in the $2\ell\text{SS}+0\tau_{\text{had}}$ and $3\ell+0\tau_{\text{had}}$ Channels	112
7.3	Fake Background Estimation in the $2\ell\text{SS}+1\tau_{\text{had}}$ Channel	113
7.4	Fake Background Estimation in the $2\ell\text{OS}+2\tau_{\text{had}}$ and $1\ell+2\tau_{\text{had}}$ Channels	113
8	Systematic Uncertainties	115
8.1	Experimental Uncertainties	116
8.2	Modelling Uncertainties	117
8.3	Handling of Systematic Uncertainties	119
8.4	Overview of Systematic Uncertainties	120
9	Statistical Analysis and Results	123
9.1	The Profile Likelihood Fit	123
9.2	Fit Model Study for the 4ℓ Channel	125
9.3	Fit to ATLAS Data in the 4ℓ Channel	135
9.4	Combined Fit for the inclusive $t\bar{t}H$ Cross-Section and STXS Setup .	141
10	Summary and Outlook	143
	Bibliography	147
A	List of MC Samples	169
B	Activation Function Definitions	173
C	Lepton Definition Optimisation	175
D	Validation Plots	177
E	Shape Comparison of DNN Inputs	195
F	Negative Weight Treatment	201
G	Signal and Control Region Optimisation for the 4ℓ Phase-Space	205
H	Transverse Momentum Reweighting	207
I	Pruning for the 4ℓ Channel	209

CHAPTER 1

Introduction

Hypothesis: All swans are white.
Initial Condition: There are swans at the lake.
Basic Statement: The swans at the lake are white.
Observation: There are black swans at the lake.

Common falsifiability example.

The term *physics* originates from the Greek word *phúsis* and means origin, nature, and property. The discipline of physics has its origins in ancient Greek philosophy, with notable achievements such as the measurement of the earth's circumference by Eratosthenes and the formulation of the Archimedes' principle by Archimedes. Other notable mathematical ones are Pythagoras's theorem and Thales's theorem.

The first formulation of modern-like epistemology as the foundation of modern physics was established during the Renaissance with two established approaches, rationalism and empiricism¹. The most notable representative of the former idea is René Descartes, most famous for his work in *Meditationes de Prima Philosophia* marking the starting point for modern philosophy and, therefore, science. While rationalism uses reasoning to find truth, empiricism relies on experience or experiments. A notable figure arguing in favour of experiments was Francis Bacon². The different approaches might resemble discussions on the relationship between theoretical and experimental physics. Both approaches are necessary and have demonstrated huge success, especially in combination. The first and most famous successful interplay was achieved with the formulation of Newton's law of motion by Isaac Newton in

¹There is also idealism.

²According to a legend, Francis Bacon died of pneumonia due to an experiment, attempting to extend the shelf life of chicken using snow.

1678 using mathematical descriptions and empirical data collected from astronomical objects.

The opening quote describes an application of the method introduced by Karl Popper, using the famous black swan example. Karl Popper attempted to deal with the problem of induction³ and demarcation, unanswered by rationalism and empiricism. In his book *Die Logik der Forschung* [1, 2]⁴ he demonstrates the inability of the induction method to generalise from certain observation. From observing a single white swan, one may not conclude that all swans are white. Furthermore, Popper introduces the method of falsifiability, effectively inverting the previous statement. Therefore, scientific theories can be proven to be incorrect rather than confirmed as true. Besides avoiding the application of induction, falsification provides criteria to distinguish scientific methods from pseudoscientific or non-scientific, dealing with the demarcation problem. Another crucial step is the formulation of basic statements derived from the hypothesis and giving rise to possible observations. In the opening quote, the hypothesis ‘*All swans are white.*’ is a theory which allows, under certain initial conditions, that describes an explicit situation, to deduce a basic statement that there is a white swan at noon at a lake. This basic statement can be tested. The set of basic statements may contain the fact that this particular swan at the lake is white or black. Observing the latter would immediately falsify the mentioned theory.

In the same spirit of progressively improving predictions in interplay with measurements, therefore following the method of falsification, the Standard Model of particle physics is formulated. It is the state-of-the-art theoretical description of three out of four fundamental forces and is the result of over seventy years of research. Two of the latest additions to the Standard Model are the top quark and the Higgs boson. The former was predicted by Makoto Kobayashi and Toshihide Maskawa in 1973 [3] attempting to explain observed CP violation by introducing a new quark generation. In 1995, the top quark was discovered by the CDF and DØ collaborations at the TEVATRON [4, 5]. The Higgs boson was independently predicted in 1964 by Peter Higgs and two research groups: François Englert and Robert Brout from the Université Libre de Bruxelles and Thomas Kibble, Carl Hagen, and Gerald Guralnik from the Imperial College in London. The introduction of the Brout-Englert-Higgs mechanism [6–9] explains the presence of massive gauge bosons and predicts the existence of the Higgs boson. In 2012, the ATLAS and CMS collaborations discovered the Higgs boson at the LHC [10–12]. With the discovery of new particles, the question of their properties came up. There were multiple theoretical candidates with different properties: the Higgs boson is a spin-1 or spin-2 particle. Others are: the electromagnetic charge of the top quark is $q' = -4/3$. The former can be tested against the spin-0 hypothesis with $H \rightarrow ZZ^* \rightarrow 4\ell$, $H \rightarrow WW^* \rightarrow \ell\nu\ell\nu$, and $H \rightarrow \gamma\gamma$ events and their impact on kinematic observables. The spin-1 and spin-2 hypotheses

³Not to be confused with mathematical induction, in German: *vollständige Induktion*.

⁴There is also an English version, translated by Karl Popper in 1959.

were excluded and therefore falsified [13]. The different charge scenarios for the top quark, namely electromagnetic charge of $q = 2/3$ or $q' = -4/3$, are tested with single-lepton $t\bar{t}$ events. The analysis strategy attempts to identify the b -jet flavour and the decay origin, either to be the leptonically or hadronically decaying top quark. The $q' = -4/3$ hypothesis was falsified [14].

However, it is not only the properties of the individual particles that are subject to measurements. The Yukawa interaction between the Higgs boson and the top quark is particularly interesting and can be tested with $t\bar{t}H$ events. It allows further exploration of the Higgs mechanism properties and vacuum stability. There are several analysis strategies targeting different Higgs boson decay modes. This thesis presents the $t\bar{t}H$ multi-lepton analysis [15] with a special focus on the non-resonant $t\bar{t}H \rightarrow 4\ell$ channel. The multi-lepton analysis predominantly targets Higgs boson decay modes to heavy gauge bosons with subsequent decay to leptons and decay modes to tau leptons with subsequent hadronic decay. The analysis is split by the number of light leptons and hadronically decaying taus, providing unique multi-lepton final states. The $t\bar{t}H$ multi-lepton analysis includes measurements of the inclusive $t\bar{t}H$ production cross-section and measurements of the $t\bar{t}H$ production cross-section in bins of the Higgs boson transverse momentum using the *Simplified Template Cross Sections* (STXS) approach. Furthermore, studies on the CP properties of the Higgs-top-top coupling are conducted.

This thesis is organised as follows. The Standard Model of particle physics is introduced in Chapter 2. It provides information on the mathematical foundation of the Standard Model with special attention on quantum chromodynamics, electroweak unification, and the Brout-Englert-Higgs mechanism. A description of the Higgs boson and the top quark and their properties, production, and decay modes follows. The last section of the chapter is dedicated to the specifics of the $t\bar{t}H$ production. The simulation of high-energy particle collisions is described in Chapter 3, presenting the essential steps of the simulation chain. It also describes and summarises the simulated samples used in the $t\bar{t}H$ multi-lepton analysis. The Large Hadron Collider and the ATLAS detector are introduced in Chapter 4. The latter includes information about the various subdetectors and the trigger system. The impact of radiation damage to the PIXEL end-caps is discussed in the last section of Chapter 4. The various reconstruction methods for analysis objects are addressed in Chapter 5 with special attention given to the lepton reconstruction as they play a significant role in the $t\bar{t}H$ multi-lepton analysis. The analysis strategy of the $t\bar{t}H$ multi-lepton analysis is presented in Chapter 6. It provides the analysis channel definitions and information about multivariate analysis techniques and their application for the channels. The 4ℓ channel is discussed with particular attention, while an additional summary is given for the remaining channels. The estimation of fake backgrounds is discussed in Chapter 7. It starts with the various sources of fake leptons and moves on to estimation methods. The chapter emphasises the 4ℓ channel and provides an overview of the remaining channels. The different sources of system-

atic uncertainties and their implementation in the statistical analysis are presented in Chapter 8. The methods for the statistical analysis are shown in Chapter 9. It includes studies on the fit model of the 4ℓ channel and results on the measured signal strength. Additionally, the combined result of all channels for the inclusive $t\bar{t}H$ production cross-section and production cross-section in STXS bins of the transverse momentum of the Higgs boson are presented. Chapter 10 summarises the results presented in this thesis and provides an outlook.

The Standard Model of Particle Physics

	I	II	III		
Mass	2.16 MeV	1.27 GeV	172.7 GeV	0	125.25 GeV
Charge	$\frac{2}{3}$	$\frac{2}{3}$	$\frac{2}{3}$	0	0
Spin	$\frac{1}{2}$	$\frac{1}{2}$	$\frac{1}{2}$	1	0
	u Up	c Charm	t Top	g Gluon	H Higgs
Quarks	4.67 MeV $-\frac{1}{3}$ $\frac{1}{2}$ d Down	93.4 MeV $-\frac{1}{3}$ $\frac{1}{2}$ s Strange	4.18 GeV $-\frac{1}{3}$ $\frac{1}{2}$ b Bottom	0 0 1 γ Photon	
	< 1.1 eV 0 $\frac{1}{2}$ ν_e Electron Neutrino	< 0.19 MeV 0 $\frac{1}{2}$ ν_μ Muon Neutrino	< 18.2 MeV 0 $\frac{1}{2}$ ν_τ Tau Neutrino	91.19 GeV 0 1 Z Z Boson	
Leptons	0.511 MeV -1 $\frac{1}{2}$ e Electron	105.66 MeV -1 $\frac{1}{2}$ μ Muon	1.78 GeV -1 $\frac{1}{2}$ τ Tau	80.37 GeV ± 1 1 W W Boson	
				Gauge Bosons Vector Bosons	Scalar Bosons

Figure 2.1: An overview of the particle content of the SM. The mass, electromagnetic charge, and spin values are shown for each particle. The values are taken from Ref. [16].

The Standard Model of Particle Physics (SM) [17–28] is the leading theory describing three out of four fundamental forces and is, therefore, the foundation for every analysis in the field of particle physics. The mathematical description of the SM

is a quantum field theory with interactions generated by applying gauge invariance under three gauge groups $SU(3)_C \times SU(2)_L \times U(1)_Y$ representing the three out of four fundamental forces. Next to the mathematical description, the SM arranges the discovered particles by their quantum numbers and subsequently by their coupling behaviour, illustrated in Figure 2.1.

The SM is divided into fermions with half-integer spin and obeying Pauli's exclusion principle and Fermi-Dirac statistics and into bosons obeying Bose-Einstein statistics and carrying integer spin. There are four vector bosons with spin one and subject to three different fundamental forces. The term *vector* boson characterises the interaction type. The photon is massless and mediates the electromagnetic force known from classical electrodynamics. The bosons associated with the weak interaction, with the charged ones mediating nuclear decays, are the massive Z and W bosons. Unlike Z bosons, the W bosons carry an electromagnetic charge of ± 1 . The eight gluons are mediators of the strong interaction, explaining atomic nuclei binding. Like the photons, they are massless but carry colour charge and can couple to each other directly. The Higgs boson is the only fundamental particle with spin zero called a scalar boson. It is a massive particle and is predicted by the Brout-Englert-Higgs mechanism [6–9], explaining massive weak gauge boson fields. It was discovered by the ATLAS and CMS collaborations at the LHC in 2012 [10–12].

Fermions are called matter particles since all visible matter is composed of them. All fermions of the SM have one-half spin and are characterised by their coupling nature into two categories: the first one describes the quark-sector having six quarks and six anti-quarks with all of them carrying colour-charge and therefore being subject to the strong interaction. The quarks are grouped into three generations, with each generation including one up-type quark with an electromagnetic charge of $q = \frac{2}{3}$ and a down-type quark with $q = -\frac{1}{3}$. The up-type quarks per generation are up, charm, and top with increasing generation, and down, strange, and bottom for the down-type quarks, respectively. As a result of the gluon self-coupling, quarks can not be observed as bare particles but will form colourless hadrons due to quark confinement. Hadrons are further classified based on their quark and quark flavour content: baryons contain three (anti-) quarks, while mesons are made of a quark and anti-quark¹. The most prominent examples of baryons are protons (uud) and neutrons (udd). These stable particles² form ordinary matter like atomic nuclei. The lightest mesons are pions (π^\pm, π^0) with quark content of the first generation and average

¹There are tetraquarks which contain four quarks. The $Z_c(3900)$ was measured by the Belle collaboration [29] and the $X(4140)$ was observed by the LHCb collaboration [30]. Furthermore, there are pentaquarks, which contain five quarks. Like the charmonium-pentaquark P_c^+ observed by the LHCb collaboration [31] in 2015.

²Some theories predict proton decays. However, these theory predictions are not successful during experiments or predict a lifetime in the order of the universe's age. A free neutron has an average lifetime of some seventeen minutes. However, neutrons can decay to protons via β -decay even in bound states like atomic nuclei.

lifetime of $\tau_{\pi^\pm} \approx 2.6 \times 10^{-8} \text{ s}$ [16] and $\tau_{\pi^0} \approx 8.43 \times 10^{-17} \text{ s}$ [16]. From a collider physics perspective, the charged pions can be considered stable. Mesons containing at least one b -quark, such as B_d^0 , B_d^\pm , or B_s^\pm , play an important role in identifying b -jets due to their long lifetime, which turns out to be especially important in top-quark physics. The application of b -jet tagging is described in Section 5.2.5.

Leptons are the second category of fermions and are not subject to strong interactions since they do not carry a colour charge. They are divided into three generations with one charged lepton and corresponding uncharged lepton. The charged lepton per generation is called electron e , muon μ , and tau τ with increasing mass per generation. The uncharged leptons are called neutrinos and are associated with their charged lepton. Per generation they are electron neutrino ν_e , muon neutrino ν_μ , and tau neutrino ν_τ . The higher-generation charged leptons are unstable and will subsequently decay into stable particles like electrons. Since the charge leptons carry an electromagnetic charge, they can exchange photons, while neutrinos only couple via the weak interaction. In the SM, neutrinos are considered to be massless.

Not all phenomena can be explained by the SM. Most notable is the exact nature and properties of dark matter and the large discrepancy between matter and anti-matter abundance in the universe. Further problems are the inclusion of gravity as an additional fundamental force and the masses of the neutrinos. Other problems are aesthetic ones, such as the hierarchy problem.

Section 2.1 introduces the local gauge invariance principle, explaining the fundamental symmetries of the SM. The theoretical description of the local gauge symmetry leading to the mathematical description of the strong interaction is presented in Section 2.2. The introduction to the Brout-Englert-Higgs mechanism is in Section 2.3, providing an overview of the mathematical description of the electromagnetic unification and necessity for the Brout-Englert-Higgs mechanism to generate massive gauge bosons. The various properties of the top quark, together with a description of the different production and decay modes of top quark pairs, are described in Section 2.5. The last Section 2.6 is dedicated to the signal process, top quark pair production in association with a Higgs boson, describing motivation, properties, and three primary analysis approaches for measurements. The multi-lepton approach is discussed in this thesis.

2.1 Introduction to the SM

The SM Lagrange density \mathcal{L}_{SM} is given by the sum of the Lagrange density for quantum chromodynamics \mathcal{L}_{QCD} , describing the strong interaction, and the Lagrange density \mathcal{L}_{EW} , describing the unified electroweak interaction, together with the Brout-Englert-Higgs mechanism:

$$\mathcal{L}_{\text{SM}} = \mathcal{L}_{\text{QCD}} + \mathcal{L}_{\text{EW}}. \quad (2.1)$$

The Lagrangian is composed of various parts which describe free fields. The fermionic fields ψ have to satisfy the Dirac Lagrange density

$$\mathcal{L}_{\text{fermion}} = i\bar{\psi}\gamma^\mu\partial_\mu\psi - m\bar{\psi}\psi, \quad (2.2)$$

implying that free fields correspond to mass eigenstates. Interactions are introduced by enforcing gauge invariance under a local gauge group, following Noether's theorem [32]. These are realised by special unitary groups $\text{SU}(N)$ ($\text{U}(1)$ for $N = 1$) with the transformation behaviour $U = \exp(ig\theta^a T_a)$ and generators T_a . The generators fulfil commutation relations $[T_a, T_b] = if_{ab}^c T_c$ with f_{ab}^c as the structure constants. The Lagrangian in Equation 2.2 is only invariant under transforming the fields $\psi \rightarrow U\psi$ by replacing the derivative with the covariant derivative

$$\partial_\mu \rightarrow D_\mu = \partial_\mu + igA_\mu^a T_a, \quad (2.3)$$

with A_μ^a as the newly introduced gauge fields with an additional kinematic term. The number of needed gauge fields to compensate for the additional free parameters is equal to the number of generators of the local gauge group. The coupling strength between the gauge and fermionic fields is reflected in the coupling strength g . The SM Lagrange density \mathcal{L}_{SM} is invariant under three local gauge groups

$$G_{\text{SM}} = \text{SU}(3)_C \times \text{SU}(2)_L \times \text{U}(1)_Y, \quad (2.4)$$

with $\text{SU}(3)_C$ corresponding to quantum chromodynamics (QCD) and strong interaction, and $\text{SU}(2)_L \times \text{U}(1)_Y$ to the unified electromagnetic and weak forces. The latter also requires introducing the Brout-Englert-Higgs mechanism to describe massive gauge bosons since the local gauge principle forbids mass terms associated with gauge fields. Furthermore, fermion masses are explained via Yukawa coupling between the Higgs boson and fermions. The local gauge groups of the SM are renormalisable and predict finite cross-sections.

2.2 Quantum Chromodynamics

Quantum chromodynamics (QCD) [33–36] is the underlying description of the strong interaction and is based on the local gauge group $\text{SU}(3)_C$ acting on the first part of the SM Lagrangian from Equation 2.1 and is given after replacing the derivative with the covariant one by:

$$\mathcal{L}_{\text{QCD}} = \sum_q \bar{\psi}_{q,a} \left[\underbrace{(i\gamma^\mu\partial_\mu - m_q)}_{\text{quark propagator}} \delta_{ab} - \underbrace{g_S\gamma^\mu\lambda_{ab}^C G_\mu^C}_{\text{quark gluon interaction}} \right] \psi_{q,b} - \underbrace{\frac{1}{4}G_{\mu\nu}^k G_k^{\mu\nu}}_{\text{gluon propagator}}. \quad (2.5)$$

The first part of the Lagrangian is similar to Equation 2.2 since quarks are spin one-half fermions with mass m_q . The sum runs over all quarks flavours $q = (u, c, t, d, s, b)$ and $a = (r, g, b)$ denotes the three colour states called *red*, *green*, and *blue* and explains the subscript of the local gauge C standing for colour. Anti-quarks carry

corresponding anti-colours, while gluons carry both colour and anti-colour. Interaction is introduced by the second part of Equation 2.5 and describes a vector coupling structure with gluon fields G_μ^C with $C = (1, \dots, 8)$ as the colour index. The coupling term includes the generators λ_{ab} of the local gauge group $SU(3)_C$ are given by the *Gell-Mann* matrices [37] and describes how interaction of gluons rotates the colour state of quarks within the $SU(3)_C$ colour space. The interaction includes all three-point vertices between quark, anti-quark, and gluon ($q\bar{q}g$) with no flavour change for quarks while preserving colour charge. The last term of Equation 2.5 includes the field strength tensor $G_{\mu\nu}^a$ for gluon fields G_μ^a defined as

$$G_{\mu\nu}^a = \partial_\mu G_\nu^a - \partial_\nu G_\mu^a - g_S f_{abc} G_\mu^b G_\nu^c, \quad (2.6)$$

with indices $a, b, c = (1, \dots, 8)$ and f_{abc} as the structure constant for the $SU(3)$, obtained by the commutators $[\lambda^a, \lambda^b] = 2if_{abc}\lambda^c$. Since the commutator is non-zero, $SU(3)$ is called a non-Abelian Lie group. Next to the description of the free gluon field propagation, the term gives rise to the gluon self-interaction mediated by three- and four-point gluon vertices. The coupling strength is given by $g_S = \sqrt{4\pi\alpha_S}$ with the strong coupling constant α_S . In perturbation theory calculations, self-interaction and loop corrections may cause divergences, leading to non-finite results for cross-section and making any physical interpretation unreasonable. There are two types of divergences:

- infrared divergences caused by either a virtual or real particle reaching zero momentum or if a massless particle emits another massless particle causing collinear divergences,
- ultraviolet divergences caused by large momenta in loop corrections for the calculation of amplitudes for a specific process.

The former are cured by the Kinoshita-Lee-Nauenberg theorem [38, 39] and the introduction of a factorisation scale μ_F . The factorisation scale plays an important role in calculating processes involving initial state hadrons and will be further discussed in Chapter 3.1. The latter is resolved by introducing an energy-scale dependence μ_R [24–26], called renormalisation scale, and evaluating the strong coupling at this scale $\alpha_S(\mu_R^2)$ and turn the coupling *constant* into a running coupling. It is characterised by the *renormalisation group equation* [40–44] with the perturbative expansion of the so-called *beta function* $\beta(\alpha_S)$ as

$$\mu_R^2 \frac{d\alpha_S}{d\mu_R^2} = \beta(\alpha_S) = -\left(b_0\alpha_S^2 + b_1\alpha_S^3 + b_2\alpha_S^4 + \dots\right), \quad (2.7)$$

with b_i determined by the i -loop β -function coefficient. Considering only the leading order contribution $-b_0\alpha_S^2$ with $b_0 = \frac{11n_c - 2n_f}{12\pi}$ and the number of quark flavours n_f and number of colours n_c , Equation 2.7 can be solved, showing the dependence of α_S on the renormalisation scale μ_R^2 with respect to a reference scale Q^2 :

$$\alpha_S(\mu_R^2, Q^2) = \frac{12\pi}{(11n_c - 2n_f) \ln(\mu_R^2/Q^2)}. \quad (2.8)$$

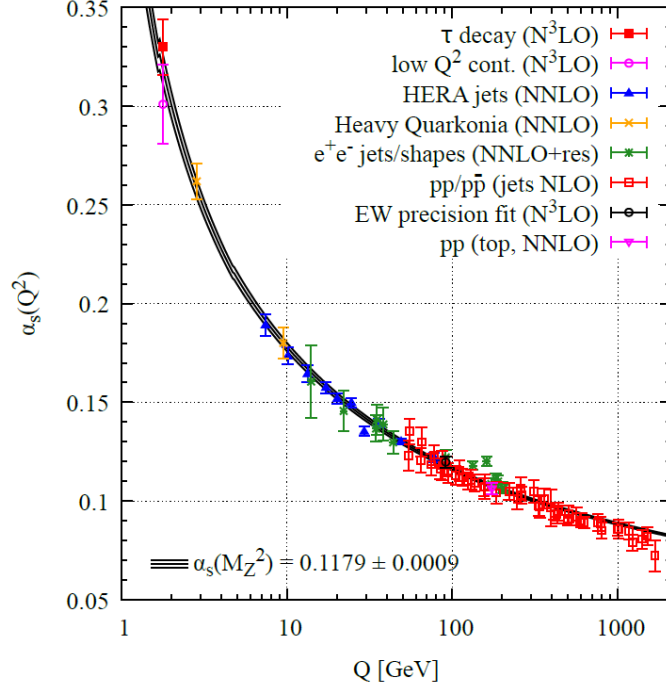


Figure 2.2: A summary of various measurements [46–62] for α_s as a function of the energy scale Q . The accuracy in perturbative QCD is given in parentheses. This figure is taken from Ref. [16].

The running coupling constant from Equation 2.8 decreases for large energy scales μ_R^2 , making it possible to use α_s as an expansion parameter for Feynman graph calculations. This property is called *asymptotic freedom* [22]. For low energy scales, the coupling increases and grows larger than unity. At those scales, the property of *confinement* is observed [45]. Multiple measurements are combined in Figure 2.2 to show the behaviour of the running constant as a function of the energy scale Q . The scale marking the breakdown of perturbation theory is called Λ_{QCD}^2 or Landau pole. The exact value depends on the used renormalisation scheme and approximation of the β -function from Equation 2.7.

2.3 Electroweak Unification and Higgs Mechanism

The electroweak unification combines the electromagnetic interaction and weak interaction into a single theory based on the local gauge symmetry groups $\text{SU}(2)_L \times \text{U}(1)_Y$. The first part of the local gauge symmetry $\text{SU}(2)_L$ requires rearranging fermions from the SM according to their chirality. Every fermion field ψ can be decomposed into a left-chiral field ψ_L and right-chiral field ψ_R using the chirality

operator $\frac{1}{2}(1 \pm \gamma^5)$ with $\gamma^5 = i\gamma^0\gamma^1\gamma^2\gamma^3$:

$$\psi_L = \frac{1}{2}(1 - \gamma^5)\psi \quad \text{and} \quad \psi_R = \frac{1}{2}(1 + \gamma^5)\psi. \quad (2.9)$$

Using the chirality operator, fermions can be grouped into doublets of left-handed particles with weak isospin $I = \frac{1}{2}$ and right-handed singlets with weak isospin $I = 0$:

$$\begin{pmatrix} u \\ d \end{pmatrix}_L, \quad \begin{pmatrix} \nu_e \\ e \end{pmatrix}_L, \quad \begin{pmatrix} c \\ s \end{pmatrix}_L, \quad \begin{pmatrix} \nu_\mu \\ \mu \end{pmatrix}_L, \quad \begin{pmatrix} t \\ b \end{pmatrix}_L, \quad \begin{pmatrix} \nu_\tau \\ \tau \end{pmatrix}_L \quad (2.10)$$

$$u_R, d_R, e_R, c_R, s_R, \mu_R, t_R, b_R, \tau_R.$$

In the SM, there are no right-handed neutrinos³. Therefore, they are not listed in Equation 2.10. The generators of the local gauge group $SU(2)_L$ are given by $\hat{T}_i = \frac{\sigma_i}{2}$ with $\sigma_{i=1,2,3}$ as the three Pauli matrices. Like the local gauge group $SU(3)_C$, the weak interaction $SU(2)_L$ is also non-Abelian. The transformation group only acts on the weak-isospin doublet and acts trivially on the weak-isospin singlet, explaining the subscript of the gauge group L subscript for *left*. The parity-violating nature of the weak interaction is motivated by experiments like the Wu experiment [63] and for neutrinos from the Goldhaber experiment [64]. The second part of the gauge group is an Abelian local gauge $U(1)_Y$ and introduces the hypercharge Y being connected to the electric charge Q and third component of the weak isospin I_3 via the Gell-Mann Nishijima formula:

$$Y = 2 \times (Q - I_3). \quad (2.11)$$

The Glashow-Weinberg-Salam mechanism describes the electroweak unification, combining the electromagnetic force and weak force into a single gauge group mechanism: gauge invariance is achieved by replacing the derivative in Equation 2.2 with the covariant derivative D_μ :

$$\partial_\mu \rightarrow D_\mu = \partial_\mu - ig \sum_{i=1}^3 \hat{T}_i W_\mu^i - ig' \frac{Y}{2} B_\mu, \quad (2.12)$$

with the coupling strength g and g' for the gauge group $SU(2)_L$ and $U(1)_Y$, respectively. The gauge fields are given by $W_\mu^{i=1,2,3}$ and B_μ . The four fields associated with the four vector bosons of the electroweak interaction W^+ , W^- , Z , and γ are constructed as linear combinations of the gauge fields. The formalism of gauge invariance forbids any mass-related terms like $-m^2 W_\mu^i W^{i,\mu}$ since it would spoil local gauge invariance. Therefore, the Glashow-Weinberg-Salam mechanism predicts the mass of the weak gauge bosons W and Z to be zero, in sharp contrast to experimental results from the UA1 and UA2 experiments [65–68]. The most precise weak boson masses are $m_W = 80.37 \text{ GeV}$ [16] and $m_Z = 91.18 \text{ GeV}$ [16].

³Furthermore, right-handed neutrinos do not interact either with photons, since they are electrically neutral, or with the Z boson as the weak isospin is zero.

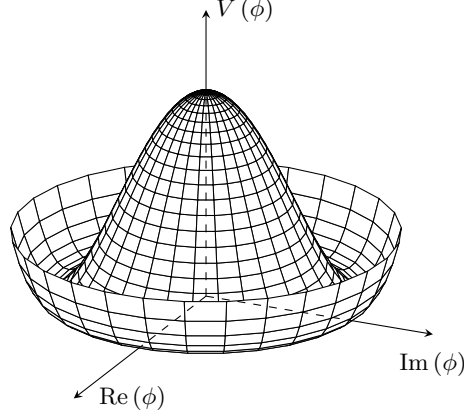


Figure 2.3: The Higgs potential with parameters $\lambda > 0$ and $\mu^2 < 0$. Due to its distinctive shape, it is sometimes called *mexican-hat* or *champagne-bottle* potential.

A solution to generate massive gauge bosons is provided by the Brout-Englert-Higgs mechanism, introducing an additional isospin doublet of complex scalar fields called the Higgs field

$$\phi = \begin{pmatrix} \phi^+ \\ \phi^0 \end{pmatrix} = \frac{1}{\sqrt{2}} \begin{pmatrix} \phi^1 + i\phi^2 \\ \phi^3 + i\phi^4 \end{pmatrix}, \quad (2.13)$$

and adding kinematic terms and a potential term called Higgs potential to the electroweak Lagrangian. The potential is given by

$$V(\phi) = \mu^2 \phi^\dagger \phi + \lambda (\phi^\dagger \phi)^2, \quad (2.14)$$

the free parameters $\lambda > 0$ and $\mu^2 < 0$ are chosen to get a non-zero vacuum expectation value $\nu^2 = -\mu^2/\lambda$ resulting in a broken gauge symmetry for the electroweak sector called *spontaneous symmetry breaking*. The Higgs potential with chosen parameters and minimum is shown in Figure 2.3. After *spontaneous symmetry breaking* occurred, the Higgs field in the unitary gauge is

$$\phi = \frac{1}{\sqrt{2}} \begin{pmatrix} 0 \\ \nu + h \end{pmatrix}, \quad (2.15)$$

with the vacuum expectation value ν and the real-valued scalar field h as the physical Higgs field, with excitations being the Higgs boson. The full Lagrangian of the electroweak interaction after enforcing gauge symmetry and *spontaneous symmetry*

breaking is given by

$$\begin{aligned}
\mathcal{L}_{\text{EW}} = & \sum_i \underbrace{\bar{\psi}_i (i\gamma^\mu \partial_\mu - m_i) \psi_i}_{\text{fermion kinematics}} - \underbrace{\frac{1}{4} B_{\mu\nu} B^{\mu\nu} - \frac{1}{4} W_{\mu\nu}^k W_k^{\mu\nu}}_{\text{gauge field kinematics}} \\
& - \sum_i \underbrace{q_i \bar{\psi}_i \gamma^\mu \psi_i A_\mu}_{\text{electromagnetic current}} \\
& - \sum_i \underbrace{\frac{g}{2\sqrt{2}} \bar{\psi}_i \gamma^\mu (1 - \gamma^5) (T^+ W_\mu^+ + T^- W_\mu^-) \psi_i}_{\text{weak charged current}} \\
& - \sum_i \underbrace{\frac{g}{2 \cos(\theta_W)} \bar{\psi}_i \gamma^\mu (g_V^i - g_A^i \gamma^5) \psi_i Z_\mu}_{\text{weak neutral current}} \\
& + \underbrace{|D_\mu h|^2}_{\text{Higgs kinematics}} - \underbrace{V(h)}_{\text{Higgs potential}} - \sum_i \underbrace{\bar{\psi}_i \frac{m_i h}{\nu} \psi_i}_{\text{Yukawa coupling}}.
\end{aligned} \tag{2.16}$$

The individual sums run over all fermion types. The Lagrangian includes all kinematic terms for the fermion, gauge boson, and Higgs field, as well as interaction terms, revealing possible coupling vertices and coupling types.

The electromagnetic current is a vector coupling proportional to a fermion's electromagnetic charge q_i . The electroweak charged current includes the left-handed chirality operator, characterising it as a vector axial vector coupling and ensuring only coupling with left-chiral fermions and right-chiral anti-fermions. The coupling includes weak isospin ladder operators T^\pm connecting the weak isospin partner of doublets during the interaction. For the lepton sector, the connection between the isospin partners only occurs within the same doublet, which is not valid for the quark sector. The observed mass eigenstates of quarks differ from the flavour eigenstates during weak interaction. The transformation between the mass eigenstates and flavour eigenstates is given by a rotation matrix called the Cabibbo-Kobayashi-Maskawa matrix (CKM matrix):

$$\begin{pmatrix} d' \\ s' \\ b' \end{pmatrix} = \begin{pmatrix} V_{ud} & V_{us} & V_{ub} \\ V_{cd} & V_{cs} & V_{cb} \\ V_{td} & V_{ts} & V_{tb} \end{pmatrix} \begin{pmatrix} d \\ s \\ b \end{pmatrix}. \tag{2.17}$$

The CKM matrix is unitary and describes the transition probability between quark generations. Since the CKM matrix is almost diagonal, the preference is to stay in the same generation. The weak charge current from Equation 2.16 is multiplied in the case of quarks by the corresponding CKM matrix element from Equation 2.17. Furthermore, in Equation 2.16, the physical fields are used, defined as linear combinations of the gauge fields $W^\pm = \frac{1}{\sqrt{2}} (W^1 \mp W^2)$. The weak neutral current also includes a chirality operator-like structure with vector component g_V and axial-vector

component g_A . The axial vector component is connected to the third component of the weak isospin I_3 , while the vector component is additionally connected to the electromagnetic charge and the weak mixing angle θ_W , also known as the Weinberg angle:

$$g_V = I_3 - 2q_i \sin(\theta_W) \quad \text{and} \quad g_A = I_3. \quad (2.18)$$

If both components are of unit value, the coupling is maximally parity violating like for the weak charged currents. However, for the weak neutral current, the coupling for right-chiral particles is purely vectorial, while for left-chiral particles, both vector and axial-vector components contribute. The different coupling behaviour and strength can be, for instance, measured in forward-backwards asymmetry measurements [69]. The physical electromagnetic current A_μ and physical weak neutral current Z_μ are defined as a mixture of the remaining gauge fields after symmetry breaking:

$$\begin{aligned} A_\mu &= B_\mu \cos(\theta_W) + W_\mu^3 \sin(\theta_W), \\ Z_\mu &= -B_\mu \sin(\theta_W) + W_\mu^3 \cos(\theta_W). \end{aligned} \quad (2.19)$$

The masses of the neutral gauge bosons γ and Z are obtained from the Higgs mechanism by diagonalising the mass matrix by Weinberg rotation with the corresponding eigenvalues as the masses. The photon remains massless after symmetry breaking, and the mass of the Z boson is given to be $m_Z = \frac{g\nu}{2\cos(\theta_W)}$ with g as the coupling constant of the weak interaction. The masses of Z and W bosons are related by $\cos(\theta_W) = \frac{m_W}{m_Z}$ and therefore $m_W = \frac{1}{2}g\nu$.

The last parts of the Lagrangian from Equation 2.16 are related to the Higgs boson. From the kinematic term, possible couplings to massive gauge bosons are derived. The Higgs potential term predicts the mass of the Higgs boson to be $m_H = \lambda\nu$. The last term describes the coupling of the Higgs boson to fermions: Fermion mass terms $-m\bar{\psi}\psi = -m(\bar{\psi}_R\psi_L + \bar{\psi}_L\psi_R)$ are not invariant under $SU(2)_L \times U(1)_Y$ local gauge group. However, adding the Higgs field preserves local gauge symmetry since $\bar{\psi}_L\phi\psi_R$ and $\bar{\psi}_R\bar{\phi}\psi_L$ are $SU(2)_L$ singlets. The result is a coupling between the physical Higgs field and the fermions, which is proportional to the mass of the corresponding fermion, also called Yukawa coupling.

2.4 The Higgs Boson

The Higgs boson was discovered in 2012 by the ATLAS and CMS collaborations [10–12]. The mass of the Higgs boson is a free parameter of the SM theory and needs to be determined experimentally. Using the Run 1 and Run 2 data set with both $H \rightarrow \gamma\gamma$ and $H \rightarrow ZZ^* \rightarrow 4\ell$ decay modes, the combined result for the Higgs boson mass is measured to be [71]:

$$m_H = 125.11 \pm 0.09 (\text{stat.}) \pm 0.06 (\text{sys.}) \text{ GeV} = 125.11 \pm 0.11 \text{ GeV}. \quad (2.20)$$

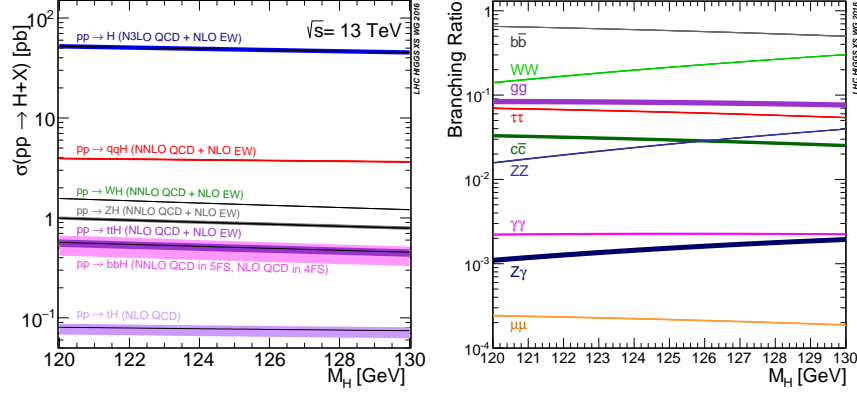


Figure 2.4: On the left side, the expected production rates for several Higgs production modes are shown as a function of the Higgs mass. The centre-of-mass energy is fixed to be $\sqrt{s} = 13$ TeV. The theory precision for each production mode is also presented together with theory uncertainties. On the right side, the branching ratios with total uncertainties for several Higgs boson decay modes are shown as a function of the Higgs boson mass. The assumed Higgs boson masses range from 120 to 130 GeV. Both figures are taken from Ref. [70].

Several studies of the spin and CP properties were conducted to test alternative hypotheses to the SM prediction of a spin-0 CP-even Higgs boson. The spin-1 and spin-2 hypotheses are excluded at a confidence level above 97.8 % using a combination of data collected at $\sqrt{s} = 7$ TeV and $\sqrt{s} = 8$ TeV and Higgs boson decay modes with different behaviour under spin and CP. The decay modes $H \rightarrow ZZ^* \rightarrow 4\ell$, $H \rightarrow WW^* \rightarrow \ell\nu\ell\nu$, and $H \rightarrow \gamma\gamma$ are used by the ATLAS collaboration [13]. The CMS collaboration conducted similar studies with the same conclusions [72]. The CP nature is further studied in the $H \rightarrow ZZ^* \rightarrow 4\ell$ decay mode using the full Run 2 data, demonstrating agreement to the CP-even prediction [73].

The production cross-section and branching ratios for the Higgs boson can be calculated from theory, assuming the values of free parameters. The cross-section for individual production modes depends on the Higgs boson mass but also on the centre-of-mass energy during the collision, the couplings, and parton distribution functions. In contrast, the branching ratios of Higgs boson decay modes depend on the Higgs boson mass, the masses of decay products and their coupling parameters. In Figure 2.4, the expected production cross-section and branching ratios are presented for Higgs boson masses from 120 to 130 GeV. The Run 2 centre-of-mass energy of $\sqrt{s} = 13$ TeV is used for the cross-section. The dominant Higgs production mode at the LHC is the gluon-gluon fusion process. Since there is no coupling between gluons and Higgs bosons, the leading perturbative contribution is a loop of massive particles such as top quarks or bottom quarks as depicted in Figure 2.5. The predicted cross-section for this production mode is $\sigma(pp \rightarrow H) = 48.52$ pb, at N3LO QCD

and NLO EW precision [74–78].

The second leading contribution to the total Higgs boson production cross-section, and the first account for direct coupling to weak gauge bosons, is the vector boson fusion (VBF). The LO Feynman diagram is shown in Figure 2.5 and can be mediated either by W or Z bosons. The characteristic features of VBF are two hard jets in the forward direction of the detector with large separation in rapidity. The expected production cross-section is more than ten times smaller than the leading gluon-gluon fusion contribution and is calculated at NNLO QCD and NLO EW precision to be $\sigma(pp \rightarrow qqH) = 3.779 \text{ pb}$ [77–82].

The third leading contribution is called Higgs-Strahlung with its LO Feynman graph shown in Figure 2.5. The production is quark initiated and mediated by a massive weak gauge boson radiating a Higgs boson, labelled as VH with $V = Z, W$. The Higgs-Strahlung production mode is sensitive to the direct Higgs boson coupling to massive gauge bosons. The presence of the gauge boson decaying to leptons leaves a distinct signature, suppressing multi-jet background, and provides good opportunities to measure specific Higgs boson decay modes such as $H \rightarrow b\bar{b}$. The production cross-section for W boson associated processes is expected to be $\sigma(pp \rightarrow WH) = 1.369 \text{ pb}$ at NNLO QCD and NLO EW precision, while the Z boson associated production is smaller with $\sigma(pp \rightarrow ZH) = 0.882 \text{ pb}$ at the same precision in QCD and EW [77–82].

The fourth leading production mode is the Higgs boson production in association with a top quark pair and is separately discussed in Section 2.6.

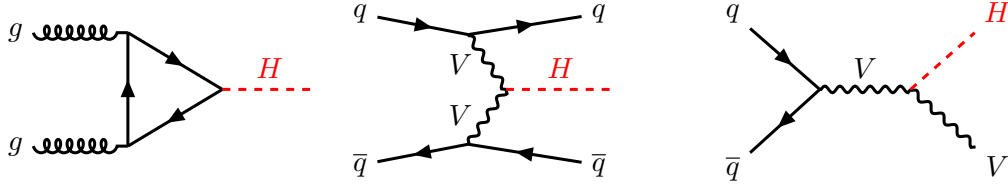


Figure 2.5: The LO Feynman graphs for the three main Higgs boson production modes at the LHC. On the left, gluon-gluon fusion is presented, where the loop is mediated by a massive quark like the top quark or bottom quark. In the middle, the LO contribution of the vector boson fusion is shown, while on the right side, the LO Feynman graph for the Higgs-Strahlung is presented.

The Higgs boson is not stable and will rapidly decay into other particles. Therefore, measuring Higgs boson properties can only be done indirectly by measuring decay products and reconstructing the Higgs boson. The expected branching ratios for the most dominant decay modes as a function of the Higgs boson mass are shown in Figure 2.4. The decay to massive fermions and gauge bosons is favoured due to the

larger coupling strength. With the measured Higgs boson mass from Equation 2.20, the most dominant branching ratio is the decay to bottom quarks $H \rightarrow b\bar{b}$, followed by the decay to W bosons $H \rightarrow WW^*$. The decay to pairs of particles whose mass is larger than half of the Higgs boson is usually suppressed since one particle is produced off-shell. Decays to massless bosons, such as gluons and photons, are mediated by a loop. For the decay to gluons, the loop is mediated by massive quarks, similar to the gluon-gluon fusion production. For the decay to photons, the loop can be additionally mediated by massive leptons and massive weak gauge bosons. A collection of LO Feynman graphs depicting the various Higgs boson decay modes with branching ratios is shown in Figure 2.6.

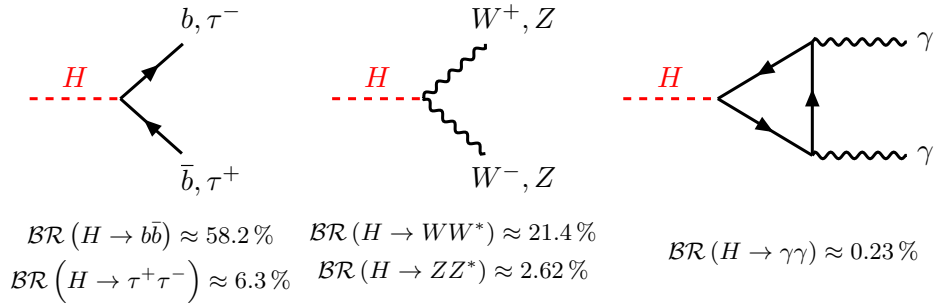


Figure 2.6: An overview of Higgs boson decay modes with a focus on the most important ones for the $t\bar{t}H$ measurement presented in this work. Below the LO Feynman graphs, branching ratios for the same decay modes are shown, assuming a Higgs boson mass of 125 GeV. The values are taken from Ref. [70].

2.5 The Top Quark

The last addition to the quark sector of the SM is the top quark, which was discovered by the CDF and DØ collaborations in 1995 at the TEVATRON [4, 5]. The top quark is sorted into the up-type quarks into the third generation, making it the isospin partner of the bottom quark. Furthermore, as the top quark is a fermion, it is a spin one-half particle with an electric charge of $q = \frac{2}{3}$ as all other up-type quarks. The top quark is with its mass of $m_t = 172.57 \pm 0.29$ GeV [16] the heaviest elementary particle of the SM. The large decay width of $\Gamma_t = 1.42^{+0.19}_{-0.15}$ GeV [16] results in a short lifetime of $\tau_t \approx 10^{-25}$ s which is smaller than the typical hadronisation timescale. The majority of top quarks decay before forming bound states, preserving properties like spin information and passing them down to the decay products. Usually, such information gets lost during hadronisation. Therefore, the top quark allows studying *bare quarks*. Top quarks are produced at the LHC in abundance, either in single-top-quark production or as pairs in top-quark pair production. There are also three and four top quark production processes. The single-top-quark one is mediated by electroweak production processes, while the top-quark pair one is

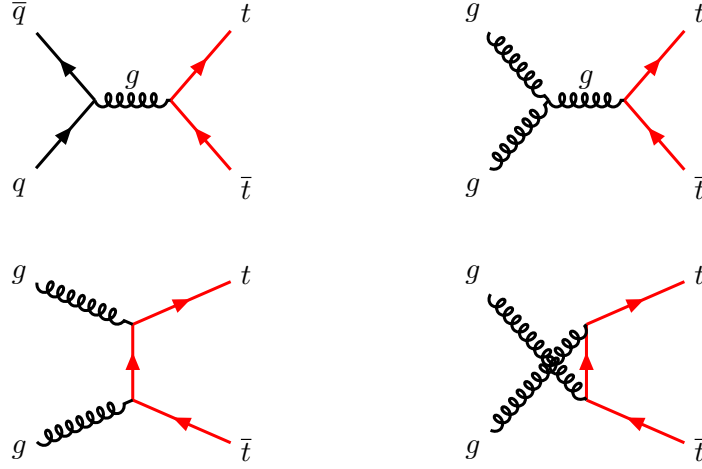


Figure 2.7: The four LO Feynman graphs for top quark pair production. There is one $q\bar{q}$ initiated process and three gluon-gluon initiated ones.

predominately mediated by QCD interactions. The pair production is the most common production mechanism and features one $q\bar{q}$ initiated and three gluon-gluon initiated processes. The LO Feynman graphs for the production of a top quark pair are shown in Figure 2.7. The production mode depends on the initial state particles: at the TEVATRON $p\bar{p}$ collisions are used with the consequence that $\approx 85\%$ of top quark pairs are produced by $q\bar{q}$ initiated processes due to the presence of valence anti-quarks in the initial state. The LHC collides protons. Therefore, anti-quarks are only available as sea quarks. The gluon-gluon production modes dominate, with $\approx 90\%$ of top quark pairs produced by gluon fusion. The top quark pair production is measured by various collaborations at a wide range of available centre-of-mass energies with $p\bar{p}$ and pp initial states. A summary of these measurements is given in Figure 2.8 with centre-of-mass energies ranging from $\sqrt{s} = 1.96 \text{ TeV}$ with $p\bar{p}$ collisions at the TEVATRON up to $\sqrt{s} = 13.6 \text{ TeV}$ with latest Run 3 measurements at the LHC using pp collisions. The measured values are compared with theory calculations at NNLO accuracy in QCD and NNLL soft-gluon resummation using TOP++ 2.0 [84–89]. Theoretical uncertainties arise from the choice of the renormalisation and factorisation scales, used parton distribution functions, and uncertainties on the strong coupling α_s .

The top quark decays only via electroweak forces mediated by a W boson. Unlike other quark decays, due to the large mass of the top quark, it is not kinematically suppressed since W bosons can be created on-shell. With the CKM matrix element $|V_{tb}|$ being close to unity, the top quark almost always decays to a b -quark and a W boson. The b -quark will eventually form a b -jet, while the W boson decay characterises the top quark pair decay mode further into three categories:

- *fully hadronic* is the most dominant decay mode of top quark pairs with a

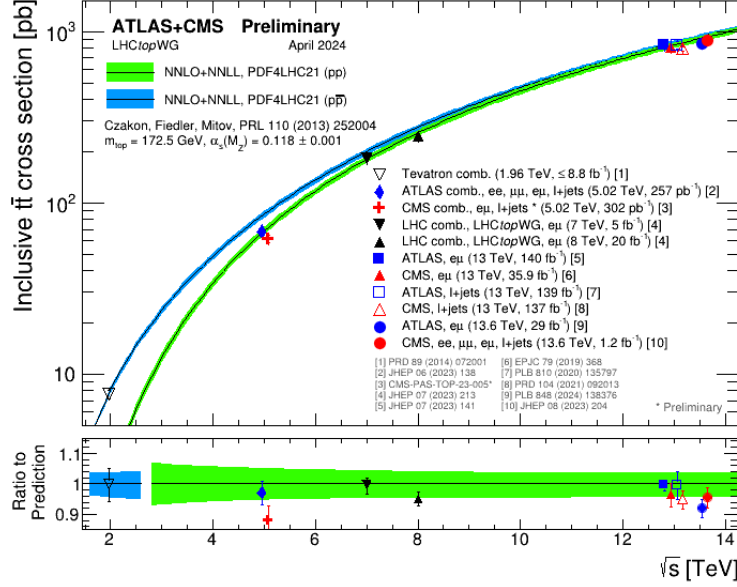


Figure 2.8: An overview of measurements of the production cross-section of top quark pairs performed at the TEVATRON and LHC. The cross-section is shown as a function of the centre-of-mass energy and covers a range of $\sqrt{s} = 1.96 \text{ TeV}$ up to $\sqrt{s} = 13.6 \text{ TeV}$ with the latest Run 3 results. The measurements are compared to NNLO QCD calculations using NNLL resummation. Theory uncertainties include choices of used renormalisation and factorisation scales and uncertainties associated with the parton density functions and strong coupling constant. This Figure is taken from Ref. [83].

branching ratio of \mathcal{BR} (fully hadronic) $\approx 46\%$. Both W bosons decay to hadrons leaving a $t\bar{t} \rightarrow W^+bW^-\bar{b} \rightarrow q\bar{q}'bq''\bar{q}'''\bar{b}$ signature at LO. This decay mode is experimentally less often used due to the large expected QCD multi-jet background and huge number of jets in the final state.

- *single-lepton* is the second dominant decay mode of top quark pairs with a branching ratio of \mathcal{BR} (single-lepton) $\approx 45\%$. One W boson decays leptonically, while the other decays to hadrons, resulting in $t\bar{t} \rightarrow W^+bW^-\bar{b} \rightarrow q\bar{q}'b\ell\nu_\ell\bar{b}$ signature at LO. The expected lepton contribution can help to suppress the multi-jet background. This mode includes a neutrino, which can not be measured directly by the ATLAS detector. This decay mode is also called *lepton+jets*.
- *dilepton* is the decay mode with the smallest branching ratio of \mathcal{BR} (dilepton) $\approx 9\%$ with both W bosons decaying to leptons. The decay mode $t\bar{t} \rightarrow W^+bW^-\bar{b} \rightarrow \ell^+\nu_\ell b\ell'^-\bar{\nu}_{\ell'}\bar{b}$ at LO involves an opposite-sign lepton pair. Usually, the opposite flavour composition $e\mu$ is used. The dilepton mode suppresses the multi-jet

background efficiently, but it has the disadvantage of a small branching ratio and two undetected final state neutrinos, resulting in an incomplete reconstruction of the top quark pair system.

The term lepton refers to electrons, muons, and taus in the categorisation above. The reported branching ratios assume lepton universality and include hadronic corrections [16]. A finer classification of top quark pair decay modes is found in Figure 2.9. Leptonic tau decays are usually sorted into the single-lepton or dilepton category as the experimental signature is similar, besides multiple undetected neutrinos.

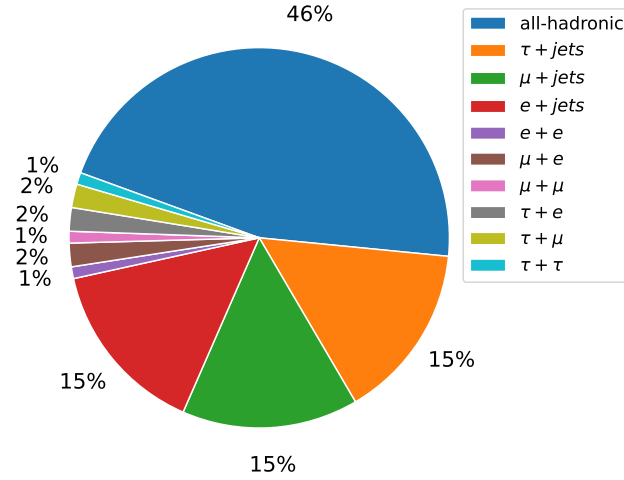


Figure 2.9: A pie chart with top quark pair decay modes split by the flavour of involved leptons.

2.6 The $t\bar{t}H$ Process

The $t\bar{t}H$ process is the fourth leading Higgs boson production mode and is one of the heaviest final states accessible at the LHC at $\sqrt{s} = 13 \text{ TeV}$, hence having a low expected production cross-section of $\sigma(pp \rightarrow t\bar{t}H) = 0.507 \text{ pb}$ with NLO QCD and NLO EW precision [77, 78, 92–94]. The first observations of the $t\bar{t}H$ process were made by the ATLAS [95] and CMS collaborations [96] using a combination of the main Higgs decay modes and Run 1 and Run 2 data. With the full Run 2 data set, not only measurements of the inclusive cross-section but also measurements of the differential cross-section and Higgs boson kinematics are possible. These allow precise studies of the coupling nature of the Higgs boson with the top quark and probing the CP properties of the Higgs-top-top interaction [97, 98]. The generalised form of the Yukawa coupling Lagrangian is given by

$$\mathcal{L} = -\frac{y_t}{\sqrt{2}} \bar{\psi}_t \left(\kappa' \cos(\alpha_t) + i\kappa' \gamma^5 \sin(\alpha_t) \right) \psi_t h, \quad (2.21)$$

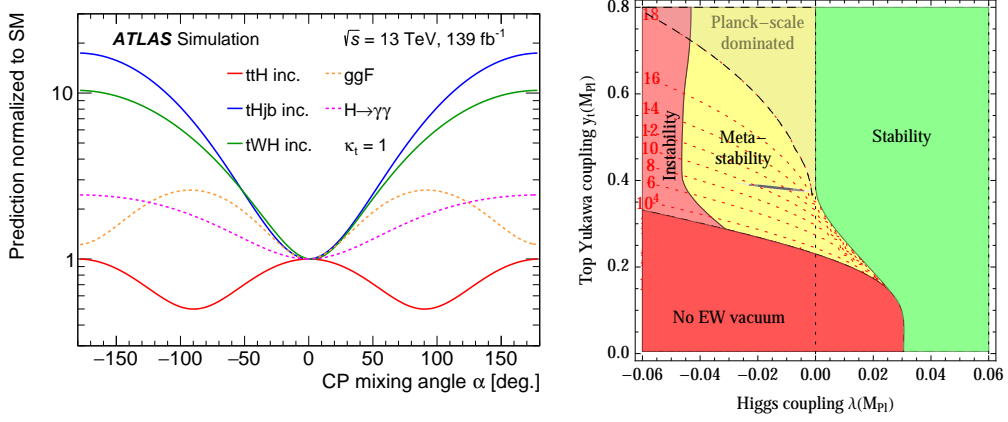


Figure 2.10: On the left side, the expected production cross-sections for the $t\bar{t}H$, $tHj\bar{b}$, and tWH processes are shown as a function of the CP mixing angle α_t . The production modes are normalised to the SM prediction. Furthermore, the relative change in the branching ratio of the $H \rightarrow \gamma\gamma$ decay mode and the gluon-gluon fusion production mode are presented. The coupling modification is set to unity for all processes. This Figure is taken from Ref. [90]. On the right side, the electroweak vacuum stability is shown as a function of the Higgs self-coupling and top Yukawa coupling, both evaluated at the Planck scale. The figure is taken from Ref. [91].

with y_t being the SM coupling strength for the interaction of top quarks with the Higgs field h . The coupling depends on the CP angle α_t mixing both scalar and pseudoscalar coupling types and κ' modifying the coupling strength. The SM expectation is given by $\alpha = 0$ and $\kappa' = 1$ with a pure scalar and CP-even coupling and no modification to the y_t coupling strength, which is expected to be close to unity. The pure pseudoscalar and CP-odd case are obtained for $\alpha = \pi/2$. The modifications of the Yukawa coupling have a large impact on the inclusive cross-section for both $t\bar{t}H$ and tH production. The predicted cross-section for both processes is illustrated on the left side in Figure 2.10 as a function of the CP mixing angle α_t , normalised to the SM prediction. The coupling modification κ' is set to unity. Measurements of the $t\bar{t}H$ and tH production directly probe the coupling type to be either scalar, pseudoscalar, or a mixing of both [99–105]. The presence of CP mixing also impacts the Higgs boson production cross-section in the gluon-gluon fusion mode as well as the $H \rightarrow \gamma\gamma$ decay mode [90], as shown on the left side of Figure 2.10.

The CP nature is not only an aspect probed by the $t\bar{t}H$ process. Additionally, this process is also sensitive to the Higgs boson self-coupling. The Higgs boson potential from Equation 2.16 after symmetry breaking includes trilinear and quadratic Higgs self-couplings proportional to λ_3 and λ_4 :

$$V(h) = \frac{m_H^2}{2}h^2 + \lambda_3\nu h^3 + \lambda_4 h^4. \quad (2.22)$$

The Higgs boson mass is given by $m_H = 2\lambda\nu^2$, while the self couplings are $\lambda_3 = \lambda = m_H^2/2\nu^2$ and $\lambda_4 = \lambda/4 = m_H^2/8\nu^2$, and therefore connected to the vacuum expectation value ν and shape of the Higgs boson potential.

The natural candidates for Higgs boson self-coupling are di-Higgs boson events where self-coupling is mediated at tree-level [106]. However, single Higgs boson production and decay can provide a similar sensitivity on λ_3 through NLO corrections [107,108]. Especially, in VH and $t\bar{t}H$ production, differential measurements are important for λ_3 determination, since non-flat effects are expected [109]. The interplay between the Higgs boson self-coupling and the top Yukawa coupling can further test the Higgs mechanism and the electroweak vacuum stability [91,110–114], as shown on the right side in Figure 2.10

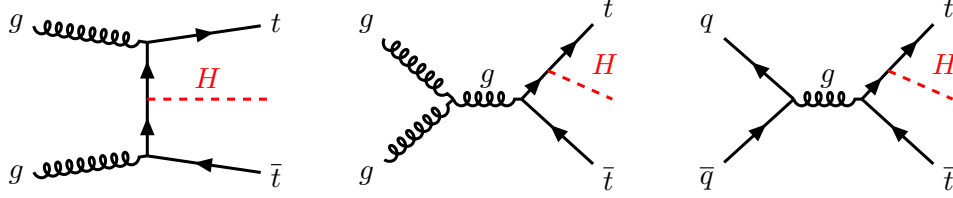


Figure 2.11: Three LO Feynman graphs for the Higgs boson production in association with a top quark pair.

The $t\bar{t}H$ production is either gluon or quark-anti-quark initiated by the production of a top quark pair radiating a Higgs boson. An overview of the LO Feynman graphs for the $t\bar{t}H$ production is shown in Figure 2.11. The $t\bar{t}H$ process is measured with various signatures targeting different decay modes of the Higgs boson and top quark pair described in Section 2.4 and Section 2.5, respectively. The decay mode of the Higgs boson defines the general analysis category with its unique experimental and theoretical advantages and disadvantages.

The cleanest Higgs boson decay mode is given by $H \rightarrow \gamma\gamma$ arising in a diphoton signature with an invariant mass close to the Higgs mass. The remaining jet activity and leptons originate from the top quark system decaying all-hadronically or leptonically, including both single- and dilepton decay modes. The $t\bar{t}(H \rightarrow \gamma\gamma)$ analysis features a simple background composition with most background events originating from $\gamma\gamma + \text{jets}$ and $t\bar{t} + \text{jets}$ events and a clean diphoton signature with little ambiguities. Due to the resonance nature of this process, the measurement is expected to give precise results for the low transverse momentum regime of the Higgs boson. However, the decay mode to photons has the lowest branching ratio, and the $t\bar{t}(H \rightarrow \gamma\gamma)$ measurement is dominated by statistical uncertainties. Measurements for this process have been done by the ATLAS and CMS collaborations, including CP interpretations [115–118]. Another resonance channel is given by $H \rightarrow ZZ^* \rightarrow 4\ell$

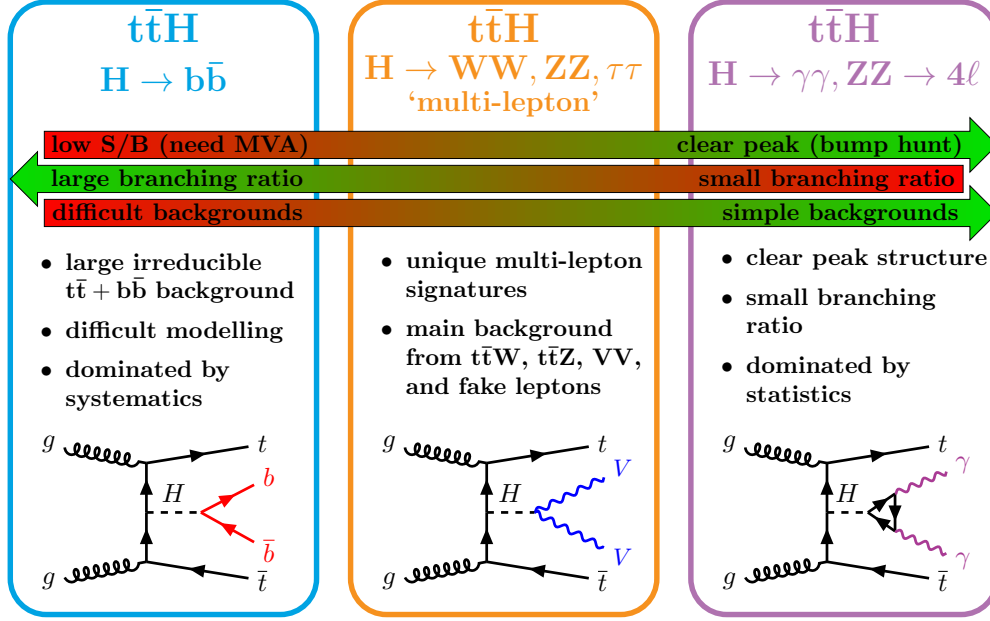


Figure 2.12: Overview of various $t\bar{t}H$ analyses performed at the ATLAS experiment. The targeted Higgs boson decay modes are depicted together with advantages and disadvantages for each analysis. The term *fake lepton* is discussed in Chapter 7. Inspired by a figure from Tamara Vazquez Schroeder.

with similar features. Measurements by the ATLAS and CMS collaborations include studies on EFT interpretation and the coupling nature of Higgs bosons to vector bosons [119, 120].

The Higgs boson decay mode with the largest branching ratio is to bottom quarks $H \rightarrow b\bar{b}$ and is targeted in the $t\bar{t}(H \rightarrow b\bar{b})$ analysis. The analysis is split into single-lepton and dilepton channels⁴, defined by the decay of the top quark system. The most challenging aspect for the $t\bar{t}(H \rightarrow b\bar{b})$ analysis is background estimation. The most dominant one arises from the $t\bar{t} + \text{jets}$, and especially from $t\bar{t}b\bar{b}$ production, mimicking the same final state signatures. The background processes have much larger cross-sections than the targeted signal process. At the same time, a clean resonance peak cannot be reconstructed, leading to the need for multivariate analysis to define pure signal regions and control regions populated with important backgrounds to constrain them. Furthermore, the $t\bar{t}b\bar{b}$ production is difficult to model due to the massive heavy flavour quarks created by gluon splitting, thus limiting a precise background estimation and signal extraction. Therefore, one of the most dominant sources of uncertainties arises from systematic ones, originating from theoretical modelling. Unlike the $t\bar{t}(H \rightarrow \gamma\gamma)$ process, the $t\bar{t}(H \rightarrow b\bar{b})$ process has a sensitivity to the high Higgs boson transverse momentum regime, therefore enabling

⁴The measurement done by the CMS collaboration also included the all-hadronic decay channel.

$t\bar{t}H$ production cross-section measurements in bins of the Higgs boson transverse momentum. Both measurements done by the ATLAS and CMS collaborations include CP interpretations of the Higgs-top-top coupling [121–124].

The $t\bar{t}H$ multi-lepton analysis challenges are in between, compared to the previously mentioned analyses as depicted in Figure 2.12. The statistical and systematic uncertainties of the measurement are expected to balance each other. The best sensitivity on Higgs boson transverse momentum is an intermediate regime between the low regime covered by the $t\bar{t}(H \rightarrow \gamma\gamma)$ and high regime accessed by $t\bar{t}(H \rightarrow b\bar{b})$. The final states involve multiple combinations of charged light leptons, electrons and muons, with targeted Higgs boson decay modes to massive gauge bosons $H \rightarrow ZZ^*$ and $H \rightarrow WW^*$, but also to τ lepton pairs, subsequently decaying to light leptons or hadrons. In a previous analysis using data collected by the ATLAS detector during 2015 – 2017, corresponding to an integrated luminosity of 80 fb^{-1} , the measured cross-section was determined to be

$$\begin{aligned} \sigma_{t\bar{t}H} = 294_{-162}^{+182} \text{ fb} = & 294_{-127}^{+132} \text{ (stat.)} +_{-74}^{+94} \text{ (exp.)} \\ & +_{-56}^{+73} \text{ (bkg. th.)} +_{-39}^{+41} \text{ (sig. th.) fb,} \end{aligned} \quad (2.23)$$

corresponding to a significance of 1.8σ excess above the background-only expectations [125]. The reported production cross-section agrees with the SM prediction but suffers from statistical and systematic uncertainties. The analysis strategy of the 4ℓ channel used signal regions defined by the flavour combination of the four leptons. In one of the regions, a boosted decision tree was trained to separate $t\bar{t}H$ events from other background ones. The signal strength with respect to the SM prediction with a Higgs boson mass of $m_H = 125 \text{ GeV}$ in the 4ℓ channel was measured during the combination of all channels to be:

$$\mu_{t\bar{t}H} = 0.52_{-0.72}^{+0.93} = 0.52_{-0.72}^{+0.93} \text{ (stat.)} +_{-0.24}^{+0.52} \text{ (sys.)}. \quad (2.24)$$

The 4ℓ channel was dominated by statistical uncertainties.

The $2\ell\text{SS}+0\tau_{\text{had}}$ and 3ℓ channel had a large background induced by $t\bar{t}W$. The normalisation of the $t\bar{t}W$ process was further constraint in dedicated analysis regions. The measured normalisation factors excess updated predictions by a factor of up to 1.7 depending on the region. Furthermore, missmodelling in $t\bar{t}W$ enriched regions is observed. The $t\bar{t}H$ multi-lepton measurement presented in this work uses an updated version of the $t\bar{t}W$ process modelling, including corrections for missing higher-order QCD and EW effects such as additional tW scattering [126] and charge asymmetric production of $t\bar{t}W^+$ and $t\bar{t}W^-$. The predictions are validated with inclusive and differential measurements reducing the observed tension [127].

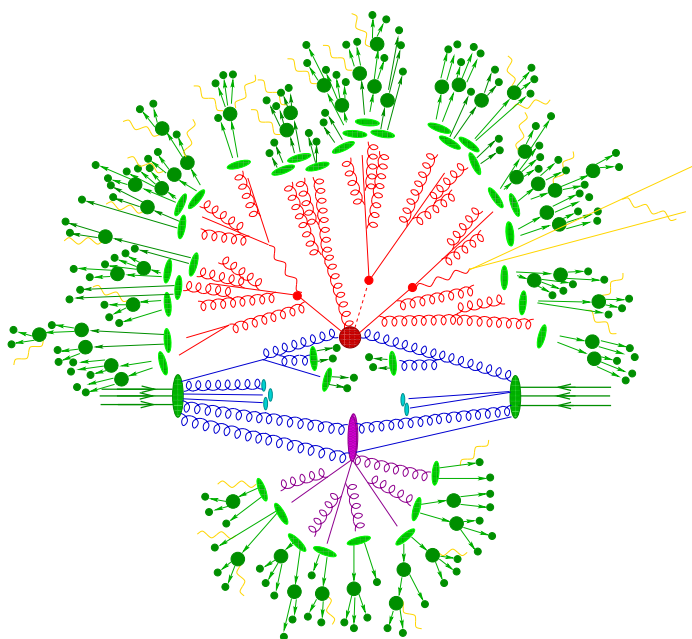


Figure 3.1: An illustration of a $t\bar{t}H$ event generated in pp collision. The hard interaction, parton showering, hadronisation, and subsequent hadron decays are shown. All three processes occur within a few femtometers and can not be resolved by to-date methods. This figure is taken from Ref. [128].

Simulation of particle collisions is implementing perturbative quantum field theory with additional phenomenological models, which is tested against collected data that is measured experimentally, for instance, by the ATLAS or CMS collaboration. To

compare theory and data, several steps of simulation are performed. In Figure 3.1, the creation of a $t\bar{t}H$ event is illustrated from generation at the primary interaction to the transition of partons to colourless hadrons. On top, not shown in Figure 3.1, a detector simulation is run, modelling the response and acceptance of the ATLAS detector. The simulation has to be done in various steps, applying different approaches of perturbative and non-perturbative quantum field theory due to the large covered energy scales and values of the strong interaction α_s . For high energy scales, the coupling constant is small, and perturbative calculations are assumed to provide a good approximation of the hard interaction initiated by partons of the incoming protons. It is marked with a red circle in Figure 3.1. The hard interaction takes place at energy scales of $\mathcal{O}(1 \text{ TeV})$. A full discussion and description of the hard interaction in terms of matrix element calculation is presented in Section 3.1. As shown in purple, secondary interactions can also occur and are associated with a smaller momentum transfer. The products of the hard interaction undergo parton showering as the energy scale decreases¹. Depending on the parton shower implementation, the energy scale ranges from $\mathcal{O}(100 \text{ GeV})$ to $\mathcal{O}(1 \text{ GeV})$. Approximations are needed to deal with the corresponding limitations of perturbation theory. Parton showers act in the soft and collinear limit and add emissions successively to initial and final state partons of the matrix element generation as shown in blue in Figure 3.1. Section 3.2 discusses the different assumptions and techniques. At energy scales close to the proton's mass, perturbation theory breaks down since the coupling becomes large. The transition of partons to colourless hadrons is described by phenomenological hadronisation models such as the cluster or Lund string model. They are discussed in Section 3.3. The transition is depicted in Figure 3.1 as light green ovals and resulting hadrons shown in dark green. These hadrons eventually decay to more stable particles like pions, kaons, or lambda hadrons and are the physical particles that the ATLAS detector can detect.

The entire simulation chain with chosen parameters and models defines a sample. A complete list of generated samples used for the measurement of the $t\bar{t}H$ multi-lepton process can be found in Section 3.4.

3.1 Matrix Element Generation

In pp collisions, the constituents of the protons called partons interact. Partons are valence quarks, (uud) in the case of a proton, but also gluons radiated from other partons, together with sea quarks created in gluon splitting. The inclusive cross-section for a process $pp \rightarrow X$ is approximated utilising the factorisation theorem [129]:

$$\sigma_{pp \rightarrow X} = \sum_{i,j} dx_i dx_j f_i(x_i, \mu_F^2) f_j(x_j, \mu_F^2) \sigma_{ij \rightarrow X}(x_i p_i, x_j p_j, \mu_R^2, \mu_F^2). \quad (3.1)$$

¹The parton shower can be considered as a link between hard and soft QCD with the energy scale as a model parameter.

The evaluation of Equation 3.1 is process dependent, while the sum runs over all configurations of partons which can induce the desired process, whether it is a SM or BSM process. The parton distribution function (PDF) $f_i(x_i, \mu_F^2)$ [130–134] describes the probability to find a parton i within a proton carrying a momentum fraction x_i of the proton at an energy scale q^2 . In Equation 3.1, the energy scale is given by the factorisation scale μ_F^2 , separating the hard scattering process from soft radiation, which is resummed into the PDFs. The value of the factorisation scale μ_F^2 is a free parameter. It is often chosen to be related to the kinematic properties of the produced final state particles in the hard interaction. The evolution of PDFs from a reference scale is given by the DGLAP equations, which are the renormalisation group equations² for the factorisation scale [135–137]:

$$\begin{aligned}\frac{\partial q_i(x, q^2)}{\partial \log(q^2)} &= \frac{\alpha_S}{2\pi} \int_x^1 \frac{dz}{z} \left[P_{qq}(z) q_j\left(\frac{x}{z}, q^2\right) + P_{qg}(z) g\left(\frac{x}{z}, q^2\right) \right] \\ \frac{\partial g(x, q^2)}{\partial \log(q^2)} &= \frac{\alpha_S}{2\pi} \int_x^1 \frac{dz}{z} \left[P_{gq}(z) q_j\left(\frac{x}{z}, q^2\right) + P_{gg}(z) g\left(\frac{x}{z}, q^2\right) \right].\end{aligned}\tag{3.2}$$

The universal spin-averaged splitting functions for massless particles $P_{ij}(z)$ are shown in Figure 3.2. In Figure 3.3, PDFs for gluons and the lightest quarks are depicted for two different scales as a function of the momentum fraction with respect to the proton. The scale dependence of processes strongly depends on the PDFs and not necessarily on the parton level cross-section $\sigma_{ij \rightarrow X}(x_i p_i, x_j p_j, \mu_R^2, \mu_F^2)$. The parton level cross-section is calculated as a perturbative series in the coupling constants, starting from the Born configuration referred to as leading-order (LO) followed by higher order contributions like next-to-leading order (NLO). For high-energy scales, the couplings tend to be smaller. Therefore, the perturbation series uses α_S and the weak coupling α_{EW} as expansion parameters:

$$\sigma_{ij \rightarrow X} = \underbrace{\sigma_{ij \rightarrow X}^{\text{Born}}}_{\text{LO prediction}} \left[1 + \underbrace{\frac{\alpha_S}{2\pi} \sigma_{ij \rightarrow X}^{(1)}}_{\text{NLO correction}} + \underbrace{\frac{\alpha_S}{2\pi} \sigma_{ij \rightarrow X}^{(2)}}_{\text{NNLO correction}} + \dots \right]. \tag{3.3}$$

The partonic cross-section depends on the factorisation scale μ_F and renormalisation scale μ_R ; the latter is introduced to deal with ultra-violet divergences, described in Section 2.2. The scales μ_R and μ_F are non-physical quantities, and observables should ideally not depend on them. However, the approximate theoretical predictions obtained from perturbative calculations do, since they are evaluated at a fixed order. At LO, an observable is a monotonous function of μ_R and μ_F ; the dependency is reduced by considering higher order terms, motivating calculations at NLO or even NNLO. In the limit of considering all higher-order corrections, the observable does

²Furthermore, this is the origin of the μ_F dependence of PDFs.

not depend on the scales. The renormalisation scale is often set to the same value as the factorisation scale. The partonic cross-section is computed from fixed-order calculations

$$\sigma_{ij \rightarrow X} = \sum_{e=0}^{\infty} \int_{e+f} d\Phi_{e+f} \left| \sum_{c=0}^{\infty} \mathcal{M}_{e+f}^c(\Phi_{e+f}) \right|^2 \quad (3.4)$$

$$\text{with} \quad d\Phi_{e+f} = SF \prod_{i=0}^{e+f} \frac{d^3 \vec{p}_i}{(2\pi)^3} \frac{1}{2E_i},$$

with f final state particles, e real emissions, and c virtual corrections. The physics interaction described by Feynman rules is included in the scattering amplitude \mathcal{M}_{e+f}^c . In contrast, the probability distributions of kinematics are described by the phase-space factor $d\Phi_{e+f}$ with the symmetry factor S accounting for identical final state processes and F as the flux factor. Fixed order calculations are implemented in various automated tools, called event generators. A list of generators used for this analysis is found in Section 3.4.

$$\begin{aligned} \text{Quark splitting: } & = P_{qq} = C_F \frac{1+(1-z)^2}{z} & \text{Gluon splitting into quark-antiquark: } & = P_{q\bar{q}} = C_F \frac{1+z^2}{z} \\ \text{Gluon splitting into quark-antiquark: } & = P_{gq} = C_F \frac{1+z^2}{z} & \text{Gluon splitting into gluon-gluon: } & = P_{gg} = 2C_A \frac{(1-z)(1-z^2)}{z(1-z)} \\ \text{Gluon splitting into gluon-gluon: } & = P_{gg} = 2C_A \frac{(1-z)(1-z^2)}{z(1-z)} & \text{Gluon splitting into quark-antiquark: } & = P_{gq} = T_R (z^2 (1-z)^2) \end{aligned}$$

Figure 3.2: The universal splitting functions for QCD interactions at LO. The splitting functions in the top row are the same since the underlying process is symmetric. The splitting functions are spin-averaged and assume massless particles. The constants are $T_R = \frac{1}{2}$, $C_A = N_C = 3$, and $C_F = \frac{N_C^2 - 1}{2N_C} = \frac{4}{3}$.

3.2 Parton Shower

A parton shower promotes final state partons from matrix element generation to jets³ by successive emission of additional partons. An example of parton emission is the simple case of $e^+e^- \rightarrow q\bar{q}g$ described by the differential cross-section dominant contribution

$$\frac{d\sigma_{q\bar{q}g}}{d\cos(\theta) dz} \approx \sigma_{q\bar{q}} C_F \frac{\alpha_S}{2\pi} \frac{2}{\sin^2(\theta)} \frac{1+(1-z)^2}{z}, \quad (3.5)$$

³The term *jets* is used in hindsight, since jets are analysis objects defined by various parameters, as described in Section 5.2.5.

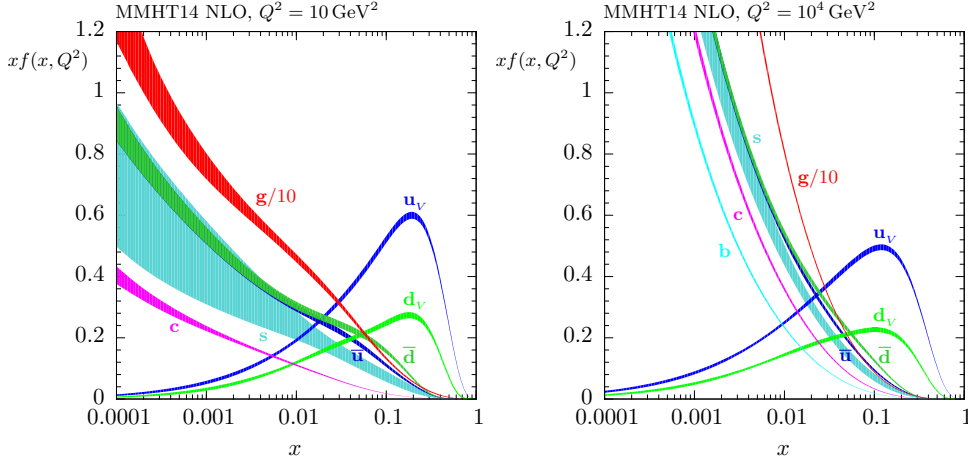


Figure 3.3: The parton distribution functions of the MMHT2014NLO set for the lightest quarks and gluon as a function of the momentum fraction x . The PDF sets are shown at different energy scales. On the left side, they are evaluated at a scale of 10 GeV^2 and on the right side, at a scale of 10^4 GeV^2 . The Figures are taken from Ref. [138].

with θ as the angle between the quark and gluon and z as the energy fraction of the gluon. A neat property of Equation 3.5 is the factorisation into $\sigma_{q\bar{q}}$ and the emission part. For very soft emission $z \rightarrow 0$ or collinear emissions $\theta \rightarrow 0, \pi$, the cross-section diverges. Equation 3.5 describes the emission of a gluon from a $q\bar{q}$ dipole and can be generalised for gluon radiated from a single quark to

$$d\sigma_{q\bar{q}g} \approx \sigma_{q\bar{q}} \sum_{\text{partons}} C_F \frac{\alpha_S}{2\pi} \frac{d\theta^2}{\theta^2} dz \frac{1 + (1-z)^2}{z}, \quad (3.6)$$

with $\sin(\theta) \approx \theta$. Choosing the transverse momentum of the radiated particle with respect to the parent particle instead of the angle θ is an equivalent choice as an *evolution variable*. For a general *evolution variable* t the emission of a parton i from a parent parton j is given by

$$d\sigma_{n+1} \approx d\sigma_n \sum_i \frac{\alpha_S}{2\pi} dz P_{ij}(z). \quad (3.7)$$

The universal splitting functions $P_{ij}(z)$ in QCD are already defined in Figure 3.2. The splitting of gluons to quark pairs plays a minor role for parton showering. By integrating out Equation 3.7 the *double log* structure is revealed

$$d\sigma(X + n \text{ emissions}) \approx d\sigma(X) \times \alpha_S^n \left[\ln^{2n} \left(\frac{Q^2}{t} \right) + \mathcal{O} \left(\ln^{2n-1} \left(\frac{Q^2}{t} \right) \right) \right] \quad (3.8)$$

for some defined energy scale Q^2 and processes X with n emissions. The first logarithmic contribution is the most dominant one, while the remaining sub-leading ones are usually not described well by the parton shower. To deal with divergences originating from virtual and unresolved contributions, a cut-off value is defined, acting as a resolution parameter. For implementation purposes, the Sudakov form factors $\Delta(t_1, t_2)$ are used, describing the probability that a parton does not radiate from scale t_1 to scale t_2 :

$$\Delta(t_1, t_2) = \exp \left[- \int_{t_2}^{t_1} \frac{dt}{t} \frac{\alpha_S}{2\pi} \int_{z_{\min}}^{z_{\max}} dz P_{ij}(z) \right]. \quad (3.9)$$

Starting from an initial scale t_{initial}^2 , the first emission of a parton occurs at scale t_2^2 calculated using Equation 3.9. If the t_2^2 value is below the hadronisation scale of $t^2 \approx 1 \text{ GeV}^2$, the shower evolution is terminated and hadronisation starts, if the value is above the hadronisation scale, t_2^2 is replaced as the initial scale.

3.3 Hadronisation Models

The description for the transition of partons to hadrons can not be derived with perturbative means and relies on phenomenological models. Perturbation theory breaks down since α_S increases. At those large α_S values, quark confinement is observed. The commonly used hadronisation models are the Lund string model [139, 140] and cluster model [141, 142]. The Lund string model uses a linear potential to describe the effective QCD potential between two quarks with field lines forming tube-like regions. The latter property gives the model the name *string*. The fragmentation into hadrons is then performed by repeatedly splitting the string into $q\bar{q}$ pairs. The fragmentation is controlled via the fragmentation function

$$f(z) \propto \frac{(1-z)^a}{z} \exp \left(\frac{-bm_T^2}{z} \right) \quad (3.10)$$

with the transverse mass m_T and the parameter a and b determined by experiments. The Lund-Bowler shape can modify the fragmentation function to better describe heavy quarks. The creation of different quark pairs is realised by tunnelling with probability

$$\mathcal{P} \propto \exp \left(\frac{\pi m_T^2}{\kappa} \right) = \exp \left(\frac{\pi p_T^2}{\kappa} \right) \left(\frac{\pi m^2}{\kappa} \right), \quad (3.11)$$

with κ as the string tension constant, and p_T as the transverse momentum and m the mass. Equation 3.11 suppresses contributions of heavy quarks. The Lund string model is implemented in PYTHIA. The cluster model is based on colour preconfinement [143] and gluon splitting to form clusters. A cluster with a high mass will eventually decay into smaller clusters, which will further decay to two hadrons depending on the available phase-space and spin combination. Reconnection of three

$q\bar{q}$ clusters is also allowed and will form two baryons. The cluster model is used by HERWIG and SHERPA; the latter uses a modified one. A description of hadronisation models utilised in the MC samples for this analysis is presented in Section 3.4.

3.4 Monte Carlo Samples

Process	ME Generator	ME order	Parton shower	PDF	Tune
$t\bar{t}H$	POWHEG-Box	NLO	PYTHIA 8	NNPDF 3.0nlo	A14
	POWHEG-Box	NLO	PYTHIA 7.0.4	NNPDF 3.0nlo	H7-UE-MMHT
	POWHEG-Box	NLO	PYTHIA 8 with varied p_T^{hard}	NNPDF 3.0nlo	A14
$t\bar{t}W$	SHERPA 2.2.10	MEPS@NLO	SHERPA	NNPDF 3.0nnlo	SHERPA default
	MADGRAPH5_aMC@NLO	FxFx NLO	PYTHIA 8	NNPDF 3.0nlo	A14
	POWHEG-Box	NLO	PYTHIA 8	NNPDF 3.0nlo	A14
	POWHEG-Box	NLO	HERWIG 7	NNPDF 3.0nlo	H7-UE-MMHT
$t\bar{t}W$ (EW)	SHERPA 2.2.10	LO	SHERPA	NNPDF 3.0nnlo	SHERPA default
	MADGRAPH5_aMC@NLO	LO	PYTHIA 8	NNPDF 3.0nlo	A14
$t\bar{t}l\bar{l}$	MADGRAPH5_aMC@NLO	NLO	PYTHIA 8	NNPDF 3.0nlo	A14
	MADGRAPH5_aMC@NLO	NLO	HERWIG 7	NNPDF 3.0nlo	H7-UE-MMHT
	MADGRAPH5_aMC@NLO	NLO	PYTHIA 8	NNPDF 3.0nlo	A14 Var3C
	MADGRAPH5_aMC@NLO	LO	PYTHIA 8	NNPDF 3.0lo	A14
$t\bar{t} \rightarrow W^+bW^-\bar{b}l^+l^-$	MADGRAPH5_aMC@NLO	NLO	PYTHIA 8	NNPDF 3.1nlo	A14
$t\bar{t}l\bar{l}$	POWHEG-Box	NLO	PYTHIA 8	NNPDF 3.0nlo	A14
$t\bar{t}t$	POWHEG-Box	NLO	HERWIG 7.1.3	NNPDF 3.0nlo	H7-UE-MMHT
	MADGRAPH5_aMC@NLO	LO	PYTHIA 8	NNPDF 2.3lo	A14
Single top (t -, Wt -, s -channel)	POWHEG-Box	NLO	PYTHIA 8	NNPDF 3.0nlo	A14
$VV, VVjj, VVV$	SHERPA 2.2.2(1)	MEPS@NLO	SHERPA	NNPDF 3.0nlo	SHERPA default
$Z \rightarrow \ell^+\ell^-$	SHERPA 2.2.1	MEPS@NLO	SHERPA	NNPDF 3.0nlo	SHERPA default
$Z \rightarrow \ell^+\ell^-(\gamma \rightarrow e^+e^-)$	POWHEG-Box	NLO	PYTHIA 8	CTEQ 6L1nlo	A14
$Z \rightarrow \ell^+\ell^-(\gamma^* \rightarrow e^+e^-)$	POWHEG-Box	NLO	PYTHIA 8	CTEQ 6L1nlo	A14

Table 3.1: An overview of signal and background samples. For each sample, the configuration in terms of matrix element generator and accuracy, PDF set, parton shower model, and used set of tunable parameters are shown. The alternative samples to estimate systematic uncertainties are marked in blue.

This section gives an overview of MC samples used in the analysis, describing used ME generators and PS models and their configuration. Most MC samples are processed with a full ATLAS detector simulation response [144] based on GEANT4 [145]. A small fraction of samples, including processes like tWH , $tHqb$, and $t\bar{t}t\bar{t}$, are processed using fast simulation (AF2) replacing the full GEANT4 calorimeter response by a parametrisation of shower shapes [146]. The impact on observables for this analysis is negligible.

To model the impact of in- and out-time pileup effects, PYTHIA 8 [147] is used to generate additional pp collisions, which are overlaid on the hard scattering process. The A3 tune is used [148]. The simulated events are reweighted for each mc16 sub-campaign to match different pileup conditions observed in data [149].

For all samples involving top quarks, the mass of the top quark is set to $m_t = 172.5$ GeV, while the mass of b -quarks during top-quark decays is set to $m_b = 4.95$ GeV for POWHEG or MADSPIN and $m_b = 4.75$ GeV for SHERPA. The top

quark decays exclusively to b -quarks for all samples involving top quarks. For all samples involving a Higgs boson, its mass is set to be 125 GeV. All samples generated with PYTHIA [147] for parton showering and hadronisation use the A14 set of tunable parameters, together with the NNPDF 2.3lo PDF set with a default value of $\alpha_S = 0.130$ [150]. For samples involving top quark pairs, decay of bottom and charm hadrons is modelled using EVTGEN 1.6.0 [151].

An overview of processes and generators is shown in Table 3.1. Alternative samples are produced to estimate systematic uncertainties associated with the parton shower, hadronisation models, and matrix element generators and their matching. A description is added for the relevant processes in Table 3.1. Further details on the used samples are found in Appendix A.

3.4.1 $t\bar{t}H$ Production

The $t\bar{t}H$ signal process events are generated with POWHEG BOX v2 [152–156] at NLO accuracy using the NNPDF3.0NLO PDF set [157]. The parton shower and hadronisation step are performed with PYTHIA 8.2.30 [147]. The h_{damp} parameter regulating the high- p_T radiation during matching of POWHEG matrix elements to the parton shower is set to $0.75 \times (m_t + m_{\bar{t}} + m_H) = 352.5$ GeV. The theoretically predicted cross-section at NLO QCD and NLO EW accuracy at $\sqrt{s} = 13$ TeV is evaluated to be 507^{+35}_{-50} fb [70]. The uncertainties are obtained by varying the renormalisation and factorisation scales and combined PDF+ α_s . The calculations are done using MADGRAPH5_aMC@NLO.

Modelling uncertainties associated with initial state radiation (ISR) for the $t\bar{t}H$ signal process are estimated with weights during matrix element generation and parton shower evaluation. Final state radiation (FSR) is evaluated by scaling the QCD emission scale by a factor of 0.5 and 2.0. The impact of the renormalisation and factorisation scales, μ_R and μ_F , are estimated by varying the central value by a factor of 0.5 and 2.0 in the matrix element while using the VAR3C UP and VAR3C DOWN variation of the A14 tune in the parton shower.

The impact of different parton shower algorithms, hadronisation models, and underlying event modelling is evaluated by comparing the nominal configuration POWHEG + PYTHIA using the same generated POWHEG events but using HERWIG 7.0.4 [158, 159] for the parton shower and hadronisation step. The H7UE set of tunable parameters [158] is used along with the MMHT2014LO PDF set [138]. The NLO matching uncertainties are estimated by varying the p_T^{hard} parameter, effectively chaining the definition of the hardness of the *Powheg* emission [160].

3.4.2 $t\bar{t}W$ Production

The nominal $t\bar{t}W$ sample is generated using SHERPA 2.2.10 [161,162]. The matrix element is calculated with up to one additional parton at NLO accuracy and up to two additional partons with LO accuracy using COMIX [163] and OPENLOOPS [164–166]. The NNPDF3.0NNLO PDF set is used in the matrix element. The generated events are interfaced with the SHERPA parton shower [167] based on the Catani-Seymour dipole formalism and using the MEPS@NLO prescription [168]. The merge scale is set to 30 GeV. The renormalisation and factorisation scales are set to $\mu_R = \mu_F = H_T/2$, with H_T as the scalar sum of transverse masses $\sqrt{p_T^2 + m^2}$ of all final state particles after matrix element generation. The SHERPA default tune is used.

The nominal sample is generated at NLO in the strong coupling constant α_S . Additional higher-order corrections corresponding to EW contributions are dealt with in two separate ways: First, event-by-event correction factors are derived to correct for virtual NLO EW of order $\alpha_{EW}^2\alpha_S^2$ contributions as described in Ref [169]. Furthermore, LO corrections of order α_{EW}^3 are applied, reducing the expected inclusive $t\bar{t}W$ cross-section by 3.9 % with respect to the NLO QCD prediction [161,170]. Second, an additional sample is generated using SHERPA 2.2.10 with LO accuracy in QED correcting for real emissions of sub-leading EW corrections at order $\alpha_{EW}^3\alpha_S$ [171]. The resultant sample is normalised to $\sigma(t\bar{t}W) = 722_{-78}^{+70}(\text{scale}) \pm 7(\text{PDF}) \text{ fb}$ [172] instead of the total cross-section of $\sigma(t\bar{t}W) = 614.7 \text{ fb}$ calculated by SHERPA taking both NLO QCD and NLO EW effects into account [172].

Similar to the $t\bar{t}H$ samples, the uncertainties on μ_R and μ_F are estimated for $t\bar{t}W$. An additional sample is generated with MADGRAPH5_aMC@NLO interfaced with PYTHIA 8 FxFx [173] to estimate ambiguities due to different matrix element generator, parton shower, and parameter choices, and matching and merging schemes. To further cover differences due to parton shower modelling, alternative samples are generated with POWHEG+PYTHIA 8 and POWHEG+HERWIG 7. The uncertainty is evaluated by comparing the predictions with the nominal prediction by SHERPA.

3.4.3 $t\bar{t}(Z/\gamma^*)$ Production

The production of $t\bar{t}Z/\gamma^*$ MC samples is performed using MADGRAPH5_aMC@NLO 2.8.1 [174] at NLO accuracy in QCD and the NNPDF3.0NNLO PDF set in the matrix element. The renormalisation and factorisation scales are set to $\mu_R = \mu_F = H_T/2$ with H_T as the scalar sum of transverse masses $\sqrt{p_T^2 + m^2}$ of all final state particles after matrix element generation. The decay of top-quarks is simulated at LO with MADSPIN [175,176] preserving all spin correlations. The shower and hadronisation step is performed by PYTHIA 8.244.

The $t\bar{t}Z/\gamma^* \rightarrow (\ell^+\ell^-)$ samples are normalised to the predicted cross-section at NLO accuracy in both QCD and EW for an on-shell Z boson and off-shell $\gamma^* \rightarrow \ell^+\ell^-$ con-

tributions with corrections at one-loop level in α_S [70]. The resulting cross-section for $t\bar{t}\ell^+\ell^-$ with a cut on the low mass distribution of $\ell^+\ell^- > 1\text{ GeV}$ is $162 \pm 21\text{ fb}$.

3.4.4 Diboson Production

Diboson events are generated with the SHERPA 2.2 program, matched with the SHERPA parton shower based on the Catani-Seymour dipole formalism, and merged with the MEPS@NLO prescription. Events are calculated with up to one additional parton at NLO and up to three additional partons at LO using the OPENLOOPS library. Fully-leptonic decay modes with up to four charged leptons in the final state are generated with SHERPA 2.2.2, while semi-leptonic with up to two charged leptons in the final state are generated with SHERPA 2.2.1. The EW contribution $VVjj$ with $V = W, Z$ in the fully-leptonic decay mode is simulated at LO with SHERPA 2.2.2 using the G_μ scheme for pure electroweak interactions at the electroweak scale. All samples are generated with the NNPDF 3.0nnlo PDF set and the SHERPA default set of tunable parameters.

3.4.5 Single Boson Production

The simulation of V +jets events with $V = W, Z$ is done with SHERPA 2.2.1 at NLO matrix-element accuracy with two additional partons and up to four additional partons at LO accuracy using COMIX and OPENLOOPS. The NNPDF 3.0nnlo PDF set is used for the matrix element calculation. The matching is done with the MEPS@NLO prescription while showering is done with the SHERPA default parton shower. The set of tuned parameters for the PS is used, which is provided by the SHERPA authors. All samples are normalised to the NNLO predicted cross-sections.

3.4.6 $t\bar{t}$ and Single-Top Production

Samples for the production of $t\bar{t}$ and single top quark events are generated with POWHEG BOX v2 [152–155, 177–179] at NLO accuracy in QCD. In the matrix element, the NNPDF3.0NLO PDF set is used. To perform parton shower and hadronisation, generated events are interfaced with PYTHIA 8.2.30. The h_{damp} is set to $1.5 \times m_t$ [180]. To avoid overlap of generated tW events with $t\bar{t}$, the diagram removal scheme is used [181].

To further enhance contributions with additional heavy-flavour jets, like c - and b -jets, originating from gluon splitting, samples are generated with the same settings as the nominal $t\bar{t}$ sample but with a filter applied. By using the Monte-Carlo truth record, generated events are filtered into the categories $t\bar{t} + b\bar{b}$, $t\bar{t} + b$ with a veto on $t\bar{t} + b\bar{b}$, and $t\bar{t} + \geq 1c$ with a veto on $t\bar{t} + \geq 1b$. The generated filtered events are combined with the nominal samples by replacing the corresponding heavy-flavour events and keeping the $t\bar{t}$ + light events from the nominal sample. To estimate modelling uncertainties on $t\bar{t} + b\bar{b}$ contribution, a NLO sample is generated in the four-flavour scheme using POWHEGBOXRES [182, 183] and OPENLOOPS [164, 165]. The nominal

prediction of $t\bar{t}$ events is generated in the five-flavour scheme, assuming massless b -quarks described in the initial state by parton distribution functions. In contrast, the four-flavour scheme allows massive b -quarks generated at matrix element level, including mass effects, avoiding the generation of b -quarks through gluon splitting $g \rightarrow b\bar{b}$ by evolution of parton distribution functions via DGLAP equations. The NNPDF3.1NNLONF4 PDF set [157] is used, excluding the b -quark PDF. The factorisation scale and h_{damp} are set to $\frac{1}{2} \sum_{i=t,\bar{t},b,\bar{b}} m_{T,i}$, the renormalisation scale is set to $\frac{1}{2} \sqrt{m_{T,t} \cdot m_{T,\bar{t}} \cdot m_{T,b} \cdot m_{T,\bar{b}}}$. The POWHEG internal parameter h_{bzd} controlling the damping function is set to 5. The mass of the b -quarks is set to $m_b = 4.95 \text{ GeV}$. The events are interfaced with PYTHIA 8.2 to perform parton showering and hadronisation.

The $t\bar{t}$ samples are normalised to the predicted cross-section of $\sigma(t\bar{t})_{\text{NNLO+NNLL}} = 832 \pm 51 \text{ pb}$ with NNLO accuracy in QCD and NNLL soft-gluon resummation using TOP++ 2.0 [84–89, 184]. The three single top quark productions are normalised to $\sigma(tW)_{\text{NLO+NNLL}} = 71.7 \pm 3.8 \text{ pb}$, $\sigma(t, \text{s-chan})_{\text{NLO+NNLL}} = 6.35^{+0.23}_{-0.20} \text{ pb}$, and $\sigma(t, \text{t-chan})_{\text{NLO+NNLL}} = 216.97^{+9.46}_{-8.18} \text{ pb}$. All cross-section calculations are done at NNLO accuracy in QCD and NNLL soft-gluon resummation [185] using TOP++ 2.0.

3.4.7 Samples for Minor Backgrounds

There are several minor backgrounds which enter the analysis. The Higgs production in association with electroweak bosons such as W and Z are simulated with PYTHIA 8.186 using the NNPDF 2.3lo PDF set and the A14 tune. Other processes including top-quarks such as the triple top-quark or $t\bar{t}WW$ production are generated with MADGRAPH5_aMC@NLO 2.3.3 at LO accuracy and interfaced with PYTHIA 8.186 using the NNPDF 2.3lo PDF set and the A14 tune of parameters. For the four top-quark production, the matrix element is also generated with MADGRAPH5_aMC@NLO 2.3.3 but at NLO accuracy. The final states are showered using PYTHIA 8.230 using the NNPDF 3.1nlo PDF set and the A14 tune of parameters. The triboson production, like ZZZ , WZZ , WWZ , and WWW , are simulated with SHERPA 2.2.2 at NLO matrix-element accuracy with no additional partons in the final state and at LO accuracy with up to three additional partons using COMIX and OPENLOOPS. The NNPDF 3.0nlo PDF set and the SHERPA default tune are used for all triboson samples.

CHAPTER 4

Experimental Setup

Every experiment requires a setup to collect data to measure quantities such as total or differential cross-section, particle properties such as masses, or coupling parameters. At the Large Hadron Collider (LHC), data is collected in proton-proton or heavy ion collisions by detectors suitable for the physics application. The operation of the detectors requires multiple specialised groups for maintaining and monitoring as well as for development and further upgrades. Other groups are tasked to check the quality of collected data, preparing a list of data collected under stable detector conditions.

The LHC is located close to Geneva at the Swiss-French border and is today's largest accelerator. It is operated by the European Organisation for Nuclear Research (CERN) with multiple large experiments located at the LHC, one of them being the ATLAS experiment using the ATLAS detector for data recording.

The following provides an overview of the LHC and the ATLAS experiment and detector. It begins with the LHC in Section 4.1, followed by an overview of the ATLAS experiment in Section 4.2. The various parts of the detector, together with the trigger system, are presented in Section 4.2.1 to Section 4.2.4, with a focus on radiation damage and its impact on the performance of the inner detector of the ATLAS detector in Section 4.3.

4.1 The Large Hadron Collider

The Large Hadron Collider (LHC) [186] is a circular collider mainly used for accelerating protons for high-energy proton-proton collisions. Aside from these, the LHC is also used for accelerating ions like lead in lead-lead collisions or lead-proton

©CERN

collisions. The LHC is situated in depth between 50 m and 175 m using the former Large Electron-Positron collider (LEP) tunnel system. It is made of concrete in a quasi-circular shape with a circumference of 27 km ranging from Geneva to the Jura Mountains.

The designed maximum centre-of-mass energy is $\sqrt{s} = 14$ TeV, which requires a set of strong magnets for bending particles in their orbit. The dipole magnets have a magnetic field strength of $B = 8$ T with more than 1200 magnets used for bending. To guarantee stable and focused beams, additionally, quadrupole magnets are used for defocusing and focusing purposes. Other higher-order multipoles, such as sextupole and octupole magnets, are used for smaller corrections, which increases beam stability. All magnets used in LHC are made of niobium-titanium alloy, which has superconductive properties below a temperature of 1.9 K. Therefore, magnets are cooled down with superfluid helium.

The acceleration step requires multiple pre-accelerators. A full sketch of the accel-

erator complex of CERN is shown in Figure 4.1, starting with the primary source of protons, which is for Run 2 hydrogen gas from a bottle. Electrons are stripped off using electric fields, leaving only protons injected into the linear-accelerator facility named LINAC2. The protons are accelerated to energies of 50 MeV using radiofrequency cavities. However, in Figure 4.1 LINAC2 is replaced with LINAC4 used for Run 3, where negative hydrogen ions are accelerated up to energies of 160 MeV. In both cases, the protons or hydrogen ions are injected into the PS BOOSTER, increasing the energy to 2 GeV. For hydrogen ions, the remaining electrons are stripped off during injection to the PS BOOSTER.

The next part of the accelerator chain is the proton synchrotron PS, the first synchrotron at CERN with a circumference of 628 m. The protons are accelerated up to 26 GeV using ordinary non-superconductor dipole magnets. With a circumference of 7 km, the Super Proton Synchrotron (SPS) is the second largest accelerator at CERN, further increasing the proton beam energy up to 450 GeV. It is the final step before injection into the LHC, and it splits the beam into two beams for collisions. There have been several periods of data taking at increasingly higher centre-mass-energy. Run 1 started in March 2010 and ended in 2012. The LHC operated at $\sqrt{s} = 7$ TeV till the end of 2011 and was increased to $\sqrt{s} = 8$ TeV. The beam energy during Run 2 was 6.5 TeV with a centre-of-mass energy of $\sqrt{s} = 13$ TeV, while in Run 3 the beam increases to 6.8 TeV with a centre-of-mass energy of $\sqrt{s} = 13.6$ TeV.

In addition to the centre-of-mass energy, the instantaneous luminosity \mathcal{L} is an important property of a particle collider. Integrated over time, it quantifies the size of the data set collected by an experiment. The number of events N is related to the integrated luminosity $\int \mathcal{L} dt$ via the cross-section σ for an arbitrary process by:

$$N = \sigma \int \mathcal{L} dt. \quad (4.1)$$

To increase the number of expected events for a process, the integrated luminosity has to be increased, as the production cross-section only changes as a function of the centre-of-mass energy¹. The instantaneous luminosity depends only on the collider properties and is given by

$$\mathcal{L} = f \frac{N_1 N_2 n_b}{4\pi\sigma_x\sigma_y}, \quad (4.2)$$

with N_1 and N_2 as the number of particles in the colliding bunches, n_b as the total number of bunches stored in the accelerator ring, and f as the collision frequency. The beam has a Gaussian shape in the transverse direction and is characterised by the Gaussian width σ_x and σ_y in the horizontal and vertical directions. The LHC has a designed instantaneous luminosity of $\mathcal{L} = 10^{34} \text{cm}^{-2} \text{s}^{-1}$ [186]. The delivered integrated luminosity values, together with the recorded ones, and the values passing quality criteria to be used in physics analyses are summarised in Figure 4.2. Most of the data was recorded towards the end of Run 2 in 2018. Particle beams are not

¹In practice, trying to increase the luminosity is easier than building a larger collider leading to higher centre-of-mass energies

continuous but consist of multiple bunches. The mean number of interactions per bunch crossing, sometimes called pile-up, is presented in Figure 4.3 with mean values for each period of Run 2. The average number of interactions per bunch crossing during Run 2 is $\langle\mu\rangle = 33.7$. The small peaks for 2017 and 2018 originate from low pile-up runs for electroweak precision measurements.

There are four large experiments located at the LHC. The large multi-purpose detectors are ATLAS and CMS [187,188]. The ATLAS detector is located at Point 1 close to the CERN main site in Meyrin, while CMS is located at Point 5 close to Cessy in France. Both focus on a large range of precision measurements of SM processes involving top quarks and Higgs bosons. The LHCb detector [189] is located at collision point eight and focuses on B -meson physics featuring an asymmetric forward detector. The last large experiment is located at collision point two and is called ALICE [190]. It specialises in heavy ion physics and research on quark-gluon plasma.

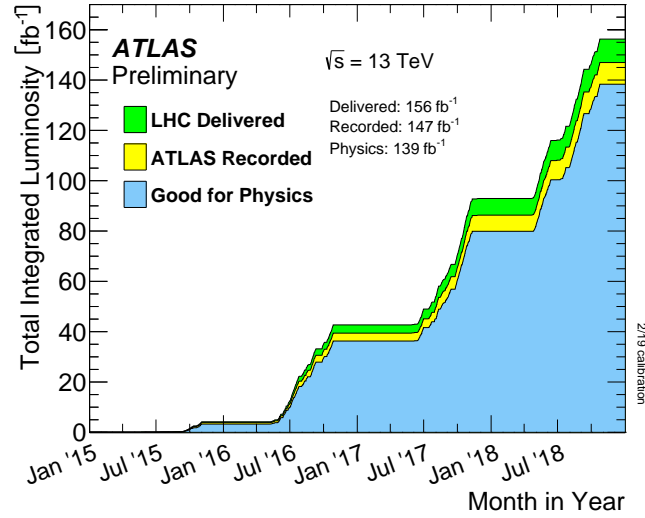


Figure 4.2: Summary of the collected integrated luminosity during Run 2 by ATLAS in proton-proton collisions at $\sqrt{s} = 13$ TeV. This figure shows a previous measurement. The current size of the dataset collected during Run 2 was corrected to $\approx 140 \text{ fb}^{-1}$. The green part shows the delivered integrated integrated luminosity by the LHC. In contrast, the yellow part is the amount of integrated luminosity recorded by the ATLAS detector, and the blue is the amount of integrated luminosity passing quality criteria for physics analyses. This figure is taken from Ref. [191].

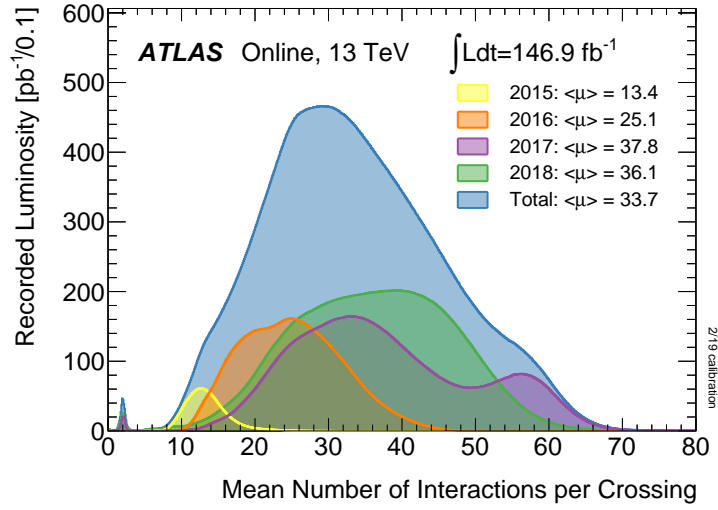


Figure 4.3: Summary of the average number of interactions per bunch crossing for each period of Run 2. This Figure is taken from Ref. [191].

4.2 The Atlas Experiment

The ATLAS experiment, an acronym for **A Toroidal LHC ApparatuS**, is one of the four large experiments located at the LHC. The ATLAS detector is a multi-purpose detector designed for a large range of physics applications. It has the largest volume compared to all other main experiments at LHC, having a total length of 44 m, a height of 25 m, and weighs approximately 7000 t. As depicted in Figure 4.4, the detector has a leek-like² shape with an almost full 4π solid angle coverage around the interaction point. Each layer is specialised for the detection of specific particle types and their kinematic properties. The inner detector, as the name suggests, is closest to the interaction point and measures tracks from charged particles, measuring transverse momentum and reconstructing vertices. Charged particle tracks are bent using a solenoid magnet with a magnetic field strength of 2 T. A detailed description of the detector is in Section 4.2.1, while in Section 5.2.1, the track and vertex reconstruction from inner detector signals are explained. There are two calorimeter systems for stopping both electromagnetic and hadronic particle types. The calorimeter is used for energy measurements, and a description is found in Section 4.2.2. The outermost sub-detector is the muon spectrometer. It is dedicated solely to the transverse momentum measurement of muons using a toroid magnet system with a magnetic field strength of 4 T. Other particles will deposit their energy into the calorimeter system and are less likely to reach the muon spectrometer. The muon spectrometer

²There were intense discussions during lunch breaks on the question, whether the leek-shape or onion-shape description of the ATLAS detector is more appropriate. The author is part of the leek-shape faction, in German: *Lauch-Fraktion*.

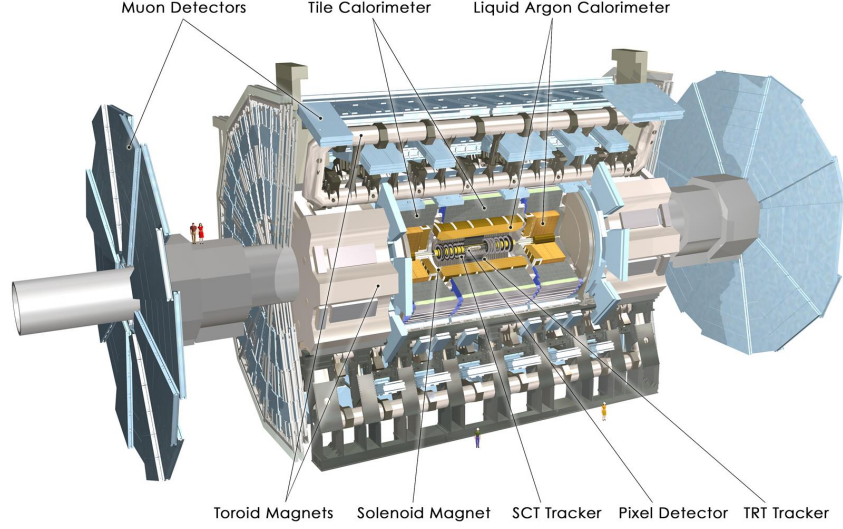


Figure 4.4: A sketch of the ATLAS detector at the LHC at CERN. The various sub-detector parts are shown [187], together with the height and length of the full detector. Humans are shown for scale on the left of the ATLAS detector. ©CERN

is explained in Section 4.2.3.

The ATLAS right-handed coordinate system has its origin at the nominal interaction point in the middle of the detector. The z -axis is defined along the beam line with the x - and y -axis in the transverse plane. The positive x -axis points to the centre of the LHC, while the y -axis points upwards to the surface. Since the detector has a cylindrical shape, instead of Cartesian coordinates, spherical coordinates are used. The azimuthal angle ϕ is defined in the transverse plane around the z axis and θ as the polar angle. The latter is commonly replaced with the pseudorapidity

$$\eta = -\ln \left(\tan \left(\frac{\theta}{2} \right) \right) = \frac{1}{2} \ln \left(\frac{|\vec{p}| + p_z}{|\vec{p}| - p_z} \right), \quad (4.3)$$

with the momentum vector \vec{p} and its z -component in Cartesian coordinates. The pseudorapidity is closely related to the rapidity as they are equal in the relativistic limit, where masses can be neglected. Differences in pseudorapidity $\Delta\eta$ are invariant under Lorentz-boosts in z -direction. Since the difference in azimuthal angle $\Delta\phi$ is Lorentz-invariant in the z -direction by construction, distances between two points

$$\Delta R = \sqrt{\Delta\phi^2 + \Delta\eta^2} \quad (4.4)$$

in the $\eta - \phi$ plane, which replaced the $x - y$ plane, are also Lorentz-invariant under boosts in the z -direction.

4.2.1 Inner Detector

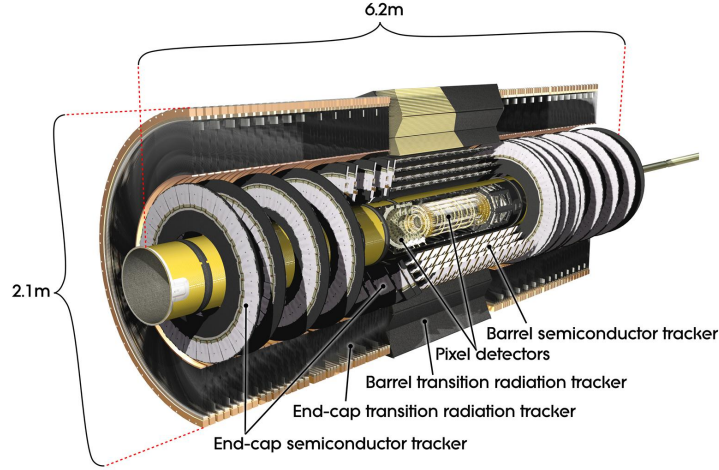


Figure 4.5: A sketch of the ID sub-detector of the ATLAS detector. The ID is closest to the interaction point and consists of the three sub-detectors PIXEL, SCT, and TRT. In the central region, all components have a layer structure, while forward- and backward regions are covered with end-caps or disks. ©CERN

The innermost sub-detector part of the ATLAS detector is the inner detector (ID) [192, 193]. It is a tracking detector measuring hits of charged particles in the active material. Tracks are then reconstructed from those hits; a full description is in Section 5.2.1. A solenoid magnet [194] is placed around the ID with a magnetic field of 2 T, bending charged particles and allowing measurements of the transverse momentum due to their bending radius. The magnetic field, together with the granularity and spatial resolution, are key properties for the transverse momentum measurements and vertex identification. The latter is essential for the identification of the hard scattering or primary vertex as well as for secondary vertices used for b -jet identification. This turns out to play an important role in the measurement of every process involving top quarks, like the $t\bar{t}H$ multi-lepton analysis. The ID is relatively compact, with a length of 6.2 m and a cylindrical shape with a diameter of 2.1 m. It consists of three subsystems: the Pixel Detector (PIXEL), the Semiconductor Tracker (SCT), and the Transition Radiation Tracker (TRT). A sketch of the ID is shown in Figure 4.5. The central region around the interaction point is covered with multiple layers of the three sub-components with varying coverage in terms of pseudorapidity. The forward- and backward regions are covered by end-caps, sometimes called disks. The PIXEL detector is closest to the interaction point and is divided into four layers in the barrel region and three pixel end-caps on each side of the PIXEL detector. The barrel part has 1 736 modules covering a pseudorapidity range of $|\eta| < 2.5$, while each pixel disk has 288 modules. The innermost layer of the Pixel detector, namely

the Insertable B-Layer (IBL) [195], was added later during LS1 to improve vertex reconstruction, including secondary vertex identification, b -tagging, and to add a redundancy layer to the PIXEL system in view of the expected radiation damage. In total, there are 92 million silicon pixels with the size of $50 \times 400 \mu\text{m}^2$. In case of IBL, the pixel size is $50 \times 250 \mu\text{m}^2$.

The SCT is placed around the PIXEL detector and features four layers of silicon-strip sensors [196] in the barrel region, and in total, nine end-caps for the forward- and backward region, providing additional information for tracking. The silicon-strip sensors are arranged in pairs with a stereo angle to each other, improving spatial resolution. The achieved spatial resolution in the transverse plane is approximately $16 \mu\text{m}$, while in z -direction it is $580 \mu\text{m}$. The SCT has 4000 modules, 2112 in the barrel region and 1976 for the end-caps, with approximately six million read-out chips.

The last part of the ID is the TRT, which features approximately 300 000 straw tube detectors divided into barrel and end-cap regions. The tubes are aligned with the beam pipe in the barrel region, while in the forward- and backward regions, they are orthogonal to the beam pipe. Adding further tracking information, the transition radiation is utilised to obtain additional information on the Lorentz factor γ and, therefore, the mass of charged particles traversing the straw tubes. The mass information is used to distinguish between electrons and hadrons like pions.

The transverse momentum resolution of the ID depends on the transverse momentum of the incoming particle. Overall, the relative momentum resolution is:

$$\sigma_{p_T}/p_T = 0.05 \% \cdot p_T \oplus 1.0 \%. \quad (4.5)$$

4.2.2 Calorimeter System

The calorimeter system envelopes the ID and measures energies of hadrons, electrons and photons via interaction with the detector material, which is called showering. A shower cascade is induced by an incident particle passing through the active material of the calorimeter, where it either emits radiation or undergoes pair production. This procedure is repeated, creating a shower cascade until critical energy is reached, preventing further radiation or pair production and stopping the cascade process. The energy of the incident particle is deposited into the calorimeter material and can be determined by the length of the shower cascade. Since the underlying interaction types for electrons or photons and hadrons are different, the calorimeter system is divided into the electromagnetic calorimeter ECAL [197] and the hadronic calorimeter HCAL [198] as shown in Figure 4.6. Photons and electrons mainly interact via electromagnetic interaction with the ECAL, while hadrons interact via the strong force with the HCAL material.

The ECAL is a *Liquid Argon Calorimeter* (LAR) using Lead plates as absorbers and liquid Argon as the active material. Both materials are samples, which makes the LAR a sampling calorimeter. An electron or photon starting a shower cascade will ionise Argon atoms, and due to the applied voltage, the produced ions and electrons drift

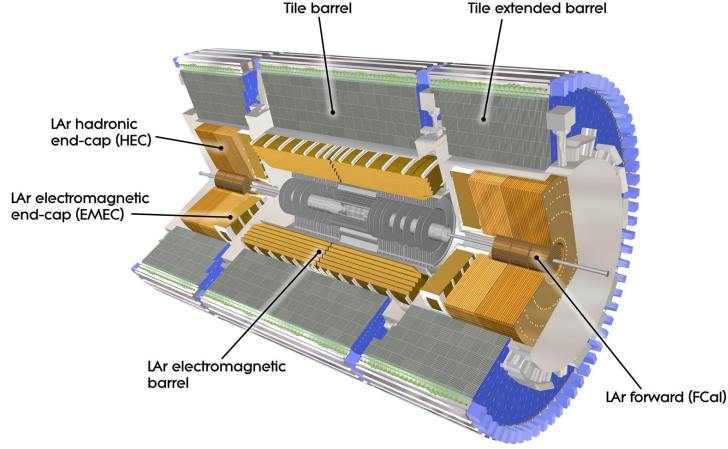


Figure 4.6: A sketch of the calorimeter system of the ATLAS detector. The calorimeter system is split into an ECAL for measuring the energies of electrons and photons and into a HCAL for hadronic particles [187]. The calorimeter system is spatially split into the barrel and forward and backward regions. ©CERN

towards the absorber material, which induces a signal. The thickness of the ECAL is approximately 22 radiation length³, designed to stop most incoming electrons and photons reliably. The ECAL requires a fine resolution for measuring differences in shower shapes, which is a distinguishing feature between electrons and photons. The resolution in terms of $\Delta\eta \times \Delta\phi$ is between 0.025×0.025 to 0.1×0.1 , depending on the pseudorapidity range. The ECAL is split into a barrel part covering $|\eta| < 1.475$ and two end-caps covering $1.35 < |\eta| < 3.2$. Especially the separation between photons is highly important to identify $\pi^0 \rightarrow \gamma\gamma$ decays. Therefore, the first layer of the barrel region is finely segmented in the η direction. In contrast, the remaining two layers have a coarser granularity to measure the shower cascades' main energy. In the range $|\eta| < 1.8$, a thin pre-sampling layer is used, which corrects for energy losses of electrons and photons interacting with the solenoid material. The achieved energy resolution is:

$$\sigma_E/E = 10\%/\sqrt{E} \oplus 0.7\%. \quad (4.6)$$

The hadronic calorimeter HCAL or *Tile Hadronic Calorimeter* is in the outer part of the calorimeter systems around the ECAL and is a sampling calorimeter using steel as the absorber material and scintillating tiles as the active material for the barrel region. The barrel region covers the range of $|\eta| < 1.7$ with a granularity in terms of $\Delta\eta \times \Delta\phi$ of 0.1×0.1 and an overall energy resolution of:

$$\sigma_E/E = 50\%/\sqrt{E} \oplus 2\%. \quad (4.7)$$

³A radiation length is defined as the depth of an incident particle passing through the calorimeter material, decreasing the particle energy to $1/e$ of the initial energy.

The barrel section is split into the *Long-Barrel* (LB) ranging to $|\eta| < 1.0$ and the *Extended Barrel* (EB) on both sides of the HCAL system covering $0.8 < |\eta| < 1.7$. The barrel section has a thickness of approximately 7.4 radiation lengths, stopping most hadronic jets and preventing particle leakage into the muon spectrometer system. The LAr hadronic end-caps system is placed in the forward- and backward regions, covering a pseudorapidity range of $1.5 < |\eta| < 3.2$ with two disks on each detector side. Copper is used as the absorber, with liquid Argon as the active material, giving the calorimeter system its name. The granularity depends on the pseudorapidity and ranges between 0.1×0.1 and 0.2×0.2 in terms of $\Delta\eta \times \Delta\phi$. The calorimeter system is completed with the forward calorimeter FCAL extending the pseudorapidity, covering $3.1 < |\eta| < 4.9$. The FCAL consists of three modules using liquid Argon as the active material but a different absorber. The first module uses copper, which is mostly used for photon or electron-induced showers, while the remaining two modules use tungsten as the absorber to measure hadronic shower activities. The energy resolution is:

$$\sigma_E/E = 100\%/\sqrt{E} \oplus 10\%. \quad (4.8)$$

4.2.3 Muon Spectrometer

The outermost part of the ATLAS detector is the muon spectrometer (MS) system dedicated to identifying and measuring muons [187]. Muons are created in collisions or as decay products with an energy of about $\mathcal{O}(100 \text{ MeV})$ up to $\mathcal{O}(100 \text{ GeV})$. Hav-

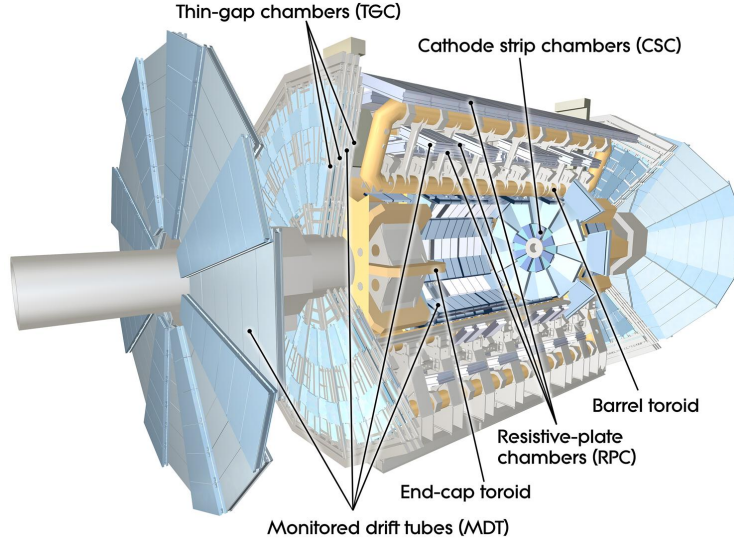


Figure 4.7: A sketch of the muon spectrometer system of the ATLAS detector. It is split into four components and spatially divided into the barrel and end-cap regions.

©CERN

ing a 200 times larger mass than electrons, muons at this energy scale are minimal ionising particles (MIP) and interact with the detector material feebly, traversing through the ID and calorimeter system. Other particles like photons, electrons, and hadrons will be stopped earlier.

The various subsystems are enclosed with a magnetic field of 4 T, created by eight 25 m long air-core toroidal magnets [199] in the barrel region $|\eta| < 1.4$ and additionally two toroidal end-caps [200] for the forward- and backward regions in the range of $1.6 < |\eta| < 2.7$. A sketch of the MS is presented in Figure 4.7. Four MS subsystems are used for muon track identification and transverse momentum measurements from track curvatures. The main components are Monitored Drift Tubes (MDT) with a total number of 354 240 distributed in 1 171 chambers. The MDT has a spatial resolution of $35\mu\text{m}$ per tube and $80\mu\text{m}$ per chamber in the longitudinal direction, allowing for precise muon candidate measurements. In the forward direction at pseudorapidity ranges $2.0 < |\eta| < 2.7$, Cathode-Strip Chambers (CSC) are used due to their high time resolution compared to MDT. For the same reason, Resistive Plate Chambers (RPC) are placed in the barrel region, and Thin Gap Chambers (TGC) are placed in the end-cap regions. The RPC and TGC also provide information to the trigger system. For a muon with $p_T = 1\text{ TeV}$, the relative transverse momentum resolution of the MS is:

$$\sigma_{p_T}/p_T = 10\%. \quad (4.9)$$

4.2.4 Trigger System

The bunch crossing frequency of 40 MHz and the average number of 33.7 interactions per bunch during Run 2 results in approximately 1.7 billion proton-proton collisions per second. If stored, this would occupy 60 Tb of storage per second. From an analysis perspective, most of the recorded events are uninteresting as they may feature only elastic proton-proton collisions. Furthermore, from a data management perspective, processing such an amount of data would be impossible⁴. To reduce the amount of collected data, a two-level trigger system is used to filter events that have interesting properties. The *Level-1* trigger (L1) is a hardware-based trigger system [187, 201, 202] and selects events featuring muons, electrons, photons, or jets⁵ with high transverse momentum as they are typical features of inelastic proton-proton collisions. Events with a large amount of E_T^{miss} or transverse energy will also pass. The L1 trigger decides on a subset of the detector response, like RPC and TGC information for muons or reduced-granularity information from the calorimeter system for jets, electrons, and photons. Information from the ID is excluded due to the computationally expensive track fitting. For each passing event, the L1 trigger also defines one or more Regions-of-Interest (RoI) around interesting features, providing extra information on the coordinates and type for the next trigger level. Events that pass the L1 trigger are stored temporarily to the *Read-Out System*. The L1 trigger reduces the initial event rate to some 100 kHz.

⁴At least by today's standards.

⁵Including also τ_{had} candidates.

The second trigger is a high-level trigger (HLT), which is a software trigger using previous information passed by the L1 trigger together with the RoI as input. The HLT decides to use the full detector information on object candidates and RoI. If none of the candidates passes the criteria, the event is discarded, and the remaining passing events are stored on disk. The HLT reduces the rate to some 1 kHz.

4.3 Radiation Damage Effects on the Pixel Detector

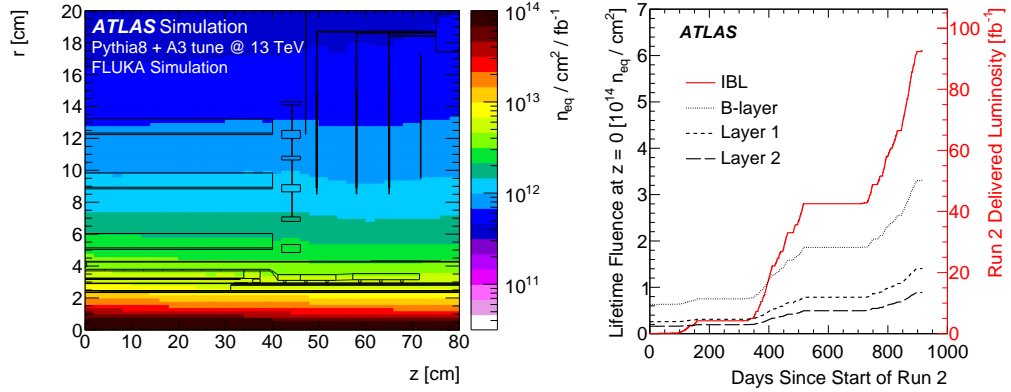


Figure 4.8: On the left side are predicted fluence values as a function of the radial and longitudinal components of the PIXEL detector. The predictions are obtained from simulation with PYTHIA 8 [147] modelling inelastic proton-proton events while FLUKA [203] simulated the particle transport through the detector material. On the right side, the accumulated fluence values are shown for the four layers of the barrel region of the PIXEL detector covering the first three periods of Run 2. Both figures are taken from Ref. [204]

The PIXEL detector of the ID is a silicon-based tracking detector closest to the interaction point. The basic building blocks for the various layers of the PIXEL detector are modules featuring a silicon sensor, front-end electronics, and flex-hybrids with control circuits. The silicon sensor is the part sensitive to the detection of charged particles. Signals are measured as hits and later fitted to form a track, determining the transverse momentum and reconstructing primary and secondary vertices. The ATLAS PIXEL detector is separated into four layers at the barrel region, with the IBL as the innermost layer. All sensors of the four layers are composed of n^+ -in- n planar oxygenated silicon sensors [205, 206], with a thickness of $250 \mu\text{m}$ and $200 \mu\text{m}$ for the IBL⁶. Two types of interaction can occur in the sensor: ionising interactions and non-ionising ones. The former is used for signal detection and is induced by traversing minimal-ionising particles, leading to the creation of deposited charges

⁶The ID uses at high $|z|$ values also n^+ -in- p 3D sensors with a thickness of $230 \mu\text{m}$ [207], however this section only focus on the planar ones.

via ionisation of the silicon bulk. The charges drift to electrodes and are digitised. Non-ionising interactions from heavy particles and nuclei with silicon atoms cause damage to the silicon bulk and its lattice structure. The defects can be categorised into point defects ranging from displacement of silicon atoms, vacancies, or (non) silicon interstitials. Several point defects form cluster defects, which change the properties of the silicon pn-junction by adding additional energy gaps. The macroscopic effects are a reduced signal collection efficiency caused by charge trapping or an increasing leakage current. A change in the doping concentration especially changes the depletion voltage and the electric field inside the sensor. The ID is exposed to a large amount of radiation, which causes cumulative damage during data taking. Furthermore, the amount of radiation damage to a sensor depends strongly on the position of the sensor, as shown on the left side in Figure 4.8. The expected fluence normalised to a 1 MeV neutron radiation is simulated using inelastic proton-proton events generated by PYTHIA 8 [147], while the modelling of particle transport is done by FLUKA [203]. On the right side of Figure 4.8, the cumulative fluence for all four layers for partial Run 2 is depicted, demonstrating a radial dependence.

The spatial dependence is further studied for the end-cap part of the PIXEL detector, called PIXEL disks. To quantify the impact of radiation damage on the PIXEL disks, the corrected⁷ cluster charge is used. In Figure 4.9, the change in the shape of the corrected cluster charge distribution from the start of Run 2 till the end of Run 2 is compared. The upper row shows the impact on the individual pixel disk, neglecting the different sides of the detector. The lower row compares three different radius values, ignoring any disk dependence and therefore z -dependence, splitting the pixel disk uniformly into: $90 \text{ mm} < R_1 \leq 110 \text{ mm}$, $110 \text{ mm} < R_2 \leq 130 \text{ mm}$, and $130 \text{ mm} < R_3 \leq 150 \text{ mm}$. The cluster charge distribution follows a Landau function convoluted with a Gaussian. The Landau parameter LP , sometimes called the location parameter, provides a satisfactory estimation of the cluster charge. The trend of LP during Run 2 as a function of the integrated luminosity, and therefore to the amount of radiation damage, is shown in Figure 4.10. The three PIXEL disks are compared on the left side, effectively testing the z -dependence of the radiation damage distribution. Only minor differences between the PIXEL disks are observed, indicating a small z -dependence. On the right side, the estimated Landau parameters of the radius regions are compared, demonstrating more significant differences and indicating R -dependence.

The modelling of radiation damage effects [204] on the ID is part of the MC simulation chain during detector simulations. The MC simulation for the radiation damage digitisation is done in several steps. Figure 4.11 shows the trajectory of a particle passing through the detector material. It demonstrates the impact on the sensor and visualises the several steps for digitisation, from charge creation to detection

⁷The cluster charge is corrected by the incident angle.

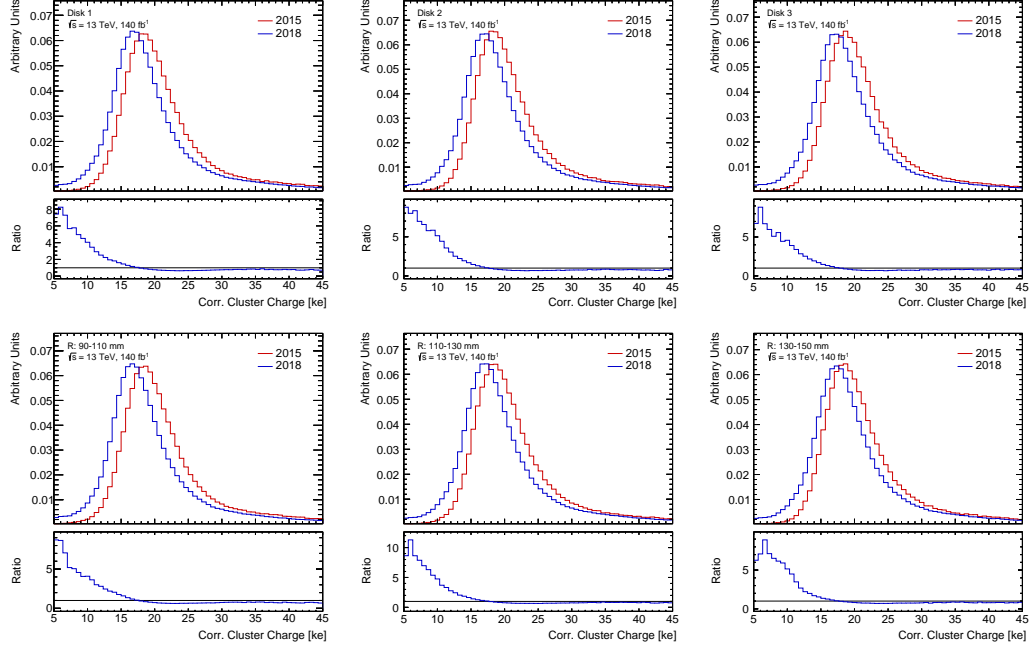


Figure 4.9: Comparison of the corrected cluster charge distribution for data taken from the start and end of Run 2. The top row compares the three PIXEL disks, neglecting any side dependence of the detector. The bottom row compares three radii, defined by a uniform splitting of the PIXEL disks and neglecting any z -dependence.

and conversion into digital signals. As the minimal-ionising particles pass through the detector, charge carriers are released. The electric field inside the sensor will drift them to the collecting electrodes. The electric field changes depending on the accumulated damage in terms of fluence, type of radiation, and temperature. The electric field is calculated using the *Technology Computer Aided Design* (TCAD) simulations [209] based on the Chiochia model [210]. However, the calculation is computationally expensive. Therefore, an interpolator is used: Electric fields are interpolated from generated TCAD maps with fixed fluence values accumulated by the sensor and the applied voltage. A summary of fluence values and detector settings are shown in Table 4.1 for each run period. In contrast, in Figure 4.12, a collection of interpolated electric fields is shown, demonstrating the impact of radiation damage in the barrel layers of the PIXEL detector. The path of the charge carriers is influenced by the electric field $E(z)$ with the sensor depth z and the applied magnetic field B . It is quantified by the Lorentz-angle θ_L

$$\tan(\theta_L) = \frac{rB}{|z_f - z_i|} \int_{z_i}^{z_f} \mu(E(z)) dz, \quad (4.10)$$

with z_i and z_f as the initial and final position of the path, r as the Hall scattering factor, and μ as the charge mobility. The spatial resolution also depends on the

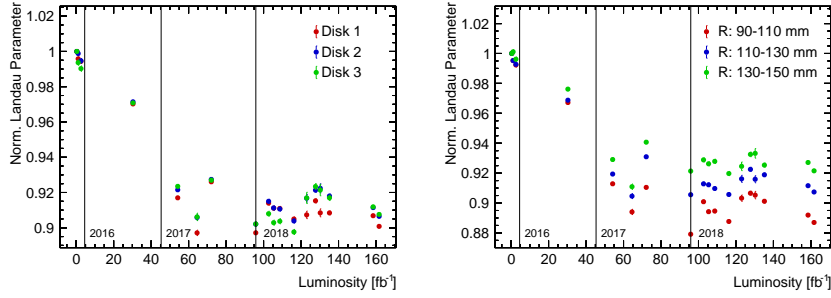


Figure 4.10: Trend of the Landau parameter as the estimator for the corrected cluster charge. On the left side, the z -dependence is studied by comparing the three PIXEL disks with each other, while on the right side, the different radius values are compared, studying R -dependencies.

Sub-Part	Year	Fluence [$10^{14} n_{eq}$]	HV [V]	Temp. [$^{\circ}C$]	Dig. Thres. [ToT]	Ana. Thres. [e]
IBL	2015	1.70	80	-3	0	2550
	2016	3.20	80	15	0	2550
	2017	6.74	350	-20	0	2550
	2018	10.3	400	-20	0	2000
B-Layer	2015	1.16	250	-2	3	3500
	2016	2.19	350	-10	5	5000
	2017	4.60	350	-20	5	5000
	2018	7.03	400	-20	3	5000
Layer 1	2015	0.48	150	-2	3	3500
	2016	0.90	200	-10	5	3500
	2017	1.90	200	-20	5	3500
	2018	2.90	250	-20	5	3500
Layer 2	2015	0.32	150	-2	3	3500
	2016	0.61	150	-10	5	3500
	2017	1.28	150	-20	5	3500
	2018	1.96	200	-20	5	3500
Disks	2015	0.32	300	-13.8	5	3500
	2016	0.61	150	-13	5	3500
	2017	1.29	150	-20	5	4500
	2018	1.97	250	-20	5	3500

Table 4.1: An overview of the main PIXEL detector settings for each period of data taking during Run 2. The values of radiation exposure in terms of fluence are shown for the PIXEL detector parts by the end of the data-taking period [208].

Lorentz angle. For the PIXEL disks, $\theta_L = 0$ is applied, as the electric field is parallel to the magnetic field. In addition to the magnetic field, thermal drift and diffusion also influence the charge trajectory. Due to cluster defects caused by radiation damage, charges can be trapped, inducing or screening a fraction of their charge. This is modelled with the Ramo potential, described by the Ramo-Shockley theorem [211, 212]. The last step is the digitisation of signals.

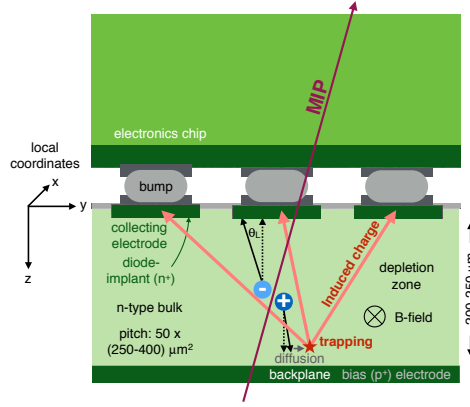


Figure 4.11: A sketch of a minimal ionising particle, creating charges in the silicon bulk. Charges drift through diffusion as well as electric and magnetic fields. Due to radiation damage, charges can be trapped. This figure is taken from Ref. [204]

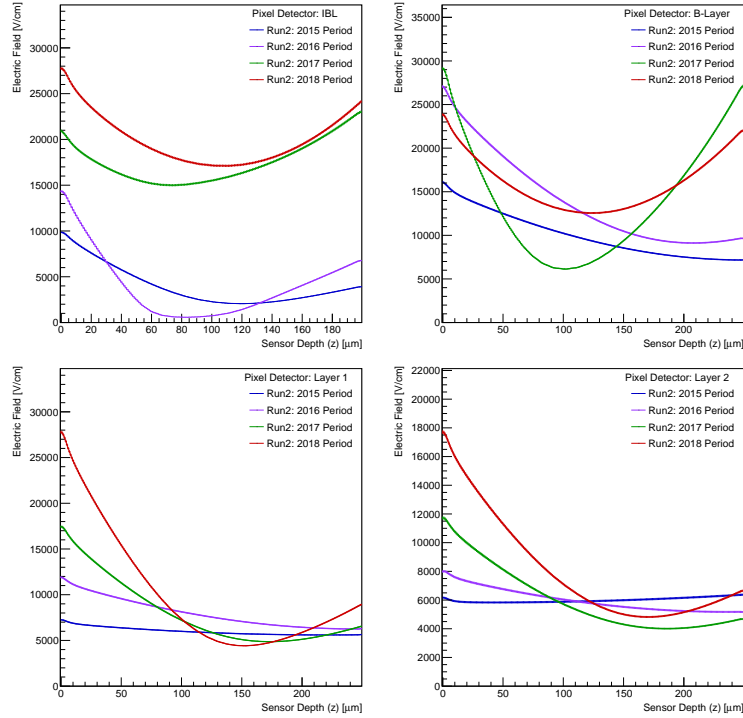


Figure 4.12: The electric field maps for the four layers of the barrel region of the PIXEL detector. The change of the electric field is driven by the changed detector setting summarised in Table 4.1 and radiation damage dealt to the layers during Run 2. The large offset for IBL is caused by different voltages applied. The used fluence values are taken from the end of each period.

CHAPTER 5

Definition and Reconstruction of Physics Objects

Can you tell me what an electron is? It depends on your definition.

Elizaveta Shabalina

The ATLAS detector does not directly measure physics objects, like electrons, jets, or muons. Particles, decay products of created mother particles or directly produced during hard scattering, will leave characteristic signals in the parts of the ATLAS detector. These signals are used to reconstruct physics objects used during the analysis, involving multiple steps and choices on used working points, defining the *quality* of an object. *Tight* selections have the advantage of high-quality cuts and, therefore, high purity but at the cost of a small expected yield. For *loose* objects, the opposite holds. Another crucial aspect is the calibration of physics objects, usually done with known reference objects. The object reconstruction, selection, and calibration are performed on data and each MC sample, described in Section 3.4.

This chapter presents the trigger selection and definition of physics objects used in the $t\bar{t}H$ multi-lepton analysis. The first Section 5.1 describes the trigger selections strategy, while in Section 5.2, the various physics object reconstructions are discussed. Starting from definitions of tracks and vertices in Section 5.2.1, followed by lepton reconstruction techniques in Section 5.2.2, with a special focus on non-prompt lepton rejection in Section 5.2.3. A complete overview of the used leptons is presented in Section 5.2.4. Other important physics objects, like jets, b -jets, τ_{had} , and $E_{\text{T}}^{\text{miss}}$, are introduced in Section 5.2.5 to Section 5.2.7. The overlap removal procedure is shown in Section 5.3.

5.1 Event Quality and Trigger Strategy

Only events with at least one reconstructed vertex with ≥ 2 associated tracks with a minimal transverse momentum of $p_T > 500$ MeV and a reconstructed primary vertex are considered. Events from the *good-run-list* passing data quality criteria are selected, and events containing significant noise, data corruption, or unstable detector conditions are discarded.

Events are further selected by combining single lepton (SL) and dilepton (DL) triggers. A summary of the trigger selection for each analysis channel, defined in Chapter 6, is presented in Table 5.1. The logical *or* is used. A list of trigger settings for each period of data taking for single lepton triggers is summarised in Table 5.2 and for dilepton triggers in Table 5.3. The dimuon trigger p_T thresholds are asymmetric, while for dielectron triggers, they are symmetric. They are almost symmetric for $e\mu$ and μe combinations.

Channel	Trigger Selection
$2\ell\text{SS}+0\tau_{\text{had}}$	SL DL
$3\ell+0\tau_{\text{had}}$	SL DL
4ℓ	SL DL
$2\ell\text{SS}+1\tau_{\text{had}}$	SL DL
$1\ell+2\tau_{\text{had}}$	SL
$2\ell\text{OS}+2\tau_{\text{had}}$	SL DL

Table 5.1: An overview of the trigger selection for each analysis channel is defined in Chapter 6. The logical *OR* is used for the combination of SL and DL for all analysis channels except for the $1\ell+2\tau_{\text{had}}$ channel, which uses naturally only SL.

single lepton triggers (2015)	
μ	HLT_mu20_iloose_L1MU15 HLT_mu50
e	HLT_e24_lhmedium_L1EM20VH HLT_e60_lhmedium HLT_e120_lhloose
single lepton triggers (2016, 2017 and 2018)	
μ	HLT_mu26_ivarmedium HLT_mu50
e	HLT_e26_lhtight_nod0_ivarloose HLT_e60_lhmedium_nod0 HLT_e140_lhloose_nod0

Table 5.2: List of lowest p_T -threshold, un-prescaled single lepton triggers used for the Run 2 data taking periods.

Dilepton triggers (2015)	
$\mu\mu$ (asymm.)	HLT_mu18_mu8noL1
ee (symm.)	HLT_2e12_lhloose_L12EM10VH
$e\mu, \mu e$ (\sim symm.)	HLT_e17_lhloose_mu14
Dilepton triggers (2016)	
$\mu\mu$ (asymm.)	HLT_mu22_mu8noL1
ee (symm.)	HLT_2e17_lhvloose_nod0
$e\mu, \mu e$ (\sim symm.)	HLT_e17_lhloose_nod0_mu14
Dilepton triggers (2017 and 2018)	
$\mu\mu$ (asymm.)	HLT_mu22_mu8noL1
ee (symm.)	HLT_2e24_lhvloose_nod0
$e\mu, \mu e$ (\sim symm.)	HLT_e17_lhloose_nod0_mu14

Table 5.3: List of lowest p_T -threshold, un-prescaled dilepton triggers used for the Run 2 data taking periods.

5.2 Object Reconstruction and Definition

This section presents the different reconstruction and calibration techniques for physics objects. Most interactions in pp are elastic. Triggers select more interesting inelastic ones, like a $t\bar{t}H$ event. Created particles decay rapidly during the collision and cannot be detected directly. However, some particles have sufficiently long lifetime or decay length $\tau c > 500 \mu\text{m}$ to travel the distance between the interaction point and the detector. Elementary particles reaching the detector are electrons, muons, and photons, with the former two playing an essential role in the $t\bar{t}H$ multi-lepton analysis. Other detectable particles are pions, kaons, protons, or neutrons, primarily found in jets as they are created due to QCD colour confinement or as decay products of other unstable hadrons.

5.2.1 Track and Primary Vertex Reconstruction

Particles carrying electric charge will leave hits in the different layers of the inner detector (ID). These hits are the starting point for further track reconstruction. The three-dimensional measured hits are grouped with a connected component analysis [213] into clusters called space-points [214]. The track reconstruction is performed with a tracking algorithm [215] using track seeds formed from three space points as input. The reconstruction is divided into three steps: pattern recognition, ambiguity resolution, and TRT extension. The pattern recognition fits various combinations for track candidates using the ATLAS Global χ^2 Track Fitter [216] using the pion hypothesis for modelling the energy loss due to interaction with the detector material. Ambiguities between tracks sharing the same hits are removed during fitting. The final set of tracks is defined by adding information from the TRT and checking their

compatibility. Track candidates are parametrised by

$$\tau = (d_0, z_0, \phi, \theta, q/|\vec{p}|), \quad (5.1)$$

with d_0 and z_0 as the transversal and longitudinal impact parameters, ϕ as the azimuthal angle, θ as the polar angle, and the charge over momentum ratio $q/|\vec{p}|$. For the electron reconstruction, tracks are refitted using a Gaussian-sum filter (GSF). It enhances the modeling of radiation loss and accounts for nonlinear effects caused by bremsstrahlung [217, 218]. The GSF method is a generalisation of the Kalman filter method [219].

The primary vertex (PV) is defined by vertex reconstruction algorithm [220, 221] as the vertex with the largest $\sum p_T^2$ of associated reconstructed tracks. Tracks are further used and matched with energy deposits of the electromagnetic calorimeter to define electron, muon, or τ_{had} candidates or to be matched with hadronic calorimeter energy deposits to define jet candidates.

5.2.2 Lepton Reconstruction and Definition

An extensive set of lepton definitions is used in the $t\bar{t}H$ multi-lepton analysis. All definitions are based on different quality cuts imposed on reconstructed lepton candidates. The reconstruction of electron and muon candidates is described in the following section. An overview of the used lepton definitions in the analysis is given in Section 5.2.4.

Electron Reconstruction and Identification

Electrons are charged particles, leave tracks in the ID, and deposit their energy in the electromagnetic calorimeter, creating a shower cascade through bremsstrahlung and pair production. Figure 5.1 presents a sketch of this process. Electron candidates are reconstructed from topological energy clusters matched with reconstructed tracks from the ID [222]. The electromagnetic calorimeter is divided into a grid of 200×256 elements with the size of $\Delta\eta \times \Delta\phi = 0.025 \times 0.025$. Each element defines a tower with a depth of three layers. If available, the pre-sampler is included. Local cluster candidates are seeded using a sliding window algorithm [223]. The resultant local clusters have a size of 3×5 towers with their sum of transverse energy larger than 2.5 GeV. The sliding window avoids double-counting of neighbouring cluster candidates. Finally, electron candidates are constructed by matching information from the electromagnetic calorimeter with track information from the ID. Track and cluster are considered to be matched if $|\eta_{\text{cluster}} - \eta_{\text{track}}| < 0.05$ and $-0.10 < q \times (\phi_{\text{cluster}} - \phi_{\text{track}}) < 0.05$ with q as the reconstructed charge of the track.

Electron candidates entering the central region of the ATLAS detector with $|\eta| < 2.47$, excluding the barrel-endcap transition region $1.37 < |\eta| < 1.52$, are classified as prompt leptons if they are properly reconstructed and associated with the hard

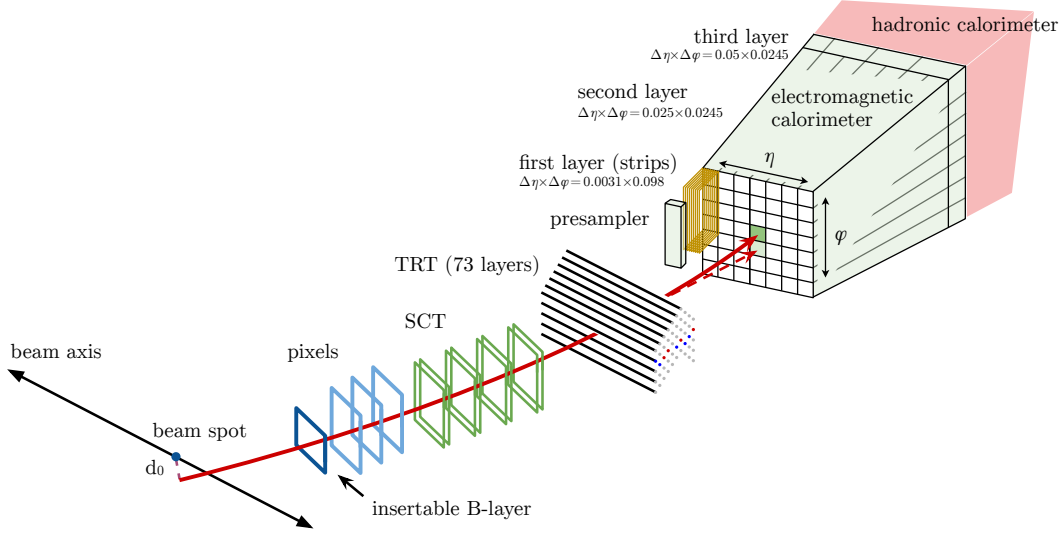


Figure 5.1: An example of an electron passing various detector parts. The electron is marked in red and leaves hits in the layers of the ID. Behind the ID, the electron is absorbed in the electromagnetic calorimeter. The dashed red line indicates a photon created by the interaction of the electron with the tracking detector material. This figure is taken from Ref. [222].

collision. In contrast, a fake lepton originates from the misreconstruction of other physics objects, like jets, mimicking electron signatures. In contrast, non-prompt leptons are *real* leptons not associated with the primary collision. They are created in semi-leptonic hadron decays, embedded in jets. Those leptons may pass isolation criteria. A discussion on non-prompt and fake lepton backgrounds and their estimation with further discrimination tools is presented in Chapter 7 and Section 5.2.3. Prompt, non-prompt, and fake leptons have different signatures affecting quantities associated with the tracking, like the number of hits in the ID, or the calorimeter system, like the depth of the electromagnetic shower cascade. A likelihood-based (LH) discriminator d_L utilises differences in these quantities to reduce non-prompt and fake contributions and is defined as:

$$d_L = \frac{L_S}{L_S + L_B}, \quad L_{S(B)}(\mathbf{x}) = \prod_{i=1}^n P_{S(B),i}(x_i). \quad (5.2)$$

The likelihood function for prompt electrons is L_S and for non-prompt or fake electrons L_B . The likelihood functions are products of probability density functions for a quantity x_i of the full vector of quantities \mathbf{x} [222, 224]. The LH identification was also used during Run 1 [225] and was adapted for Run 2 conditions. There are three defined working points with a fixed value of the LH discriminant. The working points are called *Loose*, *Medium*, and *Tight*. The measured efficiencies for the three working points as a function of transverse energy E_T and pseudorapidity are shown

in Figure 5.2. Additionally, the *LooseAndBLayer* working point is introduced with the same LH discriminant cut as *Loose* but requires at least one hit in the innermost pixel layer.

Isolation criteria on electron candidates are used to reduce non-prompt lepton contributions further. Isolation variables quantify the activity around electron candidates and can be based on calorimeter or track information. There are the following isolation variables:

- $E_T\text{TopoCone20}$ (E_T^{cone20}): is a calorimeter based isolation variable, summing up the transverse energy of topological clusters around the electron candidate in a fixed cone with radius $\Delta R = \sqrt{(\Delta\eta)^2 + (\Delta\phi)^2} = 0.2$. The deposited electron transverse energy is excluded. Contributions from pile-up are removed by the ambient energy-density technique on an event-by-event basis [226]. The radius parameter can be set to $\Delta R = 0.3$, the variable is then called $E_T\text{TopoCone30}$ (E_T^{cone30}).
- $p_T\text{VarCone30}$ ($p_T^{\text{varcone30}}$): is a track based isolation variable and is defined as the scalar sum of the transverse momentum of ID tracks associated with the primary vertex in a variable cone size with $\Delta R = \min(10\text{ GeV}/p_T, R_{\text{max}})$ and $R_{\text{max}} = 0.3$. The electron candidate track is excluded from this calculation, and only tracks with a $p_T > 1\text{ GeV}$ are considered. The maximal radius value R_{max} is often between 0.2 and 0.4. The value of 10 GeV is obtained from simulated $t\bar{t}$ events and maximises non-prompt electron rejection.
- $p_T\text{VarCone30TightTTVA}$ ($p_T^{\text{varcone30, tightTTVA}}$): is a track based isolation variable and it is similarly defined as $p_T\text{VarCone30}$. Tracks need to fulfil track-to-vertex-association (TTVA) $|z_0 \sin(\theta)| < 3\text{ mm}$ and are not associated with another vertex.

Further discussion on electron and lepton isolation can be found in Section 5.2.3. Efficiencies for electron reconstruction are derived by comparing simulated $Z \rightarrow ee$ and $J/\psi \rightarrow ee$ events with measured events in data.

Muon Reconstruction and Identification

Muons carry charge and leave tracks in the ID and outermost layer of ATLAS muon spectrometer (MS). Due to their heavier mass compared to electrons, muons feebly interact with the electromagnetic and hadronic calorimeter system, depositing a characteristic tiny amount of energy. The reconstruction of muons relies on ID and, most importantly, MS tracks, but also on calorimeter information. There are multiple strategies for the reconstruction of muons: segment-tagged (ST), calorimeter-tagged (CT), muon spectrometer extrapolated (ME), and combined (CB). The latter is used for the $t\bar{t}H$ multi-lepton analysis. For combined muons, the reconstruction of tracks is done independently in the ID and MS. With a global fit, tracks are reconstructed,

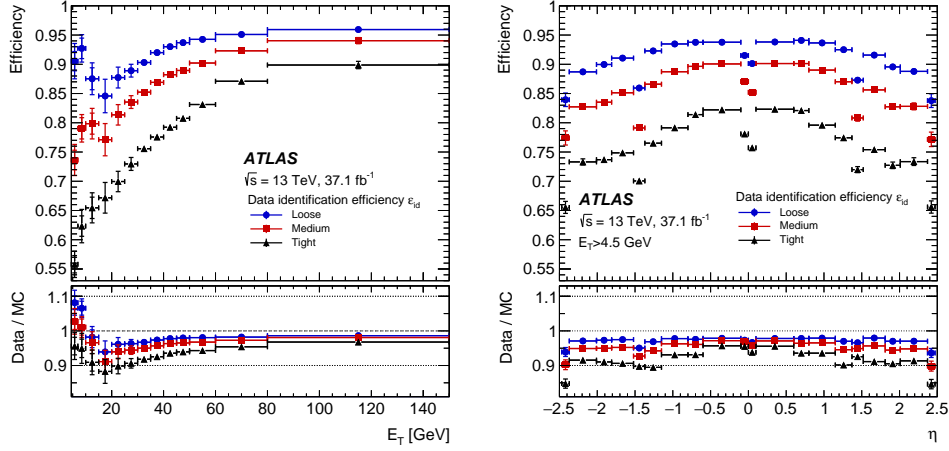


Figure 5.2: The measured LH electron-identification efficiencies for the three defined working point *Loose*, *Medium*, and *Tight* as a function of the transverse Energy E_T on the left and as a function of the pseudorapidity η on the right. The efficiencies are obtained from MC events of $Z \rightarrow ee$ and $J/\psi \rightarrow ee$ with respect to measured events. This figure is taken from Ref. [222].

accounting also for the energy loss in the calorimeter. Most muon candidates are reconstructed following the outside-in pattern recognition by reconstructing tracks in the MS and extrapolating them inwards to match them with ID tracks. There is a complementary approach called inside-out pattern recognition, reconstructing ID tracks first and extrapolating them to match them to the muon system. To suppress non-prompt and fake muon contributions, additional quality cuts are applied. Depending on the applied cuts, three working points are defined, which are called *Loose*, *Medium*, and *Tight*. Medium-quality combined muons require at least three hits in at least two layers of the monitored drift tube chambers (MDT). For muon candidates in the range of $|\eta| < 0.1$, only tracks with at least one hit in the MDT layer are allowed, requiring not more than one MDT hole layer. Medium muon candidates require a loose cut in the charge momentum compatibility. The charge momentum compatibility is a powerful variable that can discriminate between prompt and non-prompt or fake muons. Muons from hadron decays often show *kinks* in reconstructed tracks, resulting in poor fit quality during reconstruction, but also in incompatibilities in measured charge and momentum [227]. The muon isolation is done similarly for electrons, using either track or calorimeter-based variables; further discussion on muon and lepton isolation can be found in Section 5.2.3. The efficiencies are derived by comparing simulated $Z \rightarrow \mu\mu$ and $J/\psi \rightarrow \mu\mu$ events with measured events in data.

5.2.3 MVA-based Non-Prompt and Fake Lepton Rejection

Standard cut-based lepton selections using impact parameter, isolation, and identification discriminant can reject most non-prompt or fake contributions from prompt leptons. Prompt leptons originate from decays of bosons. Due to the short boson lifetime, decay products like leptons are associated with the primary vertex. In contrast, non-prompt leptons originate from heavy- or light-flavour hadron decays and are embedded in jets. These leptons can pass isolation criteria due to high p_T or improper reconstruction of the jet candidate. Fake leptons describe the misidentification of other physics objects like jets as leptons. A detailed discussion on the various sources and characteristics of non-prompt and fakes is found in Section 7. The *PromptLeptonImprovedVeto* (PLIV) tagger [228] exploits information of lepton candidates to suppress contributions of non-prompt and fake leptons further. It outperforms standard lepton quality cuts. Due to the long lifetime of heavy-flavour hadrons, secondary vertices can be reconstructed. Since non-prompt leptons originate from these hadrons, they are associated with a secondary vertex. A boosted decision tree (BDT) is trained using secondary vertex information, lepton isolation variables, and information between the lepton candidates and track jets. Additionally, a recurrent neural network (RNN) score is fed to the BDT. The RNN uses hit information from the ID and impact parameter information. The BDT aims to separate prompt from non-prompt and fake leptons.

PLIV outperforms the standard working points regarding non-prompt and fake lepton rejection. The signal efficiency for $t\bar{t}H$ ($t\bar{t}W$) events is 0.60 (0.75) to 0.75 (0.86) depending on the chosen working point. There are two working points for PLIV, optimised for the $t\bar{t}W$ and $t\bar{t}H$ multi-lepton measurements [127]. They are called *tight* and *verytight*. They come with scale factors correcting efficiencies with respect to data derived from $Z \rightarrow \ell\ell$ events. A BDT tool called *ElectronChargeFlipTaggerTool* (ECIDS) is used to reject electrons with misidentified charge. The tool utilises kinematic, charge and impact parameter information. An optimised cut on the BDT score was used for the $t\bar{t}W$ multi-lepton analysis [127] and is similarly applied for barrel and end-cap region electrons.

5.2.4 Lepton Definitions

This analysis uses various definitions for light leptons $\ell = e, \mu$ to achieve the optimal signal over background ratio for each analysis channel. A tighter definition generally leads to higher purity but reduces the expected statistics for a channel. The baseline and loosest lepton definition for electrons and muons is called *loose* (L). This definition is used within the overlap removal sequence described in Section 5.3. It is also used to associate events to one of the analysis channels described in Section 6.

Loose electron candidates require a minimum transverse momentum of $p_T > 10 \text{ GeV}$ and must satisfy $|\eta| < 2.47$, excluding the barrel-endcap transition region $1.37 <$

$|\eta| < 1.52$, which is the transition region between the barrel and end cap calorimeter components. The *LooseAndBLayerLH* electron ID working point is used with the *LooseVar_Rad* WP for lepton isolation. The *LooseVar_Rad* WP for electrons requires $E_T^{\text{cone20}}/p_T < 0.2$ and $p_{T, \text{tightTTVA}}^{\text{varcone30}}/p_T < 0.15$ with the electron candidates transverse momentum p_T . Standard requirements on the transverse impact parameter significance $|d_0|/\sigma_{d_0} < 5$ and longitudinal impact parameter $|z_0 \sin(\theta)| < 0.5$ mm are applied. They reduce contributions from charge misidentification, non-prompt electrons, and pile-up. For muon candidates in the range of $|\eta| < 0.1$ with reduced MS coverage, reconstruction is done using tracks from the ID matched to isolated energy deposits in the calorimeters consistent with minimum-ionising particles. Muon candidates must satisfy $|\eta| < 2.5$ and minimal transverse momentum $p_T > 10$ GeV. While the *LooseVar_Rad* WP for muon isolation is applied with the same cut on the track isolation $p_{T, \text{tightTTVA}}^{\text{varcone30}}$, a looser cut for the calorimeter isolation of $E_T^{\text{cone20}}/p_T < 0.3$ is used. The requirement on the transverse impact parameter significance is $|d_0|/\sigma_{d_0} < 3$, and for the longitudinal impact parameters, it is the same as for loose electron candidates.

After applying the loose lepton definition, overlap removal sequence, and analysis channel selection, a tighter optimised lepton definition is chosen to enhance signal sensitivity in signal regions or increase the purity of background processes in their respective control regions. The tighter definitions are called *loose tight* (L'), *medium inclusive* (M), *medium exclusive* (M_{ex}), and *tight* (T). All tighter electron definitions use the *TightLH* working point for identification. Further cuts are applied for all tighter electron candidates to reduce contributions from conversions: *external* conversions are suppressed by rejecting electrons having a conversion vertex (CV) within a radius of $r = 20$ mm and an associated invariant mass $m_{\text{trk-trk}}$ of tracks associated to the electron candidate and closest track, originating from the CV, with up to 100 MeV. *Internal* conversions are reduced by vetoing any electron which passes the external criteria and has a $m_{\text{trk-trk}}$ calculated at the primary vertex up

Lepton Type	e					μ			
Lepton Definition	L	L'	M	M _{ex}	T	L	M	M _{ex}	T
LooseVar_Rad isolation	Yes					Yes			
Non-prompt lepton BDT (PLIV)	No		<i>Tight</i>	<i>Tight-not-VeryTight</i>	<i>VeryTight</i>	No	<i>Tight</i>	<i>Tight-not-VeryTight</i>	<i>VeryTight</i>
Identification	Loose	Tight				Loose	Medium		
Charge misassignment veto (ECIDS)	No	Yes				None			
Conversion rejection	No	Yes				None			
Transverse impact parameter significance $ d_0 /\sigma_{d_0}$	< 5					< 3			
Longitudinal impact parameter $ z_0 \sin \theta $	< 0.5 mm								

Table 5.4: An overview of lepton definitions used for electrons and muons. Five (four) different lepton definitions for electrons (muons) are defined by isolation and identification variables and used working points for non-prompt lepton identification, charge misidentification, and conversions.

Channel	Fake and Non-Prompt Control Regions	Signal and MVA-based Control regions
$2\ell\text{SS}$	$\text{TM}_{ex}, \text{M}_{ex}\text{T}, \text{M}_{ex}\text{M}_{ex}$	TT
3ℓ	L'MM/LMM (L' for μ and L for e)	LTT
4ℓ	LLL	LLLL
$2\ell\text{SS}+1\tau_{\text{had}}$	L'L' and MM (for fake τ_{had} CR)	MM
$1\ell+2\tau_{\text{had}}$ and $1\ell+2\tau_{\text{had}}$	L	

Table 5.5: Summary of the light lepton definitions used in the six analysis channels. The definition used for each lepton selected in a given channel is indicated with labels defined in Table 5.4. Leptons are ordered in transverse momentum.

to 100 MeV. The *Electron-ChargeFlipTaggerTool* (ECIDS) is applied to all tighter electron definitions using the *tight* working point to reject electrons with misidentified charge. A short description of the ECIDS tool is presented in Section 5.2.3. Tighter muons use *Medium* identification, but neither conversion cuts nor the ECIDS tool is applied. The tighter lepton definitions mainly differ in their chosen cuts on the PromptLeptonImprovedVeto (PLIV) score. A description of the PLIV tool is presented in Section 5.2.3. The PLIV working point *tight* is associated with the M lepton definition, while the *Tight-not-veryTight* working points with the M_{ex} leptons, and *VeryTight* corresponds to T lepton definition. For the $2\ell\text{SS}+1\tau_{\text{had}}$ channel, a looser tight electron definition (L') is defined by applying the exact requirements as for *tight* electrons, but excluding any requirement on PLIV.

A complete overview of the lepton definitions and their requirements and cuts is shown in Table 5.4. Table 5.5 presents an overview of used lepton definitions for every analysis channel. The leptons are ordered in transverse momentum. The regions are split into signal and control regions defined by multivariate analysis techniques (MVA) or fake and non-prompt control regions.

5.2.5 Jets

Quarks and gluons cannot be observed as free particles due to QCD confinement. After the hard scattering process, final state partons undergo parton showering, adding soft and collinear emissions resulting from hadronisation in a stream of highly collimated hadrons traversing the detector. They can be detected as tracks in the ID and energy deposits in the electromagnetic and hadronic calorimeter. A jet reconstruction algorithm is used to combine information to a single physics analysis object called *jet*, giving rise to the initial parton originating from the primary collision or secondary vertices.

Jets are reconstructed from *particle flow objects* [229], defined by track and calorimeter information, and using the anti- k_t algorithm [230] with a single¹ radius parameter

¹The anti- k_t algorithm is called *anti* due to the negative sign in the exponent of $p_{T,i}$ and $p_{T,j}$. If the exponent is set to be +1, it is called the k_t algorithm, while setting it to zero refers to the

$R = 0.4$ and the distances

$$d_{ij} = \min \left(p_{T,i}^{-2}, p_{T,j}^{-2} \right) \frac{\Delta R_{ij}^2}{R^2} \quad \text{and} \quad d_{iB} = p_{T,i}^{-2}. \quad (5.3)$$

The indices i and j run over all clusters, and ΔR_{ij}^2 is the distance between two clusters in the $\eta - \phi$ plane. The algorithm calculates for each pair the distances if $d_{ij} < d_{iB}$ the pair ij is combined if $d_{iB} < d_{ij}$ i is called a jet and is removed from the list [231]. The procedure is terminated if no cluster is left. The anti- k_t algorithm prefers to combine harder clusters first. It results in cone-like structures around the hardest cluster, reflecting the structure of jets. An example of the different jet shapes in the $\eta - \phi$ plane is given in Figure 5.3. Two clustering results are shown using the same seed. On the left side, the anti- k_t algorithm is shown, while on the right, the k_t one. In sharp contrast to cone-based algorithms, the anti- k_t algorithm is collinear and infrared safe. Therefore, jet properties do not change due to collinear and soft, also called infrared, emissions.

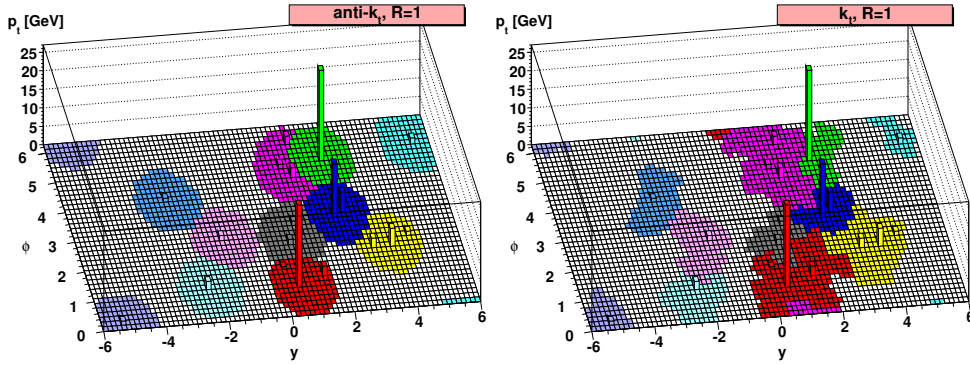


Figure 5.3: An example of two different results originating from the same seed. On the left side, the anti- k_t algorithm is used, while the k_t algorithm is used on the right. The figures are taken from Ref. [231].

The resultant reconstructed four momenta of jets need to be calibrated to account for imperfections of detector response, reconstruction algorithm, jet fragmentation, and pile-up. The calibration is done in several steps to correct each previously mentioned source. A full description is found in Ref. [232]. The first step is the origin correction: the jet four momentum is corrected while keeping its energy constant to point to the primary vertex rather than the centre of the detector. The η resolution of jets improves significantly, comparing reconstructed jets with corresponding truth jets obtained from MC simulation.

The second step subtracts energy contributions from in-time and out-of-time pile-up using an area-based p_T density subtraction [226, 233] and residual correction. The

Cambridge-Aachen algorithm, taking only distances into account.

corrected p_T for each jet is given by

$$p_T^{\text{corr.}} = p_T - \rho \times A - \alpha \times (N_{\text{PV}} - 1) - \beta \times \mu, \quad (5.4)$$

with the energy density ρ and A as the area of individual jets. The number of primary vertices is N_{PV} , and μ is the mean number of pp interactions per bunch crossing. The area A of a jet is defined via ghost association, uniformly adding ghost particles of infinitesimal momentum to an event before jet reconstruction. The area is estimated from the relative number of ghost particles associated with a jet. The residual p_T dependence for in-time pile-up α and out-of-time β are obtained from linear fits in bins of p_T and $|\eta|$. Afterwards, reconstructed jets are compared with truth jets, which do not suffer from pile-up effects.

The reconstructed jet four momentum is corrected to the particle-level energy scale with the *absolute* jet energy scale calibration. The procedure compensates biases in the jet η reconstruction caused by different calorimeter technologies and granularity. Truth jets generated from MC simulations with previously mentioned correction steps are used as reference objects.

To further improve jet calibration, a *Global Sequential Algorithm* is used [234]. It accounts for different residual dependencies in longitudinal and transverse features of the jet, as well as different jet-initiating particles. The most significant differences are observed between gluon- and quark-initiated jets. Gluon jets tend to have seeds with soft² particles with low calorimeter response and a wider transverse profile. In contrast, quark-initiated jets tend to contain hadrons with a notable fraction of the jet p_T . This causes a larger calorimeter response. The algorithm exploits chosen observables to correct the jet four momentum further.

Finally, an *in-situ* calibration is performed to correct for differences between data and MC simulations and detector response. The balance between jets and well-measured reference objects like Z bosons or photons in Z +jets or γ +jets events is used. However, the calibration in terms of accessible p_T range is statistically limited by the production mechanism of Z bosons and photons. For high p_T ranges, multijet systems are used [232].

To reduce contamination of in-time and out-of-time pile-up mimicking jet signatures, a multivariate tagging tool called *jet-vertex-tagger* (JVT) is used [235]. The tool uses track information of jets and tests their compatibility with the primary vertex. The JVT is used for central jets with a pseudorapidity of $|\eta| < 2.5$. For forward jets with a pseudorapidity larger than central jets and up to $|\eta| < 4.5$, the Forward Jet Vertex Tagger (fJVT) is used.

²The term *soft* often refers to a particle with low energy or momentum. It depends strongly on the context. For parton showers, soft particles tend to have energies of some 10 GeV, while soft particles have some 10 MeV for the calorimeter response. The opposite is called *hard* particles.

In this analysis, jets are reconstructed with an anti- k_t algorithm with a radius parameter of $R = 0.4$, implemented in the FASTJET package [236], using the jet collection *AntiKt4EMPFJet* [229]. Jets need to have a minimum transverse momentum of $p_T > 25 \text{ GeV}$ and $|\eta| < 2.5$. If explicitly mentioned, forward jets are also considered to satisfy the same transverse momentum requirement and up to $|\eta| < 4.5$. The *Tight* working point for JVT and fJVT are applied on jets with $|\eta| < 2.5$ and jets with $2.5 < |\eta| < 4.5$, respectively, to reduce contamination from pile-up jets.

***b*-jets**

Identifying jets, including b -hadrons, called b -jets, is crucial for every analysis measuring a process, including top quarks. Top quarks almost always decay to a W boson and a b -quark. For this analysis, the DL1r b -tagging algorithm [237] is used to identify b -jets against the significant background of jets containing c -hadrons or light hadrons. The former are called c -jets if they do not contain any b -hadrons, the latter are referred to as light jets if they do not contain any heavy-flavour hadron³. Hadrons containing b -quarks have unique properties, like a relatively long lifetime⁴ in the order of 1.5 ps ($c\tau \approx 450 \mu\text{m}$) and an average mean flight length of 3 mm , large mass, large decay multiplicity, and different fragmentation properties. These properties can be utilised for identification.

The algorithms *IP2D* and *IP3D* attempt to identify b -jets due to larger expected impact parameters of the decay products of b -hadrons. The *RNNIP* algorithm exploits correlations between large impact parameter tracks. Another way is to reconstruct the secondary vertex caused by the long lifetime of b -hadrons, done by the *SV1* and *JetFitter* algorithms.

The DL1r algorithm combines all previously mentioned algorithms into a fully connected multi-layer feed-forward neural network (NN). It is trained on a hybrid training set of jets from $t\bar{t}$ and $Z \rightarrow q\bar{q}$ events. The three output probabilities for b -jets p_b , c -jets p_c , and light jets p_{light} of DL1r are combined into a b -tagging score:

$$D_{\text{DL1r}} = \ln \left(\frac{p_b}{f_c \cdot p_c + (1 - f_c) \cdot p_{\text{light}}} \right). \quad (5.5)$$

The effective c -jet fraction of the training set is called f_c . In Figure 5.4, the three output probabilities and the resulting DL1r score are presented for simulated $t\bar{t}$ events with a fraction of c -jets of $f_c = 0.018$. Working points (WP) of 60 %, 70 %, 77 %, and 85 % are defined by selecting a corresponding b -tagging efficiency on simulated $t\bar{t}$ events [238,239]. The imposed cuts divide the DL1r score into five *pseudo-continuous*

³Gluon initiated jets are also called light jets in this context.

⁴The long lifetime is caused by the kinematic suppression of $b \rightarrow tW$ and the CKM suppression of $b \rightarrow uW$ and $b \rightarrow cW$.

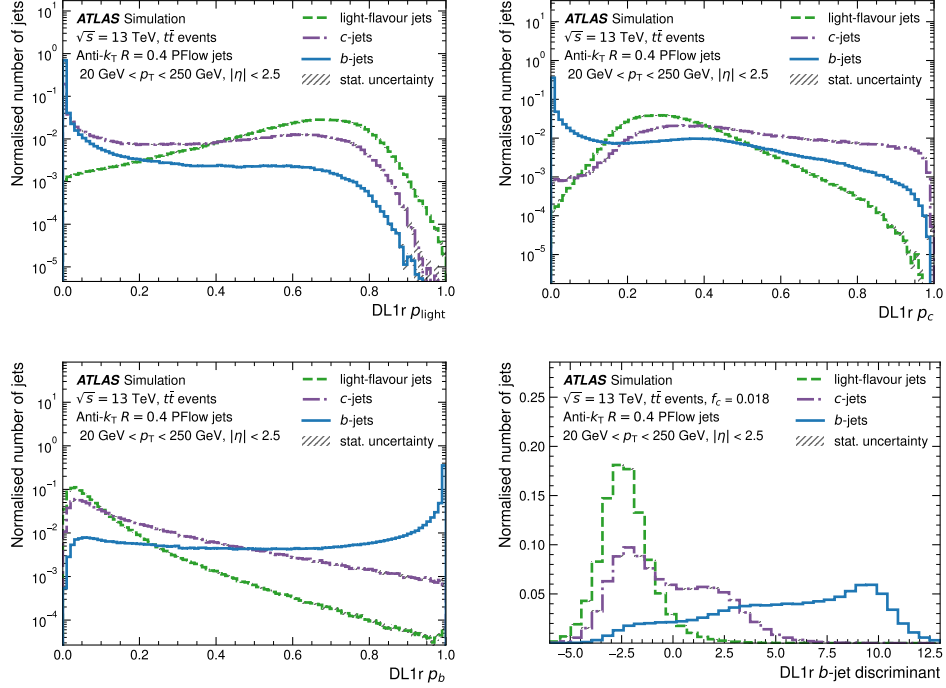


Figure 5.4: The three output scores of the DL1r algorithm for the b -jet, c -jet, and light jet probabilities, together with the DL1r score for simulated $t\bar{t}$ events with a fraction of c -jets of $f_c = 0.018$. The figures are taken from Ref. [237].

bins, bounded by the selections of 100 % and 0 %. This analysis chooses a WP of 85 %. The $2\tau_{\text{had}}$ channels use a WP of 77 % instead.

5.2.6 Hadronically decaying taus τ_{had}

The dominant decay mode of hadronically decaying τ leptons, called τ_{had} , is to one or three charged pions, up to two neutral pions, and a τ -neutrino. The hadronic decay products can be reconstructed from topocluster seeds as jets using the anti- k_t algorithm with a radius parameter of $R = 0.4$. Tracks within the seed can be further classified as core or isolated tracks based on a trained boosted decision tree. Based on the number of core tracks, τ_{had} are classified as 1-prong (3-prong) if they contain one (three) core tracks with a total charge of ± 1 . A Recurrent Neural Network (RNN) is trained on τ_{had} candidates with a $p_T > 20 \text{ GeV}$ and $|\eta| < 2.5$, excluding the transition region between the barrel and endcap calorimeters $1.37 < |\eta| < 1.52$ [240]. The set of input variables for the RNN is based on combinations of track and cluster information of τ_{had} candidates. For this analysis, the *MediumID* working point is chosen, having a signal efficiency of 75 % (60 %) for 1-prong (3-prong) τ_{had} decays. To further enhance the rejection of electrons misidentified as τ_{had} candidates with

one associated track, a boosted decision tree is trained with a 95 % efficiency for τ_{had} . It has a rejection factor of ≈ 30 up to ≈ 100 depending on p_T and η .

5.2.7 Missing Transverse Energy

During e^+e^- collisions, the centre-of-mass energy is constant since fundamental particles with sharp energy and momentum distribution interact. In contrast, in pp collisions, not the protons interact, but their constituents called partons, namely quarks and gluons. The centre-of-mass energy is not constant but probabilistic. In any case, the transverse momentum of all partons is exactly zero, and due to energy-momentum conservation, the transverse momentum of all collision products must add up to zero. Various sources may cause an imbalance. Neutrinos are a source since they do not interact with the detector material. Another is the limited detector coverage since the ATLAS detector does not cover the full solid angle and has regions with low acceptance. For instance, the transition region between the barrel and forward calorimeters. Other sources are the loss of objects in the beam pipe or due to object reconstruction inefficiencies. The imbalance is characterised by the missing transverse momentum E_T^{miss} defined as the magnitude of the x - and y -vector components in the transverse plane xy and with its azimuthal angle ϕ^{miss} as:

$$E_T^{\text{miss}} = \sqrt{(E_x^{\text{miss}})^2 + (E_y^{\text{miss}})^2} \quad \text{and} \quad \phi^{\text{miss}} = \arctan\left(\frac{E_x^{\text{miss}}}{E_y^{\text{miss}}}\right). \quad (5.6)$$

The vector components are the negative sum of all hard objects, reconstructed and calibrated physics objects, and soft signals. The soft signal term consists of tracks with $p_T > 400 \text{ MeV}$, matched to the primary collision vertex within $|d_0| < 0.5 \text{ mm}$ and $|z_0 \sin(\theta)| < 1.5 \text{ mm}$, and not associated with any physics object:

$$E_{x(y)}^{\text{miss}} = - \sum_{\text{hard objects}} p_{x(y)} - \sum_{\text{soft signal}} p_{x(y)}. \quad (5.7)$$

The E_T^{miss} is calibrated with $Z \rightarrow \mu\mu$ events having no genuine E_T^{miss} source. Contributions are only expected due to limited detector acceptance and resolution and from object reconstruction. The calibration with expected contributions originating from undetected neutrinos is tested with $W \rightarrow e\nu_e$ and $W \rightarrow \mu\nu_\mu$ events [241].

5.3 Overlap Removal

Detector signatures can be ambiguous and cause overlap with each other. An *overlap removal* procedure is applied to avoid double-counting of objects. It selects one of the overlapping objects while rejecting the remaining ones. The following overlap removal sequence is applied:

- If two electron candidates share a track or have an overlapping cluster within $\Delta R < 0.1$, the lower p_T is removed.

- Any τ_{had} within $\Delta R < 0.2$ of an electron or muon is removed.
- If a loose electron overlaps with a loose muon within $\Delta R < 0.1$, the muon is removed if it is reconstructed from a track or calorimeter deposit consistent with a minimum ionising particle, else the electron is removed.
- If a loose electron overlaps within $\Delta R < 0.2$ with a jet candidate and the jet candidate is not a b -tagged or has $p_T > 200 \text{ GeV}$, the jet candidate is removed and the object is kept as an electron.
- If a loose muon is ghost-matched to a jet candidate within $\Delta R < 0.4$ and the jet candidate is not b -tagged, the object is interpreted as a muon if the jet candidate has less than three tracks with $p_T > 500 \text{ MeV}$.
- If a loose τ_{had} candidate is found to be within $\Delta R < 0.2$ of a jet candidate, the jet candidate is removed and the τ_{had} candidate is kept.
- If a jet candidate satisfies the previous overlap removal steps and overlaps with a loose lepton in a cone with radius $R = 0.04 + 10 \text{ GeV}/p_{T,\text{lep}}$, with a maximum radius of 0.4, the jet candidate is kept, while the lepton candidate is removed.

Analysis Strategy for the $t\bar{t}H$ Multi-Lepton Process

Number of τ_{had}	2	$1\ell + 2\tau$	$2\ell + 2\tau$		4ℓ
	1		$2\ell\text{SS} + 1\tau$		
	0		$2\ell\text{SS} + 0\tau$	$3\ell + 0\tau$	
		1	2	3	4
		Number of light ℓ			

Figure 6.1: Overview of the $t\bar{t}H$ multi-lepton analysis channels.

Six analysis channels are defined depending on the Higgs boson decay mode and subsequent decay mode of decay products, together with the top quark decay mode. The channels are split by the number of light leptons $\ell = e, \mu$ and hadronically decaying τ candidates, called τ_{had} , after applying the overlap removal sequence from Section 5.3. An overview is presented in Figure 6.1: there are two zero τ_{had} channels called $2\ell\text{SS}+0\tau_{\text{had}}$ and $3\ell+0\tau_{\text{had}}$, one channel with exactly one τ_{had} called $2\ell\text{SS}+1\tau_{\text{had}}$, and two channels with two τ_{had} referred to as $1\ell+2\tau_{\text{had}}$ and $2\ell\text{OS}+2\tau_{\text{had}}$. The four-lepton channel 4ℓ requires four light leptons and is inclusive for τ_{had} candidates. The individual channel preselection targeted Higgs boson decay modes and dominant background sources are described in the following sections, while an overview is presented in Table 6.1. Machine learning techniques are used to separate $t\bar{t}H$

events from background ones in all analysis channels; however, in some, an attempt is made to separate $t\bar{t}H$ events additionally. The machine learning scores define signal-enriched regions called signal regions (SR) and background-enriched control regions (CR), constraining respective backgrounds.

There are two categories of backgrounds: the first is called *irreducible* backgrounds, which cannot be suppressed by different object definitions due to their inherent similar signature. For the $t\bar{t}H(b\bar{b})$ analysis, the $t\bar{t}+b\bar{b}$ process is an *irreducible* background due to the same final state signature with the main difference in the origin of the $b\bar{b}$ pair. Similar for the $t\bar{t}H \rightarrow 4\ell$ process with main *irreducible* background being $t\bar{t}Z$, if the top quark pair and Z boson decay to leptons. The final state has the same number of expected b -jets originating from the top quark pair and the number of expected light leptons with only kinematic differences. However, the ZZ background, especially $ZZ + \geq 1c$ and $ZZ + \text{light}$ contribution, is mostly suppressed by b -tagging requirements and enters the 4ℓ regions due to the high expected production cross-section. Those backgrounds are usually referred to as *reducible* backgrounds. For the $t\bar{t}H(b\bar{b})$ analysis, contributions of the $t\bar{t} + \text{jets}$ background, namely $t\bar{t} + c\bar{c}$ and $t\bar{t} + \text{light}$, are *reducible*, since they can be similarly suppressed by tighter requirements on b -tagging.

Another main category of *reducible* backgrounds originates from non-prompt and fake leptons, which are suppressed by tighter requirements on lepton selection and isolation. Estimating non-prompt and fake lepton backgrounds is difficult due to their significant dependencies on those requirements and the chosen analysis region. A detailed discussion on the estimation is found in Chapter 7.

A complete overview of regions for the $t\bar{t}H$ multi-lepton analysis is presented in Figure 6.2, combining individual channel preselection with machine learning scores, defining SRs and CRs. Non-prompt and fake backgrounds are estimated in designed regions enriched in these backgrounds and orthogonal to the channel preselection.

In the following, the machine learning techniques are discussed with a focus on dense neural networks in Section 6.1.1 and boosted decision trees in Section 6.1.2 since they are used in other analysis channels. The preselection description and application of the neural network for the 4ℓ channel is presented in Section 6.2, including a discussion of the training and evaluation. The construction of SR and CRs for the 4ℓ is also presented. An overview of the other analysis channels and their strategy is given in Section 6.3 to Section 6.6. In the last Section 6.7 the reconstruction strategy for the Higgs boson transverse momentum is discussed.

Channel	$2\ell SS + 0\tau_{\text{had}}$	$3\ell + 0\tau_{\text{had}}$	4ℓ
Target $t\bar{t}H$ decay	$t \rightarrow b\ell\nu_\ell, t \rightarrow bq q'$ and $H \rightarrow WW \rightarrow \ell\nu_\ell q q'$	$t \rightarrow b\ell\nu_\ell, t \rightarrow b\ell\nu_\ell$ and $H \rightarrow WW \rightarrow \ell\nu_\ell q q'$ $t \rightarrow b\ell\nu_\ell, t \rightarrow bq q'$ and $H \rightarrow WW \rightarrow \ell\nu_\ell \ell\nu_\ell$ $t \rightarrow b\ell\nu_\ell, t \rightarrow bq q'$ and $H \rightarrow ZZ \rightarrow \ell\nu_\ell q q'$ or $\ell\ell\nu\nu$	$t \rightarrow b\ell\nu_\ell, t \rightarrow b\ell\nu_\ell$ and $H \rightarrow WW \rightarrow \ell\nu_\ell \ell\nu_\ell$ $t \rightarrow b\ell\nu_\ell, t \rightarrow b\ell\nu_\ell$ and $H \rightarrow ZZ \rightarrow \ell\nu_\ell q q'$ or $\ell\ell\nu\nu$
Trigger		Single- and Dilepton	
τ_{had} candidates	0	0	–
Lepton counting	$\text{== } 2 \text{ T: } p_{\text{T}} > 15 \text{ GeV}$	$\text{== } 3 \text{ T,T,L: } p_{\text{T}} > 15, 15, 10 \text{ GeV}$	$\text{== } 4 \text{ L: } p_{\text{T}} > 10 \text{ GeV}$
Lepton details	SS	OS to others: L $p_{\text{T}} > 10 \text{ GeV}$ SS pair: T $p_{\text{T}} > 15 \text{ GeV}$ OS pair: $ m(\ell\ell) - m_{\text{Z}} > 10 \text{ GeV}$ and $m(\ell\ell) > 12 \text{ GeV}$	$\sum_i q_i = 0$ $m(llll) \notin [115 \text{ GeV}, 130 \text{ GeV}]$ OS: $m(\ell\ell) > 12 \text{ GeV}$
Central jets	≥ 3	≥ 2	≥ 2
b -jets	$\geq 1 \text{ (@85\%WP)}$	$\geq 1 \text{ (@85\%WP)}$	$\geq 1 \text{ (@85\%WP)}$
Channel	$2\ell SS + 1\tau_{\text{had}}$	$2\ell OS + 2\tau_{\text{had}}$	$1\ell + 2\tau_{\text{had}}$
Target $t\bar{t}H$ decay	$t \rightarrow b\ell\nu_\ell, t \rightarrow bq q'$ and $H \rightarrow \tau\tau \rightarrow \ell\nu_\ell \nu_\ell \tau_{\text{had}} \nu_\ell$	$t \rightarrow b\ell\nu_\ell, t \rightarrow b\ell\nu_\ell$ and $H \rightarrow \tau^+ \tau^- \rightarrow \tau_{\text{had}} \nu_\ell \tau_{\text{had}} \nu_\ell$	$t \rightarrow b\ell\nu_\ell, t \rightarrow bq q'$ and $H \rightarrow \tau^+ \tau^- \rightarrow \tau_{\text{had}} \nu_\ell \tau_{\text{had}} \nu_\ell$
Trigger	Single- and Dilepton	Single- and Dilepton	Singlelepton
τ_{had} candidates	$\text{== } 1 \text{ M: } p_{\text{T}} > 20 \text{ GeV}$	$\text{== } 2 \text{ OS M: } p_{\text{T}} > 20 \text{ GeV}$	$\text{== } 2 \text{ OS M: } p_{\text{T}} > 20 \text{ GeV}$
Lepton counting	$\text{== } 2 \text{ M: } p_{\text{T}} > 15 \text{ GeV}$	$\text{== } 2 \text{ OS L: } p_{\text{T}} > 10 \text{ GeV}$	$\text{== } 1 \text{ L: } p_{\text{T}} > 27 \text{ GeV}$
Lepton details	SS pair: $ m(\ell\ell) - m_{\text{Z}} > 10 \text{ GeV}$	OS pair: $ m(\ell\ell) - m_{\text{Z}} > 10 \text{ GeV}$ and $m(\ell\ell) > 12 \text{ GeV}$	
Central jets	≥ 3	≥ 2	≥ 2
b -jets	$\geq 1 \text{ (@85\%WP)}$	$\geq 1 \text{ (@77\%WP)}$	$> 0 \text{ (@77\%WP)}$

Table 6.1: An overview of applied selection criteria to define the six analysis channels. The object definitions relevant analysis objects are defined in Chapter 5.

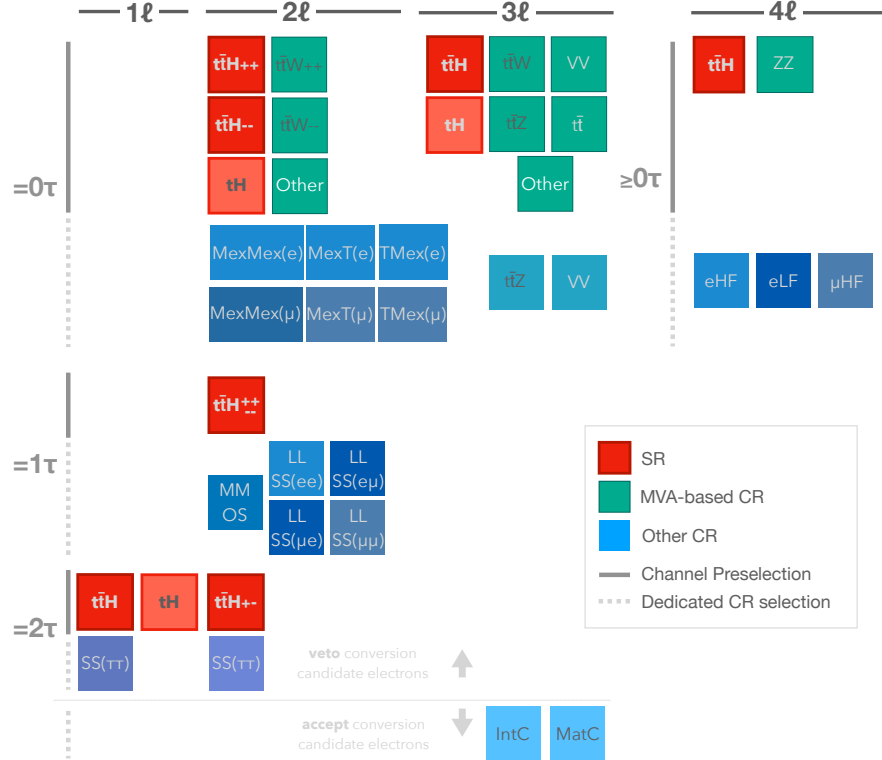


Figure 6.2: Overview of the $t\bar{t}H$ multi-lepton analysis regions per analysis channel split by the number of loose light leptons and τ_{had} candidates. The regions are further divided by either MVA defined after applying the channel preselection or regions targeting specific backgrounds. These regions are designed to be orthogonal to other analysis regions.

6.1 Machine Learning Introduction and Application

Separating signal events from background events is crucial for each analysis to enhance sensitivity to the signal process and constrain backgrounds. Some analyses featuring resonances like $H \rightarrow ZZ^* \rightarrow 4\ell$ or $H \rightarrow \gamma\gamma$ can achieve a good separation between signal and background by simple cuts on the invariant mass of the four leptons or on the diphoton invariant mass¹ and rely on the extrapolation of background estimate outside the invariant mass cuts to the signal enriched region. However, most analyses have difficult background processes with inherently similar final state signatures and kinematics and no clear or golden variable for separation. A set of cuts can be applied to increase signal sensitivity further. Still, with an increasing number of input variables, this task gets more complex and underlying correlations between variables are often hidden. Therefore, machine learning algorithms are used to increase the performance.

Machine learning algorithms use a given dataset to maximise a performance measure or learn from experience to fulfil a defined task. There are several training strategies with different applications:

- *Supervised Learning* is used for classification tasks with labelled training data. This strategy is commonly used in particle physics analyses to classify events from simulation. The inputs are usually low-level kinematic variables², or high-level features built from them by imposing physical constraints and knowledge about the target process³. True labels are provided to evaluate the performance and improve the classification. Satisfactory modelling of kinematic distributions is crucial for the training to avoid biases. After the training procedure, the algorithm can classify data events with no true label.
- *Unsupervised Learning* uses no prior information of the training dataset, forcing the algorithm to identify common patterns in the dataset. The strategy is usually used for incomplete datasets with unknown properties, such as anomaly detection or pattern recognition tasks.
- *Reinforcement Learning* is based on real-time decision making. The algorithm learns through trial and error by getting feedback by a binary or continuous succession score. The most prominent applications are self-driving cars or robotic manipulation tasks.

There are several machine learning models based on the aforementioned learning strategies. For the $t\bar{t}H$ multi-lepton analysis and especially for the 4ℓ channel, a

¹However, machine learning models such as BDTs are also used for the reconstruction of the top quark system [115] or further event classification after applying a cut on the diphoton invariant mass [117] increasing separation.

²Low-level variables are the kinematic properties of physics objects, like the transverse momentum or pseudorapidity of jets or leptons.

³Most common candidates for the $t\bar{t}H$ multi-lepton analysis are invariant masses of lepton pairs or the distance between them.

dense neural network (DNN) is used for signal and background separation utilising the supervised learning approach. Graph neural networks (GNN) and boosted decision trees (BDT) are used to reconstruct the Higgs boson transverse momentum. The remaining analysis channels use BDTs for signal and background separation tasks. In the following, a brief overview of dense neural networks and boosted decision trees is given, followed by the application of the former one for the 4ℓ channel and overviews on the application of the latter ones for the remaining channels of the $t\bar{t}H$ multi-lepton analysis.

6.1.1 Dense Neural Networks

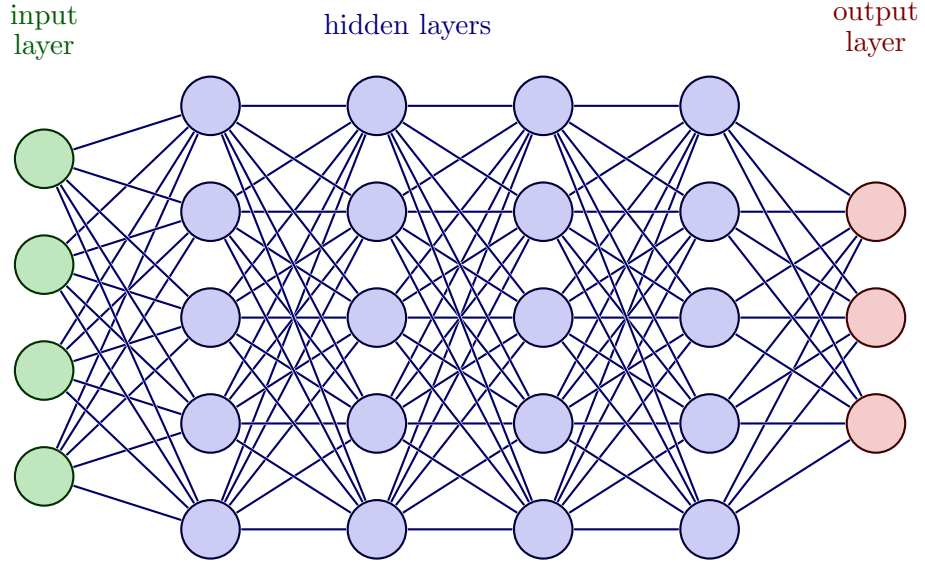


Figure 6.3: An example of a fully connected neural network. A feed-forward network is shown; information flows only in one direction from the input layer to the output one. This type of neural network is used for the 4ℓ channel.

Neural networks are motivated by the structure of human brains with neurons and connections between them. However, there are conceptual differences between biological and artificial neural networks. A dense neural network is organised in three parts, as shown in Figure 6.3, having an input layer, an output layer, and several hidden layers. The number of neurons in the input layer reflects the number of input features, such as kinematic variables of an event, fed into the network. In contrast, the output layer indicates the number of classes the classification task defines. The number of hidden layers with the number of neurons for each layer can be arbitrarily chosen. However, the performance of the neural network may change. In Figure 6.3, neurons are connected to each neuron of the next layer, allowing information only to flow in one direction from the input to the output layer. Therefore, such net-

works are called fully connected and feed-forward⁴. Neurons are used to process signals, while chemical reactions trigger biological neurons; artificial neurons use activation functions to process information to the next one. The activation functions are continuously differentiable and feature non-linear behaviour, resulting in non-trivial solutions. The most commonly used activation functions are *rectified linear unit (ReLU)*⁵, *exponential linear unit (ELU)*, *scaled exponential linear unit (SELU)*, or *leaky rectified linear unit (Leaky ReLU)*, with definitions found in Appendix B. Some activation functions have special properties for score interpretations: for a multiclass neural network, the softmax function

$$a(x_i) = \frac{\exp(x_i)}{\sum_j \exp(x_j)}, \quad (6.1)$$

for a neuron i , while j runs over all neurons in the output layer, can be used for probabilistic interpretation as it defines a probability distribution with $\sum_i a(x_i) = 1$. For binary scores, saturated functions like the sigmoid are used, fulfilling a similar purpose. The calculation of the output for a neuron is given by

$$y' = a\left(\sum_i x_i \cdot w_i + b\right) \quad (6.2)$$

with x_i as input from the previous layer and weight w_i and bias b from the current layer, evaluated with the activation function a . During training, sometimes referred to as learning, weights w_i are adjusted using the back-propagation method [242] to improve the performance on the training data. The performance is evaluated using a loss function $L(y', y)$, measuring the distance between the true value y and the value y' predicted by the model. The weights are updated according to the gradient of the loss function. The back-propagation is computationally expensive and is done by successively applying the chain rule. There are several algorithms used for the back-propagation, such as the *stochastic gradient descent (SGD)* or *NAdam* algorithm [243]. The *PyTorch* library is used for model building and training [244].

The training procedure involves several techniques to increase a model's performance and avoid *overfitting*, which refers to models being sensitive to noise in the training dataset, resulting in poor performance on unseen data and, therefore, small generalisation ability. Overfitting can be prevented by adding penalty terms to the loss function, favouring smaller weights [245, 246], or by setting a percentage of input values for neurons of a given layer to be zero. The latter is called *dropout* [247]. It reduces the number of model parameters and avoids the model relying on specific

⁴Biological neural networks are neither fully connected nor feed-forward; they also feature leaky behaviour.

⁵Negative input values are always mapped to be zero, resulting in a loss of information for those values and, in extreme cases, to the inactivity of neurons. Nevertheless, this function is commonly used due to its simplicity. The Leaky ReLU function is an alternative since it corrects the loss of information.

nodes. The early stopping mechanism is a method to monitor overfitting by evaluating the model on a validation set. The training is terminated once the validation loss function does not improve.

6.1.2 Boosted Decision Trees

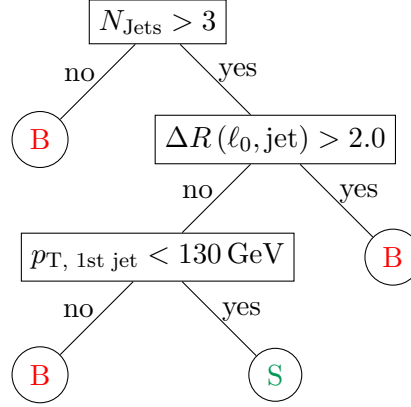


Figure 6.4: An example of a decision tree with a depth of three. The variables are chosen from the list of input features from the $2\ell\text{SS}+0\tau_{\text{had}}$ channel.

Boosted decision trees (BDT) are a multivariate analysis tool used in high-energy particle physics. Decision trees are a set of decisions which binary split input data based on selected input features [248–250]. A sketch of a decision tree is shown in Figure 6.4 for a simplified analysis, splitting the dataset by a given value and with a depth of three. The terminal nodes are called leaves and represent a class label, or if the output score is a continuous variable, it can be interpreted in a probabilistic manner. The latter is called a *regression* tree. A learning process can be induced by maximising a metric for information gain or minimising entropy for each node split, improving the tree structure. The learning process is terminated if some criteria are matched, like the depth of trees, or no improvement is observed. Multiple decision trees can be combined into a single, much stronger classifier [251] by boosting method forming a *forest*. Each created decision tree will be assigned a weight corresponding to its accuracy. The final combined classifier is the weighted sum of the individual tree output classifier. There are three commonly used boosting algorithms: the adaptive boost algorithm (AdaBoost) algorithm [252], the *eXtreme Gradient Boosting* (XGBoost) algorithm [253], and the *Gradient Boosting* algorithm [254]. The former was commonly used in early Run 2 analyses. However, all mentioned BDTs used for $t\bar{t}H$ multi-lepton analysis use the latter algorithm based on the gradient descent method. BDTs are characterised by a set of tunable parameters, like the maximal depth of a tree, sometimes also defined by the number of terminal nodes or leaves. Another characteristic is the maximal number of used input features per tree, with features randomly selected from the full set of features. In the context

of the AdaBoost algorithm, trees including input features with no separation power will be disfavoured, and a small weight will be applied. Other parameters are the used loss function, learning rate, or number of total trained trees.

6.2 The 4ℓ Channel

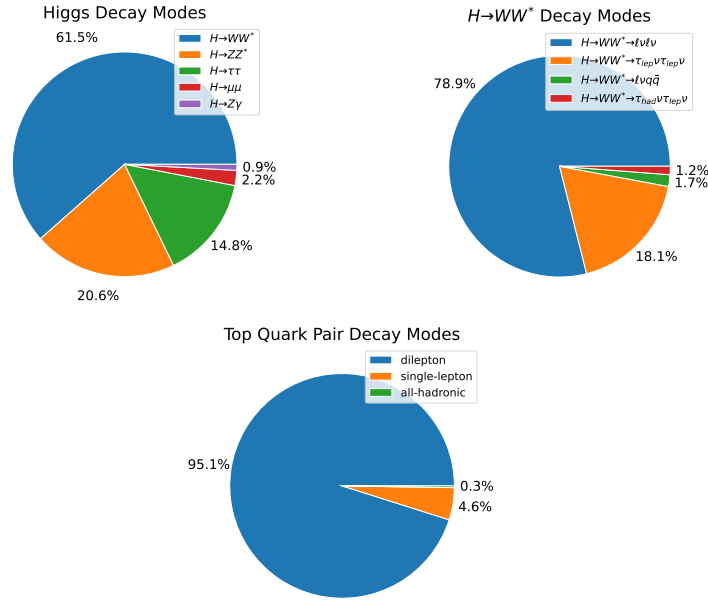


Figure 6.5: An overview of Higgs boson and top quark pair decay modes covered by the 4ℓ channel. The values are based on truth information obtained from simulation after applying preselection criteria. On the left side, the various Higgs boson decay modes are presented, while on the right, the most dominant decay mode $H \rightarrow WW^*$ is further classified by the individual decay modes of the W bosons. Below, the decay modes of the top quark pair are shown, with the dileptonic decay being the most dominant.

The 4ℓ channel preselection requires four light leptons with a minimal transverse momentum of $p_T > 10$ GeV using both single- and dilepton triggers. The *loose* lepton definition presented in Section 5.2.4 is used for all four leptons. In Appendix C, an optimisation of the used lepton definition is presented, disavouring tighter definitions. The sum of charges of four leptons needs to add up to zero. Each event requires at least two central jets with at least one b -jet passing the 85 % DL1r working point.

There are some requirements on lepton combinations. For each same-flavour opposite

sign (SFOS) lepton pair, the invariant mass needs to be $m(\ell^+\ell^-) > 12 \text{ GeV}$, to reduce contributions of low-mass resonance quarkonia decays. Events with an invariant mass of the four leptons close to the Higgs boson mass, $m(4\ell) \notin [115 \text{ GeV}, 130 \text{ GeV}]$, are vetoed. It ensures statistical orthogonality to other $H \rightarrow ZZ^* \rightarrow 4\ell$ analyses, like Ref. [73]. In the previous $t\bar{t}H$ multi-lepton analysis, an additional requirement is applied by vetoing every SFOS pair with $|m(\ell\ell) - m_Z| < 10 \text{ GeV}$. This cut efficiently reduces most backgrounds but would remove $\approx 30\%$ of signal events. Since statistical uncertainties are expected to dominate, such signal reduction is to be avoided. Therefore, the Z-veto is dropped. Instead, the channel strategy uses neural networks to perform similarly regarding background suppression while keeping the signal $t\bar{t}H$ events.

The veto on the four lepton invariant mass close to the Higgs boson mass has a significant impact on the 4ℓ final state, effectively suppressing the $H \rightarrow ZZ^*$ decay mode, and results in $H \rightarrow WW^* \rightarrow \ell\nu_\ell\ell\nu_\ell$ decay mode being the most dominant one. A pie chart based on truth information from simulation demonstrates the different fractions of Higgs boson decay modes covered by the 4ℓ channel in Figure 6.5. It also provides a finer categorisation of the dominant $H \rightarrow WW^*$ decay mode. Additionally, the top quark decay modes are presented, showing that the top quark pair almost always decays dileptonically.

The dominant prompt backgrounds for the $t\bar{t}H \rightarrow 4\ell$ process arise from $t\bar{t}Z$ production with dileptonic decaying top quark pair and $Z \rightarrow \ell\ell$, and from diboson ZZ production with both bosons decaying to leptons. Other minor prompt backgrounds originate from tWZ and $t\bar{t}t\bar{t}$. The most dominant non-prompt background arises from $t\bar{t}$ production with two additional non-prompt leptons. The estimation of the non-prompt backgrounds is described in Section 7.1. Table 6.4 shows the expected yields after applying preselection criteria. The preselected events are utilised to train a dense neural network (DNN). In Figure 6.6, various distributions of kinematic variables like transverse momentum of leptons are presented, but also high-level variables like invariant masses of lepton pairs or scalar sum of transverse momentum for jets $H_{T,\text{jets}}$. Particularly, variables such as the missing transverse energy or jet and b -jet multiplicities demonstrate a satisfactory level of modelling. In Appendix D, a collection of kinematic variables for the preselection is presented, including post-fit distributions.

6.2.1 Neural Network Approach for the 4ℓ Channel

In the following, the various aspects of applying a three-class dense neural network for the 4ℓ channel are presented, aiming to separate $t\bar{t}H$ signal events from $t\bar{t}Z$ and ZZ background ones and starting from the selection of used input features, followed by the treatment of negative event weights and splitting of the dataset into training, testing, and validation sets. Afterwards, the neural network architecture and training are explained, and then the performance is evaluated.

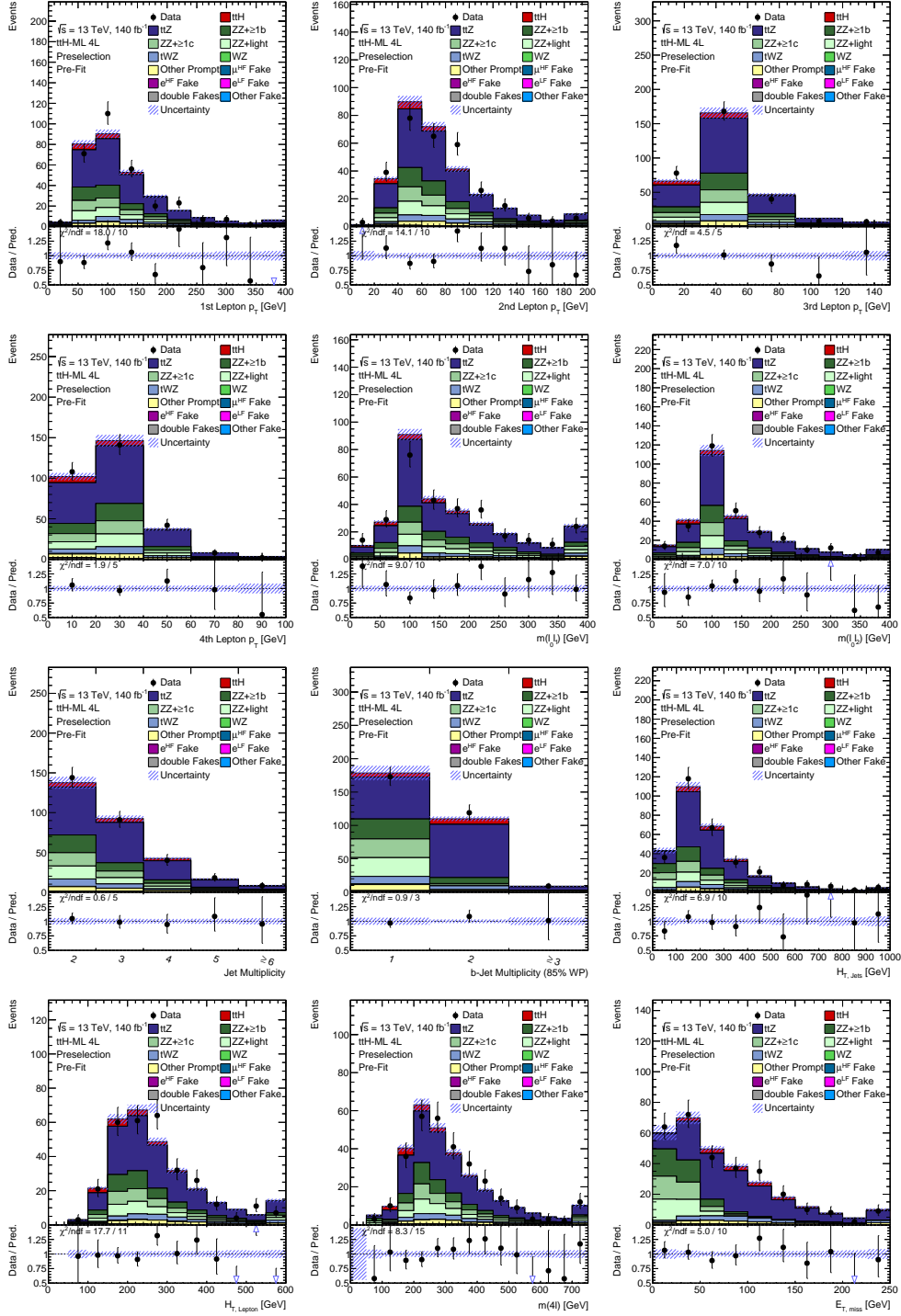


Figure 6.6: Pre-fit data MC comparison for lepton- and jet-related variables. The blue hashed bands represent each bin's MC-statistical and systematic uncertainties.

Input Features for the Neural Network

Object	Variable	Symbol(s)	# Variables: 22
Leptons	Distances between Lepton Pairs	$\Delta R_{ij}(\ell\ell)$	6
	Invariant Masses of Lepton Pairs	$m_{ij}(\ell\ell)$	6
	Scalar Sum of p_T	$H_{T,\text{lep}}$	1
	Four Lepton Invariant Mass	$m(4\ell)$	1
	Number of SFOS Pairs	n_{SFOS}	1
Jets	Number of (b-) Jets	$n_{\text{Jets}}, n_{\text{b-Jets}}$	1 + 1
	Scalar Sum of p_T	$H_{T,\text{jets}}$	1
E_T^{miss}	Magnitude	E_T^{miss}	1
Other	Stransverse Masses	$M_{T2,\text{Top}}(\ell\ell), M_{T2,\text{Boson}}(\ell\ell)$	1 + 1
	Effective Invariant Mass	$m_{\ell_2\ell_3 E_T^{\text{miss}}}$	1

Table 6.2: A list of twenty-two input variables for the DNN for the 4ℓ channel.

The neural network uses twenty-two high-level variables as input features, with an overview presented in Table 6.2. In particular, the invariant masses of all six lepton pair combinations $m_{ij}(\ell\ell)$ are fed into the neural network since they give rise to the presence of potential Z boson candidates. Appendix E presents shape comparisons between the three processes for all input features. The invariant masses of lepton pairs for $t\bar{t}Z$ and ZZ tend to have a peak around the mass of the Z boson, while no such trend is observed for $t\bar{t}H$, as shown in Figure E.1. Together with the charge and flavour information of all four leptons, combined into the number of SFOS lepton pairs, similar features are provided to the network used for the previously applied Z -veto. To further pronounce the relationship between leptons, distances between lepton pairs $\Delta R_{ij}(\ell\ell)$ are used, targeting different spatial separations, adding further information about the leptons and their origin. Furthermore, the scalar sum of transverse momentum $H_{T,\text{lep}}$ and invariant mass of all four leptons $m(4\ell)$ are added as lepton-related features. Jet-related variables are used to improve further separation between processes involving a top quark pair, $t\bar{t}H$ and $t\bar{t}Z$, from diboson ones. Significantly, the number of b -jets and jets demonstrate good separation, as the top quark pair results in a more significant amount of hadronic activity. This is further pronounced by the scalar sum of the transverse momentum of jets $H_{T,\text{jets}}$, as additional jets generated by gluon splitting in ZZ events tend to be softer, compared to jets induced by the heavier final state of $t\bar{t}H$ and $t\bar{t}Z$ ⁶. The missing transverse momentum E_T^{miss} provides the best separation between ZZ and the remaining processes, as no genuine contribution is expected from the former one. Only the magnitude E_T^{miss} is fed into the network. Additionally, variables are constructed to explore further the different decay signatures of the boson decays, $Z \rightarrow \ell\ell$ and $H \rightarrow WW^* \rightarrow \ell\nu\ell\nu$, or the top quark pair system. In the following, the effective invariant mass and stransverse mass are introduced.

⁶This trend is observed for the individual transverse momentum distributions for each jet. However, this information is passed down to the scalar sum of transverse momentum for jets $H_{T,\text{jets}}$.

Effective Invariant Mass

The spatial information of E_T^{miss} is used for the construction of the effective invariant mass $m_{\ell_2\ell_3 E_T^{\text{miss}}}$. It focuses on the separation of $t\bar{t}H$ and $t\bar{t}Z$ events by exploiting the different decay modes $t\bar{t}Z \rightarrow 4\ell 2\nu$ and $t\bar{t}(H \rightarrow WW^*) \rightarrow 4\ell 4\nu$, utilising the presence of more neutrinos in the final state of $t\bar{t}H$ and its impact on the magnitude and spatial components of E_T^{miss} . The effective invariant mass was used in the previous analysis and is constructed as follows: find the closest lepton to the hardest b -jet and the lepton with opposite charge closest to another jet or b -jet. These leptons are likely to originate from the top quark system, while the remaining opposite charge leptons originate from either a Higgs boson or Z boson. The effective invariant mass $m_{\ell_2\ell_3 E_T^{\text{miss}}}$ is then defined as the invariant mass of these leptons together with E_T^{miss} . Since the dileptonic top quark decay also involves neutrinos, the effective invariant mass $m_{\ell_2\ell_3 E_T^{\text{miss}}}$ does not feature a peak around the Higgs boson mass for $t\bar{t}H$ events, but is slightly smeared as shown in Figure 6.7.

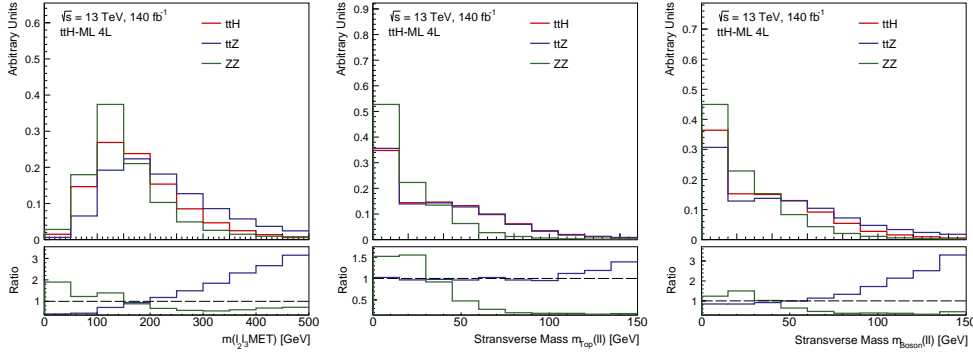


Figure 6.7: Shape comparison of the effective invariant mass and the two transverse masses for all three target processes $t\bar{t}H$, $t\bar{t}Z$, and ZZ . All distributions are normalised to unity.

Stransverse Mass

The stransverse mass is commonly used in beyond SM searches and is closely related to the transverse mass m_T^2 . The latter assumes that the undetected particle, created during the collision, is massless, being an appropriate assumption for W boson decays. However, the stransverse mass does not require such an assumption. For a pp collision induced process, creating a particle pair, which each is subsequently decaying into an observed particle with transverse momentum $p_T^{\ell\pm}$ and unobserved particle with transverse momentum $p_T^{\text{miss},i}$, the stransverse mass [255] is defined as:

$$M_{T2} = \min_{p_T^{\text{miss}}} \left[\max \left(m_T^2 \left(p_T^{\ell+}, p_T^{\text{miss},1} \right), m_T^2 \left(p_T^{\ell-}, p_T^{\text{miss},2} \right) \right) \right]. \quad (6.3)$$

Since the exact splitting is unknown, Equation 6.3 requires a minimisation over all possible momenta, $p_T^{\text{miss},1}$ and $p_T^{\text{miss},2}$ under the constraint that their sum is equal to the amount of observed missing transverse momentum p_T^{miss} . Two variables are introduced to adapt the transverse mass to the 4ℓ final state, focusing on the top quark pair system while the other explores the bosonic part. Using the same labelling of leptons as for the effective invariant mass, the transverse mass of the top quark pair $M_{T2,\text{Top}}(\ell\ell)$ is constructed using the leptons likely originating from the top quark pair and E_T^{miss} . Figure 6.7 compares the shape between the three targeted processes. The transverse mass of the top quark pair $M_{T2,\text{Top}}(\ell\ell)$ for $t\bar{t}H$ and $t\bar{t}Z$ are similar due to the presence of the top quark pair and may be utilised for better separation of the ZZ process. The transverse masses for the boson candidate $M_{T2,\text{Boson}}(\ell\ell)$ is constructed similarly. However, it uses the remaining leptons, which are also used for the effective invariant mass. For $t\bar{t}Z$, the transverse masses for the boson candidate tend to be harder, compared to $t\bar{t}H$ as shown in Figure 6.7. The transverse masses for the boson candidate and top quark pair are similar for ZZ .

Dataset and Negative Weight Treatment

The number of used MC events for each target process is shown on the left in Figure 6.8 and defines the size of the dataset. The dataset is split into two statistically independent folds using the k-folding method for training, validation, and testing. The first fold uses 50 % of the dataset for training while remaining 37.5 % for validation and 12.5 % for testing. The second fold combines testing and validation sets as training and splits the previously used training set into validation and testing with the same fractions. The data sets of $t\bar{t}H$ and $t\bar{t}Z$ are supplemented by adding alternative systematic samples, mentioned in Section 3.4. Next to the increase in training data, the alternative samples may provide robustness against systematic effects. On the right side of Figure 6.8, the relative fraction of MC statistics for each sample with respect to the full dataset is shown in blue. Furthermore, in red, the fraction of negative MC weights is shown for all three processes with respect to the full dataset.

During event generation, negative event weights occur to avoid double-counting during matching NLO matrix element contributions to the parton shower. They impact both the normalisation and shape of input distributions. The largest fraction corresponds to the $t\bar{t}Z$ process caused by the MC@NLO method. The $t\bar{t}H$ sample is generated with POWHEG matched with PYTHIA using the POWHEG method, resulting in a tiny fraction of negative MC weights. Negative weights will cause problems when calculating the gradient and loss, as the loss for each event is scaled with the event weight and may become negative⁷. There are several strategies to deal with negative weights: remove the negative ones and only use positive ones, set every

⁷This issue occurs if the calculated loss across a batch becomes negative. Using higher batch sizes may decrease the chance of getting negative loss values and, therefore, a sign flip for the gradient calculation.

event weight to unity, or take the absolute value of each weight. These strategies have the downside of changing the shape and normalisation of the input distributions. To remove negative weights while preserving both shape and normalisation, a correction factor

$$\mathcal{C} = \frac{\sum_i w_i}{\sum_{w_i > 0} w_i} \quad (6.4)$$

is derived to compensate for negative weight contributions. The corrected event weights w'_i used during the training are calculated by scaling the positive weights with the correction factor:

$$w'_i = \mathcal{C} w_i. \quad (6.5)$$

The remaining negative weights are set to zero and, therefore, dropped from the training. The impact of the different strategies on the input distributions is studied in Appendix F. The approach of using a scale factor for correcting the missing negative weights is used, as it provides a satisfactory compensation of negative weights, especially for the $t\bar{t}Z$ and ZZ data sets.

Neural Network Architecture and Training

Multiple hyperparameters control the training and architecture of the dense neural network. A list of parameters is presented in Table 6.3, defining the architecture of the network, like the number of hidden layers and nodes per layer, but also the used activation functions. Other parameters, like the learning rate, dropout index, or batch normalisation index, influence the training. Different combinations of hyperparameter settings are tested to determine the combination with the best performance, defined as the lowest mean loss concerning both folds. In total, 250 neural networks are trained with hyperparameters randomly chosen within a defined range. In Table 6.3, an overview of the used ranges and settings is presented, together with the best configuration. The neural network size is limited to three to ten hidden layers, each containing between 30 and 250 nodes chosen in step sizes of ten nodes. The learning rate controls the step size along the calculated gradient and, therefore, towards the global⁸ minimum. Choosing minimal learning rates will slow the training process, while large learning rates will cause divergent behaviour. All models have a batch size of 1064, use the softmax function as the output function, and Adam as optimiser [256]. The categorical cross-entropy

$$\mathcal{CE} = - \sum_c y_c \log(y(x)_c), \quad (6.6)$$

with y_c as the label of class c and $y(x)_c$ as the prediction for an input x , is used as loss function for all models. All models have a dropout probability of 25 % for regularisation. The optimised model applies dropout from the second to the fifth hidden layer. Batch normalisation is performed for the optimised model at the layers

⁸The loss function landscape may also have local minima.

with index 0, 1, 2, 3, 5. The training is terminated by an early stopping mechanism, checking the change of the loss function for the validation, $\Delta_{\min.}$, over a selected number of epochs, called patience. It effectively stops the training if there is no improvement in the validation loss. All models use a patience of 150 training epochs with a minimal change of the loss function of $\Delta_{\min.} = 0.001$.

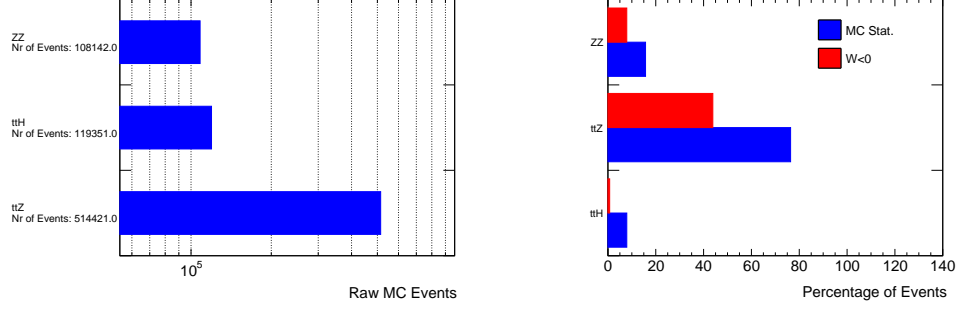


Figure 6.8: The size of the used dataset in terms of raw MC events for each process $t\bar{t}H$, $t\bar{t}Z$, and ZZ . The MC statistics are increased by adding alternative systematic samples for $t\bar{t}H$ and $t\bar{t}Z$. On the right side, the fraction of MC events for each process and the fraction of negative events for each process concerning the total dataset are presented. The largest fraction of total events and negative weights contribution is $t\bar{t}Z$.

Hyperparameter	Values	Configuration after Optimisation
Type	Classification DNN	Classification DNN
Hidden Layers	max: 10 min: 3 max: 250	6
Nodes per Hidden Layer	min: 30 step size: 10	210, 100, 230, 160, 160, 170
Activation Functions	Relu, Elu, Selu, LeakyRelu	-
Activation Functions Combination	-	Elu, Selu, LeakyRelu, LeakyRelu, Selu, LeakyRelu
Learning Rate	max: 0.0005 min: 0.00005	0.00055
Batch Size	1064	1064
Output Function	Softmax	Softmax
Loss Function	Categorical Cross-Entropy	Categorical Cross-Entropy
Optimiser	Nadam	Nadam
Dropout Probability	25 %	25 %
Dropout Index	-	1, 2, 3, 4
Batch Normalisation Indices	-	0, 1, 2, 3, 5
Patience	150	150
$\Delta_{\min.}$	0.001	0.001

Table 6.3: A list of the hyperparameters used during the optimisation. The configuration for the best model is presented on the right.

Neural Network Performance and Evaluation

Performance evaluation is the final step after training a neural network model. The loss function for the training and validation set as a function of the training epoch for both folds is shown in Figure 6.9. Both loss functions decrease and saturates. The early stopping mechanism terminates the training since the validation loss does not decrease over 150 training epochs. Overtraining is not observed since training and validation loss converge similarly. In the beginning, the training loss is over a large range greater than the validation loss. This is caused by the usage of dropout features, which artificially reduce performance during training. The effect decreases till the end of the training step. The DNN output classifiers for the $t\bar{t}H$ response for both folds are presented in Figure 6.10. The background is the combination of $t\bar{t}Z$ and ZZ . A clear separation between classified $t\bar{t}H$ and remaining background contributions is observed for both folds.

To further evaluate the performance, especially in contrast to the testing set and fold of the classifier, receiver operating characteristics curves, called ROC curves, are used. ROC curves are used for binary classification evaluation. However, it can be expanded for multiclass by favouring one class while combining the remaining classes. The ROC curve evaluates for a given classifier cut the true positive rate versus the false positive rate. The area under the curve (AUC) is then a measure for the classifier's performance, with a perfect classifier having an AUC of unity, while a random guess would result in an AUC of 0.5.

In Figure 6.11, the ROC curves for all three output classifiers are presented with the AUC values provided for each fold and training and testing set. There are no significant differences between the training or testing AUC values compared within the two folds for each classifier, indicating no large statistical fluctuations or biases of the two used folds. Comparison of the AUC values for training and testing for a given fold gives rise to generalisation performance. Large deviations would indicate different performances on the training and unseen testing sets, hence a tiny generalisation performance. For all three classifiers, the testing and training AUC values are compatible with each other, indicating no large sign of overtraining and good generalisation performance. The AUC values for the ZZ output classifier are the closest to unity as the model can separate ZZ from the remaining events easily.

This is also reflected in the confusion matrix in Figure 6.12, comparing the model's prediction with true labels with a perfect classifier represented by a diagonal confusion matrix. The model can separate ZZ events effectively; the largest misclassification occurs with $t\bar{t}Z$ due to the presence of on-shell Z bosons. Most misclassification occurs between $t\bar{t}H$ and $t\bar{t}Z$ categories due to their similar signature with the main difference in the distributions of the invariant mass of lepton pairs and number of neutrinos in the final state affecting E_T^{miss} .

To quantify the importance of an input, the *permutation feature importance* method

is applied by randomly shuffling an input feature and measuring the performance in terms of AUC. The difference of reduced AUC and nominal AUC_{nom} normalised to the nominal AUC_{nom} is used as a metric and is given by:

$$\mathcal{IP} = \frac{\Delta AUC}{AUC_{\text{nom}}} = \frac{AUC_{\text{nom}} - AUC}{AUC_{\text{nom}}}. \quad (6.7)$$

For input features with tiny importance, the \mathcal{IP} will be close to zero since the relative performance difference is tiny⁹. A ranking of the permutation importance for every input feature for all three classifiers is shown in Figure 6.13. The most important input features for all three classifiers are the missing transverse energy E_T^{miss} , followed by the invariant masses of lepton pairs. Especially for the ZZ classifier, E_T^{miss} is highly ranked since ZZ production is expected to have no genuine E_T^{miss} contribution. For $t\bar{t}H$ and $t\bar{t}Z$, the importance arises from the different decay modes of the additional boson, since the top quark pair decay is on average similar¹⁰. The Higgs boson decay $H \rightarrow WW^* \rightarrow \ell^+ \nu_\ell \ell^- \bar{\nu}_\ell$ involves additional neutrinos compared to the $Z \rightarrow \ell^+ \ell^-$ decay, affecting the expected E_T^{miss} distributions. Furthermore, the different decay modes of the involved boson influence the invariant mass and flavour combination of lepton pairs: SFOS lepton pairs are expected to have an invariant mass close to the Z boson mass. Thus, the invariant masses are important for the model's performance.

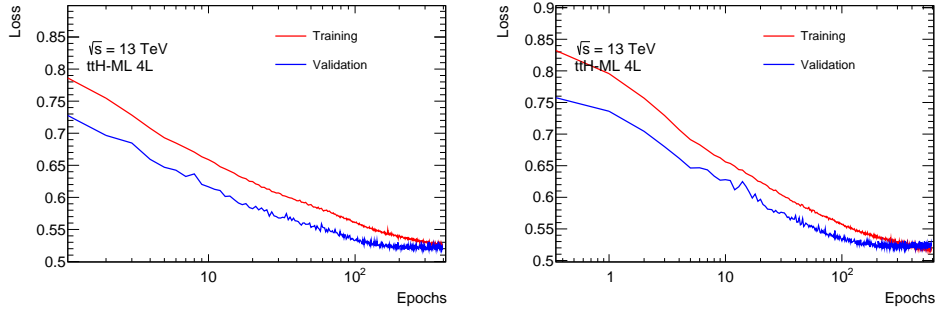


Figure 6.9: The loss as a function of the training epochs evaluated for both folds' training and validation sets.

⁹The *permutation feature importance* method is not only sensitive to the importance of a single input feature but also to the correlation of that input feature with other ones. However, in both cases, the input features are highly ranked.

¹⁰Small differences occur due to the mass of the Higgs boson compared to the Z boson, changing the recoiling system the top quark pair system.

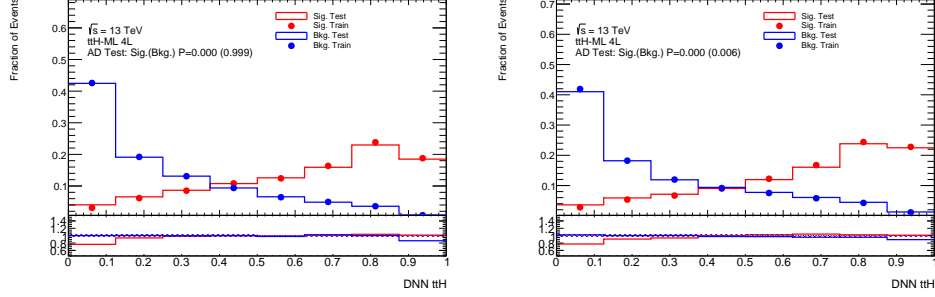


Figure 6.10: The DNN $t\bar{t}H$ classifier distributions for both folds. The background represents the combination of $t\bar{t}Z$ and ZZ .

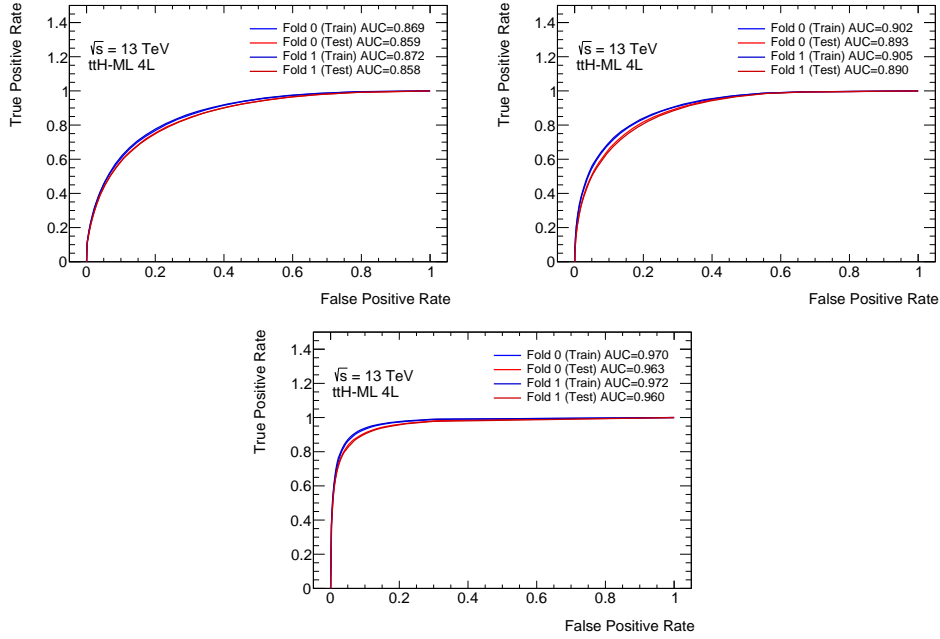
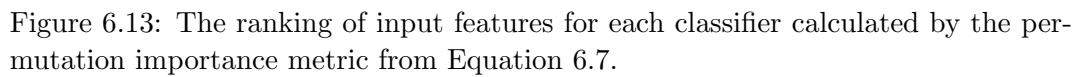
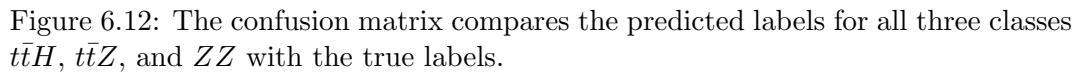


Figure 6.11: The ROC curves for the three output classifiers. The AUC values for both folds and training and validation sets are compared. The top left ROC curve corresponds to the $t\bar{t}H$ classifier, while on the right, the one for the $t\bar{t}Z$ classifier is shown. The bottom ROC curve belongs to the ZZ classifier.



6.2.2 Definition of SR and CR for the 4ℓ Channel

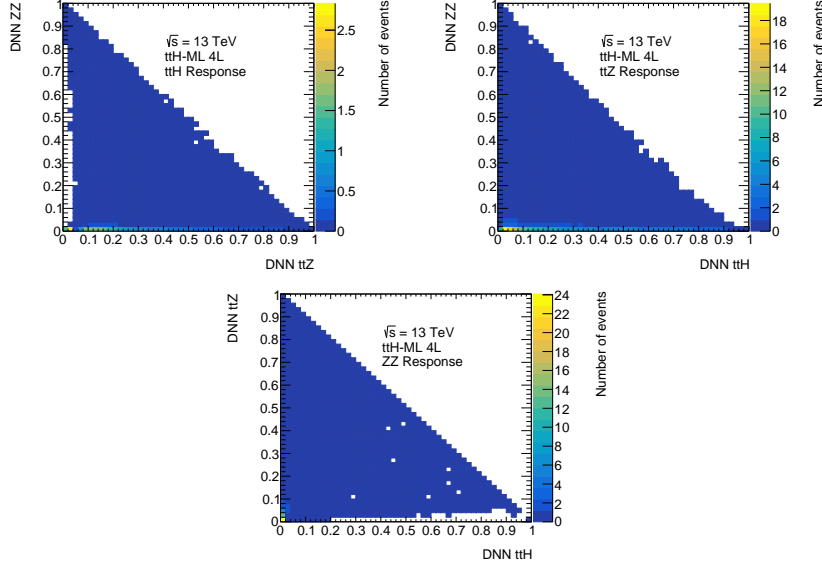


Figure 6.14: The two-dimensional planes to show the score response for a class as a function of the remaining scores. The property of the softmax output function summing up all scores to unity leads to the triangular shape. At the top left, the $t\bar{t}H$ response is shown, while on the right, the $t\bar{t}Z$ one. The bottom one shows the ZZ response.

The output classifier of the neural network can be interpreted in a probabilistic manner due to the usage of the softmax output function, assigning each event a likelihood to originate from $t\bar{t}H$, $t\bar{t}Z$, or ZZ production, with the sum of likelihoods equal to unity. The previously mentioned normalisation conditions can be used to visualise the individual scores in a two-dimensional plane with an axis as the remaining scores as shown in Figure 6.14. The ZZ events are mostly separated from the remaining $t\bar{t}H$ and $t\bar{t}Z$ events due to their distinct signature and with the highest ZZ response at $\text{DNN}_{t\bar{t}H}$ and $\text{DNN}_{t\bar{t}Z}$ close to zero as shown on the bottom of Figure 6.14. The response for $t\bar{t}H$ is mostly accumulated along $\text{DNN}_{t\bar{t}Z}$, demonstrating the difficulty of separating $t\bar{t}H$ and $t\bar{t}Z$ due to their similar signature. For $t\bar{t}Z$, the same behaviour is observed.

The classification scores define the $t\bar{t}H$ SR, enriched with $t\bar{t}H$ and $t\bar{t}Z$ sensitive bins, and a ZZ CR. The definitions of the 4ℓ analysis regions are based on the ZZ score DNN_{ZZ} with cuts obtained from the optimisation presented in Appendix G. The region definitions read as follows:

- $\text{SR}_{t\bar{t}H}$: Preselection and $\text{DNN}_{ZZ} \leq 0.1$ and

- CR_{ZZ} : Preselection and $DNN_{ZZ} > 0.1$.

The expected yields for the analysis regions are shown in Table 6.4. There are no further cuts on the $DNN_{t\bar{t}H}$ or $DNN_{t\bar{t}Z}$ score, instead the $DNN_{t\bar{t}H}$ distribution is used since it has a natural separation between the remaining process as seen on the left side in Figure 6.15¹¹. The ZZ contribution is split according to the flavour compositions of additional jets created by gluon splitting. The classification relies on truth information of hadrons embedded in jets. If a ZZ event has a jet containing a b -hadron, it is labelled as $ZZ+ \geq 1b$; if the jet contains a c -hadron but no b -hadron, it falls into the $ZZ+ \geq 1c$ category. The remaining ones are classified as $ZZ + \text{light}$ and contain light quark or gluon jets. This classification is also used in other analyses like $t\bar{t}(H \rightarrow b\bar{b})$, as described in Ref. [122]. The CR_{ZZ} uses the b -jet multiplicity as fitted distribution since it entangles the different flavour compositions of additional jets as shown in Figure 6.15. Pre-fit uncertainties are shown, including both statistical and systematic uncertainties.

Kinematic variables are presented to validate the data to MC agreement after applying the DNN_{ZZ} score cut. In Figure 6.16, the transverse momentum for each lepton together with the invariant mass of lepton pairs and all four leptons, the jet and b -jet multiplicity and the scalar sum of transverse momentum for leptons and jets, and E_T^{miss} are presented, using the first seven bins of the SR, enriched with $t\bar{t}Z$ events, acting as $t\bar{t}Z$ CR. In Figure 6.17, the same variables are shown but using the CR_{ZZ} selection. As for the preselection, the $t\bar{t}Z$ sensitive part of the $SR_{t\bar{t}H}$ and CR_{ZZ} regions demonstrate a satisfactory level of data to MC agreement. The complete set of pre- and post-fit distributions of the DNN input features is presented in Appendix D.

¹¹The splitting of the $DNN_{t\bar{t}H}$ score distribution is also unnecessary since both defined $t\bar{t}H$ SR and $t\bar{t}Z$ CR will use the $DNN_{t\bar{t}H}$ score as fitted distribution.

Process	Preselection	$SR_{t\bar{t}H}$	CR_{ZZ}
$t\bar{t}H$	15.31 ± 1.87	13.44 ± 1.85	1.87 ± 0.30
$t\bar{t}Z$	148.39 ± 1.42	117.60 ± 0.73	30.79 ± 1.50
$ZZ + \geq 1b$	39.40 ± 3.78	2.16 ± 0.27	37.24 ± 3.78
$ZZ + \geq 1c$	30.77 ± 2.58	1.17 ± 0.13	29.60 ± 2.58
$ZZ + \text{light}$	28.90 ± 4.38	0.75 ± 0.15	28.15 ± 4.38
tWZ	17.67 ± 6.79	12.28 ± 6.13	5.39 ± 2.70
WZ	1.04 ± 0.16	0.53 ± 0.12	0.51 ± 0.11
Other Prompt	12.88 ± 1.84	8.14 ± 1.44	4.74 ± 1.15
μ^{HF} Fake	0.31 ± 0.07	0.20 ± 0.05	0.11 ± 0.05
e^{HF} Fake	0.25 ± 0.07	0.15 ± 0.04	0.10 ± 0.06
e^{LF} Fake	0.27 ± 0.04	0.11 ± 0.03	0.16 ± 0.03
double Fake	1.37 ± 0.32	1.37 ± 0.32	0.0 ± 0.0
Other Fake	1.02 ± 0.58	0.36 ± 0.18	0.76 ± 0.45
Total MC	298 ± 12	158 ± 7	139 ± 10
data	301	155	146

Table 6.4: The expected yields after applying the 4ℓ preselection and SR and CR selection for the various processes and data, including systematic uncertainties. The ZZ process is split by the flavour of additional jets using the HF classification algorithm. The fake and non-prompt lepton categories are explained in Section 7.1.

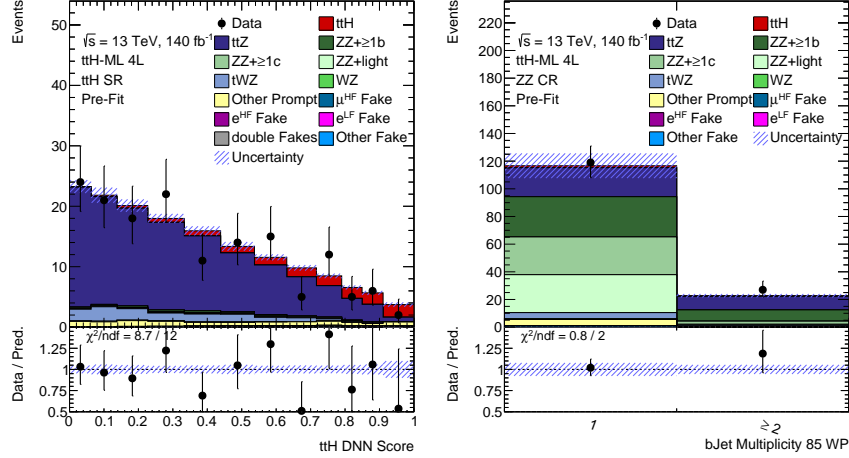


Figure 6.15: The $DNN_{t\bar{t}H}$ score distribution for the $SR_{t\bar{t}H}$ region is shown on the left. The CR_{ZZ} region on the right, the b -jet multiplicity is shown. Both distributions show total pre-fit uncertainties as blue hashed bands.

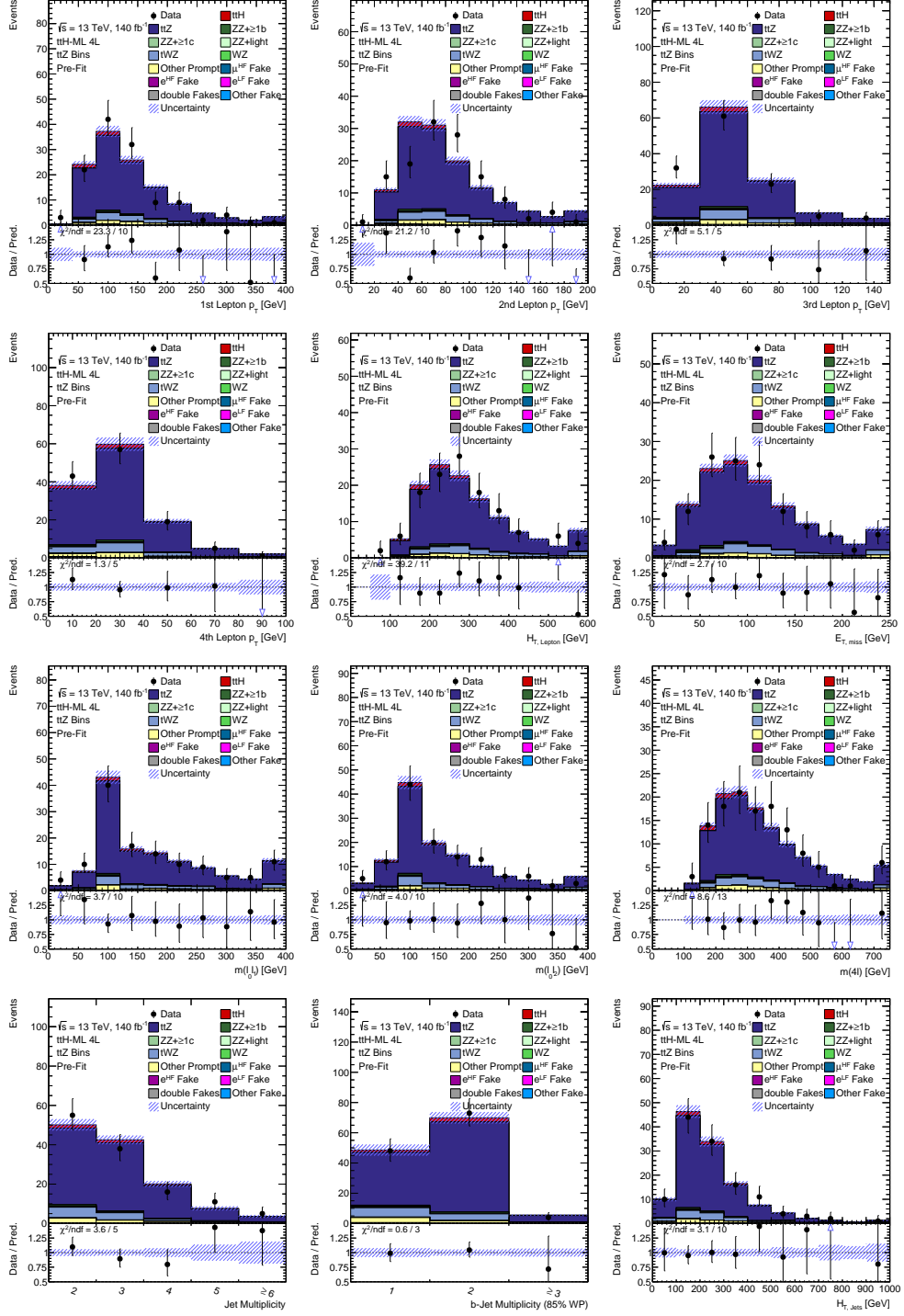


Figure 6.16: Distributions of the transverse momentum of four leptons, the scalar sum of transverse momenta of leptons and jets, the invariant mass of lepton pairs and four leptons, jet and b -jet multiplicity, and E_T^{miss} in the $t\bar{t}Z$ sensitive bins of the $\text{SR}_{t\bar{t}H}$. Total pre-fit uncertainties are shown as blue hashed bands.

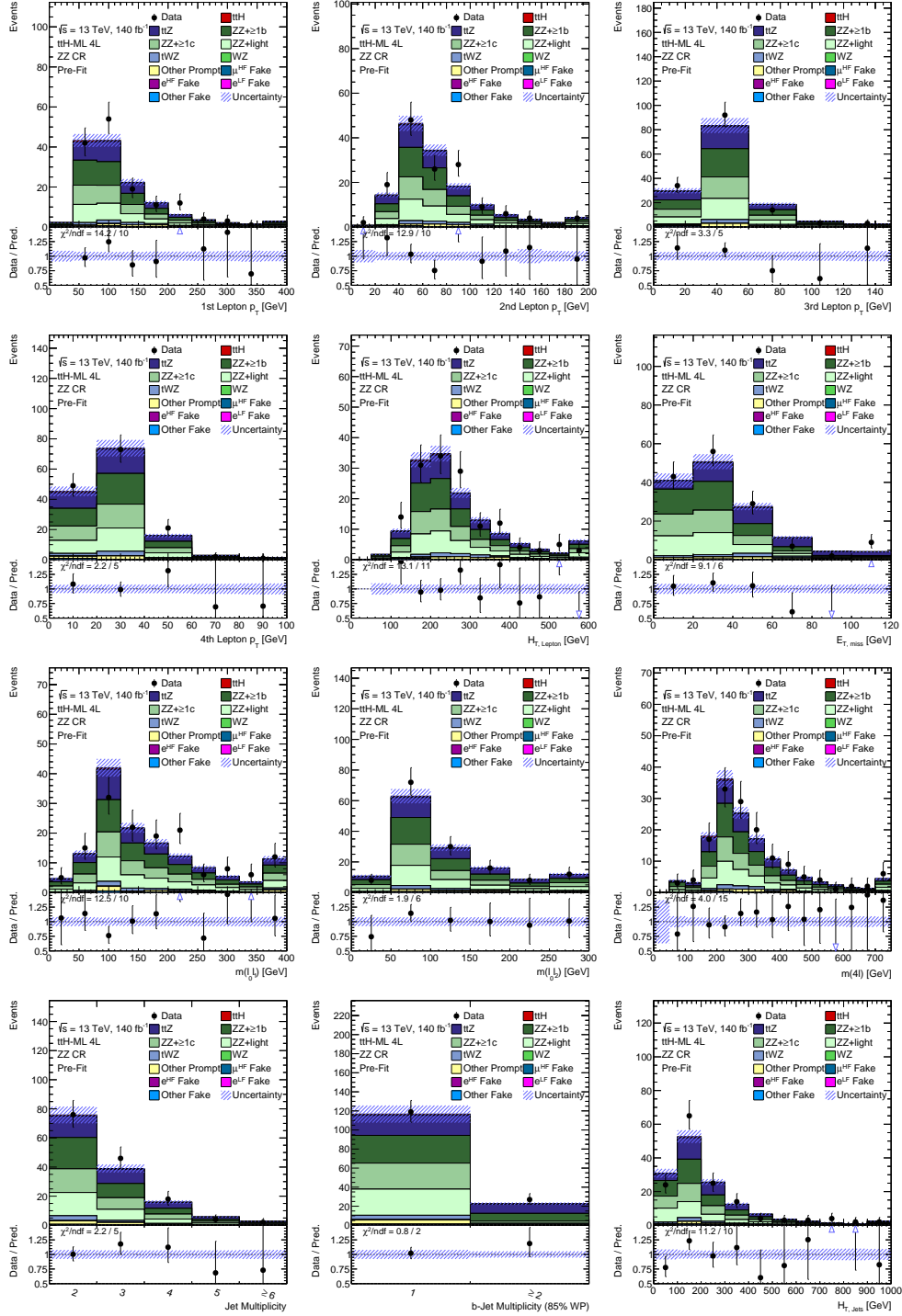


Figure 6.17: Distributions of the transverse momentum of four leptons, the scalar sum of transverse momenta of leptons and jets, the invariant mass of lepton pairs and four leptons, jet and b -jet multiplicity, and E_T^{miss} in the ZZ CR. Total pre-fit uncertainties are shown as blue hashed bands.

6.3 The $3\ell+0\tau_{\text{had}}$ Channel

The $3\ell+0\tau_{\text{had}}$ channel is sensitive to both $t\bar{t}H$ and tH ¹² processes. The preselection is shown in Table 6.1 and requires three light leptons with a total charge of ± 1 . Unlike the 4ℓ channel, which is inclusive in the number of τ_{had} candidates, the 3ℓ channel applies a veto on τ_{had} candidates. The lepton with opposite charge with respect to the remaining leptons needs to be *loose* (L), see Section 5.2.2, with a minimal transverse momentum of $p_T > 10$ GeV. The other same-sign leptons need to pass *tight* (T) criteria with a minimal transverse momentum of $p_T > 15$ GeV. Additional requirements are applied to lepton pairs to reduce certain backgrounds. Applying a Z -veto cut on each same-flavour opposite sign, $|m(\ell\ell) - m_Z| < 10$ GeV, reduces $t\bar{t}Z$ contribution, while $m(\ell^+\ell^-) > 12$ GeV reduces contributions of low-mass resonance quarkonia decays. Furthermore, the preselection requires at least two jets with at least one b -jet passing the 85% working point. The $3\ell+0\tau_{\text{had}}$ channel targets dileptonic (single-leptonic) top quark pairs decays and $H \rightarrow WW^*$ with one (two) leptonic decaying W bosons. The dominant prompt background contributions arise from $t\bar{t}Z$, $t\bar{t}W$, and diboson production VV , mainly WZ , and non-prompt and fake contributions from $t\bar{t}$ production.

The $3\ell+0\tau_{\text{had}}$ channel uses a multiclass BDT with six categories: $t\bar{t}H$, $tHjb$, $t\bar{t}W$, $t\bar{t}Z$, VV , and $t\bar{t}$ ¹³. The input features are a collection of low- and high-level variables of lepton, jets, and E_T^{miss} and their relation in terms of angular separation and invariant masses. The most essential features for the $t\bar{t}H$ separation are the number of jets and the invariant masses of lepton pairs. For the tH classification, in addition to the invariant masses of lepton pairs, jet-related variables such as the transverse momentum and distance to leptons are essential. The largest misassignments of $t\bar{t}H$ are to the $t\bar{t}Z$ and $t\bar{t}W$ category. The definition of the signal and control regions is based on optimised cuts on the output classifier¹⁴, into a $t\bar{t}H$ and tH SR, and five CRs targeting each dominant background. To better estimate the $t\bar{t}Z$ and VV processes, two CRs are also designed to target events failing the Z veto of the preselection. The number of jets further splits them: the VV CR requires two or three jets, while the $t\bar{t}Z$ CR has at least four or more jets. The previously defined CRs target the on-shell components of the $t\bar{t}Z$ and VV processes.

6.4 The $2\ell\text{SS}+0\tau_{\text{had}}$ Channel

The $2\ell\text{SS}+0\tau_{\text{had}}$ channel uses a four-dimensional multiclass BDT to separate signal $t\bar{t}H$ and tH events from the overwhelming background. Using single and dilepton triggers, the preselection requires two *tight* (T) same-sign leptons with transverse momentum $p_T > 15$ GeV and no τ_{had} candidates, and at least three reconstructed

¹²Sometimes also referred to as $tHjb$.

¹³A reweighting procedure is used to increase the statistics on this contribution, also improving shapes of physics variables.

¹⁴As in the 4ℓ channel, the classifier is interpreted probabilistically.

jets with at least one b -jet passing the 85 % DL1r working point. A summary of the preselection is found in Table 6.1. The $2\ell\text{SS}+0\tau_{\text{had}}$ targets single-lepton top quark pair decays and single-lepton $H \rightarrow WW^*$ decay modes. The most dominant prompt backgrounds arise from $t\bar{t}W$, $t\bar{t}Z$, and VV production, with fakes originating predominantly from $t\bar{t}$ production.

The BDT approach targets the categories $t\bar{t}H$, $tHjb$, $t\bar{t}W$, and Other, including $t\bar{t}Z$, $t\bar{t}$, VV , and other minor contributions. In contrast to the 4ℓ and $3\ell+0\tau_{\text{had}}$ channels, the input features of $2\ell\text{SS}+0\tau_{\text{had}}$ focus more on jets and their relation to the leptons. High-level variables such as distances, invariant masses, and low-level kinematic information are used. The linear discriminant $LD = 0.6E_{\text{T}}^{\text{miss}} + 0.4H_{\text{T}}^{\text{jets}}$ is also added as input and is motivated by a good performance, observed in the $t\bar{t}H$ multi-lepton analysis of the CMS collaboration [257]. The most crucial input features are the number of jets, the invariant masses of both leptons and the average distance between all reconstructed jets. The largest misclassification of $t\bar{t}H$ occurs with the $t\bar{t}W$ category. The output classifiers define SR and CRs with the maximum score value defining the category: Two SRs for $t\bar{t}H$ and two CRs for $t\bar{t}W$, split by the lepton charges, and a tH SR. The Other category defines a CR with primary contributions from diboson and $t\bar{t}Z$ production.

6.5 The $2\ell\text{SS}+1\tau_{\text{had}}$ Channel

The $2\ell\text{SS}+1\tau_{\text{had}}$ channel uses both single and dilepton triggers. It requires two light leptons with same-sign and $p_{\text{T}} > 15 \text{ GeV}$, passing the *Medium* (M) lepton definition as described in Table 5.4. Events with an invariant mass of $|m(\ell\ell) - m_{\text{Z}}| < 10 \text{ GeV}$ are rejected. One τ_{had} candidate with minimal transverse momentum of $> 20 \text{ GeV}$ passing the *Medium* working point is required. Furthermore, at least three reconstructed jets with at least one b -jet passing the loosest working point of 85 % are required. The $2\ell\text{SS}+1\tau_{\text{had}}$ channel targets single-leptonic $t\bar{t}$ decays with $H \rightarrow \tau^+\tau^-$ with one τ_{had} and one leptonic τ decay. The main backgrounds arise from irreducible $t\bar{t}Z$ and $t\bar{t}W$ contributions, reducible diboson production mainly from WZ , and light lepton and τ_{had} fakes originating from $t\bar{t}$ production.

The $2\ell\text{SS}+1\tau_{\text{had}}$ channel uses a three-class BDT to separate $t\bar{t}H$ signal events from $t\bar{t}W$ and $t\bar{t}$ ones using events passing the channel preselection. To increase the used MC statistics of $t\bar{t}$ for the training, a reweighting procedure similar to the $2\ell\text{SS}+0\tau_{\text{had}}$ channel is used. The input features focus on high-level variables, emphasising the relation of the two lepton systems and reconstructed jets or $E_{\text{T}}^{\text{miss}}$. After utilizing a large set of input features, the unimportant ones are removed. The most important features are the number of jets and the invariant mass of the leading lepton and $E_{\text{T}}^{\text{miss}}$.

The signal region for the $2\ell\text{SS}+1\tau_{\text{had}}$ channel is defined using the preselection but with a tighter selection of at least four reconstructed central jets. These bins are

pure in $t\bar{t}H$ signal and use the $t\bar{t}H$ BDT response to further separate background events.

6.6 The $2\ell\text{OS}+2\tau_{\text{had}}$ and $1\ell+2\tau_{\text{had}}$ Channels

Both channels require two opposite-sign τ_{had} candidates passing *Medium* (M) working point, having a minimal transverse momentum of $p_T > 20$ GeV. The $2\ell\text{OS}+2\tau_{\text{had}}$ channel uses both single and dilepton triggers, further requiring two opposite-sign *Loose* (L) leptons with $p_T > 10$ GeV and $|m(\ell\ell) - m_Z| > 10$ GeV and $m(\ell\ell) > 12$ GeV to reduce contamination from $t\bar{t}Z$ events and low-mass resonance decays, respectively. Furthermore, at least one b -jet passing 77% working point is required. The $2\ell\text{OS}+2\tau_{\text{had}}$ channel targets dileptonic $t\bar{t}$ decays with $H \rightarrow \tau_{\text{had}}\tau_{\text{had}}$, as illustrated in Table 6.1. The preselection is used for the BDT training, attempting to separate $t\bar{t}H$ events from the background using a binary classification model. The input features have a large focus on the di- τ_{had} system, with the maximum pseudo-rapidity of the two τ_{had} leptons and azimuthal separation of the di- τ_{had} system and E_T^{miss} as the most essential features. The preselection is used as SR with the binary classification score as fitted distribution.

The $1\ell+2\tau_{\text{had}}$ channel uses only single-lepton triggers, and in addition to the τ_{had} requirements, one *Loose* (L) lepton with $p_T > 27$ GeV, at least three reconstructed jets, with at least one b -jet passing 77% DL1r working point, defining the $t\bar{t}H$ SR. The tH SR is defined similarly, requiring maximal two reconstructed jets. A summary of the selection is found in Table 6.1. The $t\bar{t}H$ $1\ell+2\tau_{\text{had}}$ channel targets single-lepton $t\bar{t}$ decays and the $H \rightarrow \tau_{\text{had}}\tau_{\text{had}}$ decay mode. Binary BDT classification models are trained per region, separating $t\bar{t}H$ or tH against background contributions. A similar set of features is used, with the same features being most important for the $t\bar{t}H$ response. The most important feature of the tH BDT response is the visible invariant mass of the di- τ_{had} system. The BDT responses are used as fitted distribution for both SRs.

6.7 Higgs Boson Transverse Momentum Reconstruction

The measurement of the $t\bar{t}H$ production rate in bins of the transverse momentum of the Higgs boson p_T^H is based on the *Simplified Template Cross Sections* (STXS) [70]. It uses six bins of reconstructed transverse momentum ranging from $p_T^H \leq 60$ GeV, $60 < p_T^H \leq 120$ GeV, $120 < p_T^H \leq 200$ GeV, $200 < p_T^H \leq 300$ GeV, $300 < p_T^H \leq 450$ GeV, and $p_T^H > 450$ GeV. The Higgs boson rapidity is required to be $|y^H| \leq 2.5$. An additional bin for $|y^H| > 2.5$ is added, inclusive in p_T^H . However, the expected contribution is negligible.

The reconstruction of the transverse momentum of the Higgs boson is done with a graph neural network (GNN) [258] using events entering the signal regions of the

$3\ell+0\tau_{\text{had}}$ and $2\ell\text{SS}+0\tau_{\text{had}}$ channels. Each event is represented as a graph with nodes representing final state particles or global features. Nodes are connected by edges, providing kinematic information. The following features are used to predict Higgs boson p_T STXS bins:

- Nodes: p_T, η, ϕ , charge, b -tagging score, or particle type like lepton, jet, or E_T^{miss} ,
- Edges: $\Delta R, \Delta\eta, \Delta\phi$, and invariant masses between object pairs,
- Global: number of central and forward jets, number of pile-up μ , the scalar sum of transverse momenta of jets, leptons, and all visible objects, all lepton p_T , mass M , p_T sum of all lepton pairs or leptons with E_T^{miss} , together with $\Delta\phi$ and $\Delta\eta$ of all two lepton combinations.

The graphs are fully connected and target the STXS bins. The performance during the training is evaluated with truth information obtained from MC simulations. The best performance is observed for the high STXS bin regime with $p_T^H > 300$ GeV and with $t\bar{t}H$ events targeting the $H \rightarrow WW^*$ decay mode. Considerable misclassification occurs within the lower regimes with $p_T^H \leq 200$ GeV.

In the $2\tau_{\text{had}}$ channels, a BDT approach is used to reconstruct the transverse momentum of the Higgs boson. As input features, it uses the di- τ_{had} visible transverse momentum, the distance between the di- τ_{had} system and its invariant mass. The best reconstruction performance is observed for the $2\tau_{\text{had}}$ channels with events targeting the $H \rightarrow \tau\tau$ decay mode in the lower STXS bin regime with $p_T^H \leq 200$ GeV.

Due to limited statistics, no attempt for the reconstruction is made for the 4ℓ and $2\ell\text{SS}+1\tau_{\text{had}}$ channels. They are included in the fit, but a minor sensitivity is expected. The first and second STXS bins are merged. Furthermore, the last three bins are also combined to create a single template.

CHAPTER 7

Fake Background Estimation for the $t\bar{t}H$ Multi-Lepton Analysis

Can you tell me what a fake lepton is?

The author's question to students during every top quark meeting.

Most analyses performed by the ATLAS collaboration use the presence of leptons in the final state. The main advantages are better trigger performance and the suppression of QCD multijet background. Furthermore, leptons have higher resolutions and more minor uncertainties associated with the reconstruction than jets. In leptonic final states, another type of background than QCD inferred processes becomes dominant. It originates from the misidentification of lepton properties, misreconstruction of other physics objects as leptons, or from leptons not associated with the primary collision. These leptons are often called charge misidentified, fake, or non-prompt, respectively. These background contributions depend strongly on the lepton definition and selected analysis region. In contrast, an adequately reconstructed lepton associated with the hard scattering process is called *prompt*¹. They are associated with the hard or primary scattering vertex due to the short lifetime of electroweak or Higgs bosons. Furthermore, they inherit natural isolation since the decaying boson recoils against the remaining system².

In Figure 7.1, a sketch of various sources of charge misidentified, fake, and non-prompt leptons is presented. Charge misidentification occurs for electrons with large

¹Leptons from leptonic τ decays are also considered as prompt.

²With more considerable hadronic activity, the isolation of prompt leptons tends to decrease. However, it is still more significant compared to non-prompt ones.

transverse momentum and, therefore, with a small track curvature. This can lead to ambiguities during the track fitting. It can result in mismeasured curvatures and an incorrectly reconstructed electron charge. Bremsstrahlung causes the second source, with the produced photon creating an electron-positron pair. The positron may be reconstructed, assigning an incorrect charge. This background is most dominant in regions with same-sign lepton pairs. The charge misidentification is negligible for muons since they are minimal ionising particles and rarely undergo Bremsstrahlung. Furthermore, the muon spectrometer measures additional tracks of muons, reducing the probability of charge misidentification.

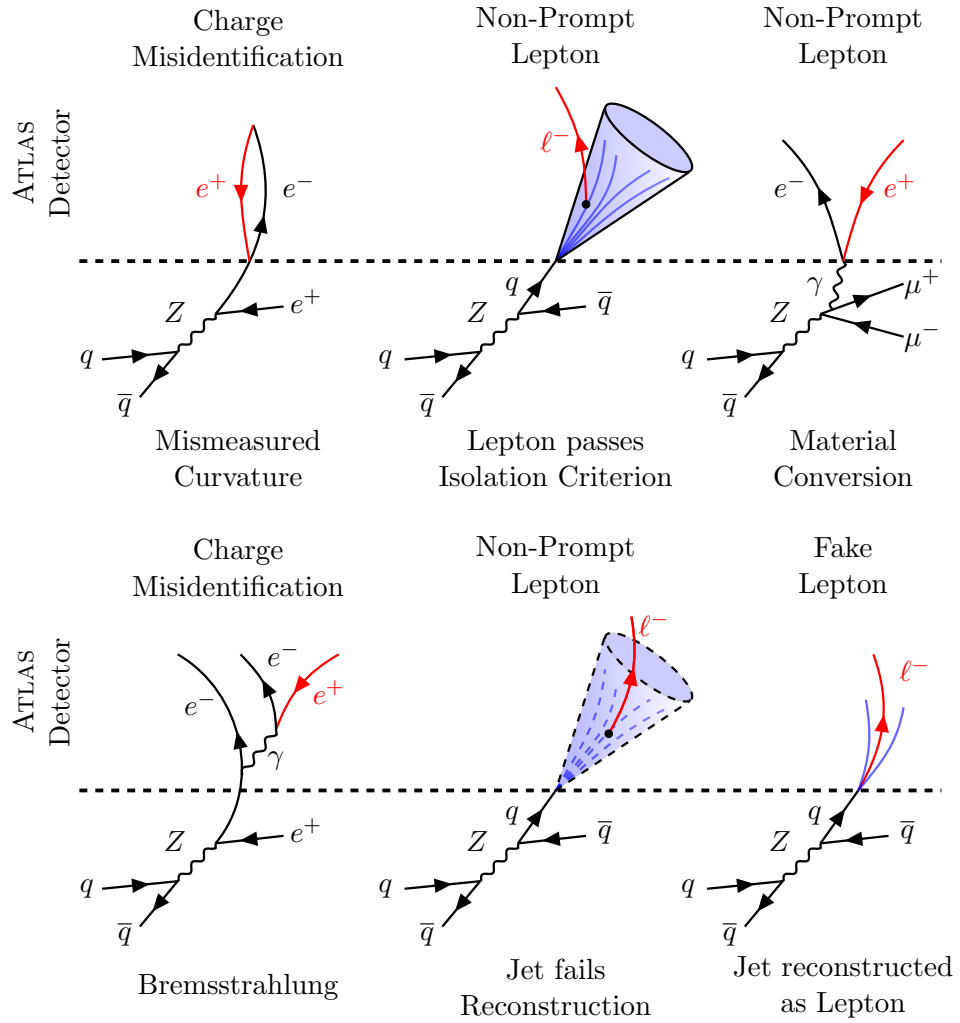


Figure 7.1: A sketch of various sources of charge misidentification, fake leptons, and non-prompt leptons. The charge misidentified, fake, and non-prompt lepton is marked in red.

Non-prompt leptons are *real* leptons that do not originate from the primary collision. They are decay products of hadrons embedded in jets. The hadrons and decay products are often boosted in one direction. Therefore, isolation requirements are an effective tool to suppress this background. However, leptons from (semi-)leptonic hadron decays may pass the isolation criterion as shown in Figure 7.1. They may also pass if the jet candidate is improperly reconstructed or fails a selection criterion. Non-prompt leptons are categorised by the flavour of the hadron. They are called heavy-flavour non-prompt if they originate from c -hadron or b -hadron decays. If they originate from light-flavour hadrons, like pions or kaons, they are called light-flavour. Another source of non-prompt electrons originates from the conversion of highly energetic photons $\gamma \rightarrow e^+e^-$ with the subsequent reconstruction of an electron or positron. The conversion often happens inside the active material of the detector, granting them the name of *material conversions*. For muons, this source is negligible. Other sources are Dalitz decays of pions, like $\pi^0 \rightarrow e^+e^-\gamma$. Their detection is difficult since the decay process leaves tracks in the ID and energy deposits in the ECAL but only little activity in the HCAL.

Fake leptons are misidentifications or reconstructions of other physics objects as leptons. Light quark jets or gluon jets can be misidentified as electrons as they leave tracks in the inner detector and energy deposits in the electromagnetic calorimeter system as depicted in Figure 7.1. Muons are reconstructed using additional information from the MS. Particle leakage to the MS can occur due to highly energetic hadronic showers escaping the HCAL. This phenomenon is called *punch-through* and can lead to misidentification of muons.

The simulation of charge misidentified, fake, and non-prompt leptons is not reliable. The rate depends on the definition of the physics object and the selected analysis regions. In the case of conversion, misidentification, and leptons from hadron decays, the simulation requires precise modelling of the detector response, which is challenging³. Due to the generally low rates in some phase space, generating events containing only misidentified, fake, and non-prompt leptons would consume many computer resources. The simulation relies on MC generators and detector simulations like GEANT4, with the latter being the most expensive part.

The rate of charge misidentified electrons is estimated in $Z \rightarrow ee$ events, comparing opposite sign and same sign lepton pair requirements. Fake and non-prompt lepton backgrounds⁴ are estimated by (semi-) data-driven techniques such as the template method and the fake factor method [259]. The template method is used in the 4ℓ , 3ℓ ,

³The detector simulation is the most expensive part of the simulation chain. *Non-prompt* leptons are created before entering the detector material. However, the detector response is crucial to decide whether the lepton is isolated or the jet in which the lepton is embedded fails jet identification.

⁴In the following, the term *fake* will be used as a synonym for both fakes and non-prompt leptons even if the former does not involve real leptons, while the latter does. Using the term fake for both emphasises the fact that they are not **prompt** leptons.

$2\ell\text{SS}+0\tau_{\text{had}}$, $2\ell\text{SS}+1\tau_{\text{had}}$ channels. The shapes of kinematic variables are obtained from MC simulation while adjusting the normalisation or fake rates from data with control regions enriched with target fake lepton backgrounds. It is a semi-data-driven technique since it partially relies on MC simulation. In the $2\ell\text{SS}+1\tau_{\text{had}}$ channel, the method is extended for estimating τ_{had} fake rates. The fake background templates are estimated by simultaneous fit with free-floating fake norm factors in all regions. This corrects the template normalisation to data and propagates the correction to other regions. This method requires good shape agreement between data and the fake template. In particular, characteristic kinematic variables, like the transverse momentum of fakes, are required to be compatible between the control and signal regions.

The fake factor method is used in the $1\ell+2\tau_{\text{had}}$ and $2\ell\text{OS}+2\tau_{\text{had}}$ to estimate τ_{had} fakes. This method relies on two lepton or τ_{had} definitions, with a looser and tighter one. The relation between the definitions is used to estimate a fake factor, extrapolating from the CRs to the SR. Fake factors are often calculated in bins of transverse momentum and corrected for shape and normalisation.

Section 7.1 presents the estimation of the fake background for the 4ℓ channel. It provides an overview of the various sources of fakes and the designed control regions. The estimation of the fake background for the 3ℓ and $2\ell\text{SS}+0\tau_{\text{had}}$ channels is shown in Section 7.2, followed by a brief overview for the $2\ell\text{SS}+1\tau_{\text{had}}$ channel in Section 7.3. For the $2\ell\text{OS}+2\tau_{\text{had}}$ and $1\ell+2\tau_{\text{had}}$ channels, the fake background estimation is presented in Section 7.4.

7.1 Fake Background Estimation in the 4ℓ Channel

In the SR, the most dominant contribution originates from events having two additional fake leptons, as shown on the left side of Figure 7.2. The double fake background can be decomposed into single fake lepton contributions. The decomposition is justified since the individual fake rates are uncorrelated. The SR's most significant fraction of double fakes originates from $t\bar{t}$ production as shown in Figure 7.2. A notable contribution enters due to the large $t\bar{t}$ production cross-section in association with extra jets. The single fake background originates primarily from WZ , tWZ , and $t\bar{t}t\bar{t}$ production⁵. The triple fake background is negligible in the signal-sensitive bins and is estimated from MC simulations due to an unreliable classification based on samples simulated with SHERPA.

The dominant fake background contributions in the 4ℓ channel originate from heavy-flavour electron fakes e^{HF} and heavy-flavour muon fakes μ^{HF} . They are created in semi-leptonic c -hadron and b -hadron decays. Additionally, the background from

⁵The contribution from $t\bar{t}$ production in the single fake category originates from misclassification of fake leptons as prompt ones.

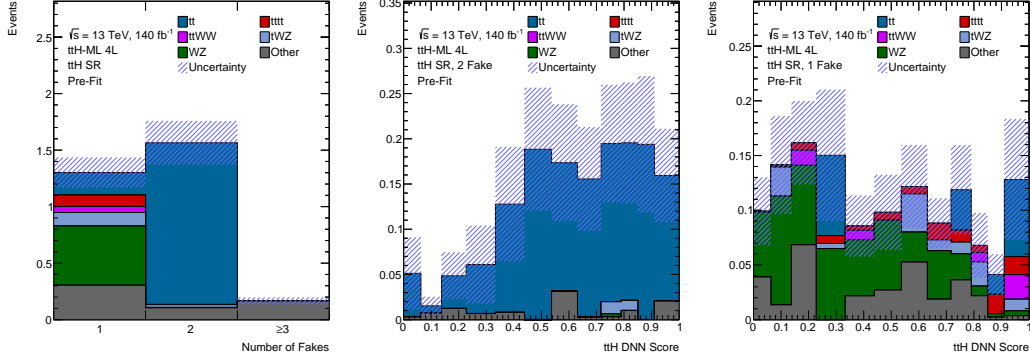


Figure 7.2: On the left side, the fake lepton multiplicity for events entering the 4ℓ SR is shown. In the middle, the $\text{DNN}_{t\bar{t}H}$ response in the SR for double fake events per process is shown, while on the right side, the response for single fake lepton events is shown.

light-flavour electron fakes e^{LF} enters the signal-sensitive regions of the 4ℓ channel. These e^{LF} fakes are created predominately in decays of light-flavour hadrons such as kaons and pions. The classification of leptons into the fake categories is based on information obtained from MC simulation⁶. Contributions of other sources of fakes are small and are combined into the Other-Fake background. It contains contributions from charge misidentification, conversions, muon fakes from light-flavour hadrons, and leptons, which cannot be classified based on information from MC simulation⁷. The Other-Fake background is solely estimated from MC simulations. The fake lepton combinations of double fakes in the SR are shown in Figure 7.3, with fakes ordered in transverse momentum. The most significant contributions are double e^{LF} fakes and combinations of heavy-flavour fakes and e^{LF} fakes from $t\bar{t}$ production.

7.1.1 Fake Control Region Definition for the 4ℓ Channel

Three regions are defined for the normalisation estimation of the dominant fake background sources for the 4ℓ channel. Table 7.1 summarises an overview of selection criteria. All three fake regions require the same lepton definition used in the 4ℓ regions. Furthermore, the regions are designed to be orthogonal to any other analysis region. Therefore, a veto on the $3\ell+0\tau_{\text{had}}$ channel preselection is applied. The criterion of no SFOS lepton pairs reduces contributions from WZ and Z +jets production, defining a region almost purely populated with $t\bar{t}$ events. The heavy-flavour CRs, $\text{CR}_{e^{\text{HF}}}$ and $\text{CR}_{\mu^{\text{HF}}}$, are defined by the lepton flavour combination $\mu^{\mp}e^{\pm}e^{\pm}$ and $e^{\mp}\mu^{\pm}\mu^{\pm}$, respectively. The same-sign lepton with the lower transverse momentum is expected to be the fake lepton. Both heavy-flavour fake regions apply the same jet

⁶This is often called *truth* information.

⁷This contribution is tiny compared to the other background contributions.

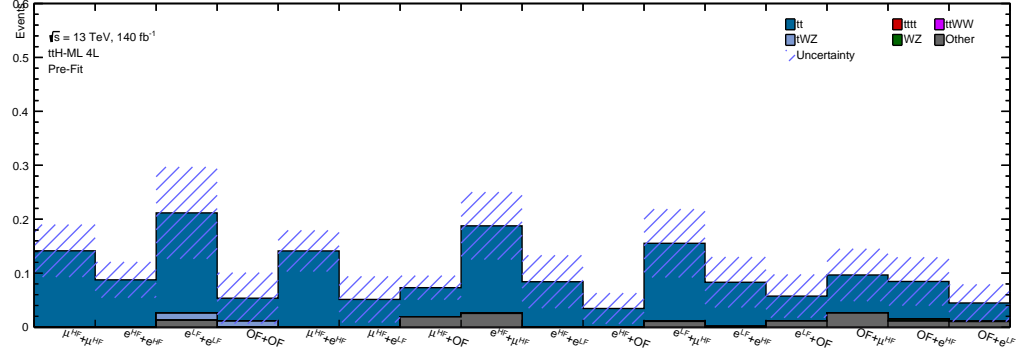


Figure 7.3: An overview of the various double fake contributions entering the SR is shown. The fake contributions are p_T ordered, and OF denotes the Other-Fake category, including conversion fakes, fakes from light muon decays, or fakes originating from τ_{had} decays. Only statistical uncertainties are shown.

Region	$CR_{\mu^{\text{HF}}}$	$CR_{e^{\text{HF}}}$	$CR_{e^{\text{LF}}}$
Lepton definition		LLL	
p_T requirement		$> 10 \text{ GeV}$	
Lepton charges		$\sum_i q_i = \pm 1$	
Lepton details	no SFOS pairs		$ m(\mu^+\mu^-) - m_Z < 10 \text{ GeV}$
Lepton flavours	$e^\mp \mu^\pm \mu^\pm$	$\mu^\mp e^\pm e^\pm$	$ m(3\ell) - m_Z > 15 \text{ GeV}$
Central jets		≥ 2	
b -jets 85 % DL1r	≥ 1		$= 0$
Additional requirements	-	veto $3\ell+0\tau_{\text{had}}$ preselection	$E_T^{\text{miss}} < 20 \text{ GeV}$

Table 7.1: Summary of the fake CR selections for the 4ℓ channel. The lepton definitions are given in Table 5.4.

requirements as the 4ℓ channel: at least two central jets and at least one b -jet passing the loosest DL1r working point of 85 %. To estimate the normalisation of e^{LF} fakes, a region enriched with Z +jets events is designed. It requires a muon pair with an invariant mass close to the Z boson mass. The reconstructed electron is the fake lepton candidate. To reduce prompt contributions from diboson WZ production, a cut on E_T^{miss} is applied. To further reduce contamination from $V\gamma$ production with subsequent photon conversion, a veto on the three-lepton invariant mass close to the Z boson mass is applied. It reduces final-state photon radiation contribution. Conversion fakes from $V\gamma$ are estimated solely from MC simulation due to an unreliable fake classification using information from samples simulated by SHERPA. A large systematic uncertainty is applied to cover potential mismodelling. Similar jet requirements are applied for the $CR_{e^{\text{LF}}}$ with at least two central jets. However, it is required that no b -jet passes the loosest working point; it reduces the contamination

from e^{HF} fakes.

The expected yield for all three fake CRs is presented in Table 7.2, and the expected contributions from various production processes are shown in Table 7.3. In Figure 7.4, Figure 7.5, and Figure 7.6 different kinematic variables are presented for the fake regions $\text{CR}_{\mu^{\text{HF}}}$, $\text{CR}_{e^{\text{HF}}}$, and $\text{CR}_{e^{\text{LF}}}$, respectively. The transverse momentum and pseudorapidity of the leptons, the scalar sum of transverse momenta for jets and leptons, and the jet multiplicity are shown. In Appendix D, the post-fit distributions are presented. The e^{HF} fake contribution is reweighted with respect to data due to an observed shape mismodelling of the transverse momentum of the fake lepton candidate⁸. All previously mentioned distributions in the $\text{CR}_{\mu^{\text{HF}}}$ and $\text{CR}_{e^{\text{LF}}}$ demonstrate a satisfactory shape agreement between MC simulation and data. After applying the reweighting procedure a satisfactory shape agreement between MC simulation and data is also observed for the $\text{CR}_{e^{\text{HF}}}$.

The $\text{CR}_{e^{\text{LF}}}$ uses for a better separation of the e^{LF} and e^{HF} fake contributions $E_{\text{T}}^{\text{miss}}$ as a discriminant. Due to different decay chains of heavy-flavour hadrons, decaying via $b \rightarrow \ell\nu + X$ or $b \rightarrow c + Y \rightarrow \ell\nu + X$, $E_{\text{T}}^{\text{miss}}$ tends to have a harder spectrum. The heavy-flavour fake CRs use the fake lepton candidate transverse momentum as fitted distribution since the fake rate is expected to depend on the transverse momentum. The fake CR distributions are shown with pre-fit uncertainties in Figure 7.7.

Process	$\text{CR}_{e^{\text{HF}}}$	$\text{CR}_{\mu^{\text{HF}}}$	$\text{CR}_{e^{\text{LF}}}$
$t\bar{t}H$	24.6 ± 2.66	20.7 ± 2.22	0.03 ± 0.02
$t\bar{t}Z$	32.7 ± 0.97	24.2 ± 0.11	1.79 ± 0.21
$ZZ + \geq 1b$	1.21 ± 0.01	0.72 ± 0.03	2.36 ± 0.39
$ZZ + \geq 1c$	1.23 ± 0.01	0.58 ± 0.11	14.84 ± 0.70
$ZZ + \text{light}$	1.70 ± 0.24	0.45 ± 0.07	341.3 ± 25.5
tWZ	1.89 ± 0.95	1.01 ± 0.51	0.80 ± 0.47
WZ	9.90 ± 1.98	3.49 ± 0.70	470.7 ± 99.6
$V\gamma$	0.0 ± 0.0	0.0 ± 0.0	286.6 ± 13.0
Other Prompt	120 ± 22	38.9 ± 15.3	11.89 ± 3.25
μ^{HF} Fake	0.54 ± 0.09	1124 ± 48	0.07 ± 0.05
e^{HF} Fake	726 ± 32	0.01 ± 0.01	400.6 ± 27.9
e^{LF} Fake	184 ± 2	0.09 ± 0.01	1055 ± 106
Other Fake	158 ± 79	72.4 ± 36.2	83.7 ± 72.9
Total MC	1265 ± 89	1287 ± 62	2660 ± 231
data	1208	1167	2993

Table 7.2: The expected yields for the fake regions $\text{CR}_{e^{\text{HF}}}$, $\text{CR}_{\mu^{\text{HF}}}$, and $\text{CR}_{e^{\text{LF}}}$. Pre-fit uncertainties are shown.

⁸An additional systematic uncertainty is applied as described in Section 8.2

Process	$CR_{e^{HF}}$	$CR_{\mu^{HF}}$	$CR_{e^{LF}}$
$t\bar{t}H$	24.6 ± 2.66	20.7 ± 2.22	0.03 ± 0.02
$t\bar{t}Z$	32.7 ± 0.97	24.2 ± 0.11	1.79 ± 0.21
$ZZ + \geq 1b$	1.21 ± 0.01	0.72 ± 0.03	2.36 ± 0.39
$ZZ + \geq 1c$	1.23 ± 0.01	0.58 ± 0.11	14.84 ± 0.70
$ZZ + \text{light}$	1.70 ± 0.24	0.45 ± 0.07	341.3 ± 25.5
tWZ	1.89 ± 0.95	1.01 ± 0.51	0.80 ± 0.47
WZ	9.90 ± 1.98	3.49 ± 0.70	470.7 ± 99.6
$V\gamma$	0.0 ± 0.0	0.0 ± 0.0	286.6 ± 13.0
$V + \text{jets}$	15.5 ± 2.92	9.41 ± 0.08	1547 ± 69
$t\bar{t}$	998 ± 32	1140 ± 48	0.04 ± 0.02
Other	70.5 ± 1.9	55.1 ± 1.2	12.6 ± 3.4

Table 7.3: The expected yield contribution for the fake regions $CR_{e^{HF}}$, $CR_{\mu^{HF}}$, and $CR_{e^{LF}}$ split by process contribution. Pre-fit uncertainties are shown.

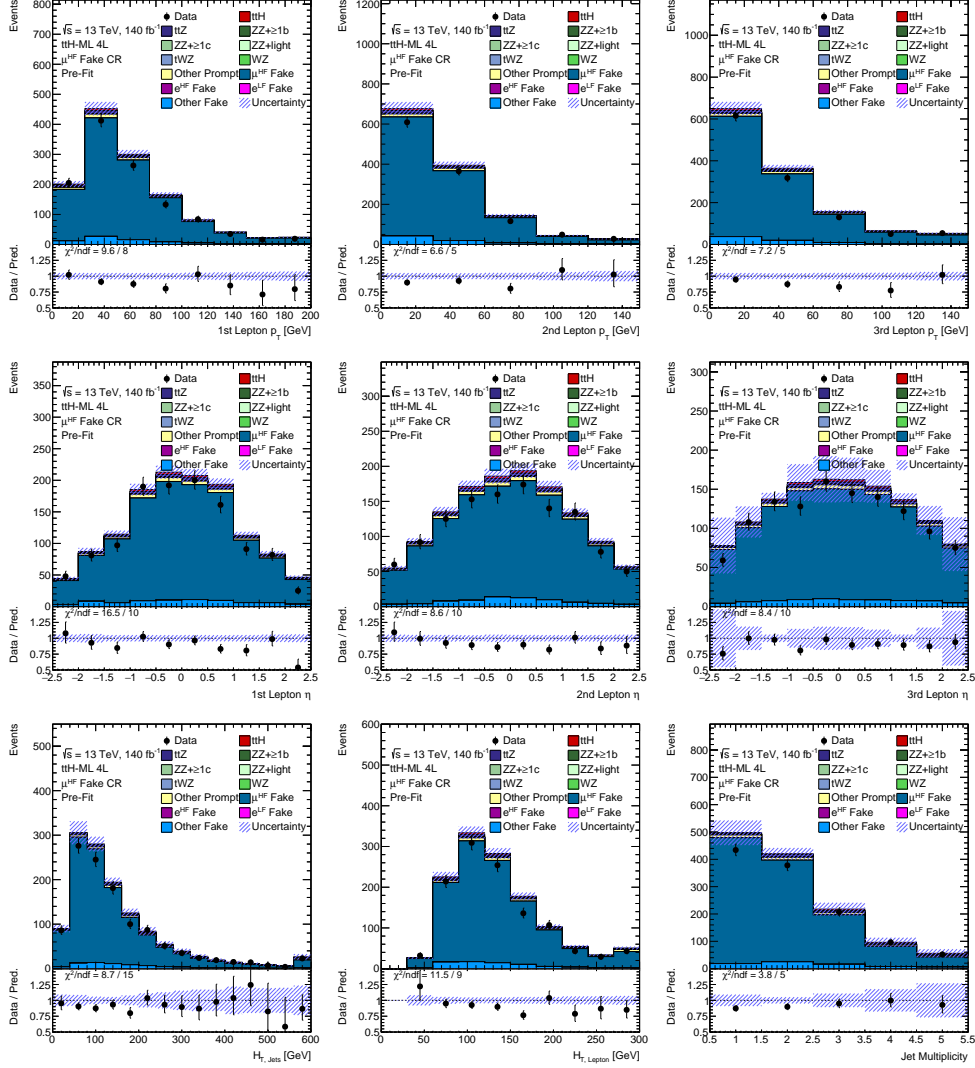


Figure 7.4: A collection of kinematic variable distributions in the $CR_{\mu_{HF}}$. The transverse momentum and pseudorapidity of the leptons are shown. Furthermore, the scalar sum of transverse momenta of jets and leptons and the jet multiplicity are presented. Total pre-fit uncertainties are shown as blue hashed bands.

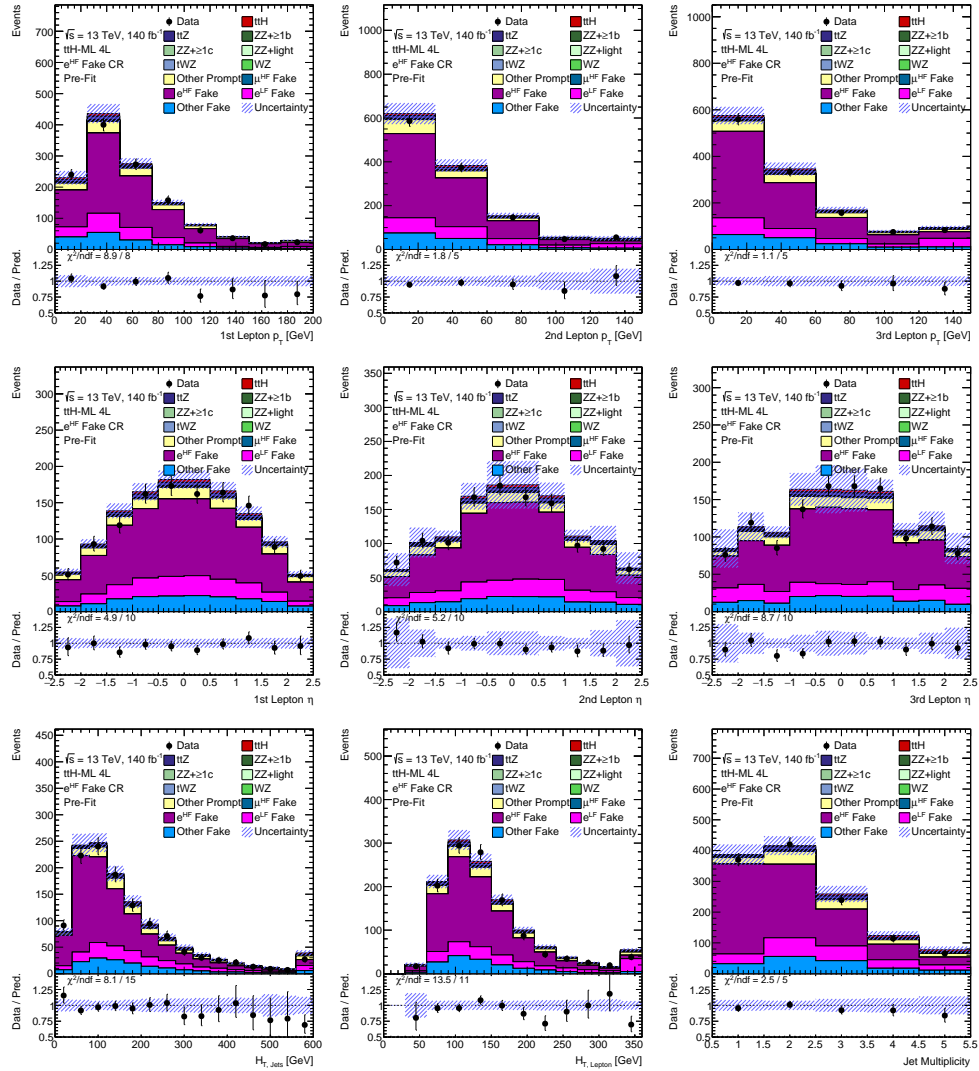


Figure 7.5: A collection of kinematic variable distributions in the CR_{eHF} . The transverse momentum and pseudorapidity of the leptons are shown. Furthermore, the scalar sum of transverse momenta of jets and leptons and the jet multiplicity are presented. Total pre-fit uncertainties are shown as blue hashed bands.

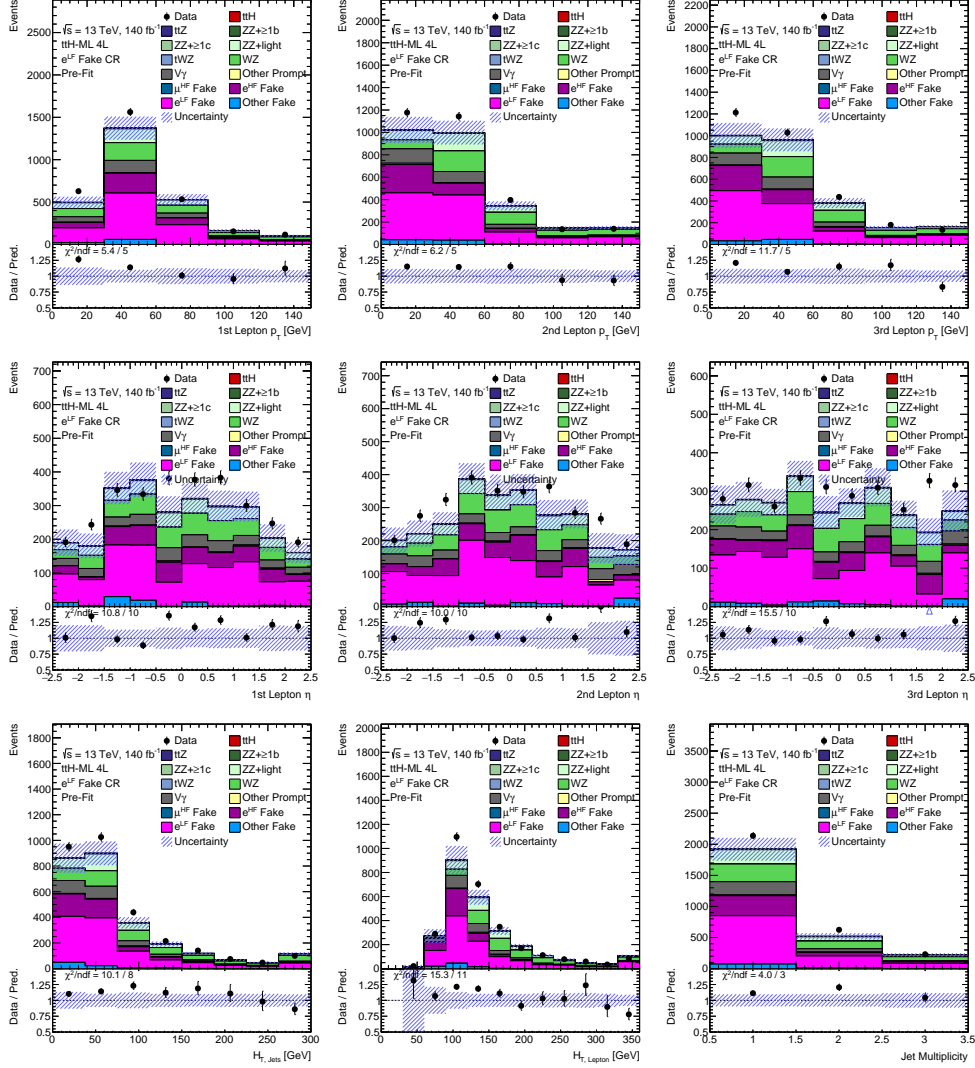


Figure 7.6: A collection of kinematic variable distributions in the $\text{CR}_{e\text{LF}}$. The transverse momentum and pseudorapidity of the leptons are shown. Furthermore, the scalar sum of transverse momenta of jets and leptons and the jet multiplicity are presented. Total pre-fit uncertainties are shown as blue hashed bands.

of Figure 7.8. Light-flavour fakes in the $\text{CR}_{e^{\text{LF}}}$ mostly originate from light-flavour jets. This source is compatible with the SR. Additional modelling uncertainties to processes creating fakes are applied to cover the differences in fake sources. Uncertainties associated with the modelling of $t\bar{t}$ events with additional b -jets are covered by comparing $t\bar{t} + \geq 1b$ events generated in the five-flavour scheme with events generated in the four-flavour scheme [182, 183]. Systematic uncertainties on the initial- and final-state QCD radiation are also included.

In Figure 7.10, the shapes of the transverse momentum of fakes from the CRs are compared with ones from the signal-sensitive bins of the SR. Only statistical uncertainties are shown. The observed shapes are compatible between the SR and CRs. Fake normalisations are estimated in their respective CR and applied to the SR during a simultaneous fit. Double fake contributions are normalised with the product of measured normalisations, depending on the fake lepton flavour combination.

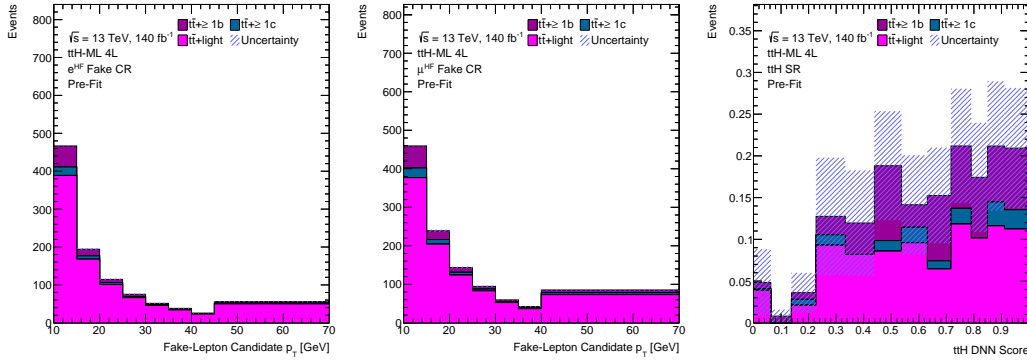


Figure 7.9: A comparison of $t\bar{t}$ events with additional b -jets, c -jets, or light jets for the heavy-flavour CR and the SR. Only statistical uncertainties are shown.

7.1.3 Fake Background Normalisation Factors

The fake normalisation factors are free-floating parameters measured in a simultaneous fit. The normalisation factors are determined with a fit to ATLAS data⁹. The normalisation factors for the dominant fake backgrounds are:

$$\begin{aligned}\mathcal{N}(e^{\text{HF}}) &= 0.95^{+0.14}_{-0.14}, \\ \mathcal{N}(\mu^{\text{HF}}) &= 0.92^{+0.06}_{-0.06}, \\ \mathcal{N}(e^{\text{LF}}) &= 1.14^{+0.22}_{-0.22}.\end{aligned}$$

All three normalisation factors are compatible with unity.

⁹A complete description of the fit procedure is found in Chapter 9.

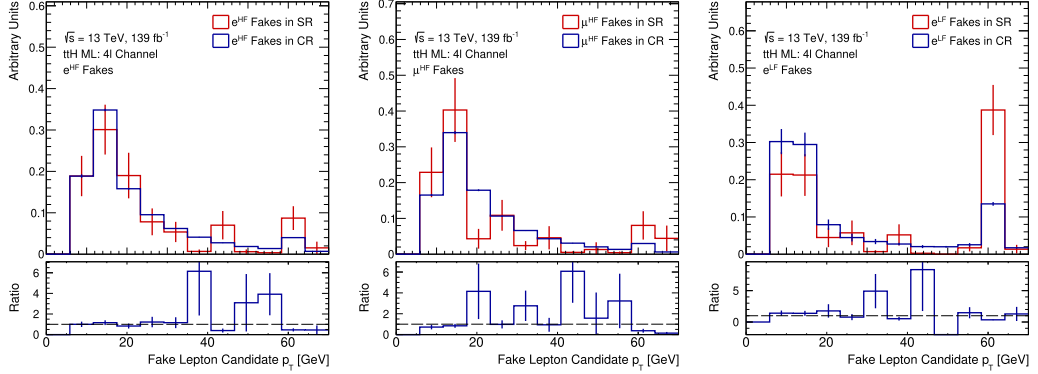


Figure 7.10: Shape comparison of the fake lepton candidate's transverse momentum of the corresponding CRs. They are compared to fakes from the five signal-sensitive bins of the SR. Double fake events are accounted for both fake contributions.

7.2 Fake Background Estimation in the $2\ell\text{SS}+0\tau_{\text{had}}$ and $3\ell+0\tau_{\text{had}}$ Channels

The fake estimation in the $2\ell\text{SS}+0\tau_{\text{had}}$ and $3\ell+0\tau_{\text{had}}$ channels uses a semi-data-driven estimation approach similar to the 4ℓ channel. Different fake backgrounds arising from other sources, like conversions, are essential. Furthermore, heavy-flavour fakes from the $2\ell\text{SS}+0\tau_{\text{had}}$ and $3\ell+0\tau_{\text{had}}$ channels are incompatible with ones from the 4ℓ channel since different lepton definitions are used. Two control regions are selected to estimate the normalisation of fake backgrounds from material and internal conversions. There are six additional regions for the background estimation of

Control Region	Conversion		Heavy-Flavour Fakes
N_{jets}	≥ 0		≥ 2
$N_{b\text{-jets}@85\%}$	0		1
Lepton Definition	L,M,M		$\text{TM}_{ex}, \text{M}_{ex}\text{T}, \text{M}_{ex}\text{M}_{ex}$
Lepton Flavours	$\mu\mu e^*$		$2\ell\text{SS}$
p_T requirement [GeV]	10,15,15		15,15
Lepton Requirement	$ m_{\ell\ell}^{\text{SFOS}} - m_Z > 10 \text{ GeV}$ $ m_{\ell\ell} - m_Z < 10 \text{ GeV}$		$m_T(\ell_0, E_T^{\text{miss}}) < 250 \text{ GeV}$ for TM_{ex} and M_{ex}T
τ_{had} candidates (M)	0		0
Region Split	Int-Con	Mat-Con	$e/\mu \times \text{TM}_{ex}, \text{M}_{ex}\text{T}, \text{M}_{ex}\text{M}_{ex}$
Region Name	$3\ell\text{Int}C$	$3\ell\text{Mat}C$	$2\ell\text{tt}(e)_{\text{TM}_{ex}}, 2\ell\text{tt}(e)_{\text{M}_{ex}\text{T}}, 2\ell\text{tt}(e)_{\text{M}_{ex}\text{M}_{ex}}$ $2\ell\text{tt}(\mu)_{\text{TM}_{ex}}, 2\ell\text{tt}(\mu)_{\text{M}_{ex}\text{T}}, 2\ell\text{tt}(\mu)_{\text{M}_{ex}\text{M}_{ex}}$

Table 7.4: Summary of the fake CRs for the $2\ell\text{SS}+0\tau_{\text{had}}$ and $3\ell+0\tau_{\text{had}}$ channel. The lepton definitions are summarised in Table 5.4. The label e^* denotes the internal conversion (Int-Con) candidate and material conversion (Mat-Con) candidate, as defined in Section 5.2.4.

heavy-flavour fakes, populated with $t\bar{t}$ events. The regions are split by the flavour of the fake lepton and the definition of leading and sub-leading lepton. Table 7.4 shows an overview of the selection criteria defining the CRs. The normalisation factors are estimated in a simultaneous fit with signal extraction.

7.3 Fake Background Estimation in the $2\ell\text{SS}+1\tau_{\text{had}}$ Channel

In the $2\ell\text{SS}+1\tau_{\text{had}}$ channel, the dominant fake background is a mixture of e^{HF} and μ^{HF} fakes from $t\bar{t}$ and diboson production and τ_{had} fakes. The primary sources of the latter are misreconstructed gluon and quark jets. A non-negligible contribution of events with double fakes enters the signal region. The fake background estimation uses the same strategy as the 4ℓ channel. Normalisation factors are measured in data and applied to the signal regions. A product of normalisation factors is applied if an event contains multiple fakes. Control regions where the normalisation factors are measured are defined similarly to the signal region of the $2\ell\text{SS}+1\tau_{\text{had}}$ channel. However, they use a looser requirement of exactly two or three central jets. There are four control regions that target expected background contributions from light lepton fakes. They require two same-sign leptons and are defined by the lepton flavour combinations. An additional control region is designed to target τ_{had} fakes. It uses the same selections as the other fake regions but requires an opposite-sign lepton pair with both leptons passing the *medium* lepton definition, as discussed in Section 5.2.4. The normalisation factors of the fake backgrounds are estimated in a simultaneous fit with the signal extraction.

7.4 Fake Background Estimation in the $2\ell\text{OS}+2\tau_{\text{had}}$ and $1\ell+2\tau_{\text{had}}$ Channels

For both $2\tau_{\text{had}}$ channels, the dominant fake background arises from double and single τ_{had} fakes from $t\bar{t}$ production. The dominant source is light quark jets. Minor sources originate from gluon-initiated jets, heavy-flavour jets, and misidentified light leptons. For the fake τ_{had} estimation, the fake factor method [259] is used. It uses the extrapolation from a τ_{had} fake enriched CR to the SR using fake factors. The CR has the same definition as the SR with the difference that only τ_{had} candidates are selected failing the RNN *medium* working point but passing the *very loose* one. The fake factor $f_{\tau_{\text{had}}}$ is defined as the ratio of τ_{had} candidates entering the SR over those entering the CR. The regions are further split by different jet and b -jet requirements, targeting different fake sources initiated by $t\bar{t}$ and Z + jets production, respectively. A summary of selection requirements is found in Table 7.5. The fake factors are measured with respect to data in the CRs and applied to the SR for correcting the rate of τ_{had} candidates. They are split in bins of p_{T} and η for both 1- and 3-prong

τ_{had} candidates, respectively.

Selections	$Z + \text{jets}$ CR	$t\bar{t}$ CR
Trigger Selection	Single- and Dilepton Triggers	
Lepton Flavours	2ℓ SS	
Lepton Definition	L,L	
p_T requirement [GeV]	10,10	
Lepton requirement	$ m_{\ell\ell} - m_Z < 10 \text{ GeV}$	$ m_{\ell\ell} - m_Z > 10 \text{ GeV}$
Numerator Fake Scale	one τ_{had} passing RNN <i>medium</i>	
Denominator Fake Scale	one τ_{had} failing RNN <i>medium</i>	
N_{jets}	≥ 0	≥ 1
$N_{b\text{-jets}}$	0	≥ 1

Table 7.5: The CR selection for the fake estimation for the $2\tau_{\text{had}}$ channels. The numerator and denominator are used to define the fake factors.

CHAPTER 8

Systematic Uncertainties

There are various sources of uncertainties considered in the $t\bar{t}H$ multi-lepton analysis. Statistical uncertainties arise from the probabilistic nature of the measurement and are limited by the number of expected or observed events. Furthermore, systematic uncertainties always influence measurement, classified into *experimental* and *modelling*. The modelling uncertainties include *theory* ones, providing uncertainties on background cross-sections.

The experimental uncertainties are associated with the experimental setup, mainly the ATLAS detector with inefficiencies in detection, identification, reconstruction, and calibration of analysis-related physics objects, but also uncertainties on the integrated luminosity.

The modelling ones are related to the MC simulations and their modelling of kinematics, affecting normalisation and shape. The MC simulation is a chain of multiple steps from matrix element generation, parton showering, and hadronisation to detector simulation, described in Chapter 3. Every step requires a choice of used parameters or model assumptions such as choice of renormalisation and factorisation scales or generator-specific parameters like h_{damp} for POWHEG or the merging scale for SHERPA. The specific choice defines a nominal configuration, while variation on those parameters is used to evaluate the impact on predictions.

In Section 8.1, uncertainties for the experimental setup are discussed, followed by an overview of modelling and theory uncertainties in Section 8.2 and Section 8.2.1, respectively. The handling of systematic uncertainties is shown in Section 8.3. An overview of all systematics, including other channel-specific ones, is found in Section 8.4.

8.1 Experimental Uncertainties

Luminosity and Pile-Up

The uncertainty on the integrated luminosity for the full Run 2 data set is 0.83% and has an impact on each process considered in the analysis. The luminosity and its uncertainty are measured using van der Meer beam separation scans described in Ref. [260]. The scale factors for pile-up are applied to simulated events matching data, while uncertainties are obtained by varying the scale factors within their uncertainties.

Charged Lepton Uncertainties

Charged lepton-related uncertainties arise from trigger, identification, and reconstruction. For electrons and muons, scale factors for the identification and isolation are derived with the tag-and-probe method using resonance cases like $Z \rightarrow \ell\ell$ and $J/\psi \rightarrow \ell\ell$ events. The scale factors account for differences between MC simulations and data and are measured in statistical independent bins of p_T and η [222, 224, 227]. The energy and momentum calibration for muon is performed using $Z \rightarrow \mu\mu$ and $J/\psi \rightarrow \mu\mu$ events, exploiting knowledge on the mass of the mother particle. A similar procedure is applied to electrons, however, using $Z \rightarrow ee$ and $J/\psi \rightarrow ee$ events. The measurements are influenced by many systematic uncertainties, which are reduced to create a simplified uncertainty model for the derived lepton scale factors. A summary of the applied systematic uncertainties is found in Table 8.1.

Jet Uncertainties

As described in Section 5.2.5, the calibration of jets is performed in multiple steps. Uncertainties arise from the jet energy scale (JES) and jet resolution scale (JER) calibration and JVT requirements. The calibration of JES is derived from test-beam data, collision data, and MC simulations, while JER is tested in dijets events using the balance method [232, 261, 262]. The measurement involves multiple sources of systematic uncertainties and is reduced by eigenvector decomposition to 31 systematic components for JES and 13 for JER, respectively. The efficiencies for the jet vertex tagger are tested in $Z \rightarrow \mu\mu + \text{jets}$ events. Using the tag-and-probe method to derive scale factors and uncertainties to account for differences between MC simulation and data. An overview of the applied systematic uncertainties is found in Table 8.1.

Flavour Tagging Uncertainties

Tagging of b -jets plays an important role in every analysis featuring top quarks. The efficiency of the b -tagging algorithm is measured in control regions with respect to data targeting specific flavours [263, 264]. Correction factors for b -jets and their uncertainties are derived using dileptonic $t\bar{t}$ events, while c -jet correction factors use jets originating from W boson decays in $t\bar{t}$ events [265]. For light flavour jets,

dijet events are used [266]. The uncertainties in the tagging of b -, c -, and light-flavour jets are evaluated as a function of p_T , including a bin-to-bin correlation. The various sources of systematic uncertainties arise from modelling differences in MC simulation or experimental ones. The latter is reduced by eigenvector decomposition into a smaller set of uncorrelated systematic uncertainties. Additional systematics for the high p_T regime of jets are included. An overview of the applied systematic uncertainties is found in Table 8.1.

Missing Transverse Energy Uncertainties

The missing transverse energy E_T^{miss} is defined as the negative sum of all hard objects and soft signal [241]. The hard object corresponds to reconstructed analysis objects, with their uncertainties propagated to the uncertainty of the hard term of E_T^{miss} . The soft term includes tracks not matched to the primary vertex nor associated with any physics object. In events with no genuine E_T^{miss} contribution, like $Z \rightarrow \mu\mu$ events, the hard and soft terms are expected to be perfectly balanced [267]. However, detector resolutions and other inefficiencies spoil this balance, allowing the test of three quantities of the soft term. All three are different projections with respect to the hard term of E_T^{miss} : (parallel) scale, parallel resolution, and transverse resolution. The systematic uncertainties for the three quantities are the maximal disagreement obtained from data with respect to MC simulations for a set of p_T^{hard} bins. Modelling uncertainties on the MC simulations are also considered.

8.2 Modelling Uncertainties

For the $t\bar{t}H$ multi-lepton analysis, multiple uncertainties regarding the modelling of the signal process and important background processes are considered. The uncertainties range from variations on the used PDF set to variations of generator-specific settings and tunes. Other sources include the choice of matrix-element generator, parton shower, and hadronisation models. Uncertainties are always evaluated with respect to a nominal configuration, described in Section 3.4.

The $t\bar{t}H$ Signal Process

Uncertainties on the choice of μ_R and μ_F and its impact are evaluated by varying both scales independently by a factor of two up and down with respect to the central value along with ISR α_S variations in the PYTHIA A14 tune. The matching between the matrix-element generator and parton shower is evaluated by comparing the nominal configuration with an alternative setup, varying the p_T^{hard} parameter, described in Ref [160]. The impact of the parton shower and hadronisation model choice is assessed by comparing the nominal sample with an alternative one, using the same POWHEG events interfaced with HERWIG, see Section 3.4.1. Uncertainties related to QCD FSR and ISR are predicted by the parton shower. They are evaluated by varying the α_S^{ISR} according to the tune variations VAR3C UP and VAR3C DOWN with

respect to the nominal configuration predicted by the A14 tune and varying α_S^{FSR} by a factor of two up and down with respect to the central value. The PDF uncertainties are evaluated by the *PDF4LHC* recommendations, reducing the uncertainties down to a small set of independent ones by eigenvector decomposition, as described in Ref. [268]. The Higgs boson decay branching fraction uncertainties are applied, following the recommendation of Ref. [70]. Furthermore, an uncertainty on the theoretical NLO calculation of the $t\bar{t}H$ production cross-section is applied with 9% arising from QCD scale variations and additional 4% from PDF+ α_S variations. Additionally, for the 2τ channels, a variation of the branching ratio for $H \rightarrow \tau\tau$ decays is applied, following the description in Ref. [70].

Background Processes

Systematic uncertainties on the modelling of $t\bar{t}W$, $t\bar{t}Z$, $t\bar{t}$, and diboson processes arise from the choice of μ_R and μ_F . They are evaluated in a similar fashion as for the $t\bar{t}H$ signal process by varying the μ_R and μ_F by a factor of two up and down with respect to the central value. PDF uncertainties on the background process are only applied to $t\bar{t}W$, following the same recommendations as for the $t\bar{t}H$ process. The parameter choice of the matrix-element generator and parton shower algorithm for $t\bar{t}W$ is compared to an alternative sample generated with MADGRAPH5_aMC@NLO and showered with PYTHIA 8 FxFx [173]. An additional systematic uncertainty on the parton shower model is applied, comparing POWHEG+PYTHIA 8 and POWHEG+HERWIG 7 and evaluating the difference with respect to the nominal prediction by SHERPA. For the $t\bar{t}Z$ and $t\bar{t}t\bar{t}$ process, the uncertainties on the parton shower are evaluated by comparing the nominal prediction with an alternative sample. The alternative samples use the same events but evaluate the parton showering and hadronisation with HERWIG 7, see Table 3.1. The modelling of additional jets for $t\bar{t}Z$ production and its uncertainties are derived by α_S^{ISR} variations. Similar to the $t\bar{t}H$ signal process, the tune variations VAR3C UP and VAR3C DOWN of the A14 tune are used.

Systematic uncertainties on $t\bar{t}$ production are used for the 4ℓ channel to cover different sources of fake leptons in the SR and fake CRs. Uncertainties on the ISR and FSR of $t\bar{t}$ and the parton shower are evaluated in a similar fashion as for the $t\bar{t}H$ samples. Uncertainties on the modelling of additional b -jets are accessed by comparing events generated in the four-flavour scheme, evaluated with respect to the corresponding contribution of the nominal $t\bar{t}$ sample, a description of the four-flavour scheme sample is found in Section 3.4.6. Only shape effects of the previously mentioned $t\bar{t}$ uncertainties are considered. The normalisation of the e^{HF} and μ^{HF} backgrounds originating predominantly from $t\bar{t}$ production is estimated during the fit procedure.

All other analysis channels use PLIV requirements to suppress fake contributions. PLIV-related uncertainties are applied to these channels, excluding the 4ℓ one.

8.2.1 Theory Uncertainties

Uncertainties on the predicted theory cross-section of minor backgrounds are applied to cover missing higher-order corrections. An uncertainty of $\pm 30\%$ is applied for the VH and triboson production cross-section. The production cross-section of $t\bar{t}t$ process has a slightly higher uncertainty of $\pm 35\%$. Other processes like tWZ or $t\bar{t}WW$ have $\pm 50\%$ cross-section uncertainty. The tZ production has an uncertainty of 5% on the production cross-section. An asymmetric uncertainty on $t\bar{t}t\bar{t}$ production of $\Delta\sigma = {}^{+70}_{-15}\%$ is applied, with the upper variation covering the central value of the ATLAS measurement [269], and the down variation reflecting the theoretical $t\bar{t}t\bar{t}$ cross-section uncertainty. The HF fraction of $t\bar{t}+\text{jets}$, namely $t\bar{t}+ \geq 1c$ and $t\bar{t}+ \geq 1b$, have an $\pm 50\%$ uncertainty. For the 4ℓ channel, the $t\bar{t}W$ production cross-section has an uncertainty of $\pm 50\%$ ¹. Furthermore, the remaining contributions of fake leptons of the 4ℓ channel are taken from MC simulation with an uncertainty of $\pm 50\%$ applied.

8.3 Handling of Systematic Uncertainties

For the statistical analysis, systematic uncertainties are implemented as templates with a corresponding nuisance parameter with a description of the fit procedure found in Section 9.1. The systematic templates can be modified to either reduce statistical fluctuations or enforce correct variations with respect to a central nominal value. In the following, some strategies are described for dealing with such issues.

Symmetrisation

Most systematic uncertainties feature an up-and-down variation with respect to the nominal configuration, like the systematic uncertainties on μ_R and μ_F . However, some systematic uncertainties show highly asymmetric behaviour with respect to the nominal template, causing problems during the fitting procedure. There are multiple symmetrisation strategies commonly used to avoid such behaviour. This analysis uses only *one-sided* and *two-sided* symmetrisation procedures². The *one-sided* approach is usually applied to systematic uncertainties with a single variation and mirrors the variation around the nominal prediction, creating an opposite variation. The *two-sided* symmetrisation is characteristically applied to systematic uncertainties with two variations, v_{up} and v_{down} , calculating the symmetrised variations per bin:

$$v^{\text{sym.}} = \pm \left| \frac{|v_{\text{up}}| - |v_{\text{down}}|}{2 \cdot v_{\text{nominal}}} \right|. \quad (8.1)$$

¹During the combined fit procedure, this uncertainty is dropped and replaced with normalisation factor, which is free-floating in all analysis regions.

²There are other methods, like taking for each bin the sum of both absolute values for up and down variation and applying half of it around the central value or applying for each bin the maximum of up and down variation symmetric around the central value.

The resultant symmetrised variations are applied symmetrically around the nominal prediction v_{nominal} . This scheme has no effect if the systematic variations are already symmetric with respect to the central value.

Smoothing

The template describing systematic uncertainties can suffer from statistical fluctuations causing constraints or unreasonable³ behaviour of nuisance parameter during the determination of the $t\bar{t}H$ signal strength. These fluctuations are caused by low available MC statistics in certain analysis phase spaces. *Smoothing* methods are used for some systematic templates to compensate for those fluctuations by averaging statistics across bins, removing spikes and smoothing the distributions. The used smoothing algorithm is 353QH TWICE [270]. It uses running medians of three $(z_i^{(3)})$ and of five $(z_i^{(5)})$, they are calculated for a set of ordered values (y_i) as:

$$\begin{aligned} (z_i^{(3)}) &= \text{median}(y_{i-1}, y_i, y_{i+1}), \\ (z_i^{(5)}) &= \text{median}(y_{i-2}, y_i, y_{i+2}). \end{aligned} \quad (8.2)$$

The algorithm performs running medians of three first, followed by five, and again by three, giving the algorithm its characteristic name. The applied sequence merges or flattens peak structures. However, it has two shortcomings. The first can be cured by an interpolation using a quadratic function, adding the character Q to the name, and resolving artificial three-value long flat structures caused by the running median sequence. The second issue arises from the discontinuity problem and is solved by running means or Hanning means:

$$z_i = \frac{1}{4}z_{i-1} + \frac{1}{2}z_i + \frac{1}{4}z_{i+1}, \quad (8.3)$$

explaining the H in the name. The last part of the name TWICE refers to the procedure of *twicing*, preventing over-smoothing.

8.4 Overview of Systematic Uncertainties

Furthermore, there are channel-specific uncertainties, like reweighting uncertainties for the $2\tau_{\text{had}}$ channels on the $\tau_{\text{had}} p_T$ and τ_{had} fake origins, evaluated similarly to the $e^{\text{HF}} p_T$ uncertainty for the 4ℓ channel. Other uncertainties correct for mismodelling of the number of jets for diboson production, deriving correction factors with respect to data.

A summary of used systematic uncertainties considered in the $t\bar{t}H$ multi-lepton analysis is presented in Table 8.1. It includes all systematic uncertainties regarding experimental, modelling, and theory uncertainties, together with information

³Unreasonable in the sense that the nuisance parameter is more sensitive to those statistical fluctuations rather than to the variation induced by the systematic uncertainty.

on applied symmetrisation or smoothing. Per default, all uncertainties affect both normalisation and shape, which is denoted with (SN). However, some systematic uncertainties only affect either normalisation (N) or shape (S). During the combination of all analysis channels, uncertainties on the cross-section of $t\bar{t}W$ and WZ are dropped and replaced with free-floating normalisation factors. PLIV-related systematic uncertainties are not applied for the 4ℓ channel.

There are channel-specific uncertainties. For the 4ℓ channel, a mismodelling of the transverse momentum of e^{HF} fakes is observed. The transverse momentum is reweighted with respect to data. An additional uncertainty is introduced, which uses the reweighted distribution as the nominal prediction and the non-reweighted one as a reference. In Appendix H, the non-reweighted distribution is presented. In the $2\tau_{\text{had}}$ channels, τ_{had} fake origins are treated similarly. Other uncertainties correct for the mismodelling of the number of jets for diboson production, deriving correction factors with respect to data. The rates on charge-misidentified leptons are taken from MC simulation in the $3\ell+0\tau_{\text{had}}$ and $2\ell\text{SS}+0\tau_{\text{had}}$ channels. An uncertainty of 20% is applied to them. For the $2\ell\text{SS}+1\tau_{\text{had}}$ channels, additional uncertainties on the mismodelling of the τ_{had} fake p_{T} are applied. The procedure follows the same approach as for the e^{HF} transverse momentum mismodelling in the 4ℓ channel.

Systematic Uncertainty	Type	Symmetrisation	Smoothing	Channel	Components
Experimental					
Luminosity	N	-	-	all	1
Pile-Up	SN	-	-	all	1
JVT	SN	-	-	all	1
Flavour Tagging	SN	-	-	all	95
Jet Energy Scale	SN	two-sided	✓	all	35
Jet Energy Resolution	SN	two-sided	✓	all	13
E_T^{miss} scale and resolution	SN	one-sided	✓	all	3
Electron Trigger+reco+ID+isolation	SN	two-sided	-	all	4
Electron Scale+Resolution	SN	two-sided	-	all	3
Electron PLIV	SN	two-sided and one-side	-	excluding 4ℓ	14
Muon Trigger+reco+ID+isolation	SN	two-sided	-	all	10
Muon Scale+Resolution	SN	two-sided	-	all	3
Muon PLIV	SN	two-sided and one-side	-	excluding 4ℓ	20
Modelling of Signal and Background Processes					
$t\bar{t}H$ ME Alternative	SN	one-sided	✓	all	1
$t\bar{t}H$ PS Alternative	SN	one-sided	✓	all	1
$t\bar{t}H$ μ_R and μ_F Variation	SN	one-sided	✓	all	2
$t\bar{t}H$ PDF α_S Variation	N	-	-	all	1
$t\bar{t}H$ PDF Variation	SN	one-sided	✓	all	30
$t\bar{t}H$ ISR and FSR Variation	SN	two-sided	✓	all	2
Higgs Branching Ratio	SN	-	-	all	5
$t\bar{t}W$ ME Alternative	SN	one-sided	-	all	1
$t\bar{t}W$ PS Alternative	SN	one-sided	-	all	1
$t\bar{t}W$ μ_R and μ_F Variation	SN	one-sided	-	all	2
$t\bar{t}W$ PDF α_S Variation	N	-	-	all	1
$t\bar{t}W$ PDF Variation	SF	one-sided	-	all	30
$t\bar{t}Z$ A14 Tune Variation	SN	one-sided	✓	all	1
$t\bar{t}Z$ PS Alternative	SN	one-sided	✓	all	1
$t\bar{t}Z$ μ_R and μ_F Variation	SN	one-sided	-	all	2
ZZ μ_R and μ_F Variation	SN	one-sided	-	all	2
WZ μ_R and μ_F Variation	SN	one-sided	-	all	2
$t\bar{t}t\bar{t}$ ME Alternative	SN	one-sided	-	all	1
$t\bar{t}t\bar{t}$ PS Alternative	SN	one-sided	-	all	1
$t\bar{t}t\bar{t}$ μ_R and μ_F Variation	SN	one-sided	-	all	2
$t\bar{t}$ PS Alternative	SN	one-sided	✓	4ℓ	1
$t\bar{t}$ $h_{\text{damp.}}$ Variation	SN	one-sided	✓	4ℓ	1
$t\bar{t}$ μ_R and μ_F Variation	SN	one-sided	-	4ℓ	2
$t\bar{t}$ ISR and FSR Variation	SN	two-sided	-	4ℓ	2
$t\bar{t}$ + HF Cross-section	N	one-sided	-	4ℓ and $3\ell + 0\gamma_{\text{had}}$	2
$t\bar{t}$ + $e^{\text{HF}} p_T$ Mismodelling	S	one-sided	-	4ℓ	2
$t\bar{t} \rightarrow \geq 1b$ 4F vs. 5F Shape	S	one-sided	-	4ℓ	1
Theory Uncertainties					
$t\bar{t}H$ Cross-section	N	-	-	all	1
$t\bar{t}H$ Cross-section for STXS	N	-	-	all	5
$t\bar{t}W$ Cross-section	N	-	-	4ℓ	1
WZ Cross-section	N	-	-	4ℓ	1
VVV Cross-section	N	-	-	all	1
$t\bar{t}t\bar{t}$ Cross-section	N	-	-	all	1
$t\bar{t}t$ Cross-section	N	-	-	all	1
$t\bar{t}WW$ Cross-section	N	-	-	all	1
tWZ Cross-section	N	-	-	all	1
tWH Cross-section	N	-	-	all	1
VH Cross-section	N	-	-	all	1
$V\gamma$ Cross-section	N	-	-	all	1
$tHj\bar{b}$ Cross-section	N	-	-	all	1
tZ Cross-section	N	-	-	all	1
Other-Fake Cross-section	N	-	-	4ℓ	1

Table 8.1: A list of systematic uncertainties used for the $t\bar{t}H$ multi-lepton analysis and for the 4ℓ channel. Uncertainties can affect both normalisation and shape, denoted by SN, while only affecting shape is labelled with S and N for only normalisation, respectively. Furthermore, the symmetrisation and smoothing options are given.

CHAPTER 9

Statistical Analysis and Results

Determining the signal strength, cross-section, or other parameters of interest, like the CP angle α_t , is a crucial task in an analysis. Predictions can be tested and excluded by comparing them to data using statistical tools.

In the following, the various tools and results are presented. The profile likelihood fit procedure is explained in Section 9.1. The different types of (pseudo-) datasets are discussed. The fit models for the 4ℓ channel are studied in Section 9.2. The signal strength measurement of the $t\bar{t}H$ process $\mu_{t\bar{t}H}$ in the non-resonant $t\bar{t}H \rightarrow 4\ell$ channel is presented in Section 9.3. The combination of all channels, which are described in detail in Chapter 6, is presented in Section 9.4. The results feature the inclusive $t\bar{t}H$ production cross-section and the production cross-section in STXS bins of the Higgs boson transverse momentum.

9.1 The Profile Likelihood Fit

The measurement of physics quantities like cross-section values is performed using the binned profile likelihood method. In this sense, a model is a collection of all analysis regions, namely signal and control regions¹, set of *nuisance parameters* (NP) $\vec{\theta}$, reflecting the various sources of systematic uncertainties, with free-floating parameters for the signal strength $\mu = \sigma_{t\bar{t}H}/\sigma_{t\bar{t}H}^{\text{SM}}$ and normalisation factors \vec{k} , constraining important backgrounds. The profile likelihood fit tests the presence of $t\bar{t}H$ signal in data with respect to MC simulation prediction, acting as SM reference for each involved process. This is also reflected in the definition of the signal strength as a value of unity would be compatible with the SM case, while values of zero would

¹Validation regions are not considered in the fitting procedure. However, the estimated fit result is applied to the validation region to check modelling or overall consistency.

indicate no presence of a signal. The binned profile likelihood for the signal plus background hypothesis for a set of data \vec{n} is defined as

$$L(\vec{n}|\mu, \vec{\theta}, \vec{k}) = \prod_{r \in \text{Regions}} \prod_{i \in \text{Bins}} P\left(n_{i,r} | \mu S_{i,r}(\vec{\theta}, \vec{k}) + B_{i,r}(\vec{\theta}, \vec{k})\right) \times \prod_{j \in \text{NP}} G(\theta_j). \quad (9.1)$$

The data for a given bin i of a region r is $n_{i,r}$, while $S_{i,r}(\vec{\theta}, \vec{k})$ is the signal prediction, and $B_{i,r}(\vec{\theta}, \vec{k})$, the background one. As a counting experiment, the underlying statistical distribution follows a Poisson distribution P . The nuisance parameters are included in the likelihood as a constraint term with Gaussian functional form, interpolated and extrapolated by three discrete values, being the nominal prediction and the up and down variations for each systematic represented by a nuisance parameter, as described in Section 8.3 on symmetrisation techniques. The Gaussian term suppresses large deviations with respect to the nominal value, acting as a penalty term.

With all components of the likelihood, the fit procedure is a multi-dimensional Likelihood maximisation problem, estimating not only the parameter of interest (POI)² and its uncertainty, but also the normalisation factors \vec{k} and nuisance parameters. The maximisation problem is translated into a minimisation problem of the negative logarithm of the likelihood function. The minimisation is done in steps of gradient and Hessian matrix calculation until a termination criterion is matched. The estimated fit parameter defines the *post-fit* configuration. Consequently, distributions and their uncertainties entering the fit are labelled as *pre-fit*. Following the *Neyman-Pearson* lemma [271], the likelihood ratio

$$\lambda(\mu) = \frac{L(\mu > 1, \vec{\theta}_\mu)}{L(\mu = 1, \vec{\theta})} \quad (9.2)$$

is the optimal discriminator for testing the hypothesis of the signal being present against the no-signal hypothesis. The likelihood ratio $\lambda(\mu)$ only depends on the POI and follows a χ^2 distribution for large data samples. Therefore, a p -value and significance σ can be calculated without creating resource-consuming pseudo-experiments [272]. The implementation of the statistical analysis is done using the HISTFACTORY package [273] for statistical model building, further using ROOFIT [274] and ROOSTATS [275] libraries of the ROOT software library [276].

This analysis uses three fit models to study the 4ℓ channel. An *Asimov* dataset uses no ATLAS data and replaces data \vec{n} in Equation 9.1 with their respective MC

²There can be multiple parameters of interest.

prediction for each bin and region. In this setup, all free-floating parameters, namely μ and \vec{k} , are expected to be unity by construction. The estimated uncertainty on these parameters is a first study on the expected precision of the POI and normalisation factors, providing this method with the name of *sensitivity* study. Furthermore, NPs are not expected to be pulled away from their nominal position. However, constraints may occur.

A *hybrid Asimov* dataset is a mixture of *Asimov* data, often constructed for the SR or signal-sensitive bins, and regions and bins unblinded to ATLAS data. A *modified pseudodata* set for the SR or signal-sensitive bins is constructed: A fit excluding the SR or signal-sensitive bins is performed with ATLAS data. The determined fit parameters are propagated to the SR or signal-sensitive bins, creating a modified Asimov dataset. A second fit considers the unblinded regions and modified data, creating the most realistic fit scenario possible before unblinding all regions and bins. In this setup, free-floating parameters and NP can diverge from unity, showing possible normalisation differences between ATLAS data and MC prediction. Especially for fake backgrounds, discrepancies occur since MC simulations are not expected to model the rate of fake leptons correctly. Furthermore, NP may be pulled, compensating differences between MC and data.

The last configuration is the fully unblinded scenario; all regions and bins are unblinded to ATLAS data.

9.2 Fit Model Study for the 4ℓ Channel

To study the signal sensitivity and the behaviour of the fit model with respect to data in CRs and low signal-sensitive bins, an *Asimov*- and *Hybrid Asimov* fit are performed. They use both regions from 4ℓ phase-space, shown in Figure 6.15 and all three fake CRs, presented in Figure 7.7. The pre-fit background compositions for all regions are shown as pie-charts in Figure 9.1, demonstrating a satisfactory purity for all regions, helping to constrain important background normalisation factors.

The signal strength $\mu_{t\bar{t}H}$, together with the normalisation factors of the most important prompt backgrounds $\mathcal{N}(t\bar{t}Z)$ and $\mathcal{N}(ZZ)$, and fake backgrounds $\mathcal{N}(e^{\text{HF}})$, $\mathcal{N}(\mu^{\text{HF}})$, and $\mathcal{N}(e^{\text{LF}})$ are free-floating in all setups. To reduce the complexity of the fit, systematic uncertainties with a small impact on the systematic template nominal configuration are dropped. This method is referred to as *pruning*. It has shape and normalisation thresholds, deciding to drop or keep systematic uncertainties. The 4ℓ channel uses a shape threshold of 0.2 and normalisation threshold of 0.05³. Systematic uncertainties with an impact larger than 99% are also pruned. The pruning thresholds and their impact on the fit model are presented in Appendix I.

³The shape impact is determined by normalising variations and nominal prediction of systematic templates to unity and evaluating bin-wise.

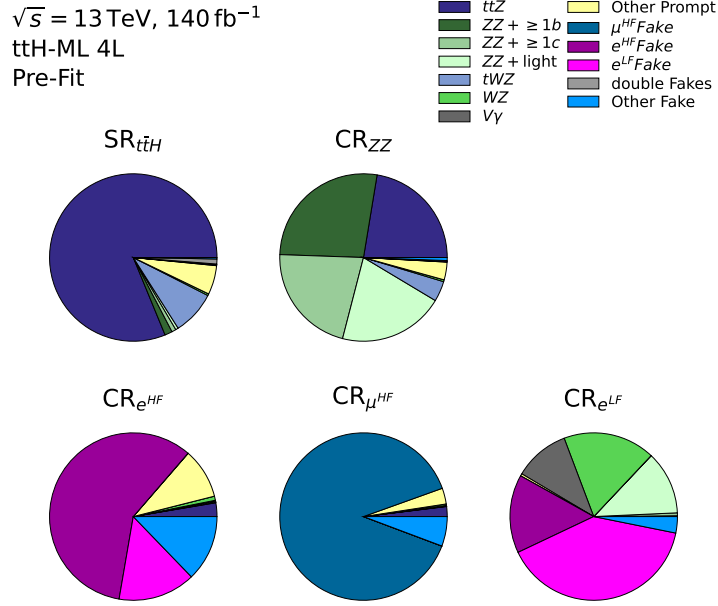


Figure 9.1: A pie chart with the pre-fit background composition for each region entering the 4ℓ analysis.

The fit using Asimov pseudodata estimates a signal strength of

$$\mu_{t\bar{t}H} = 1.00^{+0.71}_{-0.60} = 1.00^{+0.69}_{-0.57} (\text{stat.})^{+0.17}_{-0.18} (\text{sys.}), \quad (9.3)$$

which corresponds to an expected significance of 1.80σ for the 4ℓ channel. The dominant source of uncertainty arises from data statistics, while the primary source of systematic uncertainties originates from modelling, in particular from signal modelling. The remaining normalisation factors of backgrounds are shown in Figure 9.2 on the left side. The NP grouped by the three subcategories are shown in Figure 9.4. By construction, there are no pulls visible. Moreover, no large constraints on the NP are observed. The correlation matrix between fit parameters is shown in Figure 9.6. Only correlations with an absolute value of correlation larger than 20% are presented. Large correlations are expected between systematic uncertainties of the μ_R for diboson production and $\mathcal{N}(ZZ)$, between $\mathcal{N}(e^{\text{HF}})$ and $\mathcal{N}(e^{\text{LF}})$ due to contributions in both CRs and the Other Fake cross-section with the HF fake normalisations due to the presence in both CRs. A large expected anti-correlation between the $t\bar{t}H$ signal strength $\mu_{t\bar{t}H}$ and the background normalisation of the dominant background $t\bar{t}Z$ process is observed. Minor correlations are observed between the signal strength and the normalisation factors of the e^{HF} and μ^{HF} background. They are caused due to the presence of those backgrounds in the signal-sensitive bins.

The ranking of NP and background normalisation factors presented in Figure 9.8 is based on their impact on the signal strength. Four fits are performed, fixing the pre-fit value with either the up and down variation of its uncertainty or using the post-fit values instead. The impact is the difference between the nominal configuration and the resulting signal strength using one of the fits. The black markers correspond to pulls of the NPs relative to their nominal value of $\theta_0 = 0$. The red markers show the pulls of normalisation factors with respect to their nominal position $\theta_0 = 1$. The sixteen highest-ranked parameters are shown. They are a mixture of normalisation factors, modelling uncertainties, and experimental ones. The largest impact, as expected, arises from the $t\bar{t}Z$ normalisation. Further systematic uncertainties are from the theoretical calculation of the $t\bar{t}H$ production cross-section and systematics associated with the jet energy scale. Other NPs, such as the $t\bar{t} e^{\text{HF}} p_{\text{T}}$ modelling or the $t\bar{t}$ 4FS systematic, indirectly impact the signal strength through the fake normalisation factors, which are also highly ranked. Uncertainties on cross-sections of $t\bar{t}t\bar{t}$, $t\bar{t}W$, and tWZ production are also ranked. Most notably, the $t\bar{t}t\bar{t}$ cross-section uncertainty has an impact on the signal strength due to the presence of $t\bar{t}t\bar{t}$ contributions in the signal-sensitive bins.

The fit using the hybrid Asimov pseudodata estimates a signal strength of

$$\mu_{t\bar{t}H} = 1.10^{+0.73}_{-0.61} = 1.10^{+0.71}_{-0.58} (\text{stat.})^{+0.18}_{-0.19} (\text{sys.}). \quad (9.4)$$

It corresponds to a significance of 1.80σ for the 4ℓ channel. Similarly to the fit using Asimov pseudodata, data statistics is the driving source of uncertainties, followed by uncertainties of the predicted production cross-section of the signal process. In Figure 9.2 on the right side, the measured normalisation factors are shown. The normalisation factors for the prompt processes $t\bar{t}Z$ and ZZ are consistent within 1σ with the SM model prediction. The normalisation factors of the e^{HF} and e^{LF} are consistent with unity. However, for the μ^{HF} background, the normalisation is slightly smaller than unity. The post-fit distributions in all five analysis regions are shown in Figure 9.3, a satisfactory data MC agreement is observed for all unblinded regions and bins. A blinding threshold of 15% for the signal-to-background ratio is used. Therefore, the last five bins of the SR distribution are blinded and replaced with Hybrid Asimov pseudodata during the fit.

The pulls and constraints of nuisance parameters are illustrated in Figure 9.5. Only minor pulls are present for the experimental NPs. The most noticeable are related to $E_{\text{T}}^{\text{miss}}$ and are caused by the observed data MC offset in the $\text{CR}_{e^{\text{LF}}}$. Other pulls are observed for the modelling systematics, in particular for the modelling of the $t\bar{t}$ production with additional b -jets, comparing events generated in the five-flavour scheme with four-flavour scheme ones. The pull is caused in the $\text{CR}_{e^{\text{HF}}}$ with data preferring the five-flavour scheme variation of the distribution. For the theory category, the $V\gamma$ cross-section is pulled. However, the $V\gamma$ contribution predominately enters the $\text{CR}_{e^{\text{LF}}}$, but not as a prompt contribution, but with the photon converted to an

electron conversion fake. The modelling of the rate of such contributions for this phase-space region is poor; corrections via the cross-section are therefore expected. The slight pull of the $t\bar{t}W$ cross-section is caused by the $\text{CR}_{e^{\text{HF}}}$ and $\text{CR}_{\mu^{\text{HF}}}$, having a descent $t\bar{t}W$ contribution. Differences in the correlation coefficients between the Asimov setup and the Hybrid Asimov setup, shown in Figure 9.7, are tiny. Most notable is an increased correlation between the normalisation factors of the e^{HF} and e^{LF} backgrounds. It is caused by the presence of both fake backgrounds in both fake CRs and the normalisation correction in the $\text{CR}_{e^{\text{LF}}}$.

The ranking shown in Figure 9.8 on the right is similar to the Asimov case, with the expected largest impact originating from the $t\bar{t}Z$ normalisation and the uncertainty on the theoretical $t\bar{t}H$ production cross-section. None of the highest-ranked nuisance parameters show large pulls or constraints nor have significant correlation coefficients with the signal strength.

To further demonstrate the stability of the fit setup, a likelihood scan is performed in a signal strength range of $\mu_{t\bar{t}H} \in [0.0, 2.0]$ with thirty fit results, including the best-fit value. The differences of logarithmic likelihoods $-\Delta \ln(L)$ with respect to the best-fit value as a function of the signal strength are shown in Figure 9.9 for both fit setups. The result is a smooth curve with quadratic behaviour with a global minimum at the best-fit value. The 1σ interval, corresponding to the uncertainty on the signal strength, is defined by the $-\Delta \ln(L) = 0.5$ values.

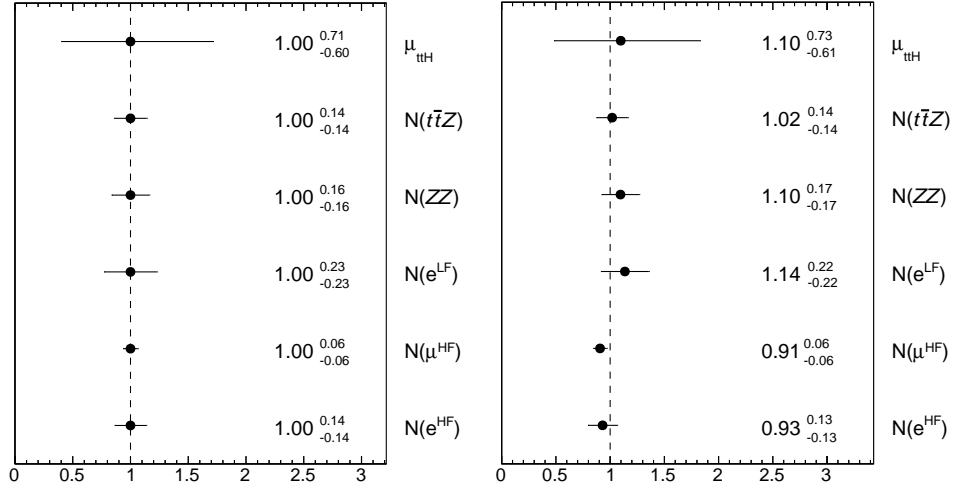


Figure 9.2: The estimated values for the signal strength, background normalisation, and fake lepton normalisation for the fit model using Asimov pseudodata in the 4ℓ channel on the left side. On the right side, the estimated parameter of the fit using Hybrid Asimov pseudodata is shown.

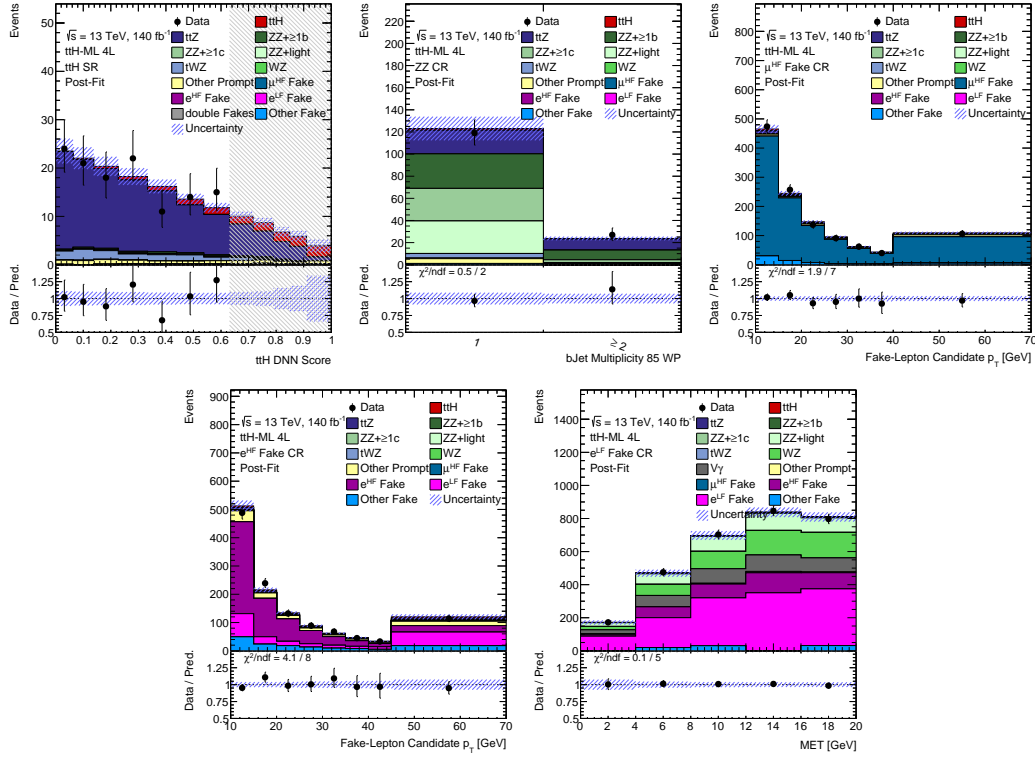


Figure 9.3: Post-Fit distributions included in the fit to extract the signal sensitivity for the 4ℓ channel of the $t\bar{t}H$ multi-lepton analysis. The error bands include both systematic and statistical uncertainties. The five signal-sensitive bins of the SR are blinded and, during the fitting procedure, replaced with a modified Asimov dataset.

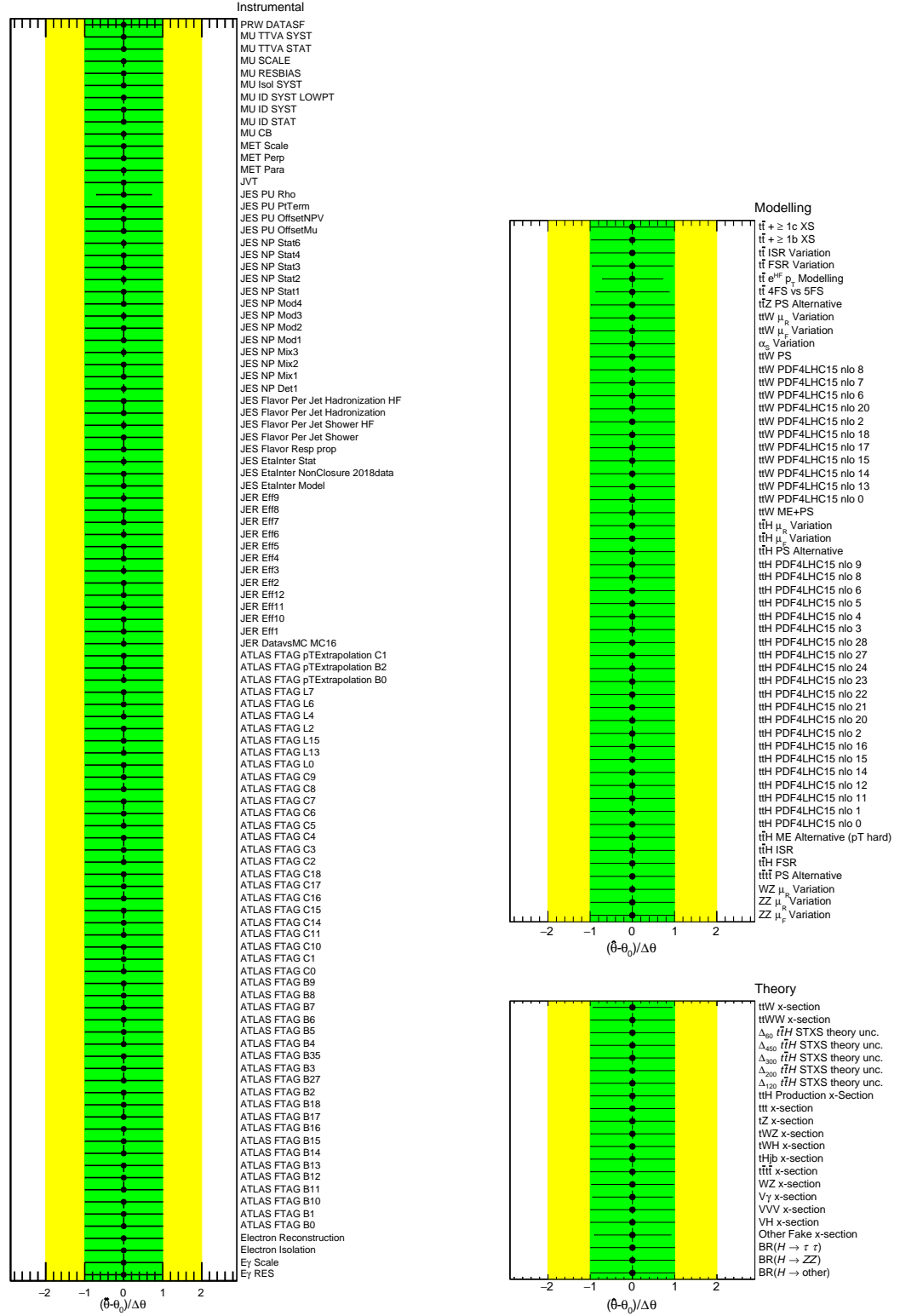


Figure 9.4: The pulls and constraints of the nuisance parameters for the experimental, modelling, and theory subcategories for the fit to Asimov pseudodata.

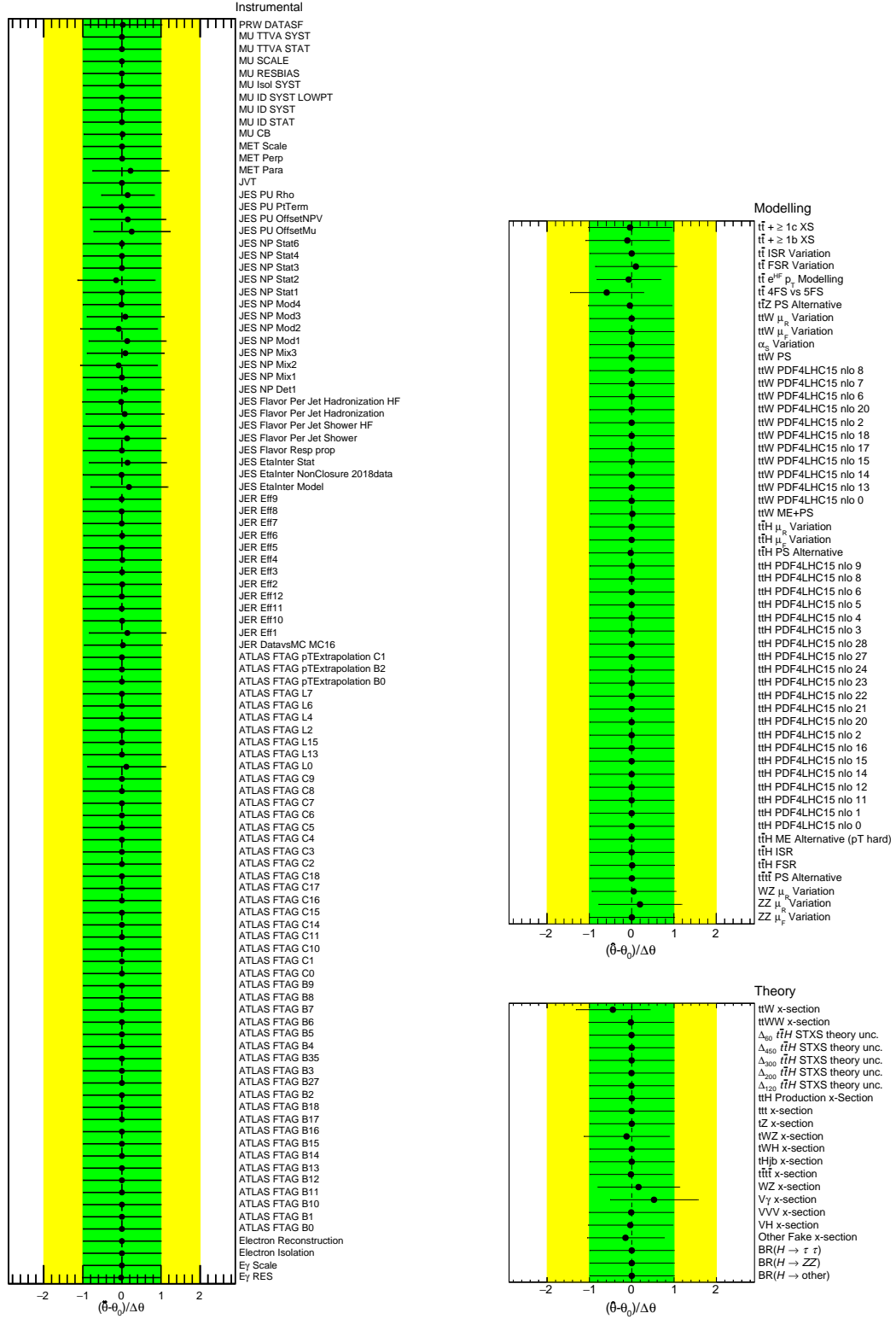


Figure 9.5: The pulls and constraints of the nuisance parameters for the experimental, modelling, and theory subcategories for the fit to Hybrid Asimov pseudodata.

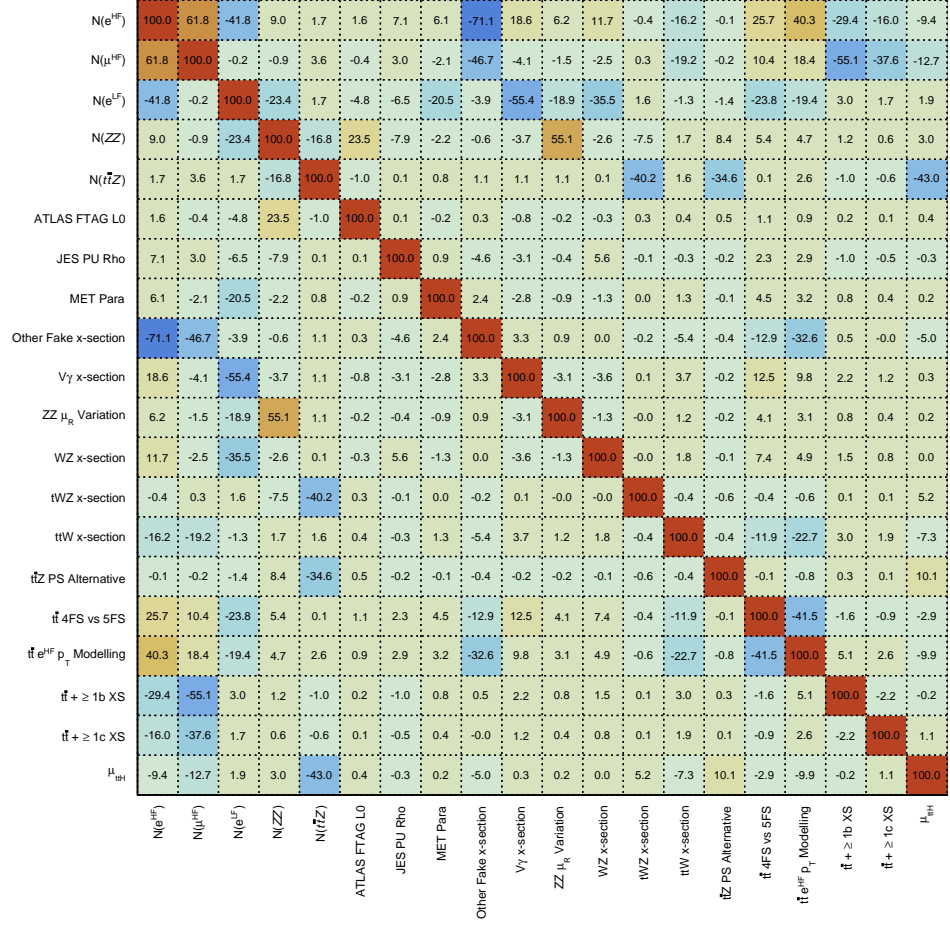
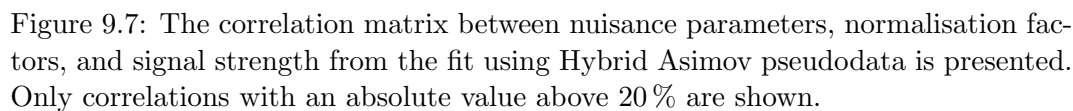


Figure 9.6: The correlation matrix between nuisance parameters, normalisation factors, and signal strength from the fit using Asimov pseudodata is presented. Only correlations with an absolute value above 20 % are shown.



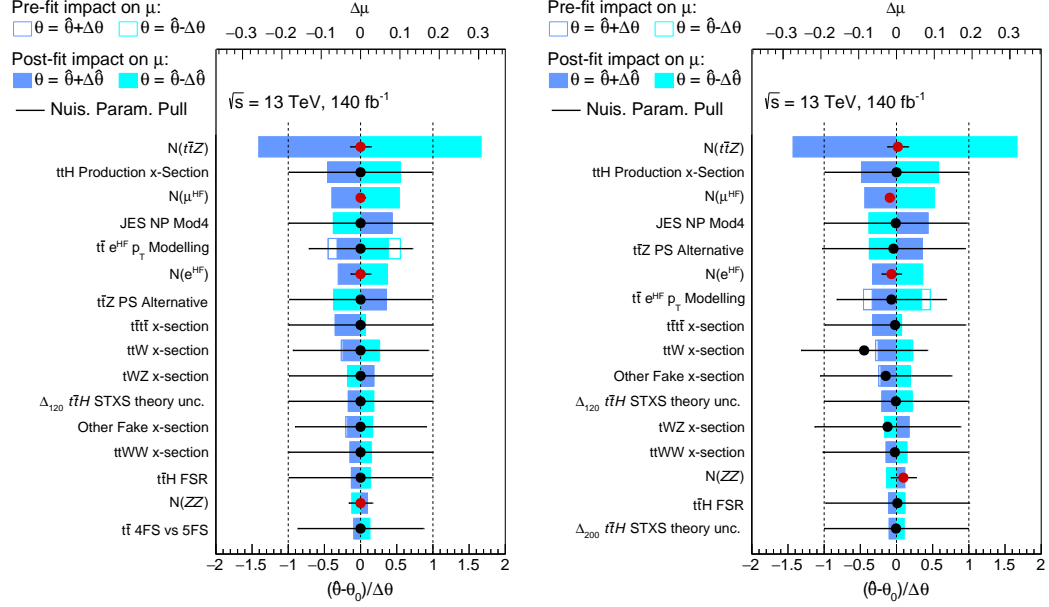


Figure 9.8: The ranking plots for the sixteen highest ranked parameters. The fit to Asimov pseudodata is presented on the left side, while the Hybrid Asimov pseudodata is used on the right side.

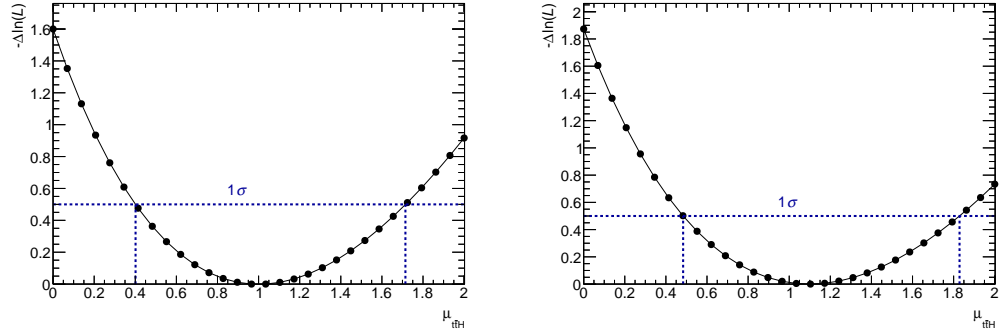


Figure 9.9: Scans of the profile likelihood are shown. For each scan, thirty fits, including the best-fit value configuration, are performed. On the left side, the fits used Asimov pseudodata, while on the right side, Hybrid Asimov pseudodata is used. The 1σ interval is defined via $-\Delta \ln(L) = 0.5$ and provides the uncertainties on the estimated signal strength.

9.3 Fit to Atlas Data in the 4ℓ Channel

The fit setup with all analysis bins unblinded to ATLAS data and applied systematics described in Chapter 8 determines a signal strength of

$$\mu_{t\bar{t}H} = 0.53^{+0.67}_{-0.53} = 0.53^{+0.66}_{-0.51} (\text{stat.})^{+0.13}_{-0.13} (\text{sys.}),$$

corresponding to an observed (expected) significance of 0.95σ (1.80σ). The normalisation factors for important background contributions are presented in Figure 9.10. No large differences between the background normalisation factors are observed compared with the Asimov and hybrid Asimov fit setups. The 4ℓ channel is dominated by statistical uncertainties. The largest source of systematics uncertainties arises from modelling ones. The pulls and constraints of NP are presented in Figure 9.11. There are no significant differences observed compared to the fit to hybrid Asimov pseudodata. The correlation matrix between the fit parameters is presented in Figure 9.12. Similarly, no significant difference is observed compared to the other fit setups. The ranking of NP and background normalisation factors are presented in Figure 9.13 with the normalisation of the $t\bar{t}Z$ background as the fit parameter with the largest impact on the signal strength. Only small differences in the ranking are observed compared to the fits to pseudodata. The most significant one is on the predicted $t\bar{t}H$ production cross-section. In the fit to ATLAS data, it has a minor impact caused by the smaller observed central value for $\mu_{t\bar{t}H}$. The normalisation of the μ^{HF} background becomes the second leading fit parameter in terms of impact on the signal strength. Systematic uncertainties on backgrounds become more important due to the smaller presence of signal in the sensitive bins. Notable systematics are the parton shower modelling of $t\bar{t}Z$ and the uncertainty on the $t\bar{t}t\bar{t}$ production cross-section. Other experimental systematics which have a significant impact on the signal in the Asimov and hybrid Asimov setup, like the *JES NP Mod 4* one, are lower ranked for the unblinded fit. It is caused by the observed smaller central value compared to other setups. Generally, systematics associated with backgrounds become more significant for the fit to ATLAS data.

The likelihood scan for the signal strength $\mu_{t\bar{t}H}$ is presented in Figure 9.14. The scan demonstrates a smooth curve with a global minimum at the observed central value. The 1σ interval for the upper limit can be constructed, providing a good estimate on the upper uncertainty of $\mu_{t\bar{t}H}$. The determination of the lower limit is difficult. The variation of $\mu_{t\bar{t}H}$ towards negative values reduces the signal contribution in the last and most signal-sensitive bin of the $\text{SR}_{t\bar{t}H}$ that results in negative expected yields. A constraint on $\mu_{t\bar{t}H}$ being semi-positive is applied to avoid such behaviour. The lower limit and uncertainty are interpreted to estimate the background-only hypothesis.

The post-fit distributions for all five analysis regions of the 4ℓ channel are presented in Figure 9.15. A satisfactory agreement between MC simulation and ATLAS data is observed. Table 9.1 presents the post-fit yields for the 4ℓ channel regions. The post-fit background compositions are given in Figure 9.16. Post-fit distributions for

validation are presented in Appendix D. They demonstrate a satisfactory data MC agreement for the 4ℓ regions and fake regions.

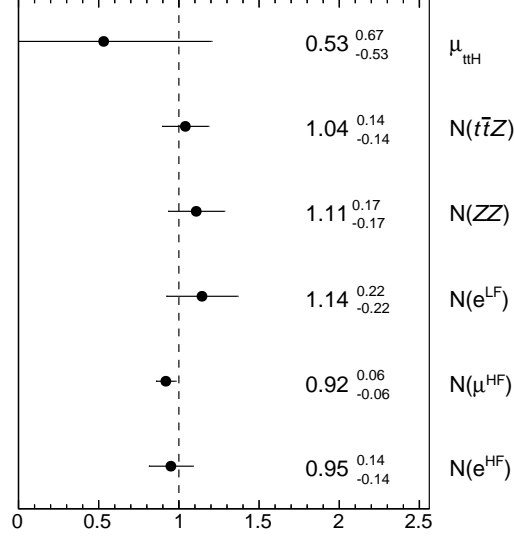


Figure 9.10: The estimated values for the signal strength, background normalisation, and fake lepton normalisation for the fit using ATLAS data in the 4ℓ channel.

Process	$SR_{t\bar{t}H}$	CR_{ZZ}	$CR_{e^{HF}}$	$CR_{\mu^{HF}}$	$CR_{e^{LF}}$
$t\bar{t}H$	7.14 ± 7.67	0.99 ± 1.07	13.1 ± 14.0	11.0 ± 11.8	0.02 ± 0.02
$t\bar{t}Z$	122.4 ± 17.0	32.03 ± 4.45	34.0 ± 4.47	25.2 ± 3.51	1.86 ± 0.38
$ZZ + \geq 1b$	2.33 ± 0.32	40.44 ± 5.36	1.34 ± 0.21	0.79 ± 0.11	2.63 ± 0.60
$ZZ + \geq 1c$	1.26 ± 0.17	29.60 ± 2.58	1.36 ± 0.22	0.63 ± 0.15	16.83 ± 2.74
$ZZ + \text{light}$	0.81 ± 0.15	32.24 ± 4.26	1.82 ± 0.28	0.49 ± 0.09	372.7 ± 75.8
tWZ	11.15 ± 5.96	4.90 ± 2.62	1.72 ± 0.92	0.92 ± 0.49	0.75 ± 0.46
WZ	0.53 ± 0.12	0.54 ± 0.11	10.2 ± 1.95	3.58 ± 0.69	491.6 ± 98.5
Other Prompt	8.14 ± 1.38	4.65 ± 1.14	110 ± 18	32.0 ± 12.6	11.50 ± 3.13
μ^{HF} Fake	0.18 ± 0.05	0.10 ± 0.04	0.49 ± 0.09	1027 ± 52	0.05 ± 0.04
e^{HF} Fake	0.14 ± 0.04	0.09 ± 0.06	684 ± 93	0.01 ± 0.01	385.4 ± 63.1
e^{LF} Fake	0.14 ± 0.05	0.19 ± 0.05	211 ± 41	0.09 ± 0.02	1260 ± 222
double Fake	1.31 ± 0.29	0.0 ± 0.0	-	-	-
Other Fake	0.33 ± 0.16	0.69 ± 0.40	143 ± 69	65.6 ± 31.5	63.7 ± 50.0
Total MC	155 ± 14	147 ± 12	1213 ± 36	1167 ± 35	2984 ± 63
data	155	146	1208	1167	2993

Table 9.1: The post-fit yields for the 4ℓ channel regions.

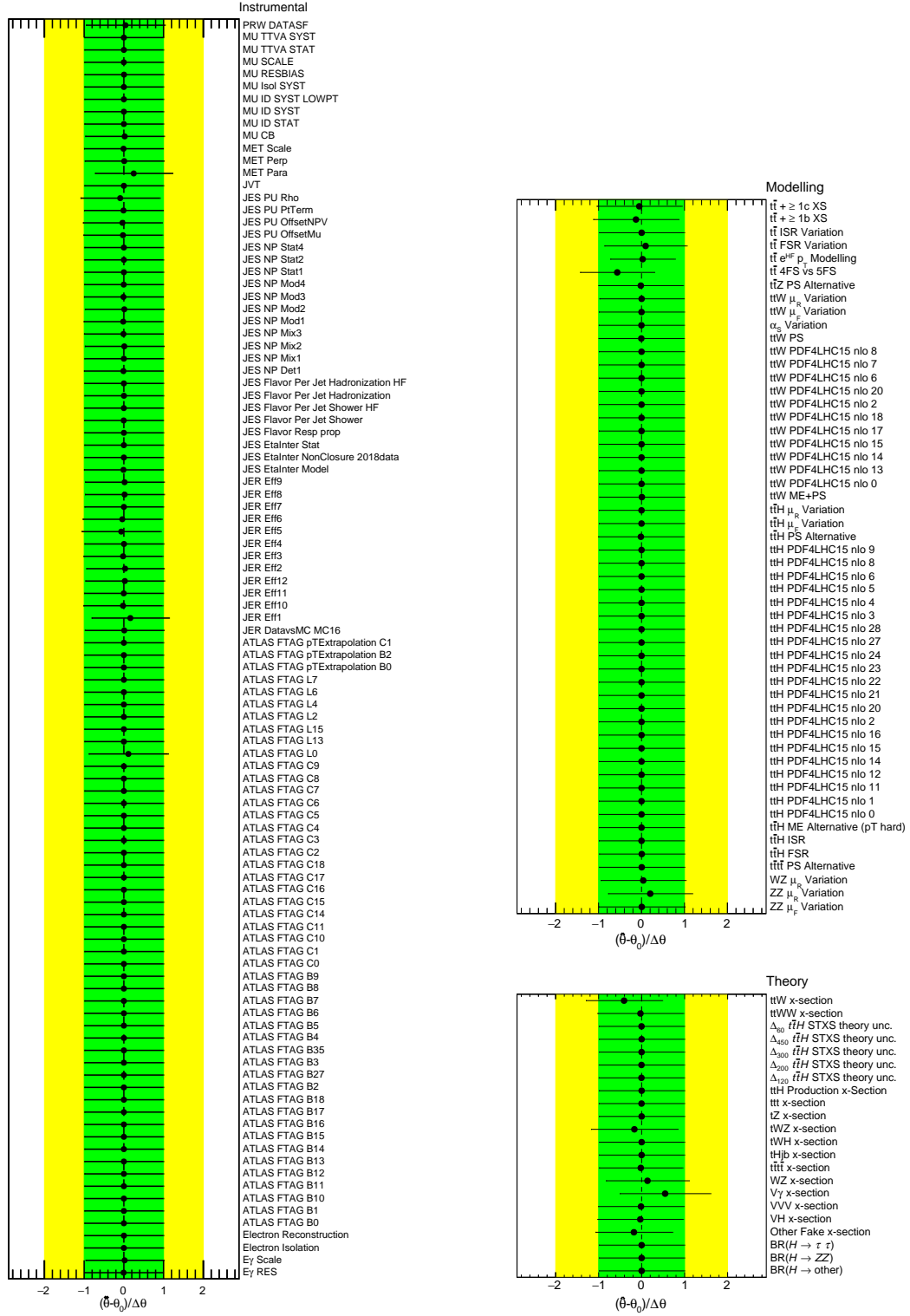


Figure 9.11: The pulls and constraints of the nuisance parameters for the experimental, modelling, and theory subcategories for the fit to ATLAS data.

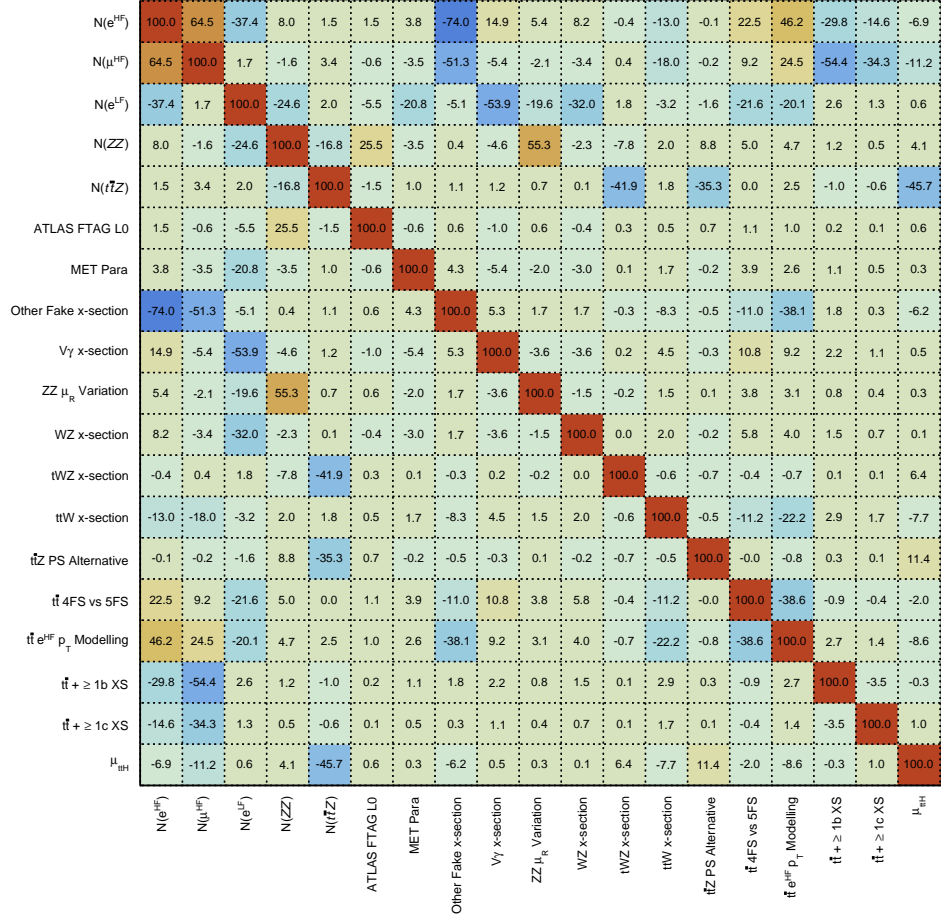


Figure 9.12: The correlation matrix between nuisance parameters, normalisation factors, and signal strength for the fit to ATLAS data. Only correlations with an absolute value above 20% are shown.

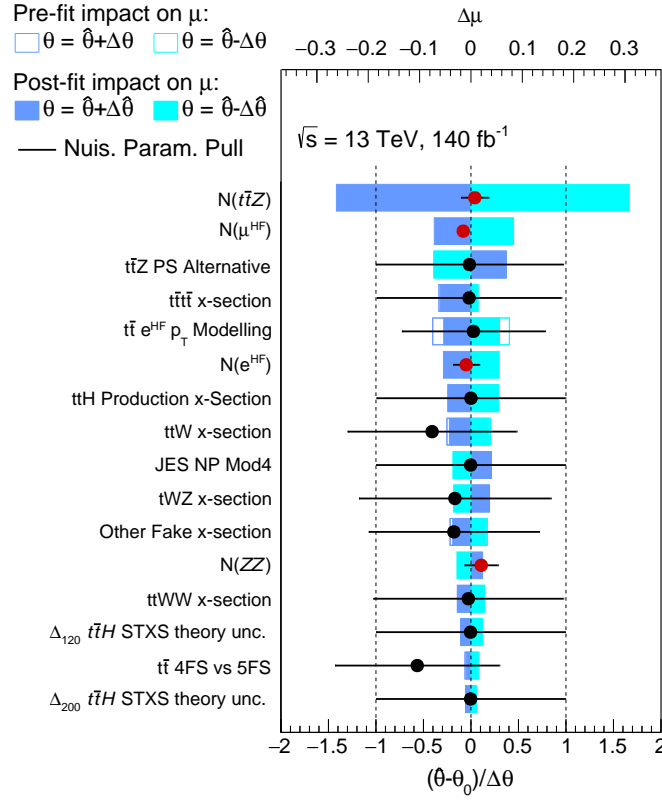


Figure 9.13: The ranking for the sixteen highest ranked parameters for the fit to ATLAS data is shown.

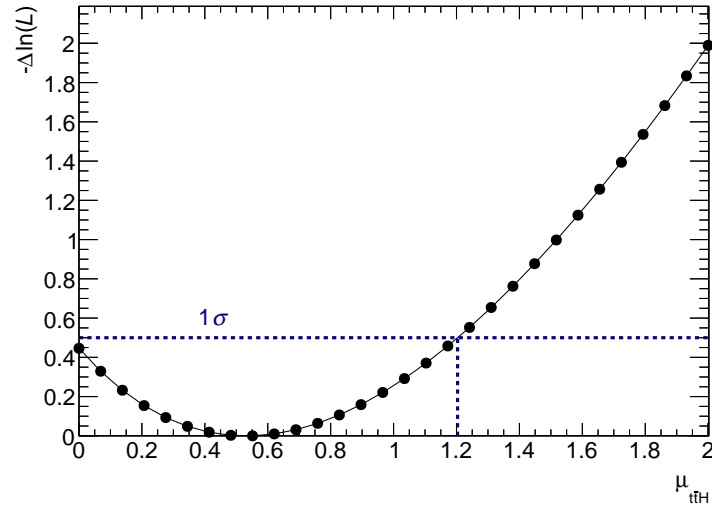


Figure 9.14: A scan of the profile likelihood for the fit to ATLAS data is shown. Thirty fits, including the best-fit value configuration, are performed.

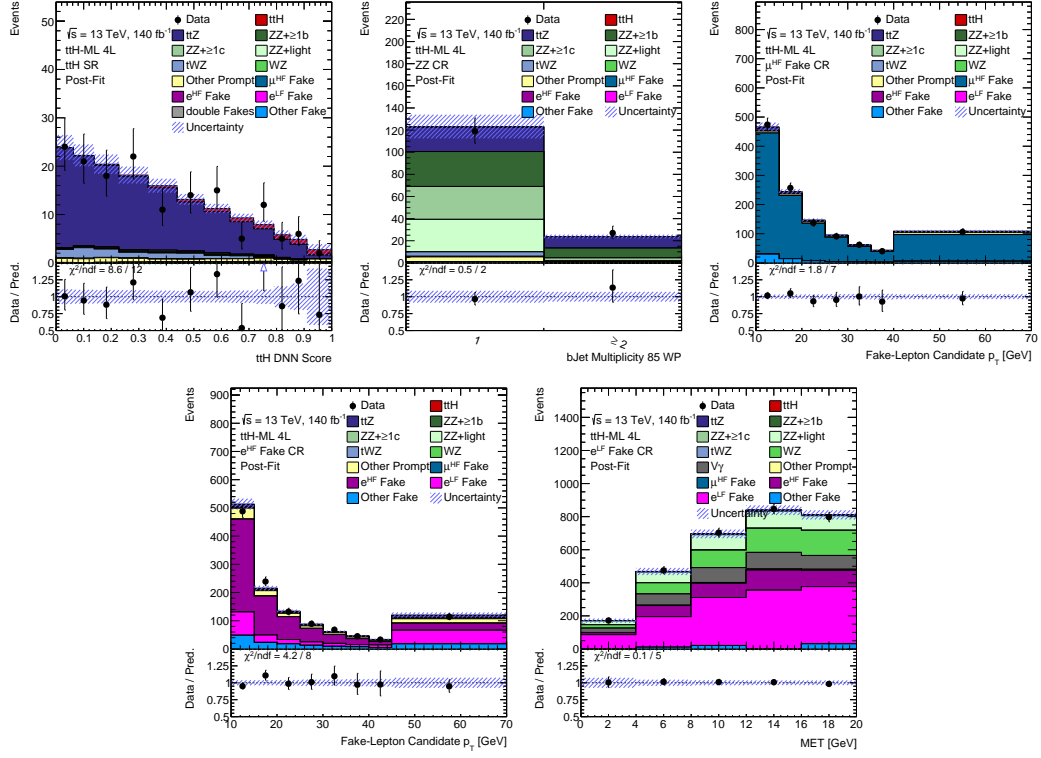


Figure 9.15: Post-Fit distributions for the 4ℓ channel of the $t\bar{t}H$ multi-lepton analysis after a fit to ATLAS data. The error bands show total uncertainties.

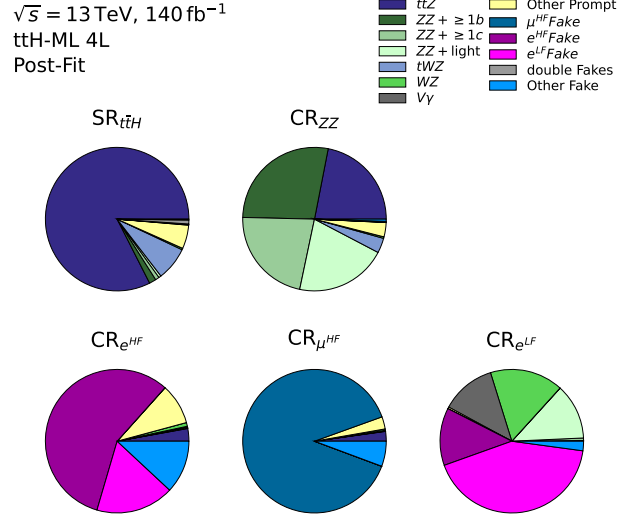


Figure 9.16: A pie chart with the post-fit background composition for each region entering the 4ℓ analysis.

9.4 Combined Fit for the inclusive $t\bar{t}H$ Cross-Section and STXS Setup

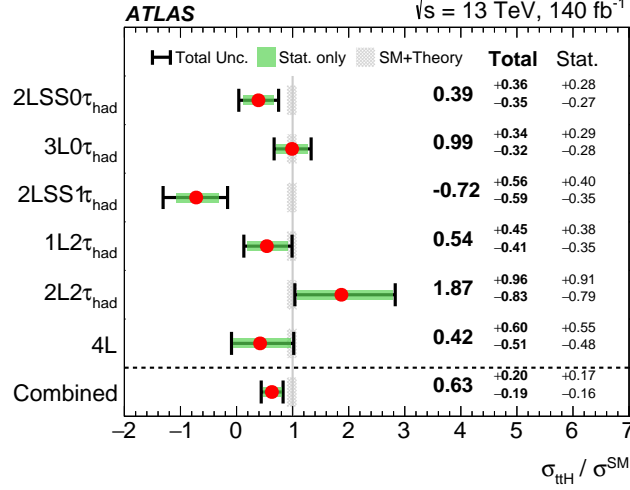


Figure 9.17: The observed signal strengths for all analysis channels and their combination. This figure is taken from Ref. [15]

The 4ℓ channel is part of the $t\bar{t}H$ multi-lepton analysis. As described in Chapter 6 and depicted in Figure 6.1, the analysis is split into various channels based on the number of light leptons and τ_{had} candidates. The individual channel-specific results are determined with a similar strategy compared to the 4ℓ channel: training of a MVA-based model for signal and background separation with the subsequent definition of SR and CR based on those MVA scores. Additionally, orthogonal CRs are defined to constrain fake backgrounds⁴. For all channels, the expected signal strength is extracted using a profile likelihood fit, including systematic uncertainties, described in Chapter 8.4 with an overview in Table 8.1. The signal strength $\mu_{t\bar{t}H}$ is a free-floating parameter in all analysis regions. The same is applied to the normalisation factors for the dominant prompt backgrounds originating from $t\bar{t}Z$, $t\bar{t}W$, and diboson production. The various normalisation factors for the fake contributions are not correlated through the full analysis since different lepton definitions and fake estimation techniques are used.

The measured signal strength is:

$$\mu_{t\bar{t}H} = 0.63^{+0.20}_{-0.19} = 0.63^{+0.17}_{-0.16} (\text{stat.})^{+0.11}_{-0.10} (\text{sys.}). \quad (9.5)$$

This corresponds to observed (expected) significance of 3.3σ (5.3σ). The observed signal strengths for all six analysis channels are presented Figure 9.17. The measured

⁴There are two additional CRs for the 3ℓ , which target prompt backgrounds.

production cross-section is found to be:

$$\sigma_{t\bar{t}H} = 321_{-99}^{+102} \text{ fb} \quad (9.6)$$

The compatibility with the Standard Model prediction of $507_{-50}^{+35} \text{ fb}$ is 7.2%. The largest deviation is observed in the $2\ell\text{SS}+1\tau_{\text{had}}$ channel which is caused by downward fluctuation in data in signal sensitive bins. The largest impact on the $t\bar{t}H$ cross-section originates from the normalisation of the dominant backgrounds $t\bar{t}Z$ and $t\bar{t}W$ and from systematic uncertainties related to the $t\bar{t}t\bar{t}$ production cross-section and the modelling of the $t\bar{t}W$ background [15].

The Higgs production cross-section is also measured in STXS bins of the transverse momentum of the Higgs boson. The reconstruction is performed using a GNN for the $0\tau_{\text{had}}$ channels and a BDT for the $2\tau_{\text{had}}$ as described in Chapter 6.7. No attempt for the reconstruction of the Higgs transverse momentum is made for the 4ℓ and $2\ell\text{SS}+1\tau_{\text{had}}$ channels due to limited statistics. They are included in the fit, but their contribution to overall sensitivity is small. Figure 9.18 presents the observed signal strengths for the STXS bin. The measurement agrees well with the SM prediction in the lower part of the Higgs transverse momentum spectrum corresponding to the $p_T^H < 120 \text{ GeV}$ STXS bin, but also in the higher STXS bin with $p_T^H \geq 200 \text{ GeV}$. The measured value for the STXS bin which covers a Higgs transverse momentum of $120 \text{ GeV} \leq p_T^H < 200 \text{ GeV}$ is lower than the SM prediction and is caused by a downward fluctuation in data and anti-correlation effects between the different STXS bin measurements. The compatibility of the STXS measurement with the SM prediction is 28 %, while the compatibility with the inclusive fit is 55 % [15].

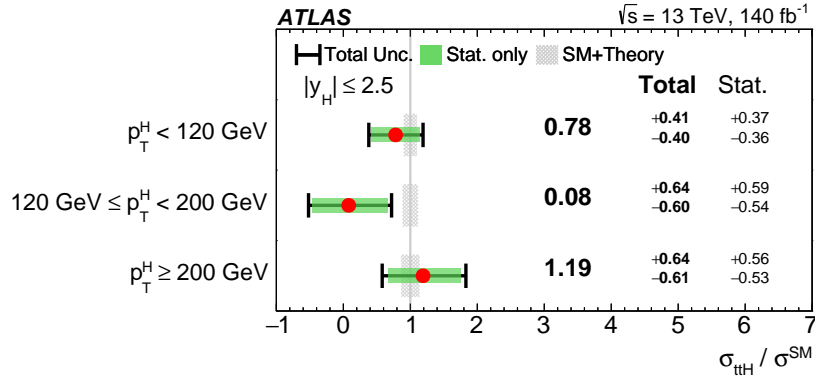


Figure 9.18: The determined signal strength for STXS bins in the combined fit setup using ATLAS data. This figure is taken from Ref. [15]

CHAPTER 10

Summary and Outlook

The $t\bar{t}H$ process provides a unique opportunity to test the SM prediction of the Yukawa coupling between the top quark and the Higgs boson. But it is also sensitive to various predictions for physics beyond the SM. The Yukawa coupling and, therefore, the $t\bar{t}H$ production plays a significant part in studying the Higgs mechanism and self-coupling of the Higgs boson. The latter becomes vital for correctly predicting differential cross-section measurements. The interplay between the top-Higgs Yukawa coupling and the Higgs self-coupling is especially sensitive to models exploring the vacuum stability of the universe. Furthermore, the $t\bar{t}H$ production is used to study sources of CP violation in the Higgs sector. The Yukawa coupling can be extended with a pseudoscalar term and coupling modifiers. The introduction of an additional CP mixing angle α_t mixes scalar CP-even with pseudoscalar CP-odd contributions. The impact on the production cross-section of the $t\bar{t}H$ and tH processes can be tested, and specific mixing scenarios can be excluded while others are favoured by the data.

This measurement uses multi-lepton final states and targets the $H \rightarrow WW^*$, $H \rightarrow ZZ^*$, and $H \rightarrow \tau\tau$ decay modes with a single- or dileptonic decay of the top quark pair. The analysis is split into six channels defined by the number of light leptons and hadronically decaying taus in the final state. The selection of unique multi-lepton final states suppresses most QCD-initiated backgrounds. Instead, the dominant background sources are from $t\bar{t}W$, $t\bar{t}Z$, and diboson production. The $t\bar{t}W$ process suffers from large discrepancies between MC prediction and measurements. With an improved modelling of this particular process, including missing higher-order Feynman graphs and corrections, a dominant background of the $t\bar{t}H$ multi-lepton analysis can now be reliably estimated. Due to multiple leptons in the final state, other reducible backgrounds originating from fake, non-prompt, and charge-misidentified

leptons become significant. These backgrounds are suppressed with dedicated experimental tools and estimated with targeted methods. All channels utilise multivariate techniques to separate signal and background events and to define signal and control regions for important backgrounds.

This thesis presents the measurement of the $t\bar{t}H$ production cross-section in the non-resonant $t\bar{t}H \rightarrow 4\ell$ channel using the full Run 2 dataset corresponding to an integrated luminosity of 140 fb^{-1} of proton-proton collisions at a centre-of-mass energy of $\sqrt{s} = 13 \text{ TeV}$. The 4ℓ channel targets primarily the $H \rightarrow WW^* \rightarrow \ell\nu\ell\nu$ Higgs boson decay mode with dileptonic decaying top quarks. The analysis uses a dense neural network approach to separate $t\bar{t}H$ signal events from $t\bar{t}Z$ and diboson background contributions. The neural network scores define distinct regions with complementary sensitivity to the targeted signal and backgrounds. Non-prompt and fake lepton backgrounds are estimated using control regions designed to target the respective backgrounds. Various systematic sources affect the measurement. Their effects are estimated and included in the measurement. They cover various sources from the experimental setup, the modelling of the signal process and dominant background processes, and cross-sections of minor backgrounds. The signal strength with respect to the SM prediction is determined by a profile likelihood fit, taking all systematic uncertainties into account.

The signal strength for the $t\bar{t}H$ production in the 4ℓ channel is expected to be

$$\mu_{t\bar{t}H} = 1.00^{+0.71}_{-0.60} = 1.00^{+0.69}_{-0.57} (\text{stat.})^{+0.17}_{-0.18} (\text{sys.}), \quad (10.1)$$

using Asimov pseudodata. The observed signal strength is found to be

$$\mu_{t\bar{t}H} = 0.53^{+0.67}_{-0.53} = 0.53^{+0.66}_{-0.51} (\text{stat.})^{+0.13}_{-0.13} (\text{sys.}), \quad (10.2)$$

which corresponds to an observed (expected) significance of 0.94σ (1.81σ) for a SM Higgs boson with a mass of 125 GeV . The precision of the measurement is primarily limited by statistical uncertainties. Systematic uncertainties play a minor role. The most significant systematic uncertainties arise from the normalisation and modelling of the dominant background process $t\bar{t}Z$, the normalisation of the μ^{HF} non-prompt background, and uncertainties on the production cross-section of background processes, like $t\bar{t}t\bar{t}$ production, that contribute to the signal region. Compared to the previous measurement using data collected in the years 2015, 2016, and 2017 of Run 2 corresponding to an integrated luminosity of 80 fb^{-1} both systematic and statistical uncertainties have improved. The previous analysis of the $t\bar{t}H$ multi-lepton process estimated a signal sensitivity of:

$$\mu_{t\bar{t}H} = 1.00^{+1.03}_{-0.79} = 1.00^{+0.96}_{-0.76} (\text{stat.})^{+0.37}_{-0.22} (\text{sys.}), \quad (10.3)$$

using Asimov pseudodata. The expected significance was 1.4σ [277]. The 4ℓ channel signal strength presented in this thesis is compared to the previous analysis by

scaling down the integrated luminosity of the Run 2 dataset to match it with the years 2015, 2016, and 2017 of Run 2. Furthermore, it is assumed that systematic uncertainties behave similarly. The resulting signal strength using the down-scaled Asimov pseudodata is estimated to be

$$\mu_{t\bar{t}H} = 1.00^{+0.94}_{-0.76} = 1.00^{+0.92}_{-0.74} (\text{stat.})^{+0.18}_{-0.19} (\text{sys.}). \quad (10.4)$$

The result corresponds to an expected significance of 1.4σ . The projection of the previous measurement to the full Run 2 dataset [277] is shown in Table 10.1. The comparison of the measurement presented in this work (previous measurement) with the up-scaled (down-scaled) projection demonstrates that statistical uncertainties slightly exceed what is expected solely from increased data statistics.

The expected integrated luminosity for Run 3 is assumed to be 300 fb^{-1} collected with an increased centre-of-mass energy of $\sqrt{s} = 13.6 \text{ TeV}$. For the combination of Run 2 and Run 3 with an expected total integrated luminosity of 440 fb^{-1} , the expected signal sensitivity for the non-resonant 4ℓ channel is:

$$\mu_{t\bar{t}H} = 1.00^{+0.42}_{-0.37} = 1.00^{+0.39}_{-0.33} (\text{stat.})^{+0.16}_{-0.16} (\text{sys.}). \quad (10.5)$$

The corresponding expected significance is 3σ . The projection neglects the increased cross-section values due to higher centre-of-mass energy. It is, therefore, a lower bound on the signal sensitivity. Significant constraints due to larger statistics are not observed. The high-luminosity LHC (HL-LHC) is expected to collect 3 ab^{-1} of data. Assuming similar systematic uncertainties and negligible change of cross-sections, the expected signal strength for the non-resonant 4ℓ channel is estimated to be:

$$\mu_{t\bar{t}H} = 1.00^{+0.23}_{-0.20} = 1.00^{+0.17}_{-0.12} (\text{stat.})^{+0.15}_{-0.15} (\text{sys.}). \quad (10.6)$$

The expected significance is 4.63σ . The systematic and statistical uncertainties reach similar values with the extensive increase in statistics. An adapted strategy and optimisation of physics objects need to be applied to exceed 5σ . An overview of the expected signal sensitivities is summarised in Table 10.1. Furthermore, the expected significances for $t\bar{t}H$ and post-fit yields for the $t\bar{t}H$ and dominant background $t\bar{t}Z$ process are shown.

By combining the 4ℓ channel measurement with the other analysis channels [15], a signal strength of

$$\mu_{t\bar{t}H} = 0.63^{+0.20}_{-0.19} = 0.63^{+0.17}_{-0.16} (\text{stat.})^{+0.11}_{-0.10} (\text{sys.}) \quad (10.7)$$

is obtained. It corresponds to an observed (expected) significance of 3.3σ (5.3σ) for a SM Higgs boson with a mass of 125 GeV . The measured production cross-section is

$$\sigma_{t\bar{t}H} = 321^{+102}_{-99} \text{ fb} \quad (10.8)$$

$\int \mathcal{L} dt$	$t\bar{t}H$	$t\bar{t}Z$	$\mu_{t\bar{t}H}$	Significance
HL-LHC 3000 fb ⁻¹	228 ± 50	2520 ± 178	$1.00^{+0.23}_{-0.20} = 1.00^{+0.17}_{-0.12} \text{ (stat.) } ^{+0.15}_{-0.15} \text{ (sys.)}$	4.63σ
Run 2 + Run 3 440 fb ⁻¹	42 ± 16	370 ± 37	$1.00^{+0.42}_{-0.37} = 1.00^{+0.39}_{-0.33} \text{ (stat.) } ^{+0.16}_{-0.16} \text{ (sys.)}$	3σ
Run 2 140 fb ⁻¹	13 ± 9	118 ± 17	$1.00^{+0.71}_{-0.60} = 1.00^{+0.69}_{-0.57} \text{ (stat.) } ^{+0.17}_{-0.18} \text{ (sys.)}$	1.8σ
Projection down to 80 fb ⁻¹	7.7 ± 6.5	67 ± 12	$1.00^{+0.94}_{-0.76} = 1.00^{+0.92}_{-0.74} \text{ (stat.) } ^{+0.18}_{-0.19} \text{ (sys.)}$	1.4σ
Previous Analysis 80 fb ⁻¹	3.1 ± 0.3	5.0 ± 0.8	$1.00^{+1.03}_{-0.79} = 1.00^{+0.96}_{-0.76} \text{ (stat.) } ^{+0.37}_{-0.22} \text{ (sys.)}$	1.4σ
Previous Analysis Projection 140 fb ⁻¹	5.4 ± 0.5	9 ± 1	$1.00^{+0.79}_{-0.64} = 1.00^{+0.71}_{-0.59} \text{ (stat.) } ^{+0.35}_{-0.25} \text{ (sys.)}$	1.7σ

Table 10.1: The expected post-fit $t\bar{t}H$ and $t\bar{t}Z$ yields, estimated signal strength, and expected significance for $t\bar{t}H$ are presented for different projections of integrated luminosity. The change in centre-of-mass energy is neglected, and systematic uncertainties are assumed to behave similarly. The previous measurement, which uses 80 fb⁻¹ of collected data, follows a different analysis strategy. Its result and projection to the full Run 2 dataset are also presented.

and has compatibility of 7.2 % with the Standard Model prediction of 507^{+35}_{-50} fb. The large deviation from the SM expectation in the $2\ell\text{SS}+1\gamma_{\text{had}}$ channel is caused by downward fluctuation in data in the signal sensitive bins of that channel. Both statistical and systematic uncertainties influence the measurement. The normalisation of the dominant irreducible background processes $t\bar{t}Z$ and $t\bar{t}W$ have a major influence on the measurement. Leading systematic uncertainties are related to the $t\bar{t}t\bar{t}$ production cross-section and the modelling of the $t\bar{t}W$ background process.

The results of the measurement of the $t\bar{t}H$ signal strengths in STXS bins of the Higgs boson transverse momentum are summarised in Table 10.2. The large deviation between the observed values and SM expectation for the STXS bin which covers a Higgs transverse momentum of $120 \text{ GeV} \leq p_T^H < 200 \text{ GeV}$ is driven by a downward fluctuation in data and anti-correlation effects between the different STXS bin measurements. Nevertheless, the compatibility of the STXS measurement with the SM prediction is 28 %. Furthermore, the compatibility with the inclusive measurement is 55 % [15].

The $t\bar{t}H$ multi-lepton analysis strategy is based on the separation of signal and background events using multivariate techniques. These techniques become increasingly popular in ATLAS analyses and will also be used for Run 3. The multivariate approach is not only for separating signal and background contributions but also for suppressing fake leptons, a leading limitation of multi-lepton analyses. The lepton definitions used in the $t\bar{t}H$ multi-lepton analysis use the PLIV tool, which already outperforms standard isolation criteria. For Run 3, an improved version will be used

p_T^H Range	STXS Bin	$\mu_{t\bar{t}H}$	$\sigma_{t\bar{t}H}$ [fb]	σ^{SM} [fb]
$p_T^H < 120$ GeV	01	$0.78^{+0.41}_{-0.40}$	231^{+122}_{-119}	297^{+20}_{-29}
$120 \text{ GeV} \leq p_T^H < 200$ GeV	2	$0.08^{+0.64}_{-0.60}$	10^{+81}_{-76}	127^{+9}_{-12}
$p_T^H \geq 200$ GeV	345	$1.19^{+0.64}_{-0.61}$	92^{+49}_{-47}	77^{+5}_{-8}

Table 10.2: The observed signal strengths and cross-sections for each STXS bin. The SM expectation for the cross-sections are given as reference. All values are taken from Ref. [15].

called *Prompt Lepton Isolation Tagger* (PLIT). Other limitations originate from uncertainties on the predicted $t\bar{t}H$ production cross-section and $t\bar{t}W$ modelling.

The results of the $t\bar{t}H$ multi-lepton analysis will be combined with other measurements like the $t\bar{t}(H \rightarrow b\bar{b})$ and $t\bar{t}(H \rightarrow \gamma\gamma)$ ones in which not only the inclusive $t\bar{t}H$ production cross-section is measured, but also the production cross-section in STXS bins of the Higgs boson transverse momentum, providing an even deeper insight into properties of the Higgs mechanism.

Bibliography

- [1] K. Popper, *Logik der Forschung - Zur Erkenntnistheorie der Modernen Naturwissenschaft*. Springer Vienna, Wien, 1935.
- [2] H. Keuth, *Karl Popper: Logik der Forschung*. Walter de Gruyter, Berlin, 2013.
- [3] M. Kobayashi and T. Maskawa, *CP Violation in the Renormalizable Theory of Weak Interaction*, Prog. Theor. Phys. **49** (1973) 652–657.
- [4] CDF Collaboration, *Observation of top quark production in $\bar{p}p$ collisions*, Phys. Rev. Lett. **74** (1995) 2626–2631.
- [5] DØ Collaboration, *Observation of the top quark*, Phys. Rev. Lett. **74** (1995) 2632–2637.
- [6] P. W. Anderson, *Plasmons, Gauge Invariance, and Mass*, Phys. Rev. **130** (1963) 439–442.
- [7] P. W. Higgs, *Broken symmetries, massless particles and gauge fields*, Phys. Lett. **12** (1964) 132–133.
- [8] F. Englert and R. Brout, *Broken Symmetry and the Mass of Gauge Vector Mesons*, Phys. Rev. Lett. **13** (1964) 321–323.
- [9] G. S. Guralnik, C. R. Hagen, and T. W. B. Kibble, *Global Conservation Laws and Massless Particles*, Phys. Rev. Lett. **13** (1964) 585–587.
- [10] ATLAS Collaboration, *Observation of a new particle in the search for the Standard Model Higgs boson with the ATLAS detector at the LHC*, Phys. Lett. B **716** (2012) 1–29.
- [11] CMS Collaboration, *Observation of a New Boson at a Mass of 125 GeV with the CMS Experiment at the LHC*, Phys. Lett. B **716** (2012) 30–61.

- [12] ATLAS and CMS Collaborations, *Measurements of the Higgs boson production and decay rates and constraints on its couplings from a combined ATLAS and CMS analysis of the LHC pp collision data at $\sqrt{s} = 7$ and 8 TeV*, JHEP **08** (2016) 045.
- [13] ATLAS Collaboration, *Evidence for the spin-0 nature of the Higgs boson using ATLAS data*, Phys. Lett. B **726** (2013) 120–144.
- [14] CDF Collaboration, *Exclusion of an Exotic Top Quark with $-4/3$ Electric Charge Using Soft Lepton Tagging*, Phys. Rev. Lett. **105** (2010) 101801.
- [15] ATLAS Collaboration, *Measurement of the Higgs boson production in association with top quarks in multilepton final states in pp collisions at $\sqrt{s} = 13$ TeV with the ATLAS detector*, arXiv:2510.23755 (2025).
- [16] P. D. Group), *Review of particle physics*, Prog. Theor. Exp. Phys. **2022** (2022) 083C01.
- [17] S. L. Glashow, *Partial Symmetries of Weak Interactions*, Nucl. Phys. **22** (1961) 579–588.
- [18] S. Weinberg, *A model of leptons*, Phys. Rev. Lett. **19** (1967) 1264.
- [19] A. Salam, *Weak and Electromagnetic Interactions*, Conf. Proc. C **680519** (1968) 367–377.
- [20] S. L. Glashow, J. Iliopoulos, and L. Maiani, *Weak Interactions with Lepton-Hadron Symmetry*, Phys. Rev. D **2** (1970) 1285–1292.
- [21] H. Georgi and S. L. Glashow, *Unified weak and electromagnetic interactions without neutral currents*, Phys. Rev. Lett. **28** (1972) 1494.
- [22] D. J. Gross and F. Wilczek, *Ultraviolet Behavior of Nonabelian Gauge Theories*, Phys. Rev. Lett. **30** (1973) 1343–1346.
- [23] H. D. Politzer, *Reliable Perturbative Results for Strong Interactions?*, Phys. Rev. Lett. **30** (1973) 1346–1349.
- [24] G. 't Hooft, *Renormalization of Massless Yang-Mills Fields*, Nucl. Phys. B **33** (1971) 173–199.
- [25] G. 't Hooft, *Renormalizable Lagrangians for Massive Yang-Mills Fields*, Nucl. Phys. B **35** (1971) 167–188.
- [26] G. 't Hooft and M. J. G. Veltman, *Regularization and Renormalization of Gauge Fields*, Nucl. Phys. B **44** (1972) 189–213.
- [27] G. 't Hooft and M. J. G. Veltman, *Combinatorics of gauge fields*, Nucl. Phys. B **50** (1972) 318–353.

- [28] C.-N. Yang and R. L. Mills, *Conservation of Isotopic Spin and Isotopic Gauge Invariance*, Phys. Rev. **96** (1954) 191–195.
- [29] Belle Collaboration, *Observation of a Charged Charmoniumlike Structure in $e^+e^- \rightarrow \pi^+\pi^- J/\psi$ at $\sqrt{s}=4.26$ GeV*, Phys. Rev. Lett. **110** (2013) 252001.
- [30] L. Collaboration, *Observation of $J/\psi\phi$ Structures Consistent with Exotic States from Amplitude Analysis of $B^+ \rightarrow J/\psi\phi K^+$ Decays*, Phys. Rev. Lett. **118** (2017) 022003.
- [31] L. Collaboration, *Observation of $J/\psi p$ Resonances Consistent with Pentaquark States in $\Lambda_b^0 \rightarrow J/\psi K^- p$ Decays*, Phys. Rev. Lett. **115** (2015) 072001.
- [32] E. Noether, *Invariant Variation Problems*, Gott. Nachr. **1918** (1918) 235–257.
- [33] H. Fritzsch, M. Gell-Mann, and H. Leutwyler, *Advantages of the Color Octet Gluon Picture*, Phys. Lett. B **47** (1973) 365–368.
- [34] D. J. Gross and F. Wilczek, *Asymptotically Free Gauge Theories I*, Phys. Rev. D **8** (1973) 3633–3652.
- [35] D. J. Gross and F. Wilczek, *Asymptotically Free Gauge Theories II*, Phys. Rev. D **9** (1974) 980–993.
- [36] S. Weinberg, *Nonabelian Gauge Theories of the Strong Interactions*, Phys. Rev. Lett. **31** (1973) 494–497.
- [37] M. Gell-Mann, *Symmetries of baryons and mesons*, Phys. Rev. **125** (1962) 1067–1084.
- [38] T. Kinoshita, *Mass singularities of Feynman amplitudes*, J. Math. Phys. **3** (1962) 650–677.
- [39] T. D. Lee and M. Nauenberg, *Degenerate Systems and Mass Singularities*, Phys. Rev. **133** (1964) B1549–B1562.
- [40] K. G. Wilson, *Nonlagrangian models of current algebra*, Phys. Rev. **179** (1969) 1499–1512.
- [41] C. G. Callan, Jr., *Broken scale invariance in scalar field theory*, Phys. Rev. D **2** (1970) 1541–1547.
- [42] K. Symanzik, *Small distance behavior in field theory and power counting*, Commun. Math. Phys. **18** (1970) 227–246.
- [43] N. H. Christ, B. Hasslacher, and A. H. Mueller, *Light cone behavior of perturbation theory*, Phys. Rev. D **6** (1972) 3543.

- [44] Y. Frishman, *Light Cone and Short Distances*, Phys. Rept. **13** (1974) 1.
- [45] K. G. Wilson, *Confinement of Quarks*, Phys. Rev. D **10** (1974) 2445–2459.
- [46] CDF Collaboration, *Measurement of the Strong Coupling Constant from Inclusive Jet Production at the Tevatron $\bar{p}p$ Collider*, Phys. Rev. Lett. **88** (2002) 042001.
- [47] ZEUS Collaboration, *Multijet production in neutral current deep inelastic scattering at HERA and determination of $\alpha(s)$* , Eur. Phys. J. C **44** (2005) 183–193.
- [48] ZEUS Collaboration, *Jet-radius dependence of inclusive-jet cross-sections in deep inelastic scattering at HERA*, Phys. Lett. B **649** (2007) 12–24.
- [49] DØ Collaboration, *Search for anomalous top quark couplings with the DØ detector*, Phys. Rev. Lett. **102** (2009) 092002.
- [50] H1 Collaboration, *Measurement of multijet production in ep collisions at high Q^2 and determination of the strong coupling α_s* , Eur. Phys. J. C **75** (2015) 65.
- [51] DØ Collaboration, *Determination of the strong coupling constant from the inclusive jet cross section in $p\bar{p}$ collisions at $\sqrt{s}=1.96$ TeV*, Phys. Rev. D **80** (2009) 111107.
- [52] B. Malaescu and P. Starovoitov, *Evaluation of the Strong Coupling Constant α_s Using the ATLAS Inclusive Jet Cross-Section Data*, Eur. Phys. J. C **72** (2012) 2041.
- [53] DØ Collaboration, *Measurement of angular correlations of jets at $\sqrt{s} = 1.96$ TeV and determination of the strong coupling at high momentum transfers*, Phys. Lett. B **718** (2012) 56–63.
- [54] CMS Collaboration, *Measurement of the Ratio of the Inclusive 3-Jet Cross Section to the Inclusive 2-Jet Cross Section in pp Collisions at $\sqrt{s} = 7$ TeV and First Determination of the Strong Coupling Constant in the TeV Range*, Eur. Phys. J. C **73** (2013) 2604.
- [55] CMS Collaboration, *Measurement of the inclusive 3-jet production differential cross section in proton–proton collisions at 7 TeV and determination of the strong coupling constant in the TeV range*, Eur. Phys. J. C **75** (2015) 186.
- [56] CMS Collaboration, *Constraints on parton distribution functions and extraction of the strong coupling constant from the inclusive jet cross section in pp collisions at $\sqrt{s} = 7$ TeV*, Eur. Phys. J. C **75** (2015) 288.
- [57] ATLAS Collaboration, *Measurement of transverse energy-energy correlations in multi-jet events in pp collisions at $\sqrt{s} = 7$ TeV using the ATLAS detector*

- and determination of the strong coupling constant $\alpha_s(m_Z)$* , Phys. Lett. B **750** (2015) 427–447.
- [58] H1 Collaboration, *Measurement of Jet Production Cross Sections in Deep-inelastic ep Scattering at HERA*, Eur. Phys. J. C **77** (2017) 215, [Erratum: Eur.Phys.J.C 81, 739 (2021)].
- [59] CMS Collaboration, *Measurement and QCD analysis of double-differential inclusive jet cross sections in pp collisions at $\sqrt{s} = 8$ TeV and cross section ratios to 2.76 and 7 TeV*, JHEP **03** (2017) 156.
- [60] CMS Collaboration, *Measurement of the triple-differential dijet cross section in proton-proton collisions at $\sqrt{s} = 8$ TeV and constraints on parton distribution functions*, Eur. Phys. J. C **77** (2017) 746.
- [61] ATLAS Collaboration, *Determination of the strong coupling constant α_s from transverse energy–energy correlations in multijet events at $\sqrt{s} = 8$ TeV using the ATLAS detector*, Eur. Phys. J. C **77** (2017) 872.
- [62] D. Britzger, et al., *Determination of the strong coupling constant using inclusive jet cross section data from multiple experiments*, Eur. Phys. J. C **79** (2019) 68.
- [63] C. S. Wu, et al., *Experimental Test of Parity Conservation in β Decay*, Phys. Rev. **105** (1957) 1413–1414.
- [64] M. Goldhaber, L. Grodzins, and A. W. Sunyar, *Helicity of Neutrinos*, Phys. Rev. **109** (1958) 1015–1017.
- [65] UA1 Collaboration, *Experimental Observation of Lepton Pairs of Invariant Mass Around $95 \text{ GeV}/c^2$ at the CERN SPS Collider*, Phys. Lett. B **126** (1983) 398–410.
- [66] UA1 Collaboration, *Further Evidence for Charged Intermediate Vector Bosons at the SPS Collider*, Phys. Lett. B **129** (1983) 273–282.
- [67] UA2 Collaboration, *Evidence for $Z^0 \rightarrow e^+e^-$ at the CERN $\bar{p}p$ Collider*, Phys. Lett. B **129** (1983) 130–140.
- [68] UA2 Collaboration, *Observation of Single Isolated Electrons of High Transverse Momentum in Events with Missing Transverse Energy at the CERN anti-p p Collider*, Phys. Lett. B **122** (1983) 476–485.
- [69] ATLAS Collaboration, *Measurement of the forward-backward asymmetry of electron and muon pair-production in pp collisions at $\sqrt{s} = 7$ TeV with the ATLAS detector*, JHEP **09** (2015) 049.

- [70] LHC Higgs Cross Section Working Group, *Handbook of LHC Higgs Cross Sections: 4. Deciphering the Nature of the Higgs Sector*, [arXiv:1610.07922 \[hep-ph\]](#).
- [71] ATLAS Collaboration, *Combined measurement of the Higgs boson mass from the $H \rightarrow \gamma\gamma$ and $H \rightarrow ZZ^* \rightarrow 4\ell$ decay channels with the ATLAS detector using $\sqrt{s} = 7, 8$ and 13 TeV pp collision data*, Phys. Rev. Lett. **131** (2023) 251802.
- [72] CMS Collaboration, *Study of the Mass and Spin-Parity of the Higgs Boson Candidate Via Its Decays to Z Boson Pairs*, Phys. Rev. Lett. **110** (2013) 081803.
- [73] ATLAS Collaboration, *Test of CP-invariance of the Higgs boson in vector-boson fusion production and in its decay into four leptons*, JHEP **05** (2024) 105.
- [74] C. Anastasiou, et al., *Higgs Boson Gluon-Fusion Production in QCD at Three Loops*, Phys. Rev. Lett. **114** (2015) 212001.
- [75] C. Anastasiou, et al., *High precision determination of the gluon fusion Higgs boson cross-section at the LHC*, JHEP **05** (2016) 058.
- [76] Y. Li, et al., *Soft-virtual corrections to Higgs production at N^3LO* , Phys. Rev. D **91** (2015) 036008.
- [77] U. Aglietti, et al., *Two loop light fermion contribution to Higgs production and decays*, Phys. Lett. B **595** (2004) 432–441.
- [78] S. Actis, et al., *NLO Electroweak Corrections to Higgs Boson Production at Hadron Colliders*, Phys. Lett. B **670** (2008) 12–17.
- [79] R. V. Harlander and W. B. Kilgore, *Next-to-next-to-leading order Higgs production at hadron colliders*, Phys. Rev. Lett. **88** (2002) 201801.
- [80] C. Anastasiou and K. Melnikov, *Higgs boson production at hadron colliders in NNLO QCD*, Nucl. Phys. B **646** (2002) 220–256.
- [81] V. Ravindran, J. Smith, and W. L. van Neerven, *NNLO corrections to the total cross-section for Higgs boson production in hadron hadron collisions*, Nucl. Phys. B **665** (2003) 325–366.
- [82] J. Baglio and A. Djouadi, *Higgs production at the LHC*, JHEP **03** (2011) 055.
- [83] LHC Top Working Group, *Standalone Summary Plots*, 2024. <https://twiki.cern.ch/twiki/bin/view/LHCPhysics/LHCTopWGSummaryPlots> (Accessed: Aug. 26, 2024).

- [84] M. Cacciari, et al., *Top-pair production at hadron colliders with next-to-next-to-leading logarithmic soft-gluon resummation*, Phys. Lett. B **710** (2012) 612–622.
- [85] P. Bärnreuther, M. Czakon, and A. Mitov, *Percent Level Precision Physics at the Tevatron: First Genuine NNLO QCD Corrections to $q\bar{q} \rightarrow t\bar{t} + X$* , Phys. Rev. Lett. **109** (2012) 132001.
- [86] M. Czakon and A. Mitov, *NNLO corrections to top-pair production at hadron colliders: the all-fermionic scattering channels*, JHEP **12** (2012) 054.
- [87] M. Czakon and A. Mitov, *NNLO corrections to top pair production at hadron colliders: the quark-gluon reaction*, JHEP **01** (2013) 080.
- [88] M. Czakon, P. Fiedler, and A. Mitov, *Total Top-Quark Pair-Production Cross Section at Hadron Colliders Through $O(\alpha_S^4)$* , Phys. Rev. Lett. **110** (2013) 252004.
- [89] M. Czakon and A. Mitov, *Top++: A Program for the Calculation of the Top-Pair Cross-Section at Hadron Colliders*, Comput. Phys. Commun. **185** (2014) 2930.
- [90] A. Collaboration, *Study of the CP properties of the Higgs Boson using Higgs production in association with top quarks using the ATLAS detector at the CERN LHC*, tech. rep., CERN, Geneva, 2020.
<https://cds.cern.ch/record/2709463>.
- [91] D. Buttazzo, et al., *Investigating the near-criticality of the Higgs boson*, JHEP **12** (2013) 089.
- [92] A. Djouadi, M. Spira, and P. M. Zerwas, *Production of Higgs bosons in proton colliders: QCD corrections*, Phys. Lett. B **264** (1991) 440–446.
- [93] S. Dawson, *Radiative corrections to Higgs boson production*, Nucl. Phys. B **359** (1991) 283–300.
- [94] M. Spira, et al., *Higgs boson production at the LHC*, Nucl. Phys. B **453** (1995) 17–82.
- [95] ATLAS Collaboration, *Observation of Higgs boson production in association with a top quark pair at the LHC with the ATLAS detector*, Phys. Lett. B **784** (2018) 173–191.
- [96] CMS Collaboration, *Observation of $t\bar{t}H$ production*, Phys. Rev. Lett. **120** (2018) 231801.
- [97] G. R. Farrar and M. E. Shaposhnikov, *Baryon asymmetry of the universe in the minimal Standard Model*, Phys. Rev. Lett. **70** (1993) 2833–2836,
[Erratum: Phys.Rev.Lett. 71, 210 (1993)].

- [98] W. Bernreuther, *CP violation and baryogenesis*, Lect. Notes Phys. **591** (2002) 237–293.
- [99] F. Demartin, et al., *Higgs production in association with a single top quark at the LHC*, Eur. Phys. J. C **75** (2015) 267.
- [100] F. Boudjema, et al., *Lab-frame observables for probing the top-Higgs interaction*, Phys. Rev. D **92** (2015) 015019.
- [101] S. Khatibi and M. Mohammadi Najafabadi, *Exploring the Anomalous Higgs-top Couplings*, Phys. Rev. D **90** (2014) 074014.
- [102] F. Demartin, et al., *Higgs characterisation at NLO in QCD: CP properties of the top-quark Yukawa interaction*, Eur. Phys. J. C **74** (2014) 3065.
- [103] J. Ellis, et al., *Disentangling Higgs-Top Couplings in Associated Production*, JHEP **04** (2014) 004.
- [104] J. Brod, U. Haisch, and J. Zupan, *Constraints on CP-violating Higgs couplings to the third generation*, JHEP **11** (2013) 180.
- [105] S. Amor Dos Santos et al., *Probing the CP nature of the Higgs coupling in $t\bar{t}h$ events at the LHC*, Phys. Rev. D **96** (2017) 013004.
- [106] ATLAS Collaboration, *Constraints on the Higgs boson self-coupling from single- and double-Higgs production with the ATLAS detector using pp collisions at $\sqrt{s} = 13$ TeV*, Phys. Lett. B **843** (2023) 137745.
- [107] G. Degrandi, et al., *Probing the Higgs self coupling via single Higgs production at the LHC*, JHEP **12** (2016) 080.
- [108] S. Di Vita, et al., *A global view on the Higgs self-coupling*, JHEP **09** (2017) 069.
- [109] F. Maltoni, et al., *Trilinear Higgs coupling determination via single-Higgs differential measurements at the LHC*, Eur. Phys. J. C **77** (2017) 887.
- [110] T. Hambye and K. Riesselmann, *Matching conditions and Higgs mass upper bounds revisited*, Phys. Rev. D **55** (1997) 7255–7262.
- [111] P. B. Arnold and S. Vokos, *Instability of hot electroweak theory: bounds on m_H and m_t* , Phys. Rev. D **44** (1991) 3620–3627.
- [112] J. A. Casas, J. R. Espinosa, and M. Quiros, *Improved Higgs mass stability bound in the standard model and implications for supersymmetry*, Phys. Lett. B **342** (1995) 171–179.
- [113] G. Isidori, G. Ridolfi, and A. Strumia, *On the metastability of the standard model vacuum*, Nucl. Phys. B **609** (2001) 387–409.

- [114] J. R. Espinosa, G. F. Giudice, and A. Riotto, *Cosmological implications of the Higgs mass measurement*, JCAP **05** (2008) 002.
- [115] ATLAS Collaboration, *CP Properties of Higgs Boson Interactions with Top Quarks in the $t\bar{t}H$ and tH Processes Using $H \rightarrow \gamma\gamma$ with the ATLAS Detector*, Phys. Rev. Lett. **125** (2020) 061802.
- [116] ATLAS Collaboration, *Measurement of the properties of Higgs boson production at $\sqrt{s} = 13$ TeV in the $H \rightarrow \gamma\gamma$ channel using 139 fb^{-1} of pp collision data with the ATLAS experiment*, JHEP **07** (2023) 088.
- [117] CMS Collaboration, *Measurements of Higgs boson production cross sections and couplings in the diphoton decay channel at $\sqrt{s} = 13$ TeV*, JHEP **07** (2021) 027.
- [118] CMS Collaboration, *Measurements of $t\bar{t}H$ Production and the CP Structure of the Yukawa Interaction between the Higgs Boson and Top Quark in the Diphoton Decay Channel*, Phys. Rev. Lett. **125** (2020) 061801.
- [119] ATLAS Collaboration, *Higgs boson production cross-section measurements and their EFT interpretation in the 4ℓ decay channel at $\sqrt{s} = 13$ TeV with the ATLAS detector*, Eur. Phys. J. C **80** (2020) 957, [Erratum: Eur.Phys.J.C 81, 29 (2021), Erratum: Eur.Phys.J.C 81, 398 (2021)].
- [120] CMS Collaboration, *Constraints on anomalous Higgs boson couplings to vector bosons and fermions in its production and decay using the four-lepton final state*, Phys. Rev. D **104** (2021) 052004.
- [121] ATLAS Collaboration, *Probing the CP nature of the top-Higgs Yukawa coupling in $t\bar{t}H$ and tH events with $H \rightarrow b\bar{b}$ decays using the ATLAS detector at the LHC*, Phys. Lett. B **849** (2024) 138469.
- [122] ATLAS Collaboration, *Measurement of Higgs boson decay into b-quarks in associated production with a top-quark pair in pp collisions at $\sqrt{s} = 13$ TeV with the ATLAS detector*, JHEP **06** (2022) 097.
- [123] ATLAS Collaboration, *Measurement of the associated production of a top-antitop-quark pair and a Higgs boson decaying into a $b\bar{b}$ pair in pp collisions at $\sqrt{s} = 13$ TeV using the ATLAS detector at the LHC*, tech. rep., CERN, Geneva, 2024. [arXiv:2407.10904](https://arxiv.org/abs/2407.10904).
<https://cds.cern.ch/record/2904447>.
- [124] CMS Collaboration, *Measurement of the $t\bar{t}H$ and tH production rates in the $H \rightarrow b\bar{b}$ decay channel using proton-proton collision data at $\sqrt{s} = 13$ TeV*, [arXiv:2407.10896](https://arxiv.org/abs/2407.10896) [hep-ex].
- [125] ATLAS Collaboration, *Analysis of $t\bar{t}H$ and $t\bar{t}W$ production in multilepton final states with the ATLAS detector*, tech. rep., CERN, Geneva, 2019.
[http://cds.cern.ch/record/2693930](https://cds.cern.ch/record/2693930).

- [126] J. A. Dror, et al., *Strong tW Scattering at the LHC*, JHEP **01** (2016) 071.
- [127] ATLAS Collaboration, *Measurement of the total and differential cross-sections of $t\bar{t}W$ production in pp collisions at $\sqrt{s} = 13$ TeV with the ATLAS detector*, JHEP **05** (2024) 131.
- [128] S. Höche, *Introduction to parton-shower event generators*, pp. , 235–295. 2015. [arXiv:1411.4085 \[hep-ph\]](#).
- [129] J. C. Collins, D. E. Soper, and G. F. Sterman, *Factorization of Hard Processes in QCD*, Adv. Ser. Direct. High Energy Phys. **5** (1989) 1–91.
- [130] J. D. Bjorken, *Asymptotic Sum Rules at Infinite Momentum*, Phys. Rev. **179** (1969) 1547–1553.
- [131] R. P. Feynman, *Very high-energy collisions of hadrons*, Phys. Rev. Lett. **23** (1969) 1415–1417.
- [132] J. D. Bjorken and E. A. Paschos, *Inelastic Electron Proton and γ Proton Scattering, and the Structure of the Nucleon*, Phys. Rev. **185** (1969) 1975–1982.
- [133] E. D. Bloom et al., *High-Energy Inelastic e - p Scattering at 6-Degrees and 10-Degrees*, Phys. Rev. Lett. **23** (1969) 930–934.
- [134] J. I. Friedman and H. W. Kendall, *Deep inelastic electron scattering*, Ann. Rev. Nucl. Part. Sci. **22** (1972) 203–254.
- [135] Y. L. Dokshitzer, *Calculation of the Structure Functions for Deep Inelastic Scattering and e^+e^- Annihilation by Perturbation Theory in Quantum Chromodynamics.*, Sov. Phys. JETP **46** (1977) 641–653.
- [136] V. N. Gribov and L. N. Lipatov, *Deep inelastic e - p scattering in perturbation theory*, Sov. J. Nucl. Phys. **15** (1972) 438–450.
- [137] G. Altarelli and G. Parisi, *Asymptotic Freedom in Parton Language*, Nucl. Phys. B **126** (1977) 298–318.
- [138] L. A. Harland-Lang, et al., *Parton distributions in the LHC era: MMHT 2014 PDFs*, Eur. Phys. J. C **75** (2015) 204.
- [139] B. Andersson, et al., *Parton Fragmentation and String Dynamics*, Phys. Rept. **97** (1983) 31–145.
- [140] T. Sjostrand, *Jet Fragmentation of Nearby Partons*, Nucl. Phys. B **248** (1984) 469–502.
- [141] B. R. Webber, *A QCD Model for Jet Fragmentation Including Soft Gluon Interference*, Nucl. Phys. B **238** (1984) 492–528.

- [142] G. Marchesini and B. R. Webber, *Monte Carlo Simulation of General Hard Processes with Coherent QCD Radiation*, Nucl. Phys. B **310** (1988) 461–526.
- [143] D. Amati and G. Veneziano, *Preconfinement as a Property of Perturbative QCD*, Phys. Lett. B **83** (1979) 87–92.
- [144] ATLAS Collaboration, *The ATLAS Simulation Infrastructure*, Eur. Phys. J. C **70** (2010) 823–874.
- [145] GEANT4 Collaboration, *GEANT4—a simulation toolkit*, Nucl. Instrum. Meth. A **506** (2003) 250–303.
- [146] ATLAS Collaboration, *The simulation principle and performance of the ATLAS fast calorimeter simulation FastCaloSim*, ATL-COM-PHYS-2010-838 (2010).
- [147] T. Sjöstrand, et al., *An introduction to PYTHIA 8.2*, Comput. Phys. Commun. **191** (2015) 159–177.
- [148] ATLAS Collaboration, *The PYTHIA 8 A3 tune description of ATLAS minimum bias and inelastic measurements incorporating the Donnachie–Landshoff diffractive model*, ATL-PHYS-PUB-2016-017 (2016).
- [149] W. Buttinger, *Using Event Weights to account for differences in Instantaneous Luminosity and Trigger Prescale in Monte Carlo and Data*, tech. rep., CERN, Geneva, 2015. <https://cds.cern.ch/record/2014726>.
- [150] ATLAS Collaboration, *ATLAS Pythia 8 tunes to 7 TeV data*, LHC/ATLAS Experiment (2014).
- [151] D. J. Lange, *The EvtGen particle decay simulation package*, Nucl. Instrum. Meth. A **462** (2001) 152–155.
- [152] S. Frixione, P. Nason, and G. Ridolfi, *A Positive-weight next-to-leading-order Monte Carlo for heavy flavour hadroproduction*, JHEP **09** (2007) 126.
- [153] P. Nason, *A New method for combining NLO QCD with shower Monte Carlo algorithms*, JHEP **11** (2004) 040.
- [154] S. Frixione, P. Nason, and C. Oleari, *Matching NLO QCD computations with Parton Shower simulations: the POWHEG method*, JHEP **11** (2007) 070.
- [155] S. Alioli, et al., *A general framework for implementing NLO calculations in shower Monte Carlo programs: the POWHEG BOX*, JHEP **06** (2010) 043.
- [156] H. B. Hartanto, et al., *Higgs boson production in association with top quarks in the POWHEG BOX*, Phys. Rev. D **91** (2015) 094003.
- [157] NNPDF Collaboration, *Parton distributions for the LHC Run II*, JHEP **04** (2015) 040.

- [158] J. Bellm et al., *Herwig 7.0/Herwig++ 3.0 release note*, Eur. Phys. J. C **76** (2016) 196.
- [159] M. Bahr et al., *Herwig++ Physics and Manual*, Eur. Phys. J. C **58** (2008) 639–707.
- [160] ATLAS Collaboration, *Studies on the improvement of the matching uncertainty definition in top-quark processes simulated with Powheg+Pythia 8*, tech. rep., CERN, Geneva, 2023. <https://cds.cern.ch/record/2872787>.
- [161] E. Bothmann, *Event Generation with Sherpa 2.2*, SciPost Phys. **7** (2019) 034.
- [162] T. Gleisberg, et al., *Event generation with SHERPA 1.1*, JHEP **02** (2009) 007.
- [163] T. Gleisberg and S. Hoeche, *Comix, a new matrix element generator*, JHEP **12** (2008) 039.
- [164] F. Cascioli, P. Maierhofer, and S. Pozzorini, *Scattering Amplitudes with Open Loops*, Phys. Rev. Lett. **108** (2012) 111601.
- [165] A. Denner, S. Dittmaier, and L. Hofer, *Collier: a fortran-based Complex One-Loop Library in Extended Regularizations*, Comput. Phys. Commun. **212** (2017) 220–238.
- [166] F. Buccioni, et al., *OpenLoops 2*, Eur. Phys. J. C **79** (2019) 866.
- [167] S. Schumann and F. Krauss, *A Parton shower algorithm based on Catani-Seymour dipole factorisation*, JHEP **03** (2008) 038.
- [168] S. Hoeche, et al., *QCD matrix elements + parton showers: The NLO case*, JHEP **04** (2013) 027.
- [169] S. Kallweit, et al., *NLO QCD+EW predictions for $V + jets$ including off-shell vector-boson decays and multijet merging*, JHEP **04** (2016) 021.
- [170] C. Gütschow, J. M. Lindert, and M. Schönherr, *Multi-jet merged top-pair production including electroweak corrections*, Eur. Phys. J. C **78** (2018) 317.
- [171] R. Frederix, D. Pagani, and M. Zaro, *Large NLO corrections in $t\bar{t}W^\pm$ and $t\bar{t}t\bar{t}$ hadroproduction from supposedly subleading EW contributions*, JHEP **02** (2018) 031.
- [172] R. Frederix and I. Tsirikos, *On improving NLO merging for $t\bar{t}W$ production*, JHEP **11** (2021) 029.
- [173] R. Frederix and S. Frixione, *Merging meets matching in MC@NLO*, JHEP **12** (2012) 061.

- [174] J. Alwall, et al., *The automated computation of tree-level and next-to-leading order differential cross sections, and their matching to parton shower simulations*, JHEP **07** (2014) 079.
- [175] S. Frixione, et al., *Angular correlations of lepton pairs from vector boson and top quark decays in Monte Carlo simulations*, JHEP **04** (2007) 081.
- [176] P. Artoisenet, et al., *Automatic spin-entangled decays of heavy resonances in Monte Carlo simulations*, JHEP **03** (2013) 015.
- [177] E. Re, *Single-top Wt -channel production matched with parton showers using the POWHEG method*, Eur. Phys. J. C **71** (2011) 1547.
- [178] R. Frederix, E. Re, and P. Torrielli, *Single-top t -channel hadroproduction in the four-flavour scheme with POWHEG and aMC@NLO*, JHEP **09** (2012) 130.
- [179] S. Alioli, et al., *NLO single-top production matched with shower in POWHEG: s - and t -channel contributions*, JHEP **09** (2009) 111, [Erratum: JHEP 02, 011 (2010)].
- [180] ATLAS Collaboration, *Studies on top-quark Monte Carlo modelling for Top2016*, ATL-PHYS-PUB-2016-020 (2016).
- [181] S. Frixione, et al., *Single-top hadroproduction in association with a W boson*, JHEP **07** (2008) 029.
- [182] T. Ježo, et al., *New NLOPS predictions for $t\bar{t} + b$ -jet production at the LHC*, Eur. Phys. J. C **78** (2018) 502.
- [183] F. Cascioli, et al., *NLO matching for $t\bar{t}b\bar{b}$ production with massive b -quarks*, Physics Letters B **734** (2014) 210–214.
- [184] M. Beneke, et al., *Hadronic top-quark pair production with NNLL threshold resummation*, Nucl. Phys. B **855** (2012) 695–741.
- [185] N. Kidonakis, *Two-loop soft anomalous dimensions for single top quark associated production with a W^- or H^-* , Phys. Rev. D **82** (2010) 054018.
- [186] L. Evans and P. Bryant, *LHC Machine*, JINST **3** (2008) S08001.
- [187] ATLAS Collaboration, *The ATLAS Experiment at the CERN Large Hadron Collider*, JINST **3** (2008) S08003.
- [188] CMS Collaboration, *The CMS Experiment at the CERN LHC*, JINST **3** (2008) S08004.
- [189] LHCb Collaboration, *The LHCb Detector at the LHC*, JINST **3** (2008) S08005.

- [190] ALICE Collaboration, *The ALICE experiment at the CERN LHC*, JINST **3** (2008) S08002.
- [191] ATLAS Collaboration, *Luminosity Public Results Run 2*, 2024.
<https://twiki.cern.ch/twiki/bin/view/AtlasPublic/LuminosityPublicResultsRun2> (Accessed: Sept. 09, 2024).
- [192] ATLAS Collaboration, *ATLAS inner detector: Technical Design Report, 1*. Technical design report. ATLAS. CERN, Geneva, 1997.
<https://cds.cern.ch/record/331063>.
- [193] ATLAS Collaboration, *ATLAS inner detector: Technical Design Report, 2*. Technical design report. ATLAS. CERN, Geneva, 1997.
<https://cds.cern.ch/record/331064>.
- [194] ATLAS Collaboration, *ATLAS central solenoid: Technical Design Report*. Technical design report. ATLAS. CERN, Geneva, 1997.
<https://cds.cern.ch/record/331067>.
- [195] ATLAS Collaboration, *Production and Integration of the ATLAS Insertable B-Layer*, JINST **13** (2018) T05008.
- [196] A. Ahmad et al., *The Silicon microstrip sensors of the ATLAS semiconductor tracker*, Nucl. Instrum. Meth. A **578** (2007) 98–118.
- [197] ATLAS Collaboration, *ATLAS liquid-argon calorimeter: Technical Design Report*. Technical design report. ATLAS. CERN, Geneva, 1996.
<https://cds.cern.ch/record/331061>.
- [198] ATLAS Collaboration, *ATLAS tile calorimeter: Technical Design Report*. Technical design report. ATLAS. CERN, Geneva, 1996.
<https://cds.cern.ch/record/331062>.
- [199] ATLAS Collaboration, *ATLAS barrel toroid: Technical Design Report*. Technical design report. ATLAS. CERN, Geneva, 1997.
<https://cds.cern.ch/record/331065>.
- [200] ATLAS Collaboration, *ATLAS end-cap toroids: Technical Design Report*. Technical design report. ATLAS. CERN, Geneva, 1997.
<https://cds.cern.ch/record/331066>.
- [201] ATLAS Collaboration, *Performance of the ATLAS Trigger System in 2015*, Eur. Phys. J. C **77** (2017) 317.
- [202] ATLAS Collaboration, *Operation of the ATLAS trigger system in Run 2*, JINST **15** (2020) P10004.

- [203] S. Baranov, et al., *Estimation of Radiation Background, Impact on Detectors, Activation and Shielding Optimization in ATLAS*, tech. rep., CERN, Geneva, 2005. <https://cds.cern.ch/record/814823>.
- [204] ATLAS Collaboration, *Modelling radiation damage to pixel sensors in the ATLAS detector*, JINST **14** (2019) P06012.
- [205] ROSE Collaboration, *3rd RD48 status report*, tech. rep., CERN, Geneva, 1999. <https://cds.cern.ch/record/421210>.
- [206] ROSE Collaboration, *Developments for radiation hard silicon detectors by defect engineering - Results by the CERN RD48 (ROSE) Collaboration*, Nucl. Instrum. Meth. A **465** (2000) 60–69.
- [207] S. Parker, C. Kenney, and J. Segal, *3D — A proposed new architecture for solid-state radiation detectors*, Nucl. Instr. and Meth. A **395** (1997) 328–343.
- [208] ATLAS Collaboration, *Measurements of sensor radiation damage in the ATLAS inner detector using leakage currents*, JINST **16** (2021) P08025.
- [209] *Silvaco*, <https://silvaco.com/tcad/>. Accessed: 2024-11-26.
- [210] V. Chiochia et al., *A Double junction model of irradiated silicon pixel sensors for LHC*, Nucl. Instrum. Meth. A **568** (2006) 51–55.
- [211] W. Shockley, *Currents to conductors induced by a moving point charge*, J. Appl. Phys. **9** (1938) 635–636.
- [212] S. Ramo, *Currents induced by electron motion*, Proc. Ire. **27** (1939) 584–585.
- [213] A. Rosenfeld and J. L. Pfaltz, *Sequential operations in digital picture processing*, J. ACM **13** (1966) 471–494.
- [214] ATLAS Collaboration, *Performance of the ATLAS Track Reconstruction Algorithms in Dense Environments in LHC Run 2*, Eur. Phys. J. C **77** (2017) 673.
- [215] T. Cornelissen, et al., *The new ATLAS track reconstruction (NEWT)*, J. Phys. Conf. Ser. **119** (2008) 032014.
- [216] T. G. Cornelissen, et al., *The global χ^2 track fitter in ATLAS*, J. Phys. Conf. Ser. **119** (2008) 032013.
- [217] ATLAS Collaboration, *Improved electron reconstruction in ATLAS using the Gaussian Sum Filter-based model for bremsstrahlung*, tech. rep., ATLAS-CONF-2012-047, 2012.
- [218] R. Frühwirth, *A Gaussian-mixture approximation of the Bethe-Heitler model of electron energy loss by bremsstrahlung*, Comp. Phys. Comm. **154** (2003) 131–142.

- [219] R. Fruhwirth, *Application of Kalman filtering to track and vertex fitting*, Nucl. Instrum. Meth. A **262** (1987) 444–450.
- [220] ATLAS Collaboration, *Reconstruction of primary vertices at the ATLAS experiment in Run 1 proton–proton collisions at the LHC*, Eur. Phys. J. C **77** (2017) 332.
- [221] ATLAS Collaboration, *Vertex Reconstruction Performance of the ATLAS Detector at $\sqrt{s} = 13$ TeV*, tech. rep., CERN, Geneva, 2015.
<https://cds.cern.ch/record/2037717>.
- [222] ATLAS Collaboration, *Electron reconstruction and identification in the ATLAS experiment using the 2015 and 2016 LHC proton-proton collision data at $\sqrt{s} = 13$ TeV*, Eur. Phys. J. C **79** (2019) 639.
- [223] W. Lampl et al., *Calorimeter clustering algorithms: description and performance*, tech. rep., ATL-LARG-PUB-2008-002, 2008.
- [224] ATLAS Collaboration, *Electron and photon performance measurements with the ATLAS detector using the 2015–2017 LHC proton-proton collision data*, JINST **14** (2019) P12006.
- [225] ATLAS Collaboration, *Electron efficiency measurements with the ATLAS detector using 2012 LHC proton–proton collision data*, Eur. Phys. J. C **77** (2017) 195.
- [226] M. Cacciari and G. P. Salam, *Pileup subtraction using jet areas*, Phys. Lett. B **659** (2008) 119–126.
- [227] ATLAS Collaboration, *Muon reconstruction performance of the ATLAS detector in proton–proton collision data at $\sqrt{s} = 13$ TeV*, Eur. Phys. J. C **76** (2016) 292.
- [228] F. He, et al., *Tagging non-prompt electrons and muons using lifetime and isolation information*, tech. rep., CERN, Geneva, 2022.
<https://cds.cern.ch/record/2800472>.
- [229] ATLAS Collaboration, *Jet reconstruction and performance using particle flow with the ATLAS Detector*, Eur. Phys. J. C **77** (2017) 466.
- [230] M. Cacciari, G. P. Salam, and G. Soyez, *The anti- k_t jet clustering algorithm*, JHEP **04** (2008) 063.
- [231] G. P. Salam, *Towards Jetography*, Eur. Phys. J. C **67** (2010) 637–686.
- [232] ATLAS Collaboration, *Jet energy scale measurements and their systematic uncertainties in proton-proton collisions at $\sqrt{s} = 13$ TeV with the ATLAS detector*, Phys. Rev. D **96** (2017) 072002.

- [233] M. Cacciari, G. P. Salam, and G. Soyez, *The Catchment Area of Jets*, JHEP **04** (2008) 005.
- [234] ATLAS Collaboration, *Jet energy measurement with the ATLAS detector in proton-proton collisions at $\sqrt{s} = 7$ TeV*, Eur. Phys. J. C **73** (2013) 2304.
- [235] ATLAS Collaboration, *Performance of pile-up mitigation techniques for jets in pp collisions at $\sqrt{s} = 8$ TeV using the ATLAS detector*, Eur. Phys. J. C **76** (2016) 581.
- [236] M. Cacciari, G. P. Salam, and G. Soyez, *FastJet User Manual*, Eur. Phys. J. C **72** (2012) 1896.
- [237] ATLAS Collaboration, *ATLAS flavour-tagging algorithms for the LHC Run 2 pp collision dataset*, Eur. Phys. J. C **83** (2023) 681.
- [238] ATLAS Collaboration, *ATLAS b-jet identification performance and efficiency measurement with $t\bar{t}$ events in pp collisions at $\sqrt{s} = 13$ TeV*, Eur. Phys. J. C **79** (2019) 970.
- [239] ATLAS Collaboration, *Performance of b-Jet Identification in the ATLAS Experiment*, JINST **11** (2016) P04008.
- [240] ATLAS Collaboration, *Identification of hadronic tau lepton decays using neural networks in the ATLAS experiment*, tech. rep., CERN, Geneva, 2019. <https://cds.cern.ch/record/2688062>.
- [241] ATLAS Collaboration, *Performance of missing transverse momentum reconstruction with the ATLAS detector using proton-proton collisions at $\sqrt{s} = 13$ TeV*, Eur. Phys. J. C **78** (2018) 903.
- [242] D. E. Rumelhart, G. E. Hinton, and R. J. Williams, *Learning representations by back-propagating errors*, Nature **323** (1986) 533–536.
- [243] T. Dozat, *Incorporating Nesterov Momentum into Adam*, pp. , 1–4. 2016.
- [244] A. Paszke, et al., *PyTorch: An Imperative Style, High-Performance Deep Learning Library*, pp. , 8024–8035. Curran Associates, Inc., 2019.
- [245] R. Tibshirani, *Regression Shrinkage and Selection Via the Lasso*, J. Roy. Statist. Soc. B **58** (1996) 267–288.
- [246] A. E. Hoerl and R. W. Kennard, *Ridge Regression: Biased Estimation for Nonorthogonal Problems*, Technometrics **12** (1970) 55–67.
- [247] N. Srivastava, et al., *Dropout: A Simple Way to Prevent Neural Networks from Overfitting*, J. Machine Learning Res. **15** (2014) 1929–1958.
- [248] L. Breiman, et al., *Classification and Regression Trees*. Chapman and Hall/CRC, 10, 2017.

- [249] Y. Freund and R. E. Schapire, *A Decision-Theoretic Generalization of On-Line Learning and an Application to Boosting*, J. Comput. Syst. Sci. **55** (1997) 119–139.
- [250] Y. Coadou, *Boosted Decision Trees and Applications*, EPJ Web Conf. **55** (2013) 02004.
- [251] R. E. Schapire, *The strength of weak learnability*, Machine Learning **5** (1990) 197–227.
- [252] Y. Freund and R. E. Schapire, *Experiments with a new boosting algorithm*, in *Proceedings of the Thirteenth International Conference on International Conference on Machine Learning*, p. , 148–156. Morgan Kaufmann Publishers Inc., San Francisco, CA, USA, 1996.
- [253] T. Chen and C. Guestrin, *XGBoost: A Scalable Tree Boosting System*, in *Proceedings of the 22nd ACM SIGKDD International Conference on Knowledge Discovery and Data Mining*, p. , 785–794. Association for Computing Machinery, New York, NY, USA, 2016.
<https://doi.org/10.1145/2939672.2939785>.
- [254] J. H. Friedman, *Greedy function approximation: A gradient boosting machine.*, Annals Statist. **29** (2001) 1189–1232.
- [255] C. G. Lester and D. J. Summers, *Measuring masses of semiinvisibly decaying particles pair produced at hadron colliders*, Phys. Lett. B **463** (1999) 99–103.
- [256] D. P. Kingma and J. Ba, *Adam: A Method for Stochastic Optimization*, 2017.
<https://arxiv.org/abs/1412.6980>.
- [257] CMS Collaboration, *Measurement of the Higgs boson production rate in association with top quarks in final states with electrons, muons, and hadronically decaying tau leptons at $\sqrt{s} = 13$ TeV*, Eur. Phys. J. C **81** (2021) 378.
- [258] J. Zhou, et al., *Graph neural networks: A review of methods and applications*, AI open **1** (2020) 57–81.
- [259] ATLAS Collaboration, *Tools for estimating fake/non-prompt lepton backgrounds with the ATLAS detector at the LHC*, JINST **18** (2023) T11004.
- [260] ATLAS Collaboration, *Luminosity determination in pp collisions at $\sqrt{s} = 13$ TeV using the ATLAS detector at the LHC*, Eur. Phys. J. C **83** (2023) 982.
- [261] ATLAS Collaboration, *Jet energy scale and resolution measured in proton–proton collisions at $\sqrt{s} = 13$ TeV with the ATLAS detector*, Eur. Phys. J. C **81** (2021) 689.

- [262] ATLAS Collaboration, *Determination of jet calibration and energy resolution in proton-proton collisions at $\sqrt{s} = 8$ TeV using the ATLAS detector*, Eur. Phys. J. C **80** (2020) 1104.
- [263] ATLAS Collaboration, *Measurements of b-jet tagging efficiency with the ATLAS detector using $t\bar{t}$ events at $\sqrt{s} = 13$ TeV*, JHEP **08** (2018) 089.
- [264] ATLAS Collaboration, *Measurement of the c-jet mistagging efficiency in $t\bar{t}$ events using pp collision data at $\sqrt{s} = 13$ TeV collected with the ATLAS detector*, Eur. Phys. J. C **82** (2022) 95.
- [265] ATLAS Collaboration, *Measurement of b-tagging Efficiency of c-jets in $t\bar{t}$ Events Using a Likelihood Approach with the ATLAS Detector*, tech. rep., CERN, Geneva, 2018. <https://cds.cern.ch/record/2306649>.
- [266] ATLAS Collaboration, *Calibration of light-flavour b-jet mistagging rates using ATLAS proton-proton collision data at $\sqrt{s} = 13$ TeV*, tech. rep., CERN, Geneva, 2018. <https://cds.cern.ch/record/2314418>.
- [267] ATLAS Collaboration, *E_T^{miss} performance in the ATLAS detector using 2015-2016 LHC p-p collisions*, tech. rep., CERN, Geneva, 2018. <http://cds.cern.ch/record/2625233>.
- [268] J. Butterworth et al., *PDF4LHC recommendations for LHC Run II*, J. Phys. G **43** (2016) 023001.
- [269] ATLAS Collaboration, *Measurement of the $t\bar{t}t\bar{t}$ production cross section in pp collisions at $\sqrt{s} = 13$ TeV with the ATLAS detector*, JHEP **11** (2021) 1–52.
- [270] CERN, *Proceedings of the 1974 CERN School of Computing: Godøysund, Norway 11 - 24 Aug 1974. 3rd CERN School of Computing*. CERN, Geneva, 1974. <http://cds.cern.ch/record/186223>.
- [271] J. Neyman and E. S. Pearson, *On the Problem of the Most Efficient Tests of Statistical Hypotheses*, Phil. Trans. Roy. Soc. Lond. A **231** (1933) 289–337.
- [272] G. Cowan, et al., *Asymptotic formulae for likelihood-based tests of new physics*, Eur. Phys. J. C **71** (2011) 1554, [Erratum: Eur.Phys.J.C 73, 2501 (2013)].
- [273] ROOT Collaboration, *HistFactory: A tool for creating statistical models for use with RooFit and RooStats*, tech. rep., CERN, Geneva, 2012. <https://cds.cern.ch/record/1456844>.
- [274] W. Verkerke and D. P. Kirkby, *The RooFit toolkit for data modeling*, eConf **C0303241** (2003) MOLT007.
- [275] L. Moneta, et al., *The RooStats Project*, PoS **ACAT2010** (2010) 057.

- [276] R. Brun and F. Rademakers, *ROOT: An object oriented data analysis framework*, Nucl. Instrum. Meth. A **389** (1997) 81–86.
- [277] A. Sciandra, *Probing the Standard Model of particle physics with $t\bar{t}H$, WWZ and WZZ multilepton final states*, 2018.
<https://cds.cern.ch/record/2688429>. Presented 27 May 2019.

APPENDIX A

List of MC Samples

An overview of the full list of data and MC samples used in this analysis is found in Table A.1 to A.3. The names include a r- and p-tag. The former indicates the MC campaign, while the latter shows the used ATLAS software version. Only r-tag *r9364*, corresponding to the **mc16a** campaign and run year 2015 and 2016, are presented. Other r-tags are *r10201* for **mc16d** and year 2017 and *r10726* for **mc16e** for the year 2018. Samples simulated with ATLAS fast simulation are marked with a star (*). Samples can be inclusive in numbers of jets or split into single- and dilepton contributions. The V +jets samples are split into slices of the scalar sum of transverse momentum and additional filter for heavy flavour jets. The $V\gamma$ samples are split by the transverse momentum of the prompt photon.

	Year	Name
Run 2	2015	<code>data15_13TeV.AllYear.physics.Main.PhysCont.DAOD_HIGG8D1.grp15_v01.p4309</code>
	2016	<code>data16_13TeV.AllYear.physics.Main.PhysCont.DAOD_HIGG8D1.grp16_v01.p4309</code>
	2017	<code>data17_13TeV.AllYear.physics.Main.PhysCont.DAOD_HIGG8D1.grp17_v01.p4309</code>
	2018	<code>data18_13TeV.AllYear.physics.Main.PhysCont.DAOD_HIGG8D1.grp18_v01.p4309</code>

Table A.1: An overview of data containers of collected data for Run 2.

Process	Description	MC sample name
$t\bar{t}H$	$t\bar{t}H$ all-hadronic (nominal)	mc16a_13TeV_346343_PbPy8EG_A14NNPDF23_NNPDF30ME_ttH125_allhad.deriv.DAOD_HIGG8D1.e7148.s3126.r9364.p4498
	$t\bar{t}H$ single-lepton (nominal)	mc16a_13TeV_346344_PbPy8EG_A14NNPDF23_NNPDF30ME_ttH125_semilep.deriv.DAOD_HIGG8D1.e7148.s3126.r9364.p4498
	$t\bar{t}H$ dilepton (nominal)	mc16a_13TeV_346345_PbPy8EG_A14NNPDF23_NNPDF30ME_ttH125_dilep.deriv.DAOD_HIGG8D1.e7148.s3126.r9364.p4498
	$t\bar{t}H$ all-hadronic (PS alt.)	mc16a_13TeV_346346_PbH7EG_H7UE_NNPDF30ME_ttH125_allhad.deriv.DAOD_HIGG8D1.e7148.a875.r9364.p4418
	$t\bar{t}H$ single-lepton (PS alt.)	mc16a_13TeV_346347_PbH7EG_H7UE_NNPDF30ME_ttH125_semilep.deriv.DAOD_HIGG8D1.e7148.a875.r9364.p4418
	$t\bar{t}H$ dilepton (PS alt.)	mc16a_13TeV_346348_PbH7EG_H7UE_NNPDF30ME_ttH125_dilep.deriv.DAOD_HIGG8D1.e7148.a875.r9364.p4418
	$t\bar{t}H$ all-hadronic (p_T^{hard} var.)	mc16a_13TeV_602067_PbPy8EG_A14.ttH125_pThard1_allhad.deriv.DAOD_HIGG8D1.e8435.s3126.r9364.p4416
	$t\bar{t}H$ dilepton (p_T^{hard} var.)	mc16a_13TeV_602068_PbPy8EG_A14.ttH125_pThard1_dilep.deriv.DAOD_HIGG8D1.e8435.s3126.r9364.p4416
	$t\bar{t}H$ single-lepton (p_T^{hard} var.)	mc16a_13TeV_602069_PbPy8EG_A14.ttH125_pThard1_semilep.deriv.DAOD_HIGG8D1.e8435.s3126.r9364.p4416
$t\bar{t}Z$	$t\bar{t}Z \rightarrow ee$ (nominal)	mc16a_13TeV_504330.aMCPy8EG_NNPDF30NLO_A14N23LO.ttee.deriv.DAOD_HIGG8D1.e8255.s3126.r9364.p4416
	$t\bar{t}Z \rightarrow \mu\mu$ (nominal)	mc16a_13TeV_504334.aMCPy8EG_NNPDF30NLO_A14N23LO.ttmumu.deriv.DAOD_HIGG8D1.e8255.s3126.r9364.p4416
	$t\bar{t}Z \rightarrow \tau\tau$ (nominal)	mc16a_13TeV_504342.aMCPy8EG_NNPDF30NLO_A14N23LO.tttatautau.deriv.DAOD_HIGG8D1.e8255.s3126.r9364.p4416
	$t\bar{t}Z \rightarrow ee$ (A14 up var.)	mc16a_13TeV_504332.aMCPy8EG_NNPDF30NLO_A14N23LO.ttee.A14Var3cUp.deriv.DAOD_HIGG8D1.e8255.a875.r9364.p5035
	$t\bar{t}Z \rightarrow \mu\mu$ (A14 up var.)	mc16a_13TeV_504336.aMCPy8EG_NNPDF30NLO_A14N23LO.ttmumu.A14Var3cUp.deriv.DAOD_HIGG8D1.e8255.a875.r9364.p5035
	$t\bar{t}Z \rightarrow \tau\tau$ (A14 up var.)	mc16a_13TeV_504344.aMCPy8EG_NNPDF30NLO_A14N23LO.tttatautau.A14Var3cUp.deriv.DAOD_HIGG8D1.e8255.a875.r9364.p5035
	$t\bar{t}Z \rightarrow ee$ (A14 down var.)	mc16a_13TeV_504331.aMCPy8EG_NNPDF30NLO_A14N23LO.ttee.A14Var3cDown.deriv.DAOD_HIGG8D1.e8255.a875.r9364.p5035
	$t\bar{t}Z \rightarrow \mu\mu$ (A14 down var.)	mc16a_13TeV_504335.aMCPy8EG_NNPDF30NLO_A14N23LO.ttmumu.A14Var3cDown.deriv.DAOD_HIGG8D1.e8255.a875.r9364.p5035
	$t\bar{t}Z \rightarrow \tau\tau$ (A14 down var.)	mc16a_13TeV_504343.aMCPy8EG_NNPDF30NLO_A14N23LO.tttatautau.A14Var3cDown.deriv.DAOD_HIGG8D1.e8255.a875.r9364.p5035
	rare top samples	mc16a_13TeV_410397.MadGraphPythia8EvtGen.tbbar.vbsee.MEN30LO_A14N23LO.deriv.DAOD_HIGG8D1.e6086.s3126.r9364.p4308 mc16a_13TeV_410398.MadGraphPythia8EvtGen.tbbar.vbmmu.MEN30LO_A14N23LO.deriv.DAOD_HIGG8D1.e6086.s3126.r9364.p4308 mc16a_13TeV_410399.MadGraphPythia8EvtGen.tbbar.vbtautau.MEN30LO_A14N23LO.deriv.DAOD_HIGG8D1.e6086.s3126.r9364.p4308
	$t\bar{t}Z \rightarrow ee$ (low mass)	mc16a_13TeV_410276.aMcAtN10Pythia8EvtGen.MEN30NLO_A14N23LO.ttee.mll1.5.deriv.DAOD_HIGG8D1.e6087.s3126.r9364.p4416
	$t\bar{t}Z \rightarrow \mu\mu$ (low mass)	mc16a_13TeV_410277.aMcAtN10Pythia8EvtGen.MEN30NLO_A14N23LO.ttmumu.mll1.5.deriv.DAOD_HIGG8D1.e6087.s3126.r9364.p4416
	$t\bar{t}Z \rightarrow \tau\tau$ (low mass)	mc16a_13TeV_410278.aMcAtN10Pythia8EvtGen.MEN30NLO_A14N23LO.tttatautau.mll1.5.deriv.DAOD_HIGG8D1.e6087.s3126.r9364.p4416
	$t\bar{t}W$ (nominal)	mc16a_13TeV_700168.Sh_2210.ttW.deriv.DAOD_HIGG8D1.e8273.s3126.r9364.p4418
	$t\bar{t}W$ EW (nominal)	mc16a_13TeV_700205.Sh_2210.ttW_EWK.deriv.DAOD_HIGG8D1.e8307.s3126.r9364.p4590
	$t\bar{t}W$ (FxFx)	mc16a_13TeV_501720.aMCPy8EG_A14NNPDF23LO.ttW_FxFx01jNLO.deriv.DAOD_HIGG8D1.e8352.s3126.r9364.p4416
$t\bar{t}W$	$t\bar{t}W$ EW (ME alt)	mc16a_13TeV_412123.PbPy8EG_A14_NNPDF23LO.EvtWsm.deriv.DAOD_HIGG8D1.e7843.a875.r9364.p4416
	$t\bar{t}W$ (PS alt.)	mc16a_13TeV_600793.PbPy8EG_A14NNPDF23.ttWm_EW.deriv.DAOD_HIGG8D1.e8343.s3126.r9364.p4418 mc16a_13TeV_600794.PbPy8EG_A14NNPDF23.ttWm_EW.deriv.DAOD_HIGG8D1.e8343.s3126.r9364.p4592 mc16a_13TeV_600795.PbPy8EG_A14NNPDF23.ttWm_QCD.deriv.DAOD_HIGG8D1.e8343.s3126.r9364.p4418 mc16a_13TeV_600796.PbPy8EG_A14NNPDF23.ttWp_QCD.deriv.DAOD_HIGG8D1.e8343.s3126.r9364.p4418
	$t\bar{t}t\bar{t}$ (nominal)	mc16a_13TeV_412043.aMcAtN10Pythia8EvtGen.A14NNPDF31_S44topsNLO.deriv.DAOD_HIGG8D1.e7101.a875.r9364.p4416
$t\bar{t}t\bar{t}$	$t\bar{t}t\bar{t}$ (ME alt.)	mc16a_13TeV_700355.Sh_2211.tttt_muQHT2.deriv.DAOD_HIGG8D1.e8351.s3126.r9364.p4416
	$t\bar{t}t\bar{t}$ (PS alt.)	mc16a_13TeV_412044.aMcAtN10Herwig7EvtGen.H7UE_S44topsNLO.deriv.DAOD_HIGG8D1.e7102.s3126.r9364.p4416
$t\bar{t}$	$t\bar{t}$ dilepton (nominal)	mc16a_13TeV_410472.PbPy8EG_A14.ttbar_hdamp258p75.dil.deriv.DAOD_HIGG8D1.e6348.s3126.r9364.p4308
	ttbar+HF	mc16a_13TeV_411076.PbPy8EG_A14.ttbar_hdamp258p75.dil_BBFilt.deriv.DAOD_HIGG8D1.e6798.a875.r9364.p4416
	$t\bar{t} + b\bar{b}$ (4FS)	mc16a_13TeV_411077.PbPy8EG_A14.ttbar_hdamp258p75.dil_BFiltBBVeto.deriv.DAOD_HIGG8D1.e6798.a875.r9364.p4416
	$t\bar{t}$ single-lepton (PS alt.)	mc16a_13TeV_601226.PbPy8_A14_NNPDF31.ttbbs_4FS_bzd5.dilep.deriv.DAOD_HIGG8D1.e8388.a875.r9364.p5561
	$t\bar{t}$ dilepton (PS alt.)	mc16a_13TeV_411233.PovhEGHerwig7EvtGen.tt_hdamp258p75.713_SingleLep.deriv.DAOD_HIGG8D1.e7580.s3126.r9364.p4416
	$t\bar{t}$ single-lepton (h_{damp} alt.)	mc16a_13TeV_411234.PovhEGHerwig7EvtGen.tt_hdamp258p75.713.dil.deriv.DAOD_HIGG8D1.e7580.s3126.r9364.p4416
	$t\bar{t}$ dilepton (h_{damp} alt.)	mc16a_13TeV_410480.PbPy8EG_A14.ttbar_hdamp517p5_SingleLep.deriv.DAOD_HIGG8D1.e6454.a875.r9364.p4416
	$t\bar{t}$ dilepton (h_{damp} alt.)	mc16a_13TeV_410482.PbPy8EG_A14.ttbar_hdamp517p5.dil.deriv.DAOD_HIGG8D1.e6454.a875.r9364.p4416
	$ZZ \rightarrow 4\ell$	mc16a_13TeV_364250.Sherpa_222_NNPDF30NNLO_1111.deriv.DAOD_HIGG8D1.e5894.s3126.r9364.p4416
	$WZ \rightarrow \ell\nu\ell\ell$	mc16a_13TeV_364253.Sherpa_222_NNPDF30NNLO_1111v.deriv.DAOD_HIGG8D1.e5916.s3126.r9364.p4416
Diboson	$ZZ \rightarrow \ell\nu\ell\nu$	mc16a_13TeV_364254.Sherpa_222_NNPDF30NNLO_11vv.deriv.DAOD_HIGG8D1.e5916.s3126.r9364.p4416
	$WZ \rightarrow \ell\nu\ell\nu\ell$	mc16a_13TeV_364255.Sherpa_222_NNPDF30NNLO_11vvv.deriv.DAOD_HIGG8D1.e5916.s3126.r9364.p4416
	$ZZ \rightarrow \ell\ell\ell + jj$	mc16a_13TeV_364283.Sherpa_222_NNPDF30NNLO_1111jj_EW6.deriv.DAOD_HIGG8D1.e6055.s3126.r9364.p4308
	$WZ \rightarrow \ell\nu\ell\ell + jj$	mc16a_13TeV_364284.Sherpa_222_NNPDF30NNLO_1111vjj_EW6.deriv.DAOD_HIGG8D1.e6055.s3126.r9364.p4308
	$ZZ \rightarrow \ell\nu\ell\nu\ell + jj$	mc16a_13TeV_364285.Sherpa_222_NNPDF30NNLO_1111vjj_EW6.deriv.DAOD_HIGG8D1.e6055.s3126.r9364.p4308
	$WW \rightarrow \ell\nu\ell\nu + jj$ (SS, EW4)	mc16a_13TeV_364286.Sherpa_222_NNPDF30NNLO_11vvjj_ss_EW4.deriv.DAOD_HIGG8D1.e6055.s3126.r9364.p4308
	$WW \rightarrow \ell\nu\ell\nu + jj$ (SS, EW6)	mc16a_13TeV_364287.Sherpa_222_NNPDF30NNLO_11vvjj_ss_EW6.deriv.DAOD_HIGG8D1.e6055.s3126.r9364.p4308
	$ZZ \rightarrow \ell\ell\ell$ (low mass)	mc16a_13TeV_364288.Sherpa_222_NNPDF30NNLO_1111_lowM1PtComplement.deriv.DAOD_HIGG8D1.e6096.s3126.r9364.p4416
	$WZ \rightarrow \ell\nu\ell\ell$ (low mass)	mc16a_13TeV_364289.Sherpa_222_NNPDF30NNLO_1111v_lowM1PtComplement.deriv.DAOD_HIGG8D1.e6133.s3126.r9364.p4416
	$ZZ \rightarrow \ell\ell\nu\ell$ (low mass)	mc16a_13TeV_364290.Sherpa_222_NNPDF30NNLO_11vv_lowM1PtComplement.deriv.DAOD_HIGG8D1.e6096.s3126.r9364.p4416
	$ggZZ \rightarrow \ell\ell\ell$ ($m(4\ell) > 130$)	mc16a_13TeV_345705.Sherpa_222_NNPDF30NNLO_gg1111_0M4130.deriv.DAOD_HIGG8D1.e6213.s3126.r9364.p4308
	$ggZZ \rightarrow \ell\ell\ell$ ($m(4\ell) > 130$)	mc16a_13TeV_345706.Sherpa_222_NNPDF30NNLO_gg1111_130M41.deriv.DAOD_HIGG8D1.e6213.s3126.r9364.p4396
	$ggZZ \rightarrow \ell\nu\ell\nu$	mc16a_13TeV_345715.Sherpa_222_NNPDF30NNLO_gg11vvInt.deriv.DAOD_HIGG8D1.e6525.s3126.r9364.p4396
	$ggWW \rightarrow \ell\nu\ell\nu$	mc16a_13TeV_345718.Sherpa_222_NNPDF30NNLO_gg11vvWW.deriv.DAOD_HIGG8D1.e6525.s3126.r9364.p4396
	$ggZZ \rightarrow \ell\nu\ell\nu$	mc16a_13TeV_345723.Sherpa_222_NNPDF30NNLO_gg11vvZZ.deriv.DAOD_HIGG8D1.e6213.s3126.r9364.p4396

Table A.2: An overview of MC samples used in the analysis. Only samples from the mc16a campaign are shown, having a r-tag of r9364. Other campaigns are mc16d and mc16e with r-tags r10201 and r10724, respectively. The p-tags describe the used software release version. Samples processed with ATLAS fast simulation are marked with a star (*).

Process	Description	MC sample name
V + jets	$W \rightarrow \mu\nu_\mu + \text{jets}$	mc16a_13TeV.364156.Sherpa.221_NNPDF30NNLO.Wmunu_MAXHTPTV0.70_CvetoBVeto.deriv.DAOD_HIGG8D1.e5340.s3126.r9364.p4416
		...
	$W \rightarrow e\nu_e + \text{jets}$	mc16a_13TeV.364169.Sherpa.221_NNPDF30NNLO.Wmunu_MAXHTPTV1000.E.CMS.deriv.DAOD_HIGG8D1.e5340.s3126.r9364.p4416
		...
	$W \rightarrow \tau\nu_\tau + \text{jets}$	mc16a_13TeV.364170.Sherpa.221_NNPDF30NNLO.Wenu_MAXHTPTV0.70_CvetoBVeto.deriv.DAOD_HIGG8D1.e5340.s3126.r9364.p4416
		...
	$Z\mu\mu + \text{jets}$	mc16a_13TeV.364183.Sherpa.221_NNPDF30NNLO.Wenu_MAXHTPTV1000.E.CMS.deriv.DAOD_HIGG8D1.e5340.s3126.r9364.p4416
		...
	$Z\tau\tau + \text{jets}$	mc16a_13TeV.364184.Sherpa.221_NNPDF30NNLO.Wtaunu_MAXHTPTV0.70_CvetoBVeto.deriv.DAOD_HIGG8D1.e5340.s3126.r9364.p4416
		...
	$Z\mu\mu + \text{jets}$	mc16a_13TeV.364197.Sherpa.221_NNPDF30NNLO.Wtaunu_MAXHTPTV1000.E.CMS.deriv.DAOD_HIGG8D1.e5340.s3126.r9364.p4416
		...
	$Z \rightarrow ee + \text{jets}$	mc16a_13TeV.364100.Sherpa.221_NNPDF30NNLO.Zmumu_MAXHTPTV0.70_CvetoBVeto.deriv.DAOD_HIGG8D1.e5271.s3126.r9364.p4416
		...
	$Z \rightarrow \tau\tau + \text{jets}$	mc16a_13TeV.364113.Sherpa.221_NNPDF30NNLO.Zmumu_MAXHTPTV1000.E.CMS.deriv.DAOD_HIGG8D1.e5271.s3126.r9364.p4416
		...
	$Z \rightarrow ee + \text{jets}$	mc16a_13TeV.364114.Sherpa.221_NNPDF30NNLO.Zee_MAXHTPTV0.70_CvetoBVeto.deriv.DAOD_HIGG8D1.e5299.s3126.r9364.p4416
		...
	$Z \rightarrow \tau\tau + \text{jets}$	mc16a_13TeV.364127.Sherpa.221_NNPDF30NNLO.Zee_MAXHTPTV1000.E.CMS.deriv.DAOD_HIGG8D1.e5299.s3126.r9364.p4416
		...
$V\gamma$	$Z \rightarrow \mu\mu + \text{jets}$	mc16a_13TeV.364128.Sherpa.221_NNPDF30NNLO.Ztautau_MAXHTPTV0.70_CvetoBVeto.deriv.DAOD_HIGG8D1.e5307.s3126.r9364.p4416
		...
	$Z \rightarrow \mu\mu + \text{jets}$	mc16a_13TeV.364141.Sherpa.221_NNPDF30NNLO.Ztautau_MAXHTPTV1000.E.CMS.deriv.DAOD_HIGG8D1.e5307.s3126.r9364.p4416
		...
	$Z \rightarrow \mu\mu + \text{jets}$ (low mass)	mc16a_13TeV.364198.Sherpa.221_NN30NNLO.Zmm.M1110.40_MAXHTPTV0.70_Bveto.deriv.DAOD_HIGG8D1.e5421.s3126.r9364.p4416
		...
	$Z \rightarrow ee + \text{jets}$ (low mass)	mc16a_13TeV.364203.Sherpa.221_NN30NNLO.Zmm.M1110.40_MAXHTPTV280.E.CMS_BFilter.deriv.DAOD_HIGG8D1.e5421.s3126.r9364.p4416
		...
	$Z \rightarrow ee + \text{jets}$ (low mass)	mc16a_13TeV.364204.Sherpa.221_NN30NNLO.Zee.M1110.40_MAXHTPTV0.70_Bveto.deriv.DAOD_HIGG8D1.e5421.s3126.r9364.p4416
		...
	$Z \rightarrow \tau\tau + \text{jets}$ (low mass)	mc16a_13TeV.364209.Sherpa.221_NN30NNLO.Zee.M1110.40_MAXHTPTV280.E.CMS_BFilter.deriv.DAOD_HIGG8D1.e5421.s3126.r9364.p4416
		...
	$Z \rightarrow \tau\tau + \text{jets}$ (low mass)	mc16a_13TeV.364210.Sherpa.221_NN30NNLO.Ztt.M1110.40_MAXHTPTV0.70_Bveto.deriv.DAOD_HIGG8D1.e5421.s3126.r9364.p4416
		...
	$Z \rightarrow ee + \gamma$	mc16a_13TeV.364215.Sherpa.221_NN30NNLO.Ztt.M1110.40_MAXHTPTV280.E.CMS_BFilter.deriv.DAOD_HIGG8D1.e5421.s3126.r9364.p4416
		...
	$Z \rightarrow ee + \gamma$	mc16a_13TeV.364500.Sherpa.222_NNPDF30NNLO.eegamma.pty.7.15.deriv.DAOD_HIGG8D1.e5928.s3126.r9364.p4308
		...
	$Z \rightarrow \mu\mu + \gamma$	mc16a_13TeV.364504.Sherpa.222_NNPDF30NNLO.eegamma.pty.140.E.CMS.deriv.DAOD_HIGG8D1.e5928.s3126.r9364.p4308
		...
$V\gamma$	$Z \rightarrow \mu\mu + \gamma$	mc16a_13TeV.364505.Sherpa.222_NNPDF30NNLO.mumugamma.pty.7.15.deriv.DAOD_HIGG8D1.e5928.s3126.r9364.p4308
		...
	$Z \rightarrow \mu\mu + \gamma$	mc16a_13TeV.364509.Sherpa.222_NNPDF30NNLO.mumugamma.pty.140.E.CMS.deriv.DAOD_HIGG8D1.e5928.s3126.r9364.p4308
		...
	$Z \rightarrow \tau\tau + \gamma$	mc16a_13TeV.364510.Sherpa.222_NNPDF30NNLO.tautaugamma.pty.7.15.deriv.DAOD_HIGG8D1.e5928.s3126.r9364.p4308
		...
	$Z \rightarrow \tau\tau + \gamma$	mc16a_13TeV.364514.Sherpa.222_NNPDF30NNLO.tautaugamma.pty.140.E.CMS.deriv.DAOD_HIGG8D1.e5928.s3126.r9364.p4308
		...
	$W \rightarrow e\nu_e + \gamma$	mc16a_13TeV.364521.Sherpa.222_NNPDF30NNLO.enugamma.pty.7.15.deriv.DAOD_HIGG8D1.e5928.s3126.r9364.p4308
		...
Single Top	$W \rightarrow e\nu_e + \gamma$	mc16a_13TeV.364525.Sherpa.222_NNPDF30NNLO.enugamma.pty.140.E.CMS.deriv.DAOD_HIGG8D1.e5928.s3126.r9364.p4308
		...
	$W \rightarrow \mu\nu_\mu + \gamma$	mc16a_13TeV.364526.Sherpa.222_NNPDF30NNLO.munugamma.pty.7.15.deriv.DAOD_HIGG8D1.e5928.s3126.r9364.p4308
		...
	$W \rightarrow \mu\nu_\mu + \gamma$	mc16a_13TeV.364530.Sherpa.222_NNPDF30NNLO.munugamma.pty.140.E.CMS.deriv.DAOD_HIGG8D1.e5928.s3126.r9364.p4308
		...
	$W \rightarrow \tau\nu_\tau + \gamma$	mc16a_13TeV.364531.Sherpa.222_NNPDF30NNLO.taunugamma.pty.7.15.deriv.DAOD_HIGG8D1.e5928.s3126.r9364.p4308
		...
	$W \rightarrow \tau\nu_\tau + \gamma$	mc16a_13TeV.364535.Sherpa.222_NNPDF30NNLO.taunugamma.pty.140.E.CMS.deriv.DAOD_HIGG8D1.e5928.s3126.r9364.p4308
		...
VVV	s-channel	mc16a_13TeV.410644.PowhegPythia8EvtGen.A14.singletop.schan.lept.top.deriv.DAOD_HIGG8D1.e6527.s3126.r9364.p4308
	t-channel	mc16a_13TeV.410645.PowhegPythia8EvtGen.A14.singletop.schan.lept.antitop.deriv.DAOD_HIGG8D1.e6527.s3126.r9364.p4308
	t-channel	mc16a_13TeV.410658.PhPy8EG.A14.tchan.BW50.lept.top.deriv.DAOD_HIGG8D1.e6671.s3126.r9364.p4308
	t-channel	mc16a_13TeV.410659.PhPy8EG.A14.tchan.BW50.lept.antitop.deriv.DAOD_HIGG8D1.e6671.s3126.r9364.p4308
Other	$WWW \rightarrow 3\ell 3\nu$	mc16a_13TeV.364242.Sherpa.222_NNPDF30NNLO.WWW.3l3v.EW6.deriv.DAOD_HIGG8D1.e5887.s3126.r9364.p4308
	$WWZ \rightarrow 4\ell 2\nu$	mc16a_13TeV.364243.Sherpa.222_NNPDF30NNLO.WWZ.4l2v.EW6.deriv.DAOD_HIGG8D1.e5887.s3126.r9364.p4308
	$WWZ \rightarrow 2\ell 4\nu$	mc16a_13TeV.364244.Sherpa.222_NNPDF30NNLO.WWZ.2l4v.EW6.deriv.DAOD_HIGG8D1.e5887.s3126.r9364.p4308
	$WZZ \rightarrow 5\ell 1\nu$	mc16a_13TeV.364245.Sherpa.222_NNPDF30NNLO.WZZ.5l1v.EW6.deriv.DAOD_HIGG8D1.e5887.s3126.r9364.p4308
	$WZZ \rightarrow 3\ell 3\nu$	mc16a_13TeV.364246.Sherpa.222_NNPDF30NNLO.WZZ.3l3v.EW6.deriv.DAOD_HIGG8D1.e5887.s3126.r9364.p4308
	$ZZZ \rightarrow 6\ell 0\nu$	mc16a_13TeV.364247.Sherpa.222_NNPDF30NNLO.ZZZ.6l0v.EW6.deriv.DAOD_HIGG8D1.e5887.s3126.r9364.p4308
	$ZZZ \rightarrow 4\ell 2\nu$	mc16a_13TeV.364248.Sherpa.222_NNPDF30NNLO.ZZZ.4l2v.EW6.deriv.DAOD_HIGG8D1.e5887.s3126.r9364.p4308
	$ZZZ \rightarrow 2\ell 4\nu$	mc16a_13TeV.364249.Sherpa.222_NNPDF30NNLO.ZZZ.2l4v.EW6.deriv.DAOD_HIGG8D1.e5887.s3126.r9364.p4308
	tW	mc16a_13TeV.410646.PowhegPythia8EvtGen.A14.Wt.DR.inclusive.top.deriv.DAOD_HIGG8D1.e6552.s3126.r9364.p4308
	$t\bar{t}$	mc16a_13TeV.410647.PowhegPythia8EvtGen.A14.Wt.DR.inclusive.antitop.deriv.DAOD_HIGG8D1.e6552.s3126.r9364.p4308
Other	$t\bar{t}t$	mc16a_13TeV.304014.MadGraphPythia8EvtGen.A14NNPDF23.3top.SM.deriv.DAOD_HIGG8D1.e4324.s3126.r9364.p4308
	$t\bar{t}WW$	mc16a_13TeV.410081.MadGraphPythia8EvtGen.A14NNPDF23.ttbarW.deriv.DAOD_HIGG8D1.e4111.s3126.r9364.p4308
	tZ	mc16a_13TeV.410560.MadGraphPythia8EvtGen.A14.tZ.4f1.tchan.noAllHad.deriv.DAOD_HIGG8D1.e5803.s3126.r9364.p4308
	tWZ	mc16a_13TeV.410408.aMcAtNloPythia8EvtGen.tWZ.Ttoll.minDR1.deriv.DAOD_HIGG8D1.e6423.s3126.r9364.p4308
	VH	mc16a_13TeV.342284.Pythia8EvtGen.A14NNPDF23LO.WH125.inc.deriv.DAOD_HIGG8D1.e4246.s3126.r9364.p4308
	$tHjb$	mc16a_13TeV.342285.Pythia8EvtGen.A14NNPDF23LO.ZH125.inc.deriv.DAOD_HIGG8D1.e4246.s3126.r9364.p4308
	tHH	mc16a_13TeV.346799.aMcAtNloPythia8EvtGen.tHjb125.4f1.CPalpha.0.ML.ZL.deriv.DAOD_HIGG8D1.e8018.a875.r9364.p4308
	tWH	mc16a_13TeV.508776.aMCPy8EG.tWH_DR1.PS.deriv.DAOD_HIGG8D1.e8419.a875.r9364.p4416
		*
		*

Table A.3: An overview of MC samples used in the analysis. Only samples from the mc16a campaign are shown, having a r-tag of r9364. Other campaigns are mc16d and mc16e with r-tags r10201 and r10724, respectively. The p-tags describe the software version used for the release. Samples processed with ATLAS fast simulation are marked with a star (*). Samples for the V +jets process are provided in slices of the scalar sum of transverse momentum with an additional filter on heavy-flavour jets. The $V\gamma$ samples are further split by the transverse momentum of the photon.

APPENDIX B

Activation Function Definitions

The definitions of the used activation functions are:

$$\begin{aligned} \text{Rectified linear unit (Relu)} : a(z) &= \max(0, z) \\ \text{Rectified linear unit (Elu)} : a(z) &= \begin{cases} z, & \text{if } z > 0 \\ \alpha \cdot (\exp(z) - 1), & \text{if } z \leq 0 \end{cases} \\ \text{Rectified linear unit (Selu)} : a(z) &= \lambda \cdot \left[\max(0, z) + \min\left(0, \xi \cdot (\exp(z) - 1)\right) \right] \\ \text{Rectified linear unit (LeakyRelu)} : a(z) &= \max(0, z) + \kappa \cdot \min(0, z). \end{aligned} \tag{B.1}$$

The parameter of the Elu function is set to be $\alpha = 1$. For the Selu function, the parameters are $\lambda \approx 1.67$ and $\xi \approx 1.05$; the exact values are found in Ref. [244]. The negative slope parameter of the LeakyRelu function is $\kappa = 0.01$.

Lepton Definition Optimisation

Alternative lepton definition combinations are studied with the four loose lepton combination (LLLL) as a baseline. Using the lepton definitions from Chapter 5.2.4, four tighter combinations are defined and compared in terms of signal background ratio S/B , signal significance S/\sqrt{B} , and expected yields for $t\bar{t}H$ with the baseline combination. The first combination (LLMM) requires the two leading lepton to fulfil loose requirements while the remaining passes the medium definition. The leading leptons are generally less likely to be non-prompt due to their more considerable transverse momentum. Therefore, tighter requirements are applied to the subleading leptons. The second combination (MMMM) requires all lepton candidates to pass the medium definition. The third and fourth combinations are similar to the previous ones, but the tight lepton definition is used instead of medium. In Table C.1 the expected yields after applying preselection for the signal process $t\bar{t}H$, the most crucial prompt background processes, the non-prompt lepton contributions, and the values for S/B and S/\sqrt{B} for every lepton combination are presented. The tighter lepton definition combination reduces most non-prompt contributions but also removes 63 % up to 83 %, while not increasing the signal to background ratio S/B or the signal significance S/\sqrt{B} . The baseline combination LLLL is used.

Combination	LLLL	LLMM	MMMM	LLTT	TTTT
$t\bar{t}H$	15.30	5.64	4.29	3.94	2.61
$t\bar{t}Z$	148.38	71.23	56.68	52.77	37.50
$ZZ + b$	39.39	20.08	16.32	15.34	11.38
$ZZ + c$	30.76	15.67	12.78	11.79	8.90
$ZZ + \text{light}$	28.9	14.71	11.89	11.09	8.24
tWZ	17.67	9.01	7.28	6.56	4.64
Other Prompt	8.2	3.43	2.72	2.78	2.10
e^{HF} Fake	0.27	0.03	0.01	0.03	0.01
μ^{HF} Fake	0.38	0.01	0.00	0.00	0.00
e^{LF} Fake	0.26	0.08	0.01	0.07	0.01
double Fake	1.79	0.08	0.00	0.01	0.00
Other Fake	0.42	0.04	0.02	0.02	0.02
Total	291.74	140.03	112.01	104.41	75.38
S/B	0.055	0.042	0.040	0.039	0.036
S/\sqrt{B}	0.921	0.487	0.413	0.393	0.306

Table C.1: A comparison of expected yields after applying the preselection for the 4ℓ channel for various combinations of lepton definitions. Using the loose lepton definition for all four leptons results in the best value for S/B and S/\sqrt{B} . The lepton definitions are presented in Chapter 5.2.4 and in Table 5.4.

APPENDIX D

Validation Plots

Distributions of kinematic distributions in the 4ℓ channel are presented, applying the preselection criteria. In Figure D.1, the low-level kinematic information of leptons are shown. They include the transverse momentum and the pseudorapidity of all four leptons. The following kinematic variables are used as input for the dense neural network in the 4ℓ channel. Figure D.2 presents the invariant masses of lepton pairs and their spatial separation. In Figure D.3, the invariant mass of four leptons, the scalar sum of the transverse momentum of leptons and jets, and the jet and b -jet multiplicity are shown. Furthermore, the two transverse masses, the effective invariant mass, E_T^{miss} , and the number of SFOS lepton pairs are presented. All distributions show total pre-fit uncertainties including statistical and systematic uncertainties. The post-fit distributions are shown in Figure D.4, Figure D.5, and Figure D.6.

Distributions of neural network input features in the 4ℓ channel are presented in the following. In Figure D.7, the invariant masses and spatial separation between lepton pairs are presented for the $t\bar{t}Z$ -sensitive part of the $\text{SR}_{t\bar{t}H}$. Other variables like the invariant mass of four leptons, scalar sum of the transverse momentum of leptons and jets, jet and b -jet multiplicity, transverse masses, effective invariant mass, E_T^{miss} , and the number of SFOS lepton pairs are shown in Figure D.8. Total pre-fit uncertainties, including statistical and systematic uncertainties, are shown. The post-fit distributions with total post-fit uncertainties are shown in Figure D.9 and Figure D.10. The same pre-fit distributions are presented in Figure D.11 and Figure D.12 but for the CR_{ZZ} . The post-fit distributions are presented in Figure D.13 and Figure D.14.

In Figure D.15, Figure D.16, and Figure D.17 different kinematic variables are pre-

sented for the fake regions $\text{CR}_{\mu\text{HF}}$, $\text{CR}_{e\text{HF}}$, and $\text{CR}_{e\text{LF}}$, respectively. The transverse momentum and pseudorapidity of the leptons, the scalar sum of transverse momenta for jets and leptons, and the jet multiplicity are shown. Total post-fit uncertainties, including statistical and systematic uncertainties, are shown.

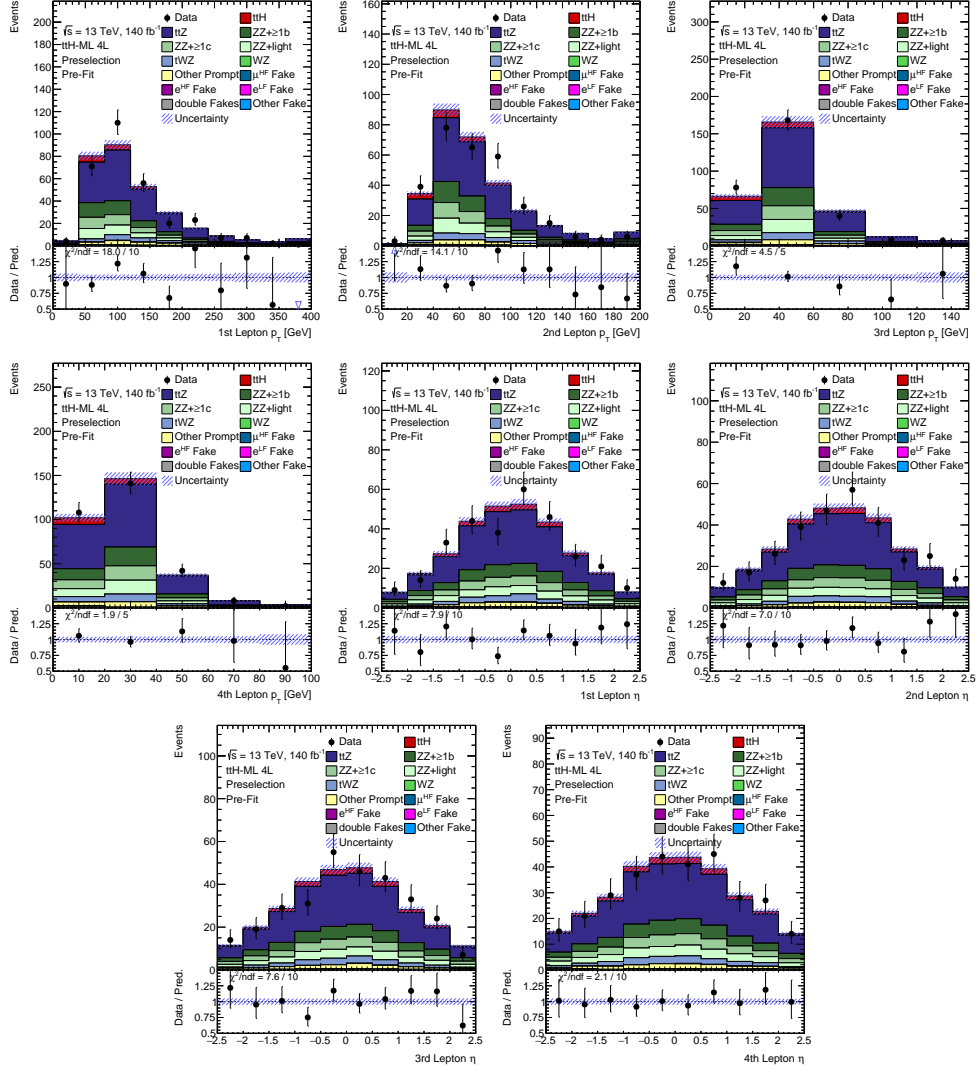


Figure D.1: Pre-fit distributions of lepton-related low-level variables after applying the preselection. The transverse momentum and pseudorapidity of leptons are presented. Total pre-fit uncertainties are shown.

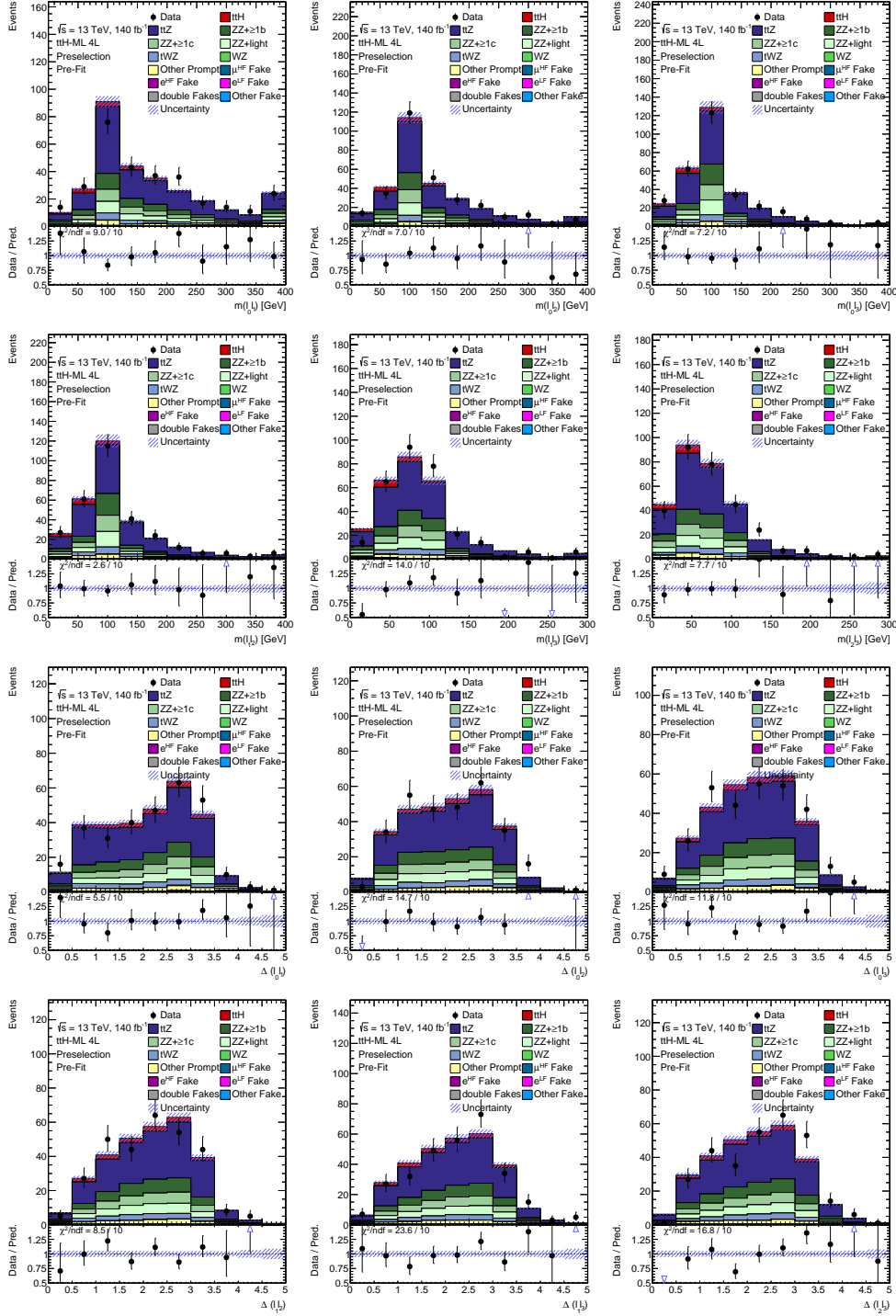


Figure D.2: Pre-fit distributions of lepton-related high-level variables after applying the preselection. The invariant masses and spatial separation of lepton pairs are presented. Total pre-fit uncertainties are shown.

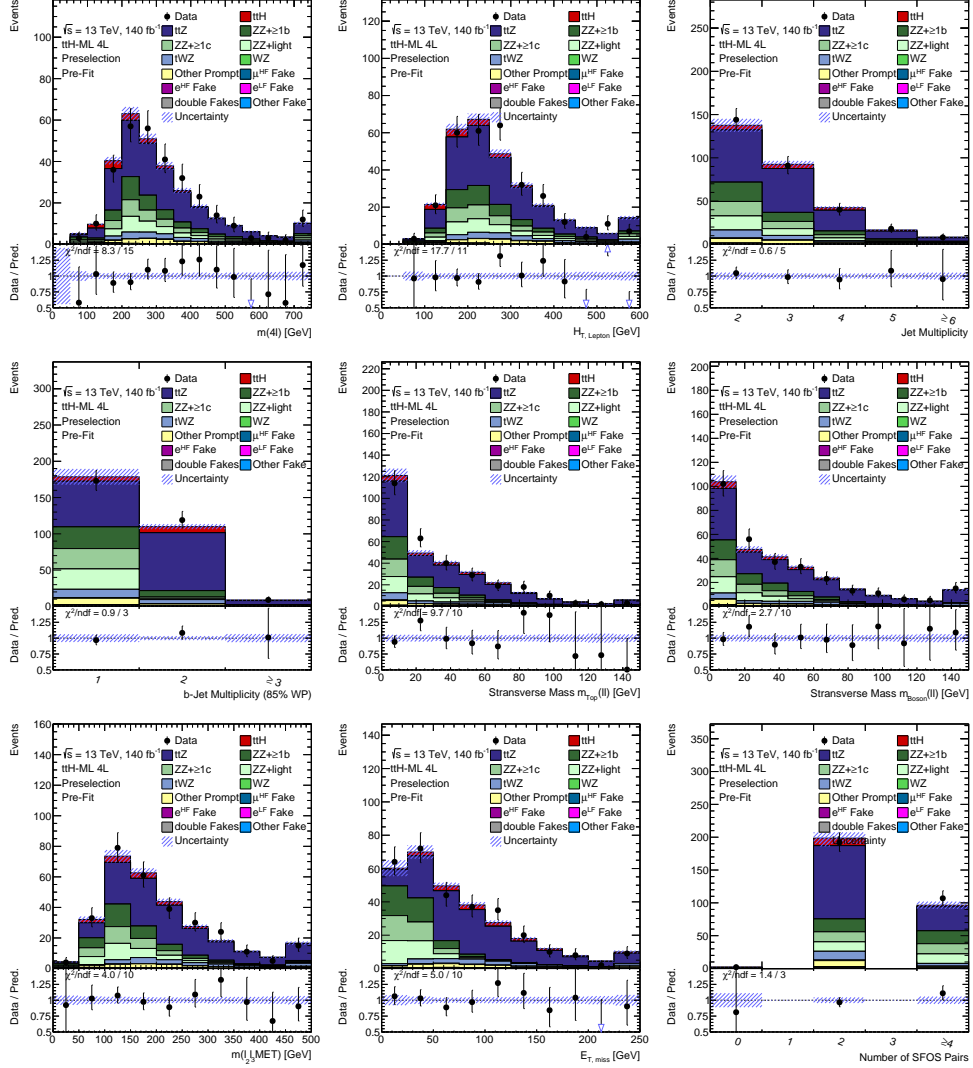


Figure D.3: Pre-fit distributions of high-level variables after applying the preselection. The invariant mass of four leptons, the scalar sum of the transverse momentum of leptons and jets, the jet and b -jet multiplicities, transverse masses, effective invariant mass, E_T^{miss} , and the number of SFOS lepton pairs are presented. Total pre-fit uncertainties are shown.

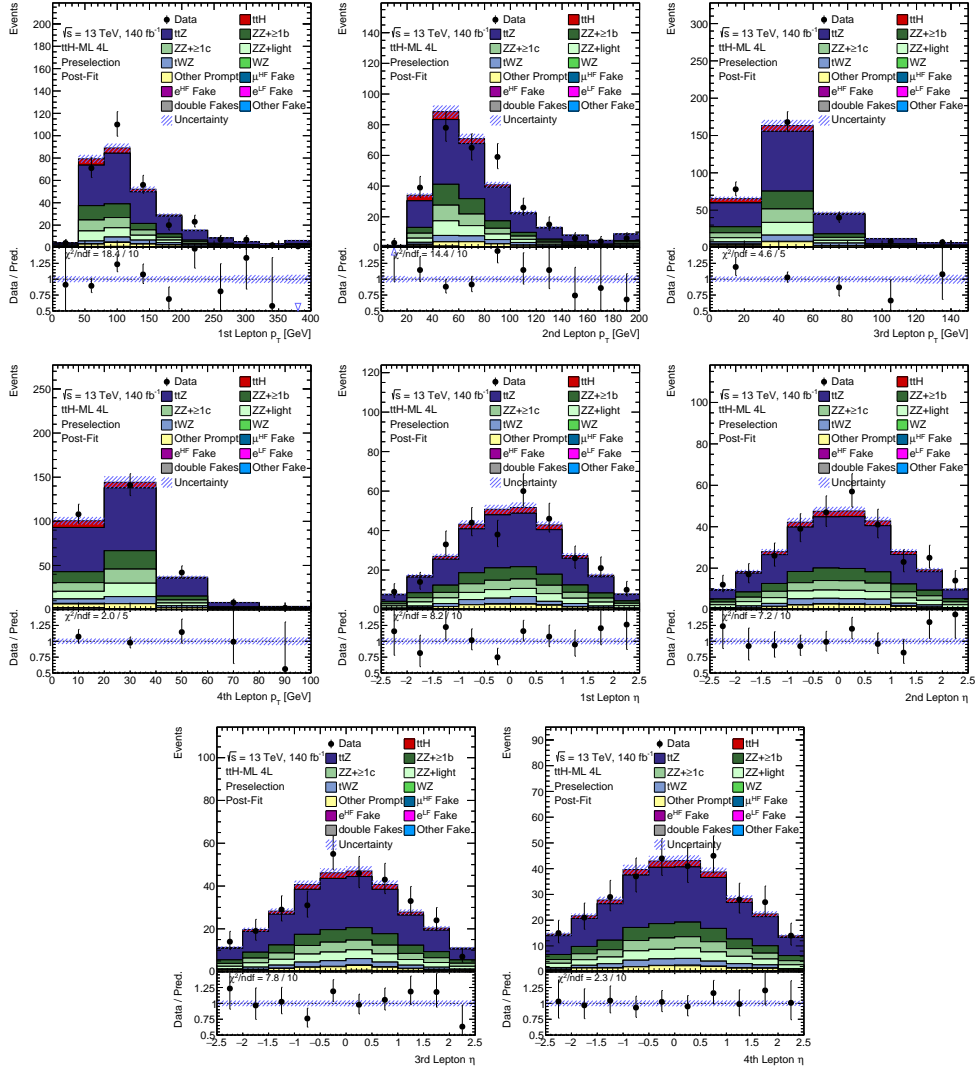
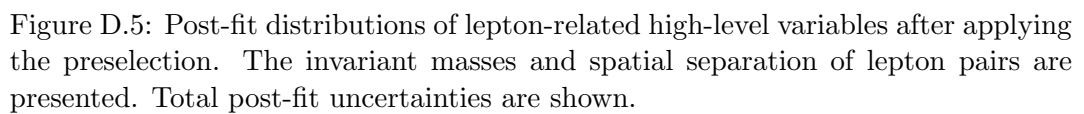


Figure D.4: Post-fit distributions of lepton-related low-level variables after applying the preselection. The transverse momentum and pseudorapidity of leptons are presented. Total post-fit uncertainties are shown.



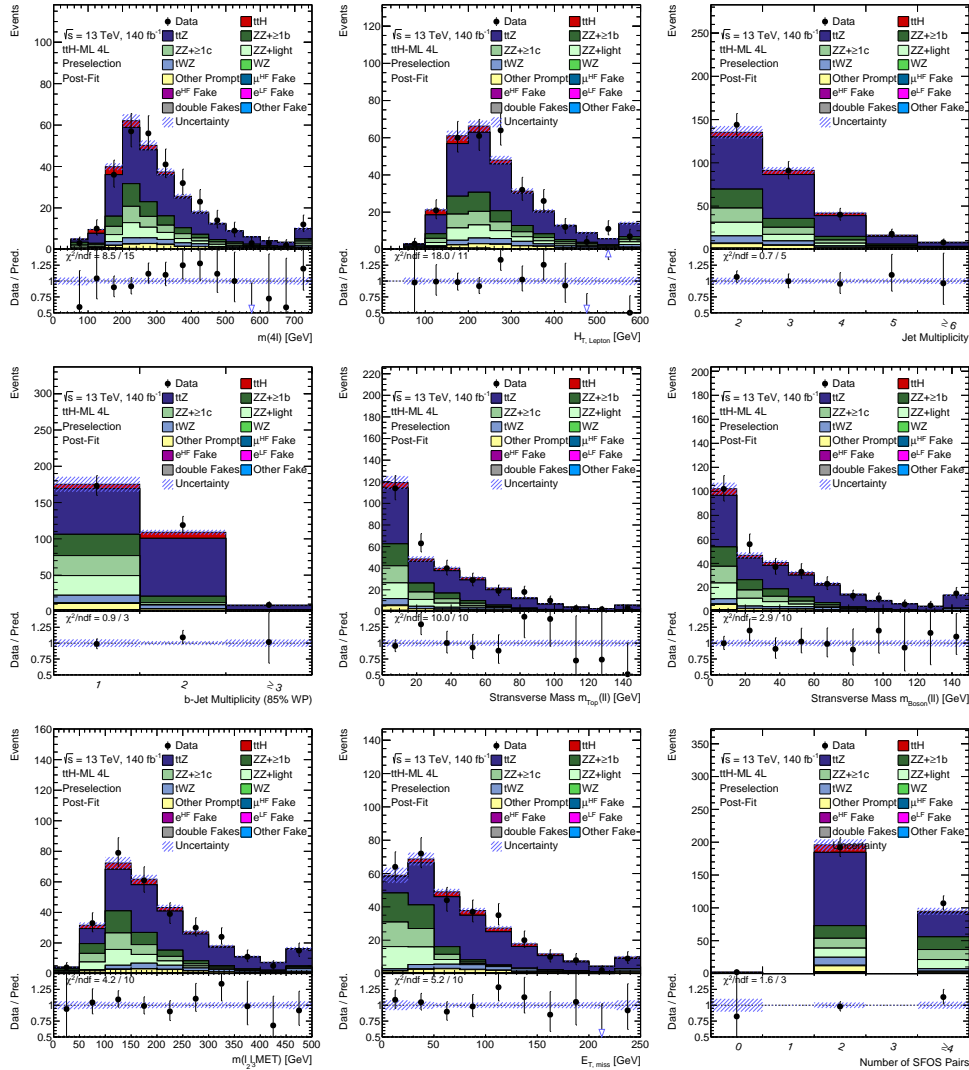


Figure D.6: Post-fit distributions of high-level variables after applying the preselection. The invariant mass of four leptons, the scalar sum of the transverse momentum of leptons and jets, the jet and b -jet multiplicities, stransverse masses, effective invariant mass, $E_{\text{T}}^{\text{miss}}$, and the number of SFOS lepton pairs are presented. Total post-fit uncertainties are shown.

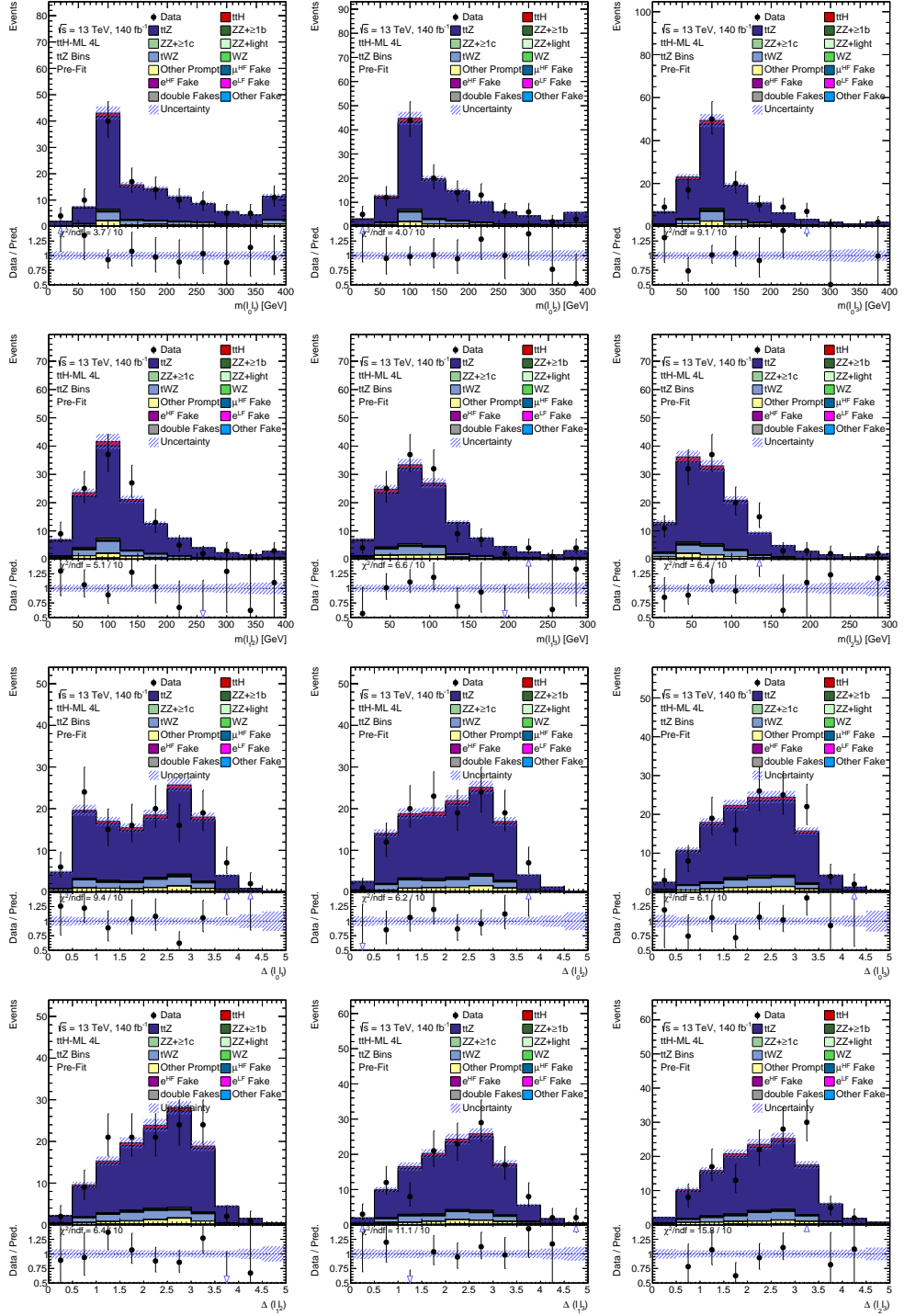


Figure D.7: Pre-fit distributions of lepton-related high-level variables in the $t\bar{t}Z$ -sensitive part of the $SR_{t\bar{t}H}$. The invariant masses and spatial separation of lepton pairs are presented. Total pre-fit uncertainties are shown.

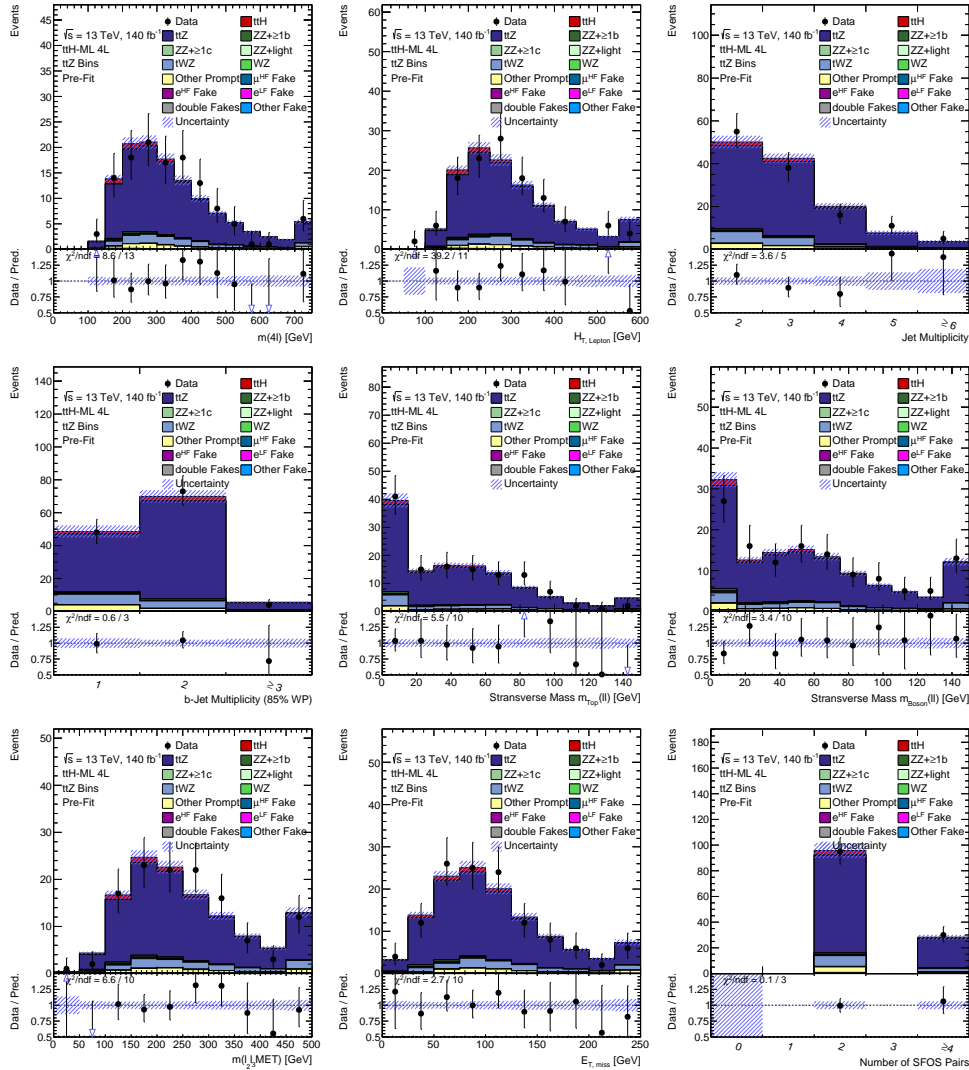


Figure D.8: Pre-fit distributions of high-level variables in the $t\bar{t}Z$ -sensitive part of the $\text{SR}_{t\bar{t}H}$. The invariant mass of four leptons, the scalar sum of the transverse momentum of leptons and jets, the jet and b -jet multiplicities, stransverse masses, effective invariant mass, $E_{\text{T}}^{\text{miss}}$, and the number of SFOS lepton pairs are presented. Total pre-fit uncertainties are shown.

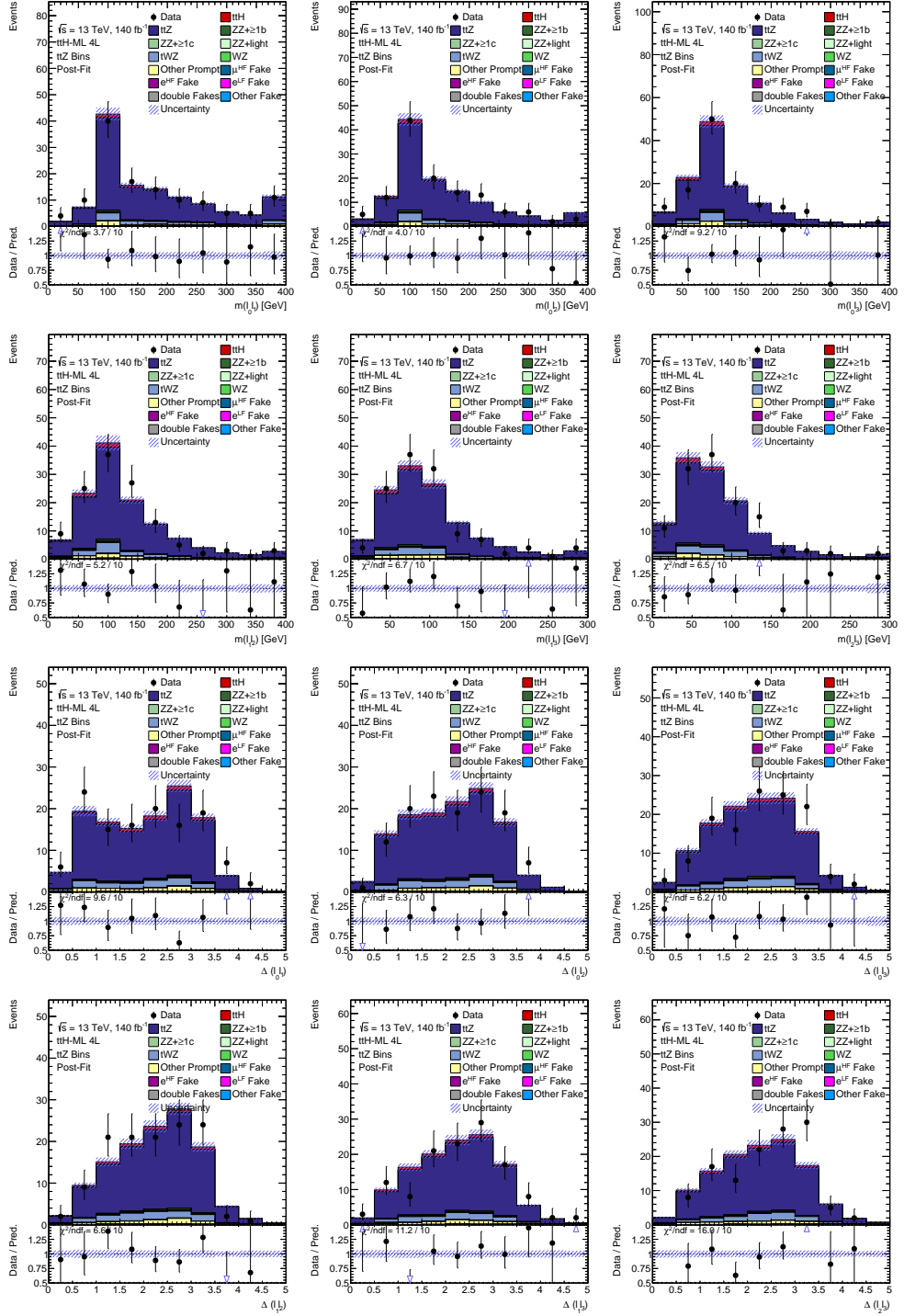


Figure D.9: Post-fit distributions of lepton-related high-level variables in the $t\bar{t}Z$ -sensitive part of the $SR_{t\bar{t}H}$. The invariant masses and spatial separation of lepton pairs are presented. Total post-fit uncertainties are shown.

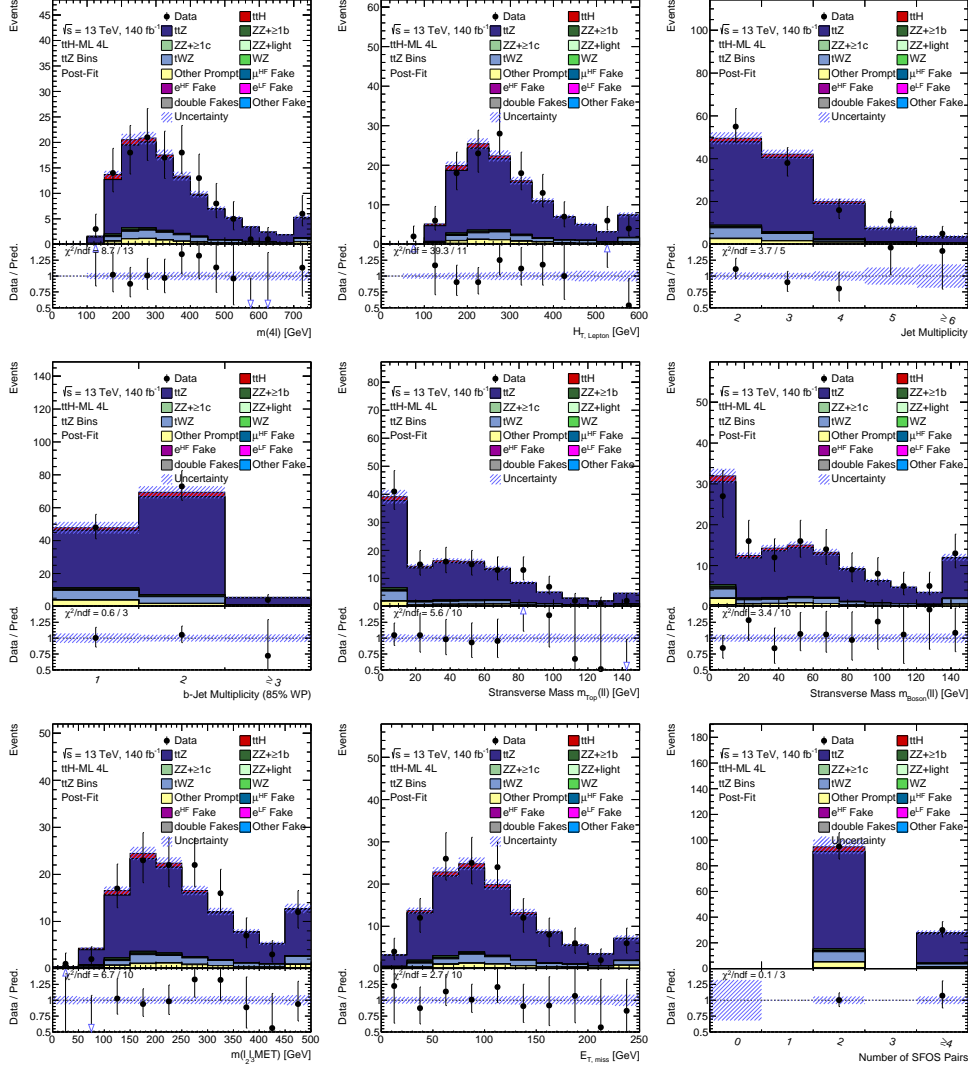


Figure D.10: Post-fit distributions of high-level variables in the $t\bar{t}Z$ -sensitive part of the $SR_{t\bar{t}H}$. The invariant mass of four leptons, the scalar sum of the transverse momentum of leptons and jets, the jet and b -jet multiplicities, transverse masses, effective invariant mass, E_{T}^{miss} , and the number of SFOS lepton pairs are presented. Total post-fit uncertainties are shown.

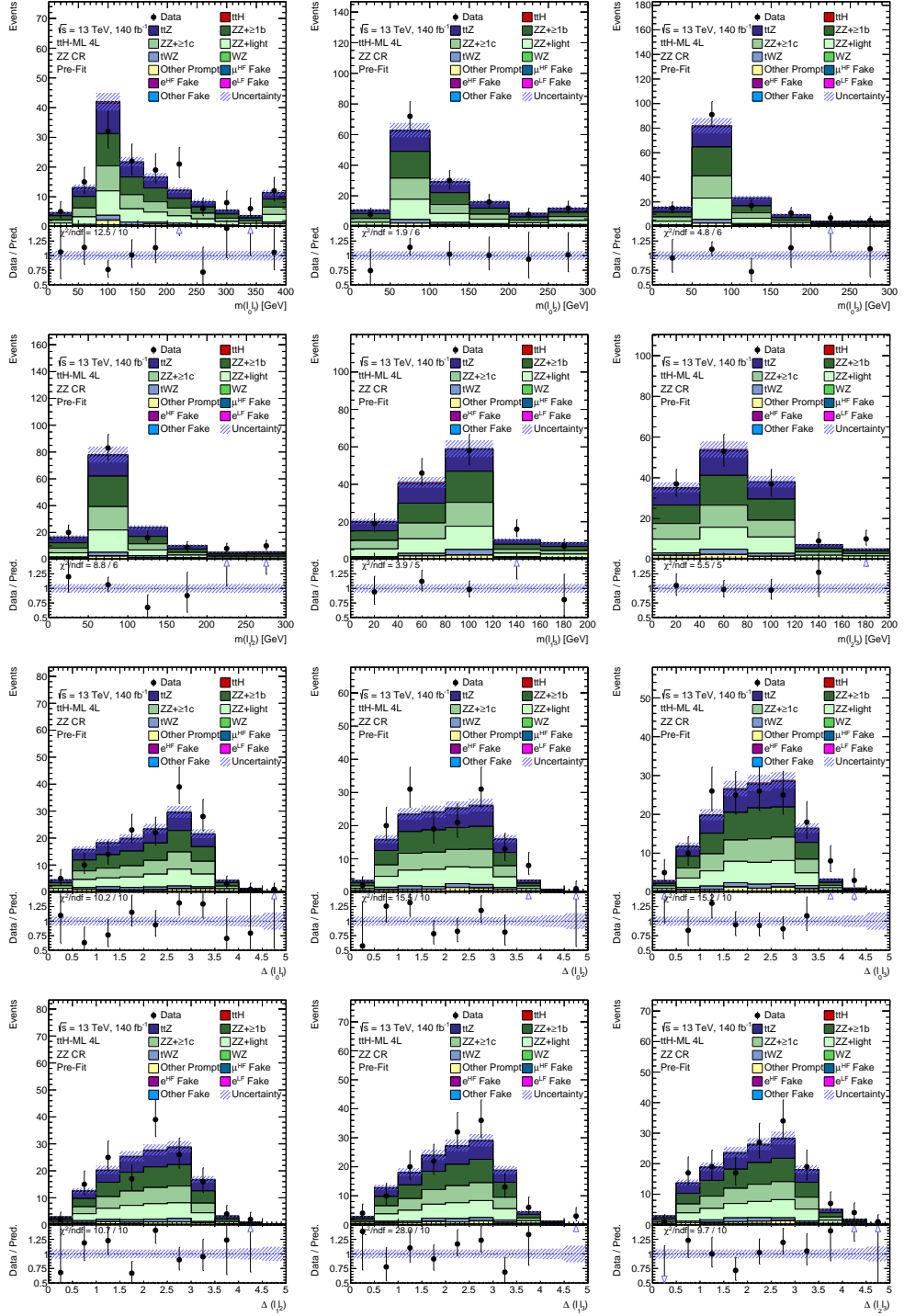


Figure D.11: Pre-fit distributions of lepton-related high-level variables in the CR_{ZZ} . The invariant masses and spatial separation of lepton pairs are presented. Total pre-fit uncertainties are shown.

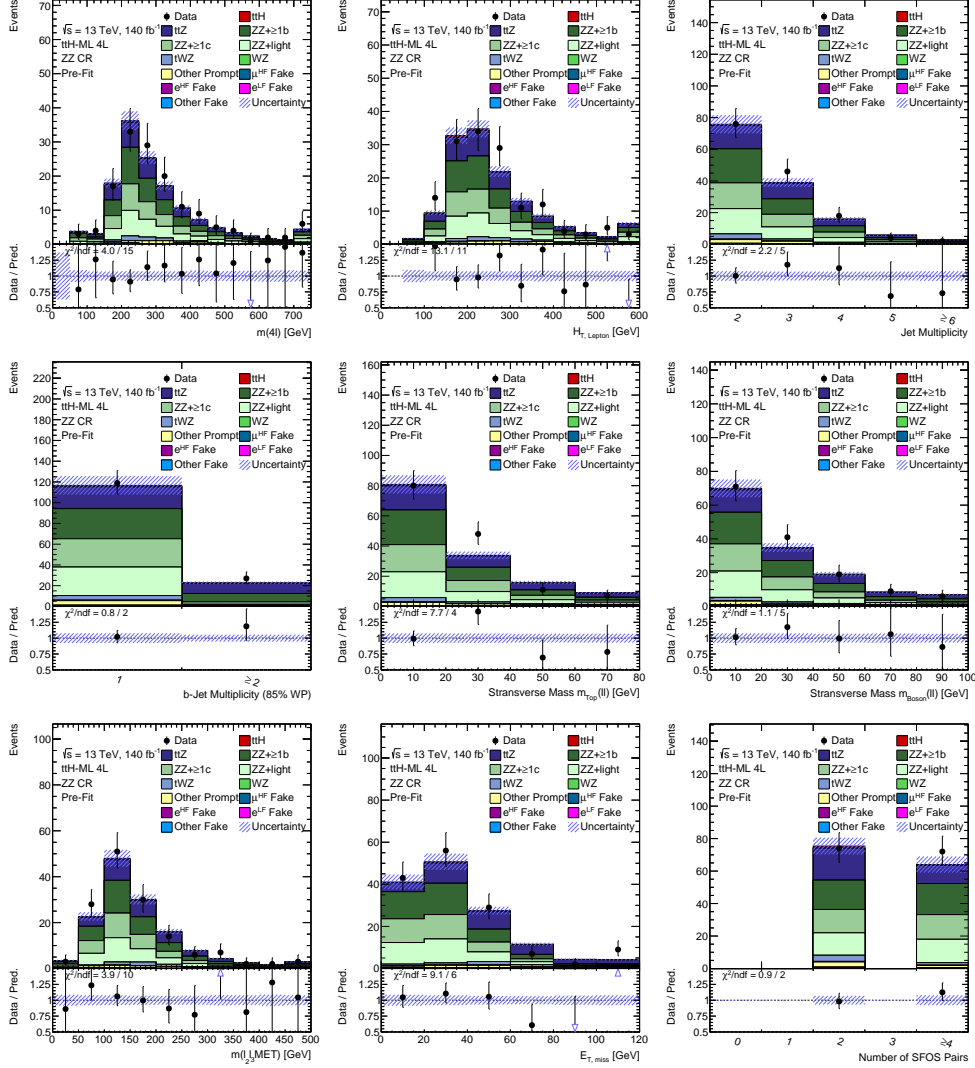


Figure D.12: Pre-fit distributions of high-level variables in the CR_{ZZ} . The invariant mass of four leptons, the scalar sum of the transverse momentum of leptons and jets, the jet and b -jet multiplicities, transverse masses, effective invariant mass, $E_{\text{T}}^{\text{miss}}$, and the number of SFOS lepton pairs are presented. Total pre-fit uncertainties are shown.

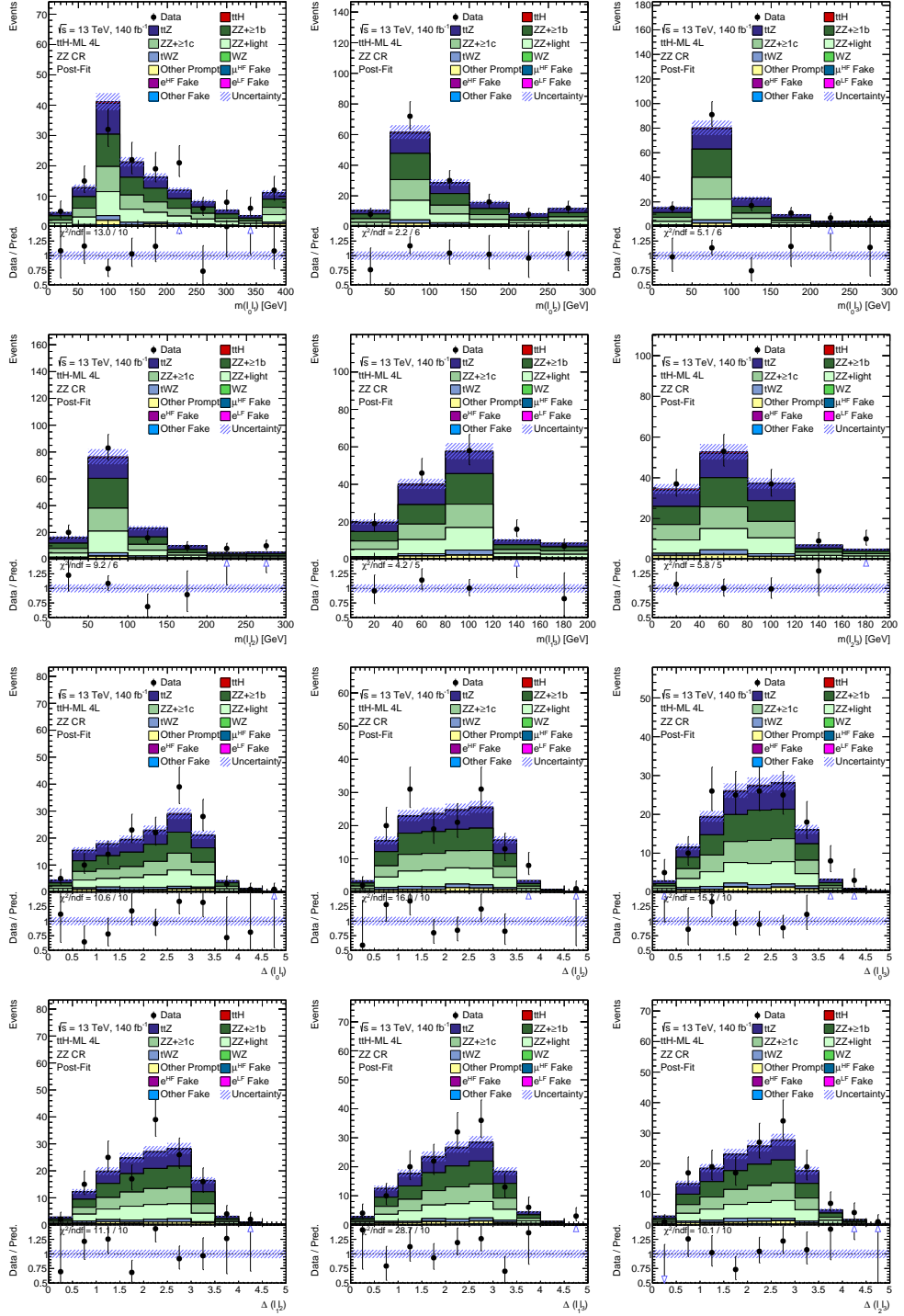


Figure D.13: Post-fit distributions of lepton-related high-level variables in the CR_{ZZ} . The invariant masses and spatial separation of lepton pairs are presented. Total post-fit uncertainties are shown.

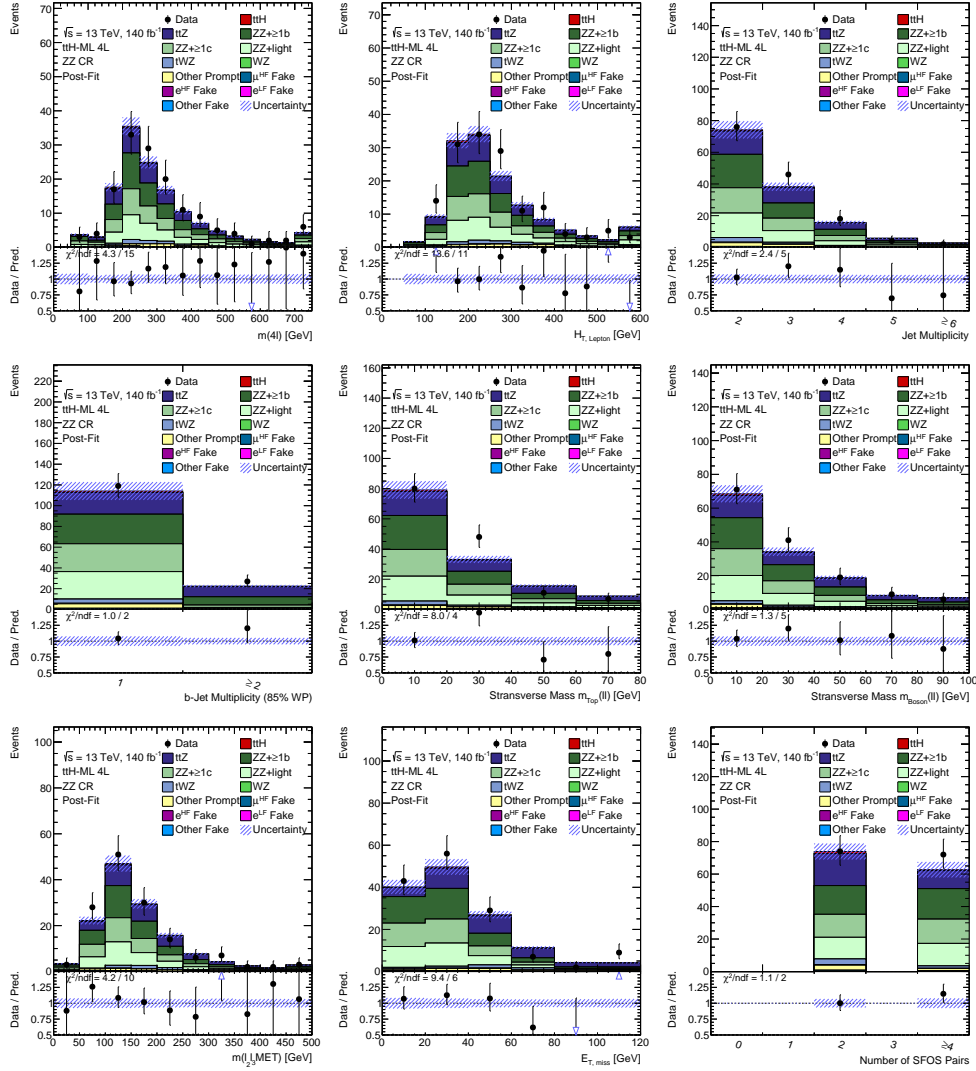


Figure D.14: Post-fit distributions of high-level variables in the CR_{ZZ} . The invariant mass of four leptons, the scalar sum of the transverse momentum of leptons and jets, the jet and b -jet multiplicities, transverse masses, effective invariant mass, $E_{\text{T}}^{\text{miss}}$, and the number of SFOS lepton pairs are presented. Total post-fit uncertainties are shown.

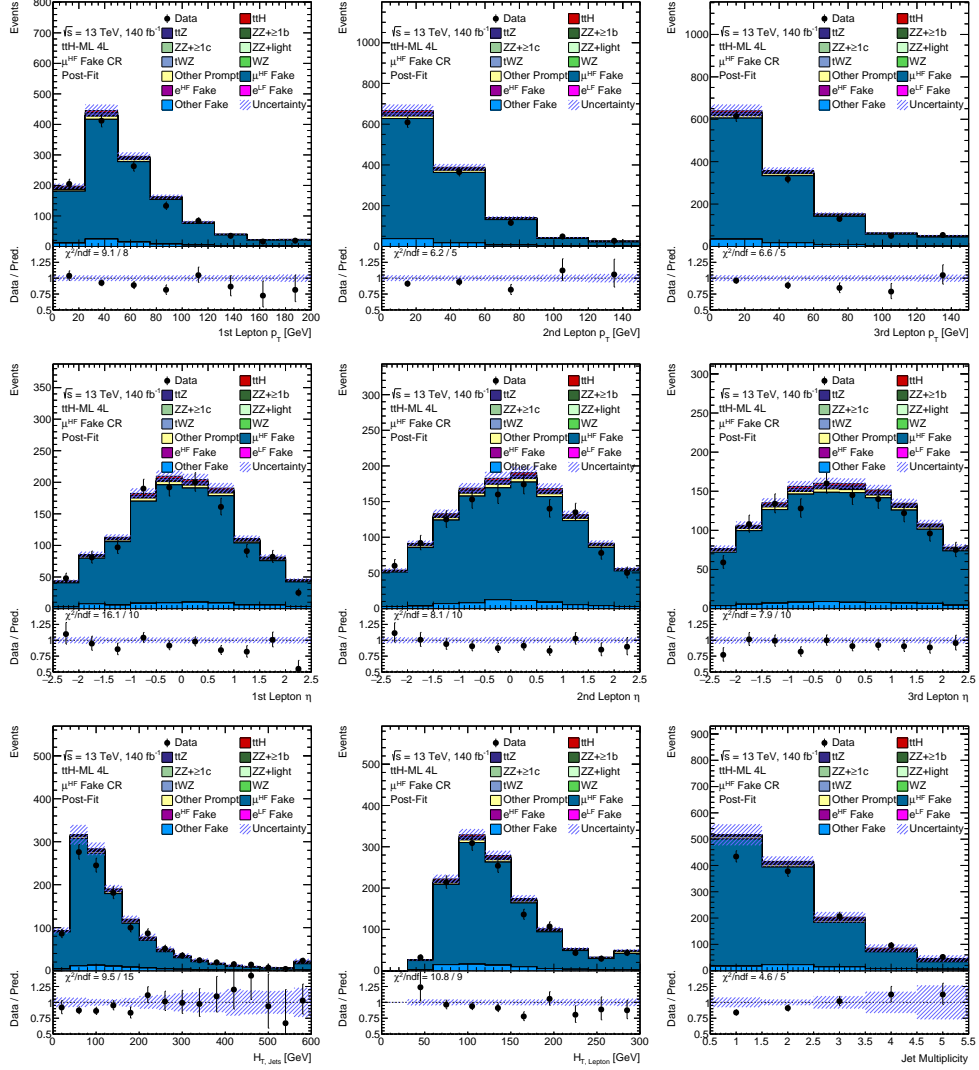


Figure D.15: Post-fit distributions of kinematic variables in the $\text{CR}_{\mu_{\text{HF}}}$. The transverse momentum and pseudorapidity of the leptons are shown. Furthermore, the scalar sum of transverse momenta of jets and leptons and the jet multiplicity are presented. Total post-fit uncertainties are shown.

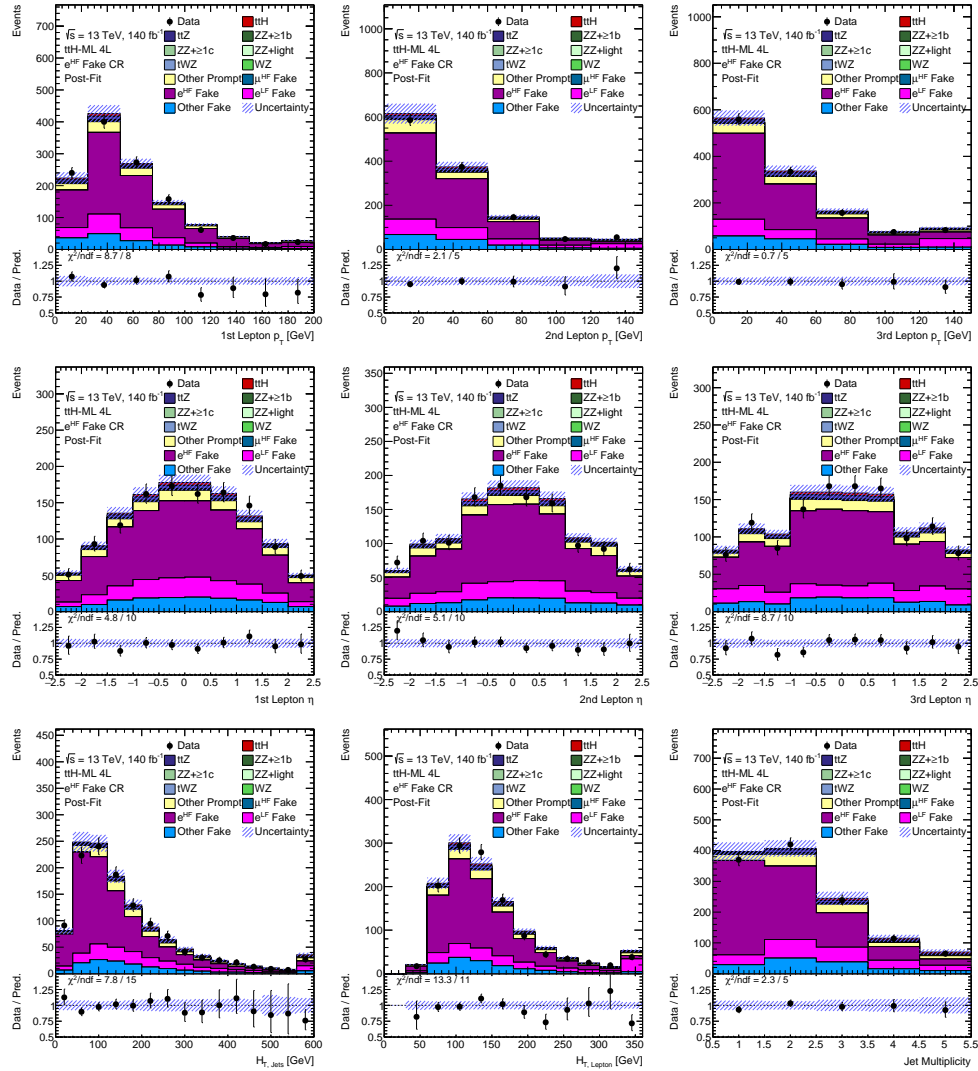
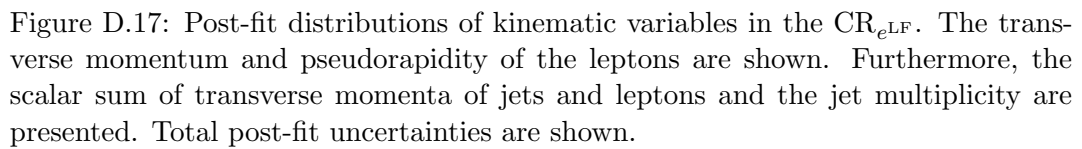


Figure D.16: Post-fit distributions of kinematic variables in the $\text{CR}_{e\text{HF}}$. The transverse momentum and pseudorapidity of the leptons are shown. Furthermore, the scalar sum of transverse momenta of jets and leptons and the jet multiplicity are presented. Total post-fit uncertainties are shown.



APPENDIX E

Shape Comparison of DNN Inputs

The shape of input distributions for all three targeted processes, $t\bar{t}H$, $t\bar{t}Z$, and ZZ , are compared in Figure E.1 to Figure E.5. All distributions are normalised to unity. Figure E.1 presents the invariant mass and distance between lepton pairs. In Figure E.2, further lepton-related variables, such as the number of SFOS, the scalar sum of the transverse momentum of all four leptons and their invariant mass, are shown. Jet-related variables such as the number of central and b -jets, together with the scalar sum of transverse momentum, are shown in Figure E.3. Figure E.4 presents other variables, such as E_T^{miss} , the effective invariant mass, and the two constructed transverse masses. The low-level variables, such as transverse momentum and pseudorapidity, are compared in Figure E.5.

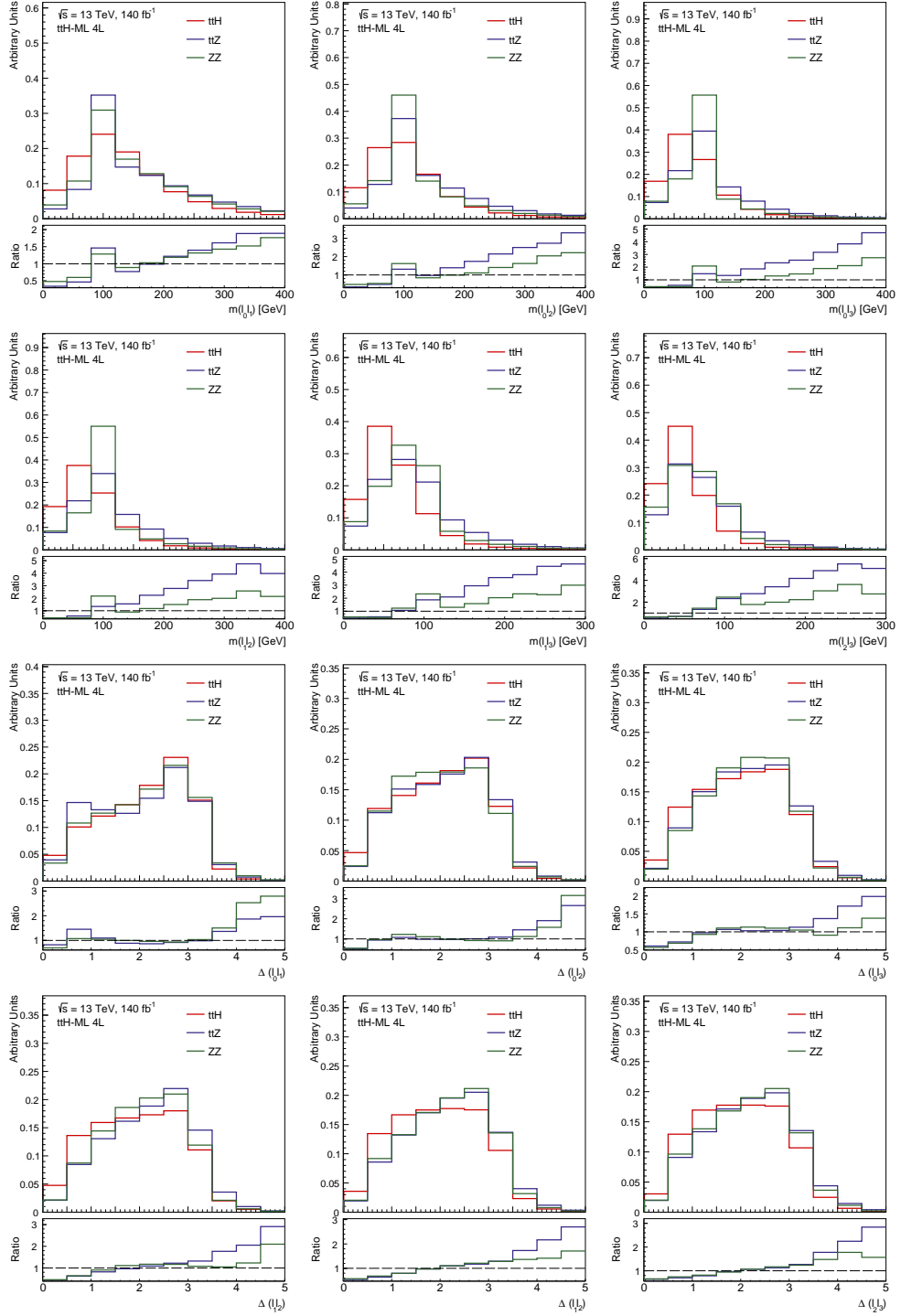


Figure E.1: Comparison of the invariant masses of lepton pairs and their distances for all three target processes ttH , ttZ , and ZZ . All distributions are normalised to unity.

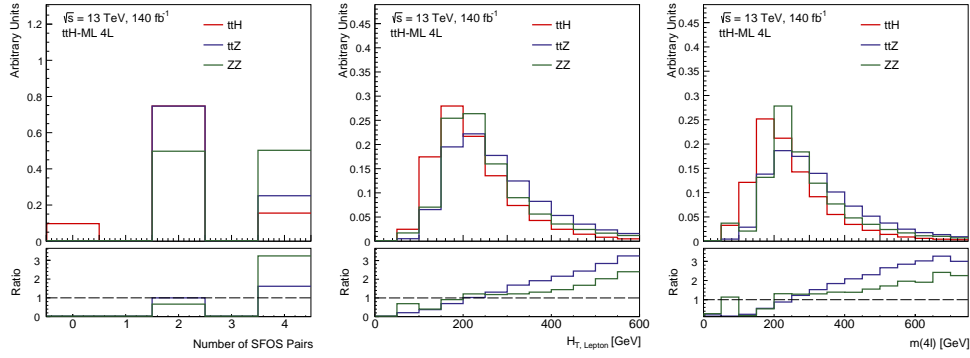


Figure E.2: Comparison of other lepton-related variables for all three target processes $t\bar{t}H$, $t\bar{t}Z$, and ZZ . All distributions are normalised to unity.

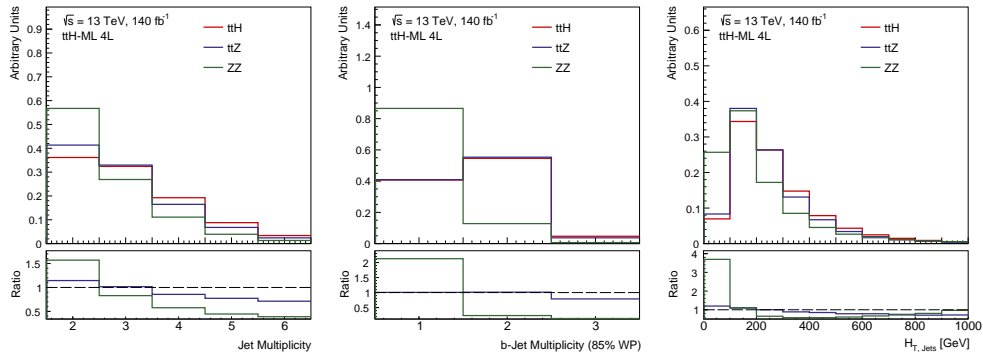


Figure E.3: Comparison of jet related variables for all three target processes $t\bar{t}H$, $t\bar{t}Z$, and ZZ . All distributions are normalised to unity.

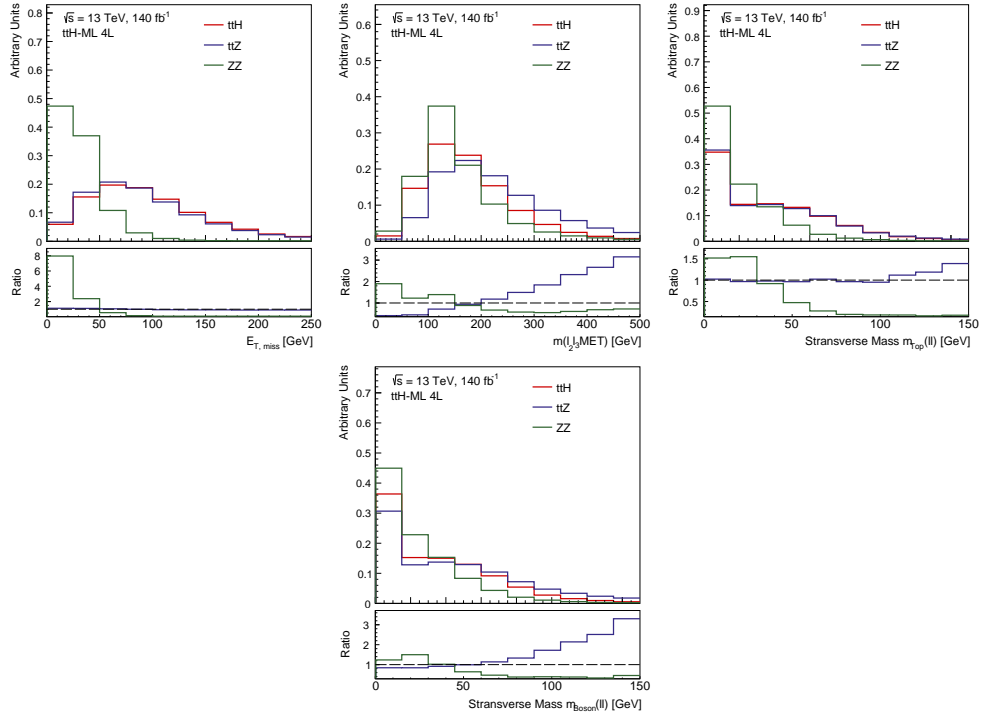


Figure E.4: Comparison of E_T^{miss} , the effective invariant mass, and the two transverse masses for all three target processes $t\bar{t}H$, $t\bar{t}Z$, and ZZ . All distributions are normalised to unity.

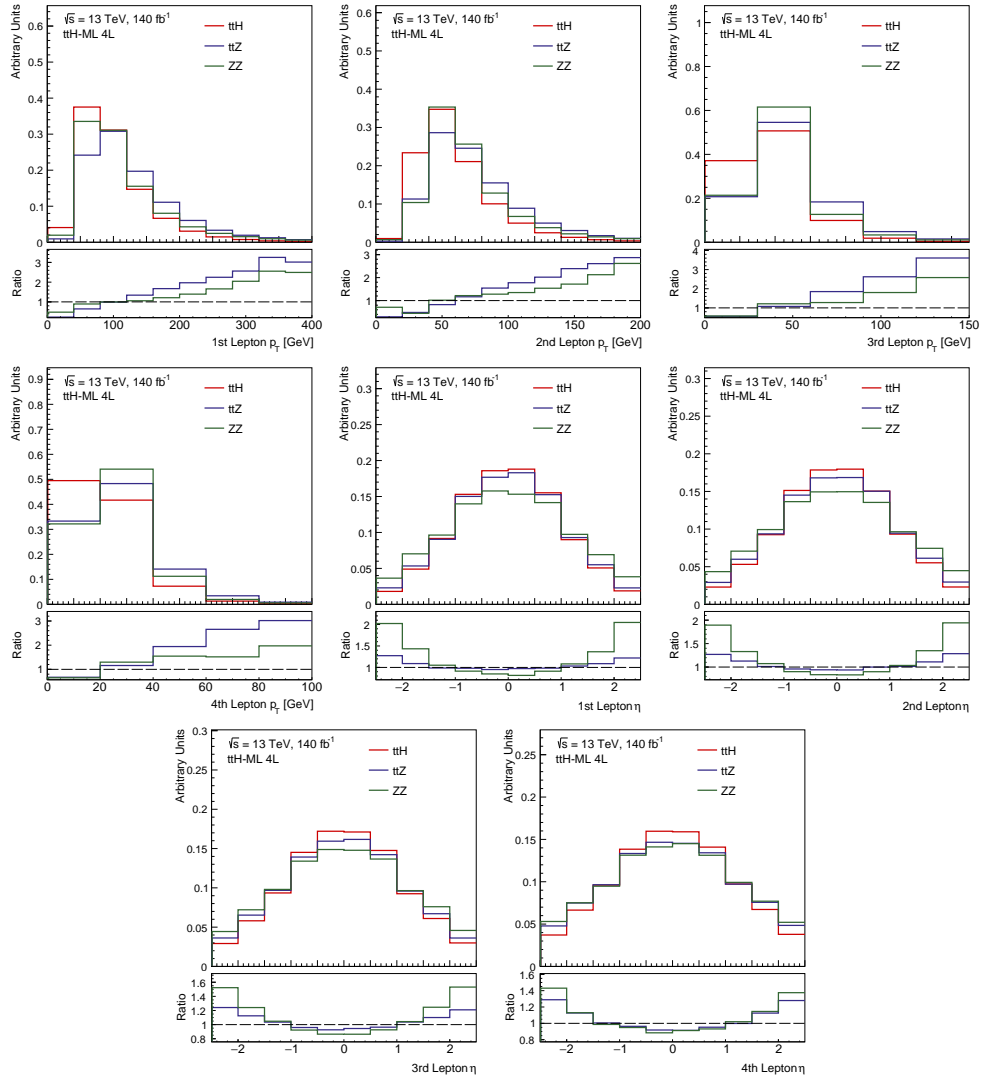


Figure E.5: Comparison of the transverse momentum and pseudorapidity of all four leptons and all three target processes $t\bar{t}H$, $t\bar{t}Z$, and ZZ . All distributions are normalised to unity.

APPENDIX F

Negative Weight Treatment

Negative weights influence the training as they change the normalisation and shape of input distributions. Furthermore, negative weights can cause a change of sign, resulting in negative loss values. The treatment of negative weights and impact on distributions is shown in Figure F.1 for the $t\bar{t}H$ samples, in Figure F.2 for the $t\bar{t}Z$ samples, and in Figure F.3 for the ZZ samples. The nominal prediction, considering both negative and positive events, is compared with scaling the positive weights with a correction factor, compensating for negative weight contributions. Furthermore, the nominal prediction is compared with taking the absolute value of weights or only positive weights. The scaling method provides a satisfactory treatment of negative events, preserving normalisation and shape, especially for $t\bar{t}Z$, having the most significant fraction of events with negative weights.

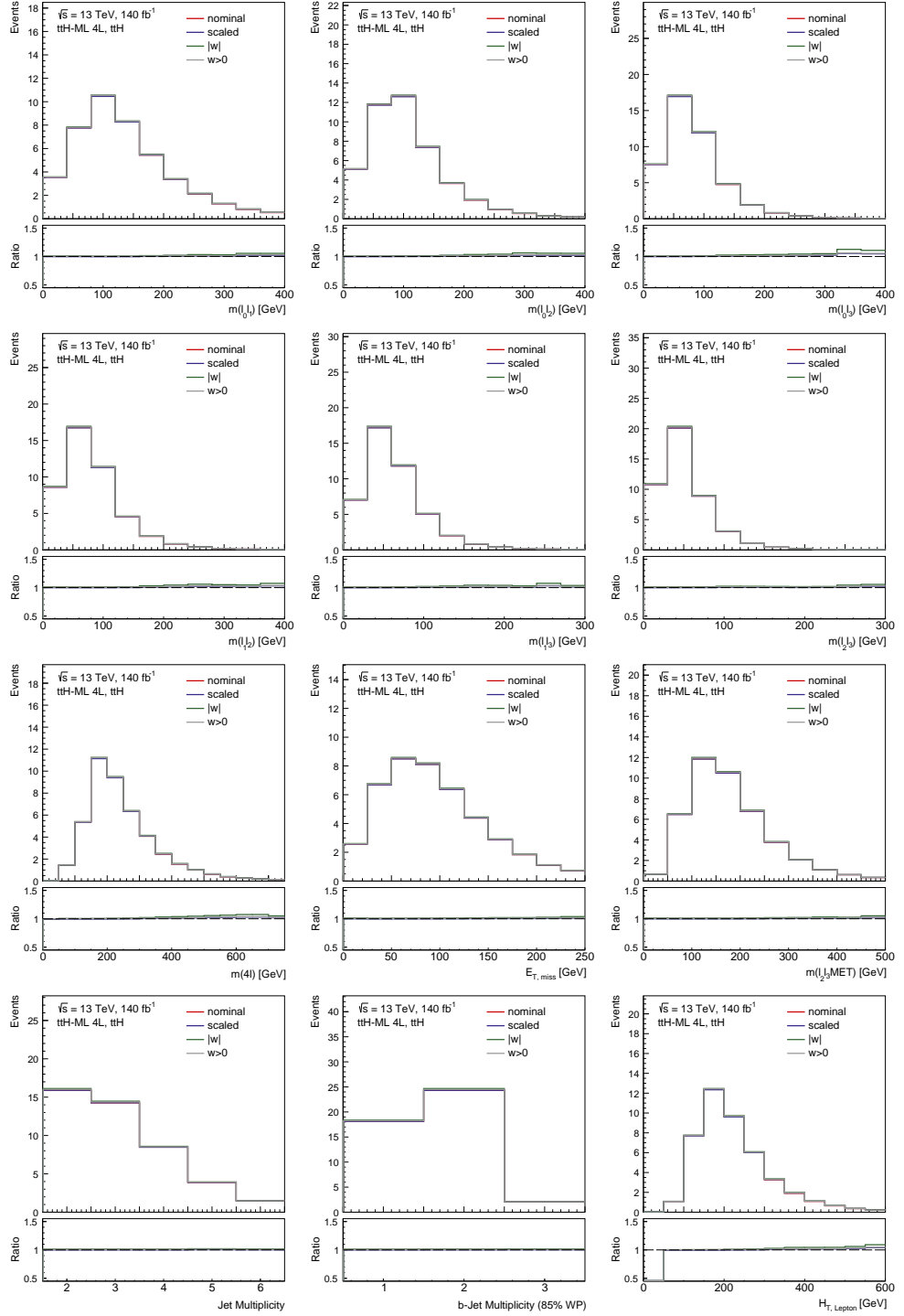


Figure F.1: Comparison of different negative weight treatments with respect to the expected nominal prediction, including both negative and positive event weights, on input distributions for the ttH samples.

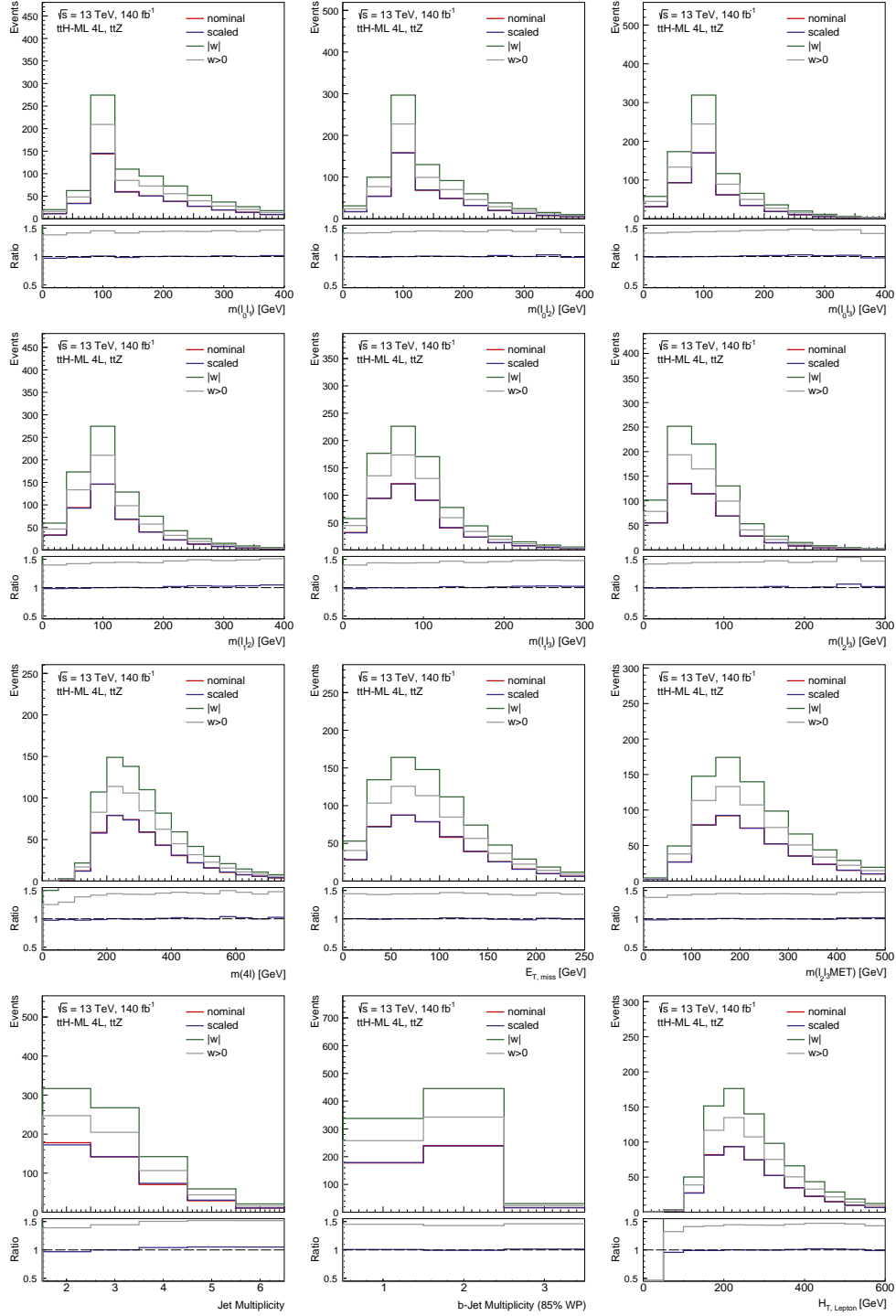


Figure F.2: Comparison of different negative weight treatments with respect to the expected nominal prediction, including both negative and positive event weights, on input distributions for the ttZ samples.

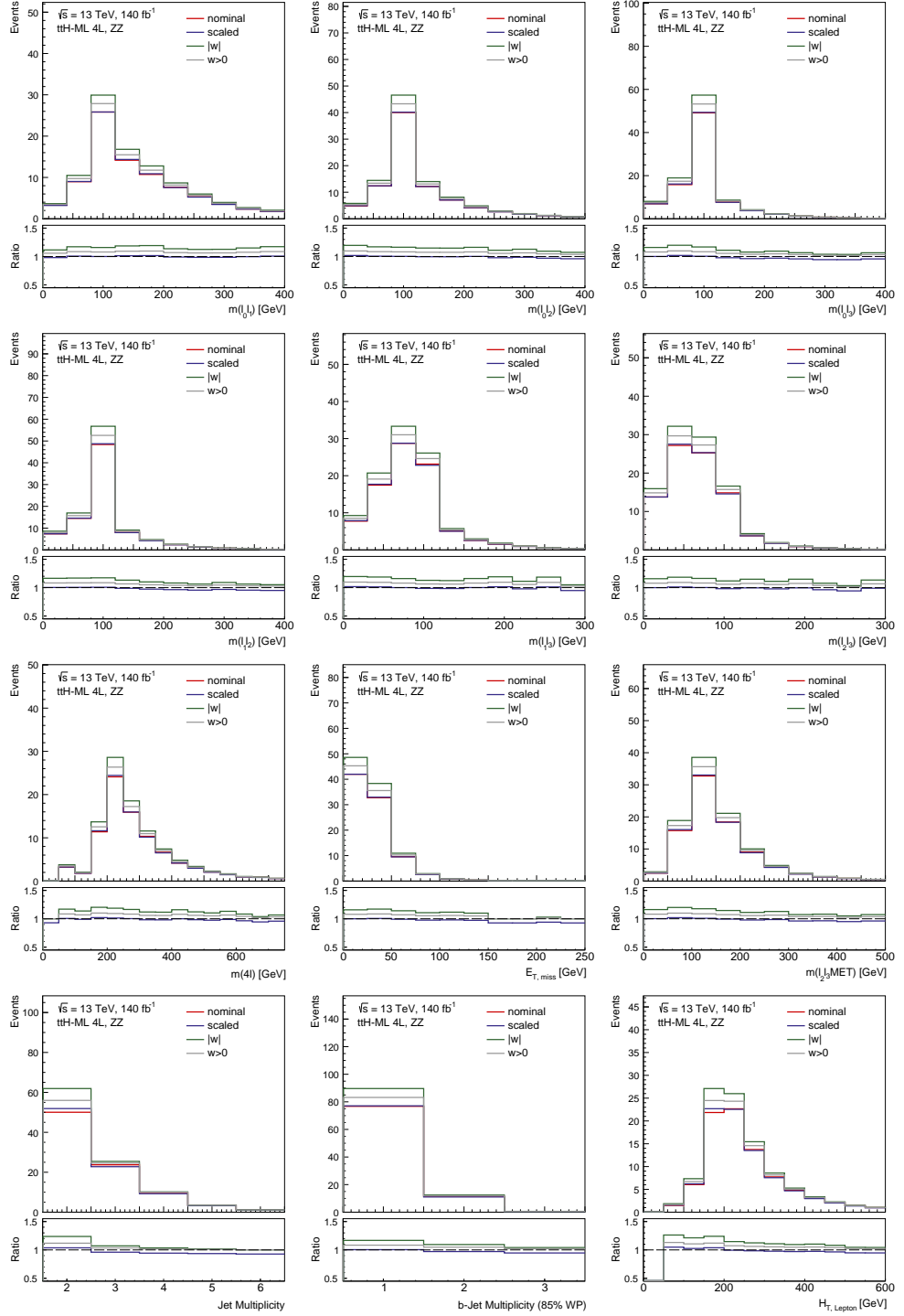


Figure F.3: Comparison of different negative weight treatments with respect to the expected nominal prediction, including both negative and positive event weights, on input distributions for the ZZ samples.

Signal and Control Region Optimisation for the 4ℓ Phase-Space

A control region for ZZ events can be designed by applying a cut on the DNN_{ZZ} score, splitting the preselection into ZZ events and remaining $t\bar{t}H$ and $t\bar{t}Z$ ones. The cut should be optimised to enhance the signal over background ratio and signal significance. On the left in Figure G.1, the signal-to-background ratios and signal significance for the remaining $t\bar{t}H$ and $t\bar{t}Z$ regions as a function of the DNN_{ZZ} are shown. The expected signal and background yields are presented on the right as a function of the DNN_{ZZ} score. To maximise signal-to-background ratio and signal significance, a cut of $\text{DNN}_{ZZ} = 0.1$ is chosen. Decreasing the cut would remove signal events, diluting the expected signal sensitivity. At the same time, a larger cut would increase the expected signal yield but also disproportionately the expected background contribution, as seen on the right in Figure G.1.

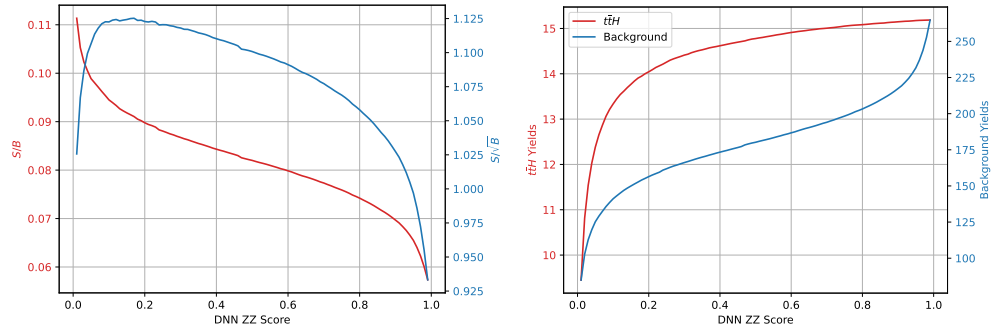


Figure G.1: On the left side, the signal-to-background ratios and signal significance for the signal-enriched region of the preselection as a function of the applied cut on the DNN_{ZZ} score. On the right side, the $t\bar{t}H$ and background yields are presented for the signal-enriched region of the preselection after applying different cuts on the DNN_{ZZ} score.

Transverse Momentum Reweighting

A mismodelling of the transverse momentum of e^{HF} fakes is observed in the $\text{CR}_{e^{\text{HF}}}$. The shape of the transverse momentum distribution for e^{HF} fakes is reweighted with respect to data. The non-reweighted distribution is presented on the left side of Figure H.1. The reweighted one is shown on the right side. An additional systematic uncertainty is introduced, which takes the reweighted distribution as nominal and the non-reweighted one as a reference. Both distributions show total pre-fit uncertainties. The mentioned systematic uncertainty is applied for the reweighted distribution.

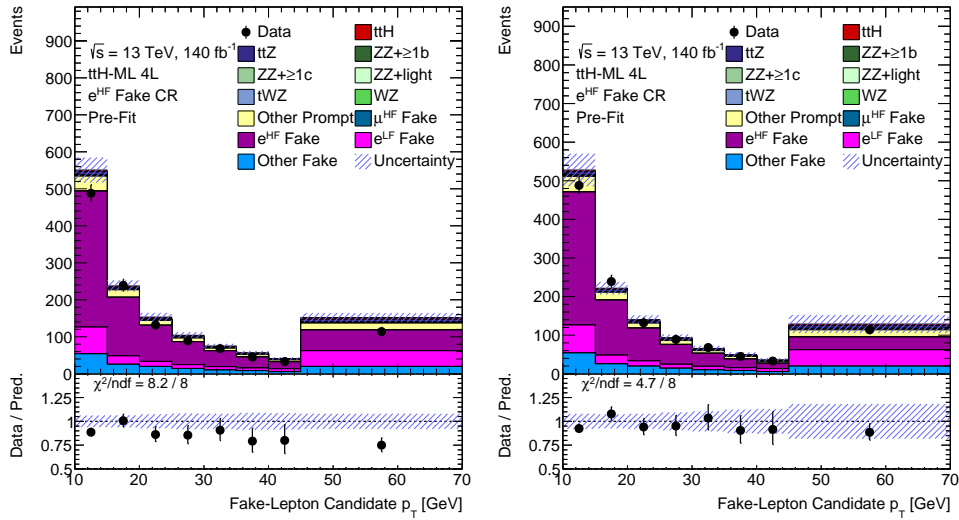


Figure H.1: On the left side, the non-reweighted distribution of the transverse momentum of the fake lepton candidate in the $\text{CR}_{e^{\text{HF}}}$ is shown. On the right side, the reweighted distribution is presented. Total pre-fit uncertainties are shown.

Pruning for the 4ℓ Channel

norm shape	no pruning	0.05	0.1	0.2
no pruning	-	-0.48 %	-2.37 %	-2.41 %
0.05	-0.12 %	-0.67 %	-2.64 %	-2.66 %
0.1	-0.21 %	-0.74 %	-2.73 %	-2.76 %
0.2	-0.21 %	-0.67 %	-2.75 %	-2.78 %

Table I.1: The relative change of expected sensitivity of the 4ℓ channel using Asimov data with respect to the no pruning case using a pruning threshold of zero for both normalisation and shape. Various shape and normalisation pruning threshold combinations are tested, using values of 0.05, 0.1, and 0.2. The thresholds for the 4ℓ channel are 0.05 for normalisation and 0.2 for shape.

Multiple shape and normalisation pruning thresholds are tested using combinations of values with 0.05, 0.1, and 0.2. In Table I.1, the relative change of sensitivity on $\mu_{t\bar{t}H}$ using Asimov data for threshold combinations are shown; the relative change is evaluated with respect to the non-pruning setup, using a shape and normalisation threshold of zero. With higher thresholds, the expected sensitivity increases. The chosen pruning thresholds for the 4ℓ channel are 0.05 for normalisation and 0.2 for shape, increasing the expected signal sensitivity by 0.67 %, which is much smaller than the expected sensitivity on $\mu_{t\bar{t}H}$ using the Asimov pseudodata. Furthermore, systematics with a normalisation impact larger than 99 % are dropped.